3D POROUS GRAPHENE-POLYMER MATERIALS FOR CO_2 CAPTURE

IRANZU BARBARIN ABARZUZA

PhD Thesis 2022

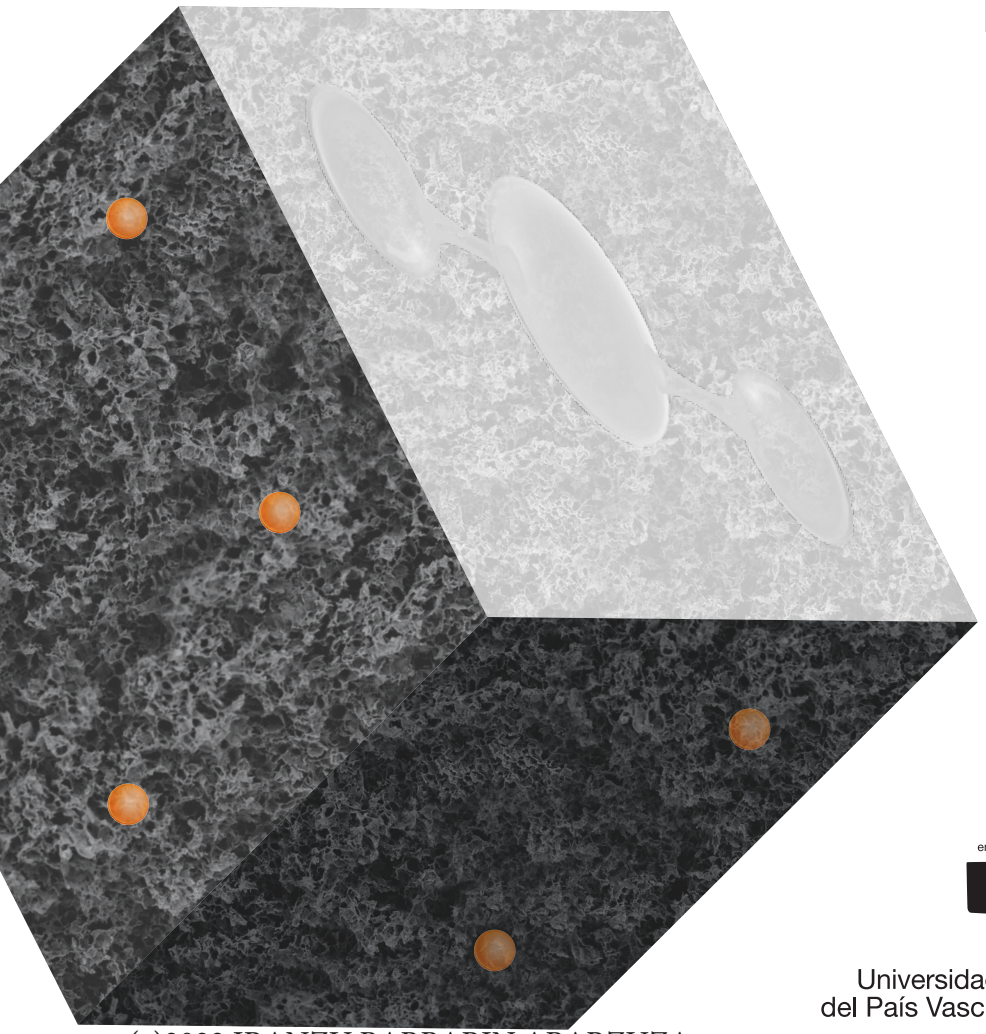

eman ta zabal zazu

Universidad del País Vasco

Euskal Herriko Unibertsitatea

3D POROUS GRAPHENE-POLYMER MATERIALS FOR CO_2 CAPTURE

Iranzu Barbarin Abarzuza

Supervisor:

Prof. Radmila Tomovska

Chemical Engineering Group

University of the Basque Country UPV/EHU

Donostia – San Sebastian

2022

POLYMAT

eman ta zabal zazu

Universidad del País Vasco

Euskal Herriko Unibertsitatea

Aita, Ama y Amaia,

Acknowledgements

First, I would like to thank my supervisor Prof. Radmila Tomovska for giving me the opportunity to do this PhD. Muchas gracias Radmila, ha sido un placer poder trabajar contigo y aprender de ti. Eres un modelo a seguir tanto personalmente como profesionalmente, por tu amabilidad, paciencia, constancia y trabajo. Todo esfuerzo tiene su recompensa. Ви благодарам многу.

I would also like to thank all the professors of the group for their discussions and advices during these years, from the TFG, TFM, and to this PhD. I also thank Ines for her support. Thank you to all the members of the polymerization processes group and other groups in POLYMAT.

Gracias Nikos por tu apoyo incondicional desde el principio de la tesis.

Thanks to the Spanish Ministry of Economy, Industry and Competitiveness for the predoctoral FPI (BES-2017-080221) fellowship received to carry out the PhD.

Contents

Chapter 1. Introduction

Chapter 2. Neat rGO monoliths: effect of synthesis conditions on properties and adsorption performance

Chapter 4. Introducing and understanding of outstanding CO_2/N_2 selectivity in 3D graphene-polymer monoliths

Chapter 5. Tailoring of textural properties of 3D composite monoliths made of graphene and highly crosslinked polymer particles towards improved CO_2 sorption

Chapter 6. Scale-up the productivity of synthesis of 3D graphene-based composite monolithic structures and study of high-pressure CO_2 adsorption performance

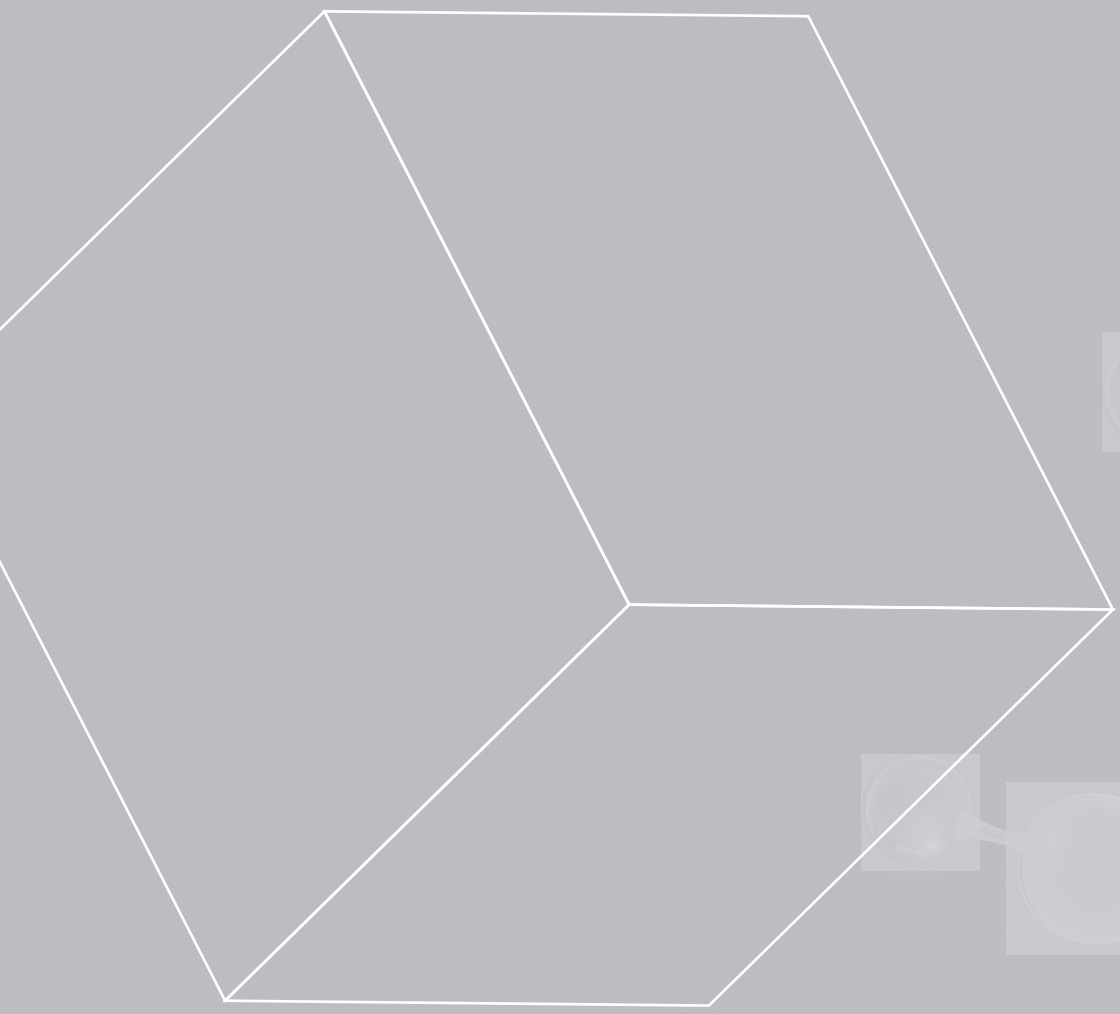

CHAPTER 1

Introduction

Chapter 1. Introduction

1.1. An insight into anthropogenic CO_2 emission

The drastic rise of carbon dioxide (CO_2) emission in the atmosphere is changing the world.

Climate change is one of the largest environmental concerns humankind is facing, believed to be caused by the gradual increase in Earth´s average surface temperature, known as global warming. All pieces of evidence point out that the substantial increase in the concentration of greenhouse gases (GHGs) in the atmosphere, where CO_2 gas is the main constituent, is the primary reason why the surface temperature increases.[1,2] The global warming impact is already perceptible to the human eyes in either physical or biological changes, such as, extreme weather, melting of glaciers, ocean acidification, and animal migration patterns.[3–6] Hence, CO_2 is the most influential GHG, the concentration of which is driven by human activities.

Since industrial revolution, the burning of fossil fuels (i.e. coal, petroleum, and natural gas) has become the principal energy source (about 80 % of the energy demanded all over the word is obtained from the combustion of fossil fuels).[7,8] Energy is consumed by different sectors such as electric power, industrial activity, transportation, residential, and commercial sectors. The increased industrialization, economy, and global population growth with high-energy requirements have caused an excessive consumption of fossil fuels, causing an uncontrolled emission of CO_2. A corresponding increase, from 280 ppm CO_2 during pre-industrial time (where the concentration was relatively constant), to just over 400 ppm today, is projected to reach 570

ppm by the year 2100, causing a rise of average global temperature by around 1.9 °C (Figure 1.1 and Figure 1.2).[9,10] According to The Intergovernmental Panel on Climate Change (IPCC):

"The situation will become worse in the future driven largely by economic and population growth will cause further warming and long-lasting changes in all components of the climate system, increasing the likelihood of severe, pervasive and irreversible impacts for people and ecosystems".[11]

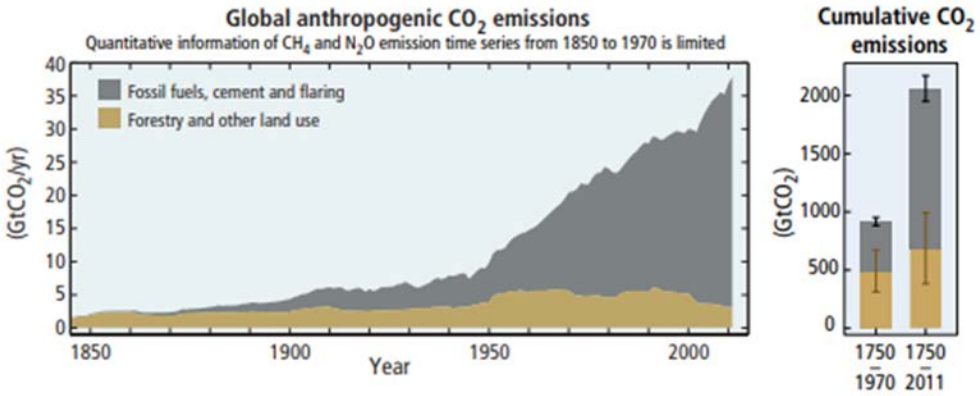

Figure 1.1. Global anthropogenic CO_2 emissions from forestry and other land use as well as from burning of fossil fuel, cement production and flaring. Cumulative emissions of CO_2 from these sources and their uncertainties are shown as bars and whiskers, respectively, on the right hand side.[11]

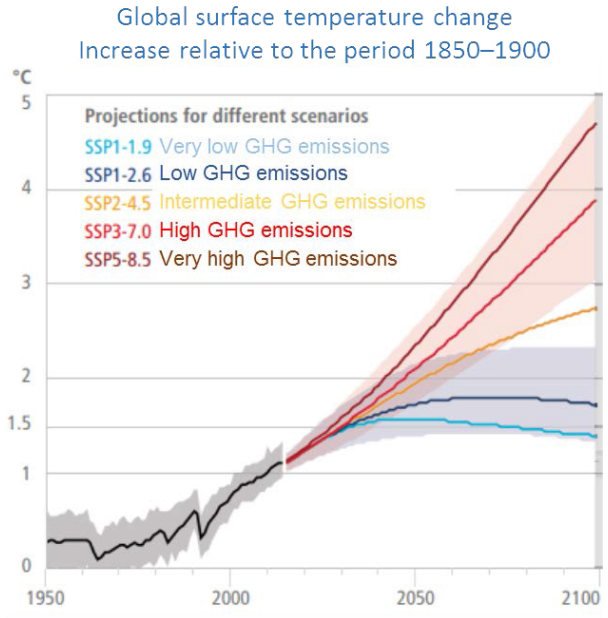

Figure 1.2. Global surface temperature changes in ºC relative to 1850-1900, under different GHG emissions scenarios. These changes were obtained by combining model simulations with observational constraints based on past simulated warming, as well as an updated assessment of equilibrium climate sensitivity.[10]

Consequently, mitigation of atmospheric CO_2 concentration is a challenging and urgent task in order to avoid deleterious environmental impact while meeting a balance between the energy and resource demands and the aspirations of the global economy. In 2015, the Paris Agreement established the Long-Term Temperature Goal of

"holding the increase in the global average temperature to well below 2 °C above pre-industrial levels and pursuing efforts to limit the temperature increase to 1.5°C above pre-industrial levels, recognising that this would significantly reduce the risks and impacts of climate change".[12]

For this reason, several approaches have been considered to be potential ways in order to reduce anthropogenic CO_2 emissions, for instance, improvement of energy efficiency or the use of renewable energy resources (solar, wind, biomass).[13–15] However, in the former approach, installation of energy saving devices may involve high cost investment. The latter, alternative energy sources and associated technologies, which have the advantage of not generating CO_2, they suffer from lack of maturity to supply us with the large energy required, so the full replacement of the combustion of fossil fuels will not be reached in the near future.[16,17] Alternatively, either carbon capture and sequestration/storage (CCS) or carbon capture and utilization (CCU) technologies are considered a viable strategy to alleviate CO_2 emissions, at least as a mid-term solution, for the improvement of environment quality.[18]

1.2. Carbon capture and sequestration (CCS) and carbon capture and utilization (CCU)

On the one hand, CCS solution transports the captured CO_2 from anthropogenic sources to a storage place (e.g. geological storage) avoiding the release into the atmosphere.[19] On the other hand, CCU uses the captured CO_2 to obtain value-added products. In Figure 1.3, the schematic illustration of both CCS and CCU technologies is presented. CCU does not consider CO_2 as a waste emission, but as a carbon source favouring the closing of the carbon cycle.[20] Nevertheless, it requires high energy for the conversion of CO_2, where the energy production is the one that produced CO_2 in the first place. In the case of CCS, its unprofitability combined with highly expensive machinery are considered the main drawbacks. In any case, the main step is to analyse the CO_2 capture process.

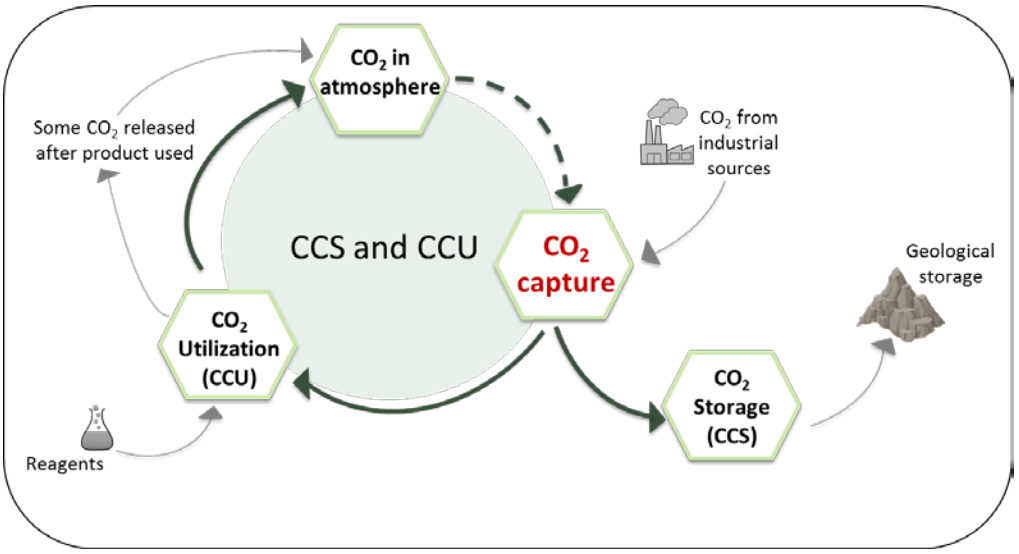

Figure 1.3. Schematic illustration of CCS and CCU technologies.

Success of CCS and CCU technologies require a development of materials that capture CO_2 in a low-cost, efficient and long-lived from a point source or large-scale productions such as power plants and other industrial processes (refineries, oil and gas production sites, chemical and petrochemical industries, iron and steel industries, cement industries, etc.). Yet, the principal point of CCS or CCU nowadays is coal-based power plants being the main contribution of the total CO_2 emissions among fossil-fuels power plants. Research on technologies that can remove CO_2 directly from the air, i.e. at low concentrations, it appears to be also a highly attractive option to bring CO_2 atmospheric concentration to a non-critical level (but so far comparably less considered).[21,22]

Furthermore, one of the principal attraction of CCS and CCU alternatives is that there is no requirement of elimination or limitation of the use of fossil fuels, while avoiding the meaningful contribution to greenhouse effect. Since the CO_2 capture is the most expensive step of CCS and

CCU, many researches have targeted to develop new approaches or improve the ongoing technologies with the aim to attain a capture cost acceptable to the energy industry.[23] In coal-fired power plants, CO_2 can be captured from different technology processes, classified as: i) pre-combustion, ii) oxy-combustion and iii) post-combustion capture.[24] The schematic representation of each technology is presented in Figure 1.4. Pre-combustion technology involves the pre-treatment separation of carbon before combustion take place, which implies high-pressure (20-30 bar) and high temperature separation.[25,26] In oxy-combustion, the nitrogen is removed from the oxidizer (air) to carry out the combustion process in highly pure oxygen. Thus, the low amount of nitrogen and high CO_2 concentration in the exhaust gas enhances the sorption efficiency. Nevertheless, the oxy-fuel combustion works at pressure in the range of 20-30 bar, and temperatures of 100-300 °C. Furthermore, if the O_2 concentration is very high, it causes problems, such as corrosion and leaks into the plant, and besides, the O_2/air separation step requires a significant auxiliary power.[27,28] The latter, post-combustion capture eliminates the necessity for substantial adjustments to combustion cycle as it can be retrofitted into existing power plants considered the most straightforward schema and forms the basis of the current infrastructure in CCS and CCU, i.e. if the capture process shuts down, the plant can still function.[29–31] Once flue gas combustion has taken place, it consists of CO_2 uptake from mainly CO_2/N_2 mixture gas at atmospheric pressures and at 40-80 °C,[32] nevertheless, it has the inconvenience that the CO_2 is much diluted in the gas stream that influences the capture efficiency. Therefore, the driving force for CO_2 separation is very low.[32] Emissions from post-combustion process typically consists of 70-75 % N_2, 10-15 % CO_2, 8-10 % H_2O, 3-4 % O_2, with trace levels of SO_X, NO_X, and other compounds.

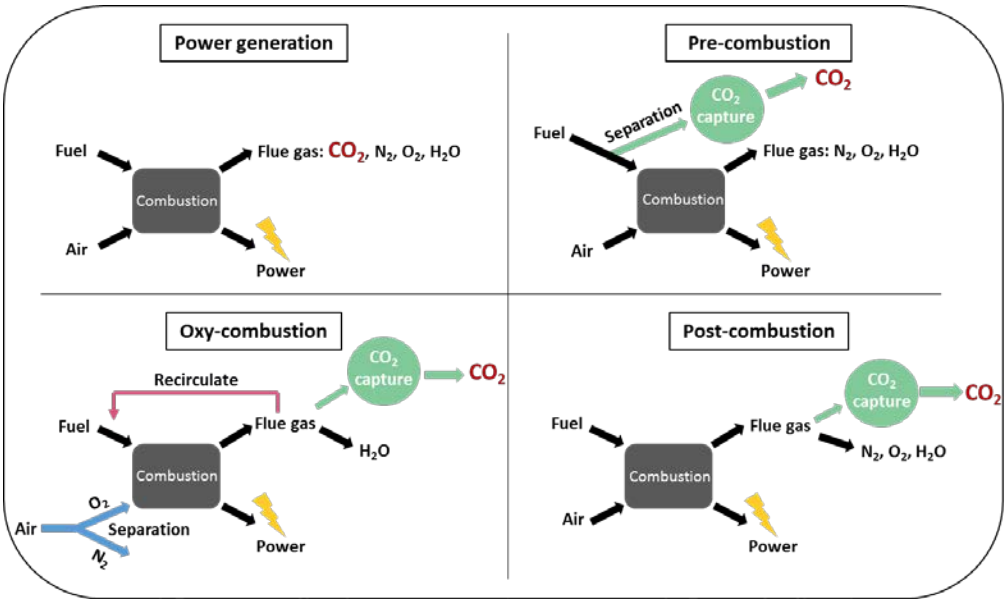

Figure 1.4. Schematic representation of fossil fuel-based power generation, pre-combustion, oxy-combustion, and post-combustion capture technologies.

Several CO_2 separation approaches from flue gas streams have been studied or even implemented for the post-combustion capture process: solvent absorption, membrane separation, cryogenic distillation, chemical looping and physical adsorption.[33] The combination of two or more approaches (namely, hybrid CO_2 capture processes) has been also taken into consideration as a possible option.[34]

Amongst these methods, solvent or liquid absorption is the most common currently used and the most extensively studied method. It employs an aqueous solution of monoethanolamine (MEA), or derivatives, as a solvent (also referred to as “scrubbing”) that operates at ordinary temperature and pressure.[35–41] This method is commercially available and in use nowadays. However, the chemically absorbed CO_2 requires high temperatures to be released afterwards

due to the chemical interactions (it causes 70 % of additional cost).[42,43] This makes the process energy-consuming during regeneration step of the solvent. So, high energy demand and cost of the process for regeneration with other drawbacks, such as the corrosivity of amine solution toward the vessels, make this technology less attractive for commercial point of view having large room of further improvement.[44–47]

On the other hand, membrane separation overcomes some of the disadvantages of conventional absorption (simple modular systems and no regeneration energy required, among others). Yet, the main drawback of this separation method is that membrane materials have poor performance, i.e. low selectivity and permeability, under flue gas operating conditions where the concentration and pressure of CO_2 is low.[48] Furthermore, membrane-based technologies for CO_2 capture are not mature because they have been briefly evaluated in order to determine the limitations and that prevent to realize the potentials of this method in an industrial scale.[49–52]

Cryogenic distillation is based on the periodic operation of cryogenically cooled packed beds and the process cycle has three consecutive steps: a cooling to temperatures below -120 °C and high pressure (where the CO_2 is solidified and separated from other gases), capture and recovery step. The low temperatures and high pressures make it an energy intensive process.[53–55]

Furthermore, chemical-looping combustion involves the use of a metal oxide as an oxygen carrier, which oxidizes the gaseous fuel producing CO_2 and water vapour. Still, the commercial scale-up of this technology depends nowadays on the availability of high performing and stable oxygen carriers.[56–59]

Adsorption, as alternative process for CO_2 capture, is a physical or chemical surface phenomenon, also known as physisorption or chemisorption, respectively.[60] By this process, the molecules of CO_2 gas (adsorbate) separates from one phase and accumulates at a surface of a solid substance (adsorbent). On the one hand, chemical adsorption o chemisorption involves establishing a chemical bond (covalent) between the adsorbate and adsorbent, and thus, the regeneration of the adsorbent is more challenging. In physical adsorption or physisorption, instead, the interaction between the substances is caused mainly by van der Waals forces and electrostatic forces having a low heat of adsorption and easy reverse process being very striking step in the carbon capture processes.

1.2.1. Physical adsorption

Physical adsorption is a surface-based phenomenon, where solid adsorbent materials have characteristic surface properties. For example, the high surface area of an adsorbent increases the surface energy and the amount of surface-active groups important for establishing larger interaction with CO_2 gas molecules. Thus, the process relies mainly on porous materials with various desired attributes, such as their equilibrium adsorption capacity, high selectivity, easy regeneration step, multicycle durability, and fast adsorption/desorption kinetics compared to other conventional technologies.[61–65]

Physical solid adsorbents must meet some relevant requirements in order to be both economical and operational for CO_2 post-combustion capture process:

1. Adsorption capacity for CO_2: Adsorption capacity is defined as the amount of CO_2 adsorbed per unit mass of the adsorbent material at thermodynamic equilibrium. The adsorption capacity of the sorbent materials is an important parameter that affects

both the sorbent quantity and process equipment size. Under similar other costs, the adsorption capacity must be in the range of 3-4 mmol/g in order to be competitive with MEA absorption system.[66]

2. Selectivity of CO_2: Selectivity is the ratio of the CO_2 adsorption capacity to that of another components at a given flue gas composition (e.g., N_2, CH_4,…) and determines the purity of the adsorbed CO_2. The purity of the CO_2 captured greatly affects sequestration and transportation, and hence, the process economics. Even though, it is ideally to determine experimentally the selectivity under competitive adsorption process, the selectivity, in most of the cases, is calculated by Ideal Adsorbed Solution Theory (IAST) from the individual adsorption isotherms of the gasses.[67]

3. Adsorption/desorption kinetics: The cycle time of an adsorption system depends on the kinetics of adsorption and desorption, and therefore, the faster are both processes, less time will be needed to capture a given volume of flue gas making the capture more economical.

4. Mechanical/thermal stability: Specific operation conditions should not damage or disintegrate the material in order to preserve the CO_2 capture process cost-effective. Therefore, the adsorbent must demonstrate high microstructure and morphological, mechanical and thermal stability.

5. Stability in cycle operation: A suitable adsorbent should be able to maintain its best adsorption capacity in repeated adsorption-desorption cycles, i.e., a long lifetime.

6. Chemical stability/tolerance to impurities: Chemical stability is another considerable criteria because a solid adsorbent material should be stable in moisture and in an oxidizing environment of flue gas and be resistant to some flue gas contaminants, such as SO_X and NO_X, so the adsorption process would not be negatively affected. Furthermore, high stability also guarantees the longer lifetime of the material before its replacement and hence will decrease the overall economy.

7. Regeneration of adsorbents: The energy needed for the regeneration process should be essentially low, i.e., regeneration step should be performed at mild conditions. This energy is directly related to heat or enthalpy of adsorption. Enthalpy of adsorption is the key thermodynamic parameter of adsorption and it can be calculated by using Van't Hoff or Clausius-Clapeyron equation.[68,69] Adsorption of CO_2 is an exothermic process, while desorption is endothermic. If the heat of adsorption is very high (i.e. a transition from physisorption, 5-40 kJ/mol, to chemisorption, 40-800 kJ/mol), the energy needed for the regeneration of the adsorbent will be high. Therefore, in order to ensure enough CO_2 capture in physisorption regime, a moderate heat of adsorption is necessary. An adsorbent is regenerated using temperature swing adsorption (TSA) or pressure swing adsorption (PSA) processes where the CO_2 is removed.[70,71]

8. Material costs: The global cost of the system represents one of the most important characteristics, and perhaps the most one. Yet, most of the studies related to CO_2 adsorption by carbon-based materials used in this PhD Thesis, are still more fundamental and the overall cost of the process was not considered, yet.

In view of the above, it is quite challenging to find a single optimal adsorbent that fulfil all of these requirements. Several research groups have considered numerous solid materials as promising candidates or useful materials for CO_2 capture from flue gas with low cost and high-performance. Adsorbents investigated so far comprise activated carbons,[72–78] porous inorganic materials (such as zeolites,[79–83] silica[84]), metal organic frameworks (MOF),[85–88] porous organic polymers (POP, such as conjugated microporous polymers,[89] covalent organic frameworks,[90,91] hypercrosslinked porous polymers,[92] porous aromatic frameworks[93]), hydroxyl metal carbonates,[94] and ionic liquids,[95] among others. Generally, high specific surface area and uniformity and tuneability of their internal pores make these materials good aspirants for CO_2 capture.[96]

Nevertheless, most of these physical adsorbents, although they fulfil several requirements, principally in regards to the CO_2 adsorption capacity, also suffer several drawbacks: difficult handling solids (powders), slow adsorption kinetics, low CO_2 selectivity and thermal, chemical and mechanical instability in cycling, thus, the scale up feasibility is low.[97] Consequently, the development of a low-cost adsorbent with high adsorption capacity, novel, versatile, cycle operations capacity, with low carbon footprint and selectivity over CO_2 vs other greenhouse gasses is still highly desired, but challenging.

Herein, the use of solid adsorbents based on graphene and its three-dimensional (3D) porous structures for CO_2 capture are first reviewed. In the same way, the main parameters affecting the adsorption process are discussed, and how could be improved by the addition of a second constituent, that in the present context refers to polymer materials. Finally, the process of emulsion polymerization that is one of the most relevant technique for the synthesis of aqueous polymer dispersions used throughout this study is described.

1.3. Graphene oxide (GO) and reduced graphene oxide (rGO)

Graphene has been intensively studied and receiving tremendous attention since its isolation in 2004.[98] Graphene, which is the composing unit of graphite, is an one-atom-thick sheet of sp^2 hybridized carbon atoms arranged into a honeycomb-like network in a single plane (2D nanomaterial).[99] It exhibits unique chemical,[100] electronic,[101–103] mechanical,[104] thermal,[105,106] and optical properties,[107] which make it with high application perspectives. Besides, it is the thinnest known material with an exceptionally theoretical specific surface area of 2630 m^2/g.[108] To date, reduction process of graphene oxide (GO) is the most easily and economically cheapest practised procedure towards large-scale production of reduced graphene oxide (rGO) or graphene.[109] Nevertheless, rGO is known as the low-quality graphene compared to pristine graphene, due to numerous physical and chemical defects. In Figure 1.5, a scheme of this synthesis procedure of graphene is presented. In the first production step, graphite oxide is obtained by the well-known oxidative treatment Hummer´s method, where graphite is oxidised.[110] Graphite oxide is made of aggregated GO sheets, where each GO consists of oxidized graphene sheets decorated mostly with hydroxyl (-OH) and epoxy (-COC-) groups on the basal plane, and carboxyl (-COOH) and carbonyl (-CO) groups located at the edges.[111] As graphite oxide still retains a layered structure, where the individual layers are bonded by van der Waals forces, after exfoliation step, individual sheets of GO are obtained. Finally, the GO is subjected to reduction, during which the restoration of the sp^2 hybridized carbon structure occurred by the removal of the oxygen-containing functional groups, giving rise to rGO or graphene. Although this graphene material still contain certain defects in the sp^2 carbon network, such as residual oxygen groups (sp^3 hybridization) and structural defects (five or seven member C-rings), it still holds useful properties for applications that demand a large amount of graphene. A more realistic insight may be attained in Figure 1.6, where an atomic scale high resolution TEM image of a single graphene

sheet obtained from porous carbon is presented, where six-carbons aromatic rings are clearly visible, even though it may be seen a presence of few five or seven-carbons rings as deffects.[112]

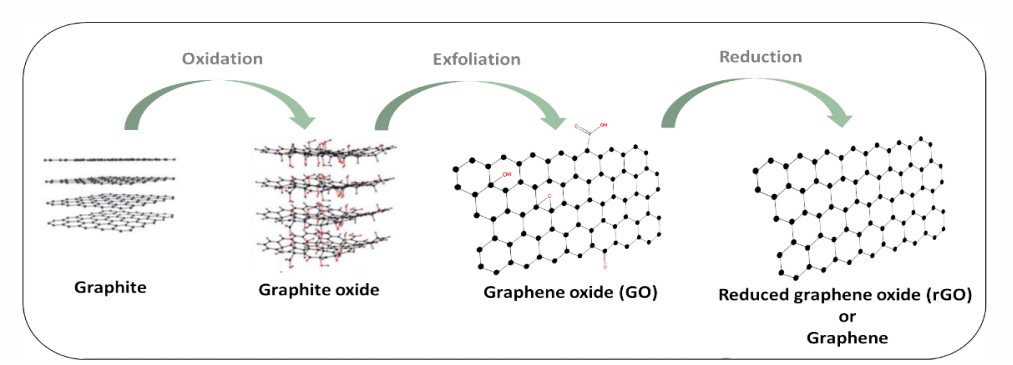

Figure 1.5. The scheme of the synthesis procedure of reduced graphene oxide or graphene.

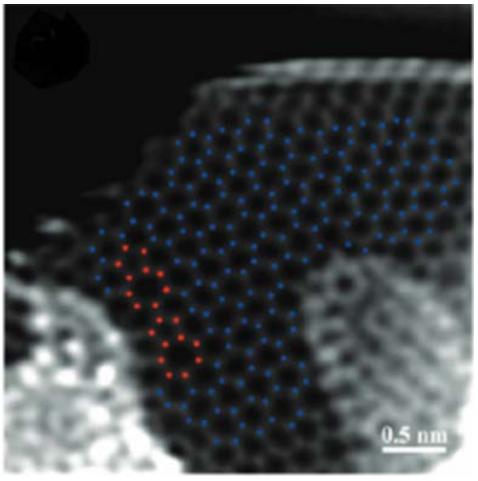

Figure 1.6. TEM image of a single graphene layer. The in-plane carbon atoms are clearly resolved, and large areas of hexagonal lattice (marked in blue) with a few five- and seven-atom ring defects (marked in red) can be seen.[112]

However, when graphene is applied practically, due to the thin structure and high surface energy, the graphene sheets or layers tend to restack resulting into structures with surface areas far below the theoretical one and lose some of their characteristic properties.[113] One solution for this problem, which moreover improve the handling of the material and its consistency, is to join the 2D graphene platelets into well-organized and hierarchically interconnected 3D structures that could retain some of the exceptional properties of the 2D material. In fact, self-assembly of 2D GO or graphene layers is an essential and low-cost strategy for developing macroscopic structures for practical application. Furthermore, the oxygen-containing functional groups provide a great opportunity to produce surface-modification reactions, which can be employed to develop functionalized graphene oxide- and graphene-based materials with desired properties.[114] Therefore, these attributes combined with thermal, mechanical, and chemical stability of the graphene increase the interest for its use as CO_2 adsorbent material.[115]

1.4. 3D graphene-based monolithic structures

Motivated by the above prospects, since 2009, porous three-dimensional (3D) graphene-based materials (e.g., graphene hydrogels/aerogels, sponges, and foams) made from graphene or GO networks have been developed.[116–119] Individual GO sheets upon losing the oxygen functionalities during reduction, wrinkle and combine together forming a self-assembled 3D structure. They attract attention in CO_2 capture, and in many other applications, due to the increase of the amount of active material per projected area, caused by the hierarchical porous structure, compared to other type of adsorbents. Not only the large surface area makes them attractive material, but also their low density, interconnected channels, stability and control of the shape and size of the pores are important factors. Moreover, the specific design of the graphene or GO layer's chemical structure can play an important role as they can be modified for not too

strong (avoiding high-energy regeneration step) and not too weak (low adsorption capacity) binding to CO_2.

Three different pore sizes regions exist in the internal 3D porous structure, according to the classification of porous materials by IUPAC: micropore < 2nm, mesopore 2-50 nm and macropore > 50 nm.[120,121] Although microporosity is required to increase surface area and adsorption capacity, microporous carbons with high surface area are frequently deficient due to the CO_2 diffusion restriction and inaccessibility to given adsorption points. The mesopores and macropores offer an easier accessibility and fast mass transport, which make them very important characteristics, too. Thus, a hierarchical 3D structure combining micropores, mesopores, and macropores is considered as an optimal adsorbent in terms of textural properties.

There are different techniques and strategies to prepare hierarchical 3D porous graphene-based materials that usually begin with a precursor GO aqueous dispersion.[122] These processes consist of integrating various nanobuilding blocks into nanostructured or even macroscopic material (monolithic structures) via different interactions within graphene layers, such as dipole interactions, electrostatic attractions, hydrophobic interactions, hydrogen bonding, and chemical bonds. However, the process mainly relies on the elimination of the oxygen-containing functional groups of the GO dispersed in water, obtaining rGO layers that are too hydrophobic to stand individual in aqueous dispersion, thus, they self-assemble creating the 3D monolithic structure. This reaction allows the formation of the 3D structure via hydrophobicity interactions and π-π stacking interactions between graphene sheets, i.e. the resulting rGO platelets become more hydrophobic and this leads to a weaker electrostatic repulsion and stronger π-π stacking interaction compared to their GO precursor. This process is template-free self-assembly method, and as the most powerful technique, was used during this PhD Thesis.

There are few ways to carry out the self-assembly process: i) Thermal reduction; ii) Chemical reduction; iii) their combination; and iv) Crosslinking method.

Thermal reduction. Although it is one of the most attractive and simple technique, high temperature, high pressures and long reaction times are required, which are difficult to proceed at large scale.[123,124] At high temperatures, the rapid heating of GO decomposes the oxygen-containing functional groups at the surface resulting in a rGO layers, however, it also removes carbon atoms from the carbon plane, which may break up the graphene sheets.[125] By varying the temperature and heating time, the degree of residual functional groups can be controlled. In 2010, Shi and co-workers,[126] reported the first example of self-assembly 2D graphene sheets into 3D macrostructures via a one-step hydrothermal process at 180 ºC for 12 h, obtaining graphene foam with interconnected porous network and excellent mechanical, electrical and thermal properties.

***Chemical reduction*.** It consists of use of a reducing agent in order to eliminate the oxygen-containing functional groups of the GO. The reduction can be achieved by adding the reducing reagent to a GO aqueous dispersion.

Combined thermal and chemical reduction. The chemical reduction reactions can be carry out at increased temperature at atmospheric pressures, to speed up the process and to shorten the reaction times.[127,128] The physical properties of the final rGO structures are significantly affected by the degree of reduction and reaction conditions. Besides, the characteristics of the starting GO aqueous dispersion, e.g., oxidation method for preparing GO, particles size and exfoliation process, also influence the final product.[129]

Hydrazine and its derivatives, e.g. hydrazine hydrate and dimethylhydrazine, are one of the most important and efficient reducing agents.[111,130,131] In any case, without any reducing agent used, the entire elimination of oxygen-containing functional groups for complete restoration of graphene has not been achieved. In 2010, Fernandez-Merino et al.,[132] studied the deoxygenation efficiency of GO suspensions by different reductants (sodium borohydride, pyrogallol, and vitamin C, in addition to hydrazine). They concluded that using hydrazine monohydrate high yield rGO was obtained, however, the high toxicity of hydrazine reagents makes not desirable the large-scale implementation.

The GO reduction process is the most used approach towards large-scale production of pristine graphene. This is why, a huge amount of different reducing agents has been investigated in order to have a basic understanding of their efficiencies (borohydrides, aluminium hydride, hydrohalic acid, sulphur-containing reducing agents, etc.).[109] Many researchers, motivated by green chemistry and environmentally friendly processes, have highlighted the need of green reductants, in order to avoid the usage of harmful and toxic agents as hydrazine. In 2017, de Silva and co-workers showed that the use of green reductants in the chemical reduction of GO, such as organic acids, plant extracts, microorganisms, sugars, proteins and amino acids.[133] Nevertheless, amongst all the green reductants, it is claimed that ascorbic acid (Vitamin C) is a powerful alternative that can compete with the widely employed hydrazine in the deoxygenation of GO.[134,135] Even still, there is no a well-defined mechanism of the reaction between ascorbic acid and GO. For example, Zhang et al.[136] demonstrated that the individual GO sheets can be readily reduced under a mild condition using ascorbic acid (AsA). The reduction of GO was performed at room temperature and resulted in a substantial removal of oxygen functionalities.

In ***crosslinking method***, multiple crosslinking molecules are selected to drive the graphene self-assembly, such as multivalent ions, metal oxides, biomolecules, polymers and

other small organic molecules.[137] In 2010, Worsley et al.[138] reported the first synthesis of 3D graphene-based aerogel by sol-gel chemistry to crosslink the individual graphene sheets through polymerization of resorcinol and formaldehyde. Then, Adhikari et al.[139] obtained a graphene-based hydrogels in the presence of polyamines, where morphological studies revealed the presence of a network structure of crosslinked nanosheets. They suggested that acid-base type electrostatic interaction and hydrogen bond are the forces occurring between the oxygen-containing functional groups on GO and the functional groups (e.g., -NH_2 or –OH) on polymers. Sui et al.[140], in 2013, demonstrated by FTIR and XPS characterization techniques that GO and polyethylenimine (PEI) were covalently linked by amine chemical bonds, forming a three-dimensional hydrogel.

Although different self-assembly routes are used, in most of the cases, the initial constituent is GO aqueous dispersion, and the final product is a 3D graphene-based monolithic structure, as it can be observed in Figure 1.7.

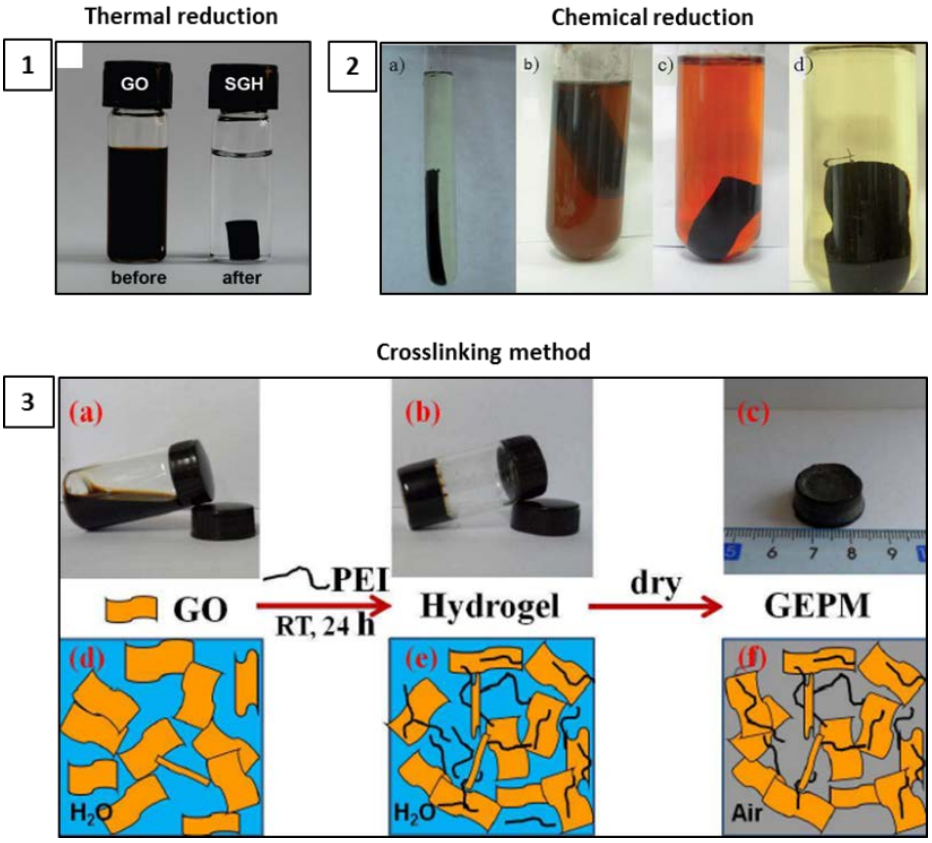

Figure 1.7. (1) Photographs of a 2 mg/mL homogeneous GO aqueous dispersion before and after hydrothermal reduction at 180 °C for 12 h.[126] (2) Photographs of graphene hydrogels prepared using various chemical reducing agents. a) Na2S. b) Vitamin C. c) HI, and d) hydroquinone.[128] (3) Illustration of the preparation process of the GO–PEI porous materials (GEPMs): digital pictures of aqueous GO dispersion (a), GO–PEI hydrogel (b), and GEPM (c) and schematic diagram of aqueous GO dispersion (d), GO–PEI hydrogel (e), and GEPM (f).[140]

Nevertheless, the self-assembly of 2D dimensional graphene into 3D materials has also been completed by other strategies, such as direct freeze-drying,[141] electrochemical deposition,[142] centrifugation of GO dispersions, and so on.[143]

Once created, the 3D porous graphene-based materials undergo certain activation processes (sometimes it can be simultaneously during production) in order to obtain materials with higher surface areas and higher micropore volumes with the aim to improve CO_2 adsorption capacity. From the various methods available, chemical activation with potassium hydroxide (KOH) is commonly used[144–146] or physical activation[147,148] in the presence of a suitable oxidizing gas, such as air, CO_2, steam, or their mixtures. On the one hand, by chemical activation, KOH reacts chemically with carbon atoms, and this reaction involves the disintegration of the structure. On the other hand, in physical activation, the oxidizing gas can introduce in-plane carbon vacancy defects (pores) into rGO sheets, since it actively reacts with the graphitic carbon atoms under specified conditions, and thus, hierarchical porous graphene-based structure is formed. Physical activation is a process of selective gasification of individual carbon atoms (not all the carbon atoms have the same reactivity) while chemical activation is not selective.[149] Nevertheless, although they are commonly used to improve the final textural properties, both chemical and physical activation techniques have several disadvantages such as additional washing stage or implementation of very high temperatures that increased the carbon footprint of the process and the costs. For example, Yun et al.[150] reported a comparative study of two 3D rGO structures that were both chemical reduced, but one of them was activated by steam gas at 900 ºC. The surface areas were 313 and 1621 m^2/g and the CO_2 adsorption capacity 2.68 and 6.31 mmol/g for non-activated and activated 3D rGO structures, respectively. Physicochemical activation, i.e. a combination of both processes, has been also used.[151] Specifically, either physical or chemical activation processes are mostly used in activated carbons materials. Activated carbons can be obtained by carbonization from almost any organic material, and as it is mentioned before, they are used as general adsorbents due to the large range of applications.[152]

It is clear that the synthesis of 3D graphene-based monoliths comprises the need of high-energy processes in a few steps of an extremely high-temperature and pressure moulding. In either case, the sustainability and environmental issue of these methods are not considered but may compromise the scale-up feasibility. Furthermore, during the production of materials with high-energy processes, the CO_2 release is high too; therefore, a negative balance of CO_2 released and captured may appear.

Numerous researches are being continuously reporting different applications of these 3D rGO structures: environmental applications (dye, gas and organic pollutant adsorption and detection),[153–155] as supports for microorganism immobilization,[156] catalysis performance,[157,158] energy storage,[159] supercapacitator,[160,161] sensors,[162] etc. In most of the reported references, they use a combination of 3D graphene-based structures with another constituent material in order to obtain a synergetic effect between them and enhance specific properties for the application required, such as polymers, ionic liquids, metals, nanoparticles, quantum dots and so on.

However, research on large CO_2 capture focused on hybrid 3D rGO materials is still limited. Addition of polymers to the 3D graphene-based structures provides many advantages.[163–165] High-performance lightweight materials could be synthesized and tailored to specific goals. As described later in this introductory chapter, the incorporation of different functional groups to the polymer backbones can modulate the interaction with CO_2. It has been demonstrated, that the functional groups containing heteroatoms, principally nitrogen, oxygen and sulphur, lead to a better interaction with CO_2.[166] Additionally, polymers are also combined with the 3D materials with the idea to improve the durability and stability, especially under processing cycles.[167]

1.4.1. 3D graphene-polymer composite monoliths for CO_2 adsorption

Understanding of the basic concepts of CO_2 adsorption process is the key method for improve or at least match high adsorption values. Two different mechanisms take part in the combination between the adsorbate from gas mixture and porous adsorbent: size exclusion or molecular sieving mechanisms and affinity-based separation.[168] By size exclusion or molecular sieving effect, a binary (or more) mixture of gases can be separated. In short, molecules with the size larger than the width of the pores of the 3D adsorbent are refused, whereas gas molecules with smaller size than the pores are adsorbed making the fractionation possible.[169] As mentioned before, CO_2 and N_2 are the predominant gases in the post-combustion technology, with a kinetic diameters close to each other, 3.30 and 3.64 Å, respectively.[170] Therefore, these values make it difficult to separate them through size exclusion technique. Besides, a proper control of pore size, pore size distribution and pore structure in 3D graphene-based composite is a challenging work that has to be assessed.[171] Nevertheless, it is worth mentioning that porous adsorbent with pores smaller than 0.7 nm (micropores) are the most efficient for CO_2 uptake at ambient temperature and pressure.[172] On the other hand, there are other differences in physical properties of CO_2 gas, such as quadrupole moment or acidity, which can be exploited in order to separate CO_2 from the gas mixture, known as affinity-based separation. Surface functionalities (heteroatoms-doped carbon surface) can exclusively interact only with CO_2 molecule via different interactions, such as electrostatic interactions.[173,174] Polymers play or can play a crucial role in CO_2 adsorption because they can be designed for having strong interactions with CO_2 molecule, i.e., design CO_2-philic groups in order to increase the amount of CO_2 captured. Furthermore, the CO_2 adsorption capacity decreases extremely at high temperatures. Thus, the surface chemistry modification of graphene-based materials is an important issue during synthesis of adsorbents with high affinity and selectivity towards CO_2. Polymers can also be synthesized with the aim to reinforce the 3D rGO structures. 3D macroassemblies are characteristic for having brittle

mechanical properties. However, the addition of polymer to these structures can lead to promising mechanical properties, improved durability and stability in cycles.

In 2013, Kemp et al.[175] reported the synthesis and adsorption capacity of porous N-doped rGO composites. Materials were obtained by the polymerization of aniline in presence of GO in aqueous medium. After that, the samples were chemically reduced by hydrazine and activated using KOH at temperatures between 400 °C to 800 °C. The best composite showed a BET surface area of 979.6 m^2/g and a CO_2 molar adsorbance capacity of 2.7 mmol/g at 25 °C. It is worth mentioning that, NGO composite was not treated by any activation process, and as a consequence, the surface area obtained was 8.5 m^2/g, because according to the authors, the polyaniline coated the rGO.

In 2017, Liu et al. synthesized a 3D sulfonated graphene coupled microporous organic polymers (MOPs) for CO_2 adsorption.[176] The MOPs were made of melamine-based porous polymer network by calcination at 450 °C. They disclosed that the adsorption capacity of CO_2 increases with an increase of the MOP content (the increase of amine loading). The highest adsorption capacity of 2.42 mmol/g CO_2 uptake at 25 °C was obtained by material that presents 38.1 wt% nitrogen content.

As in the previous cases, several type of polymers have been used in the presence of GO or rGO in order to incorporate heteroatoms into either polymer or graphene matrix, such as polythiophene,[177] polysodium 4-styrene sulfonate,[178] or polypyrrole.[179,180] All of these composites were treated by activation processes at extremely high temperatures to increase the surface area and microporosity of the materials. Thus, the incorporation of heteroatoms and the enhancement in textural properties entails an increase in CO_2 uptake capacity.

Otherwise, some of the researches reported synthesis of 3D graphene-polymer structures avoiding any activation or high-energy consuming methods. However, most of the results obtained do not achieved the high CO_2 adsorption capacities as the previous composites. For example, in 2013, Sudeep et al.[181] prepared a completely crosslinked 3D network of two dimensional GO, by polymerization using glutaraldehyde and resorcinol. The composite was activated by heating at 60 °C under high vacuum for 2 h. At room temperature, poly-GO showed adsorption capacities about 2.7 mmol/g at a high pressure of 20 atm. They explained that the observed CO_2 adsorption capacity comes from the porous morphology, through van der Waals type weak interaction between the poly-GO network and CO_2 gas molecules.

In 2019, Hsan et al.[182] reported the development of chitosan (CS) grafted GO aerogels for adsorption of CO_2 gas. CS and GO were crosslinked by using crosslinker reagents. They stated that the large number of amine groups, large surface area and high porosity, facilitates the CO_2 uptake. The CO_2 adsorption capacity of CS grafted GO aerogels was quite modest of 0.257 mmol/g at 1 bar and 25 °C.

Few different methods of constructing of monolithic porous composites have been reported in previous references. As it is explained in Section 1.4.IV, in the self-assembly by crosslinking method, polymers have been used as crosslinkers during the self-assembly of GO sheets, however this method is feasible only for polymers containing suitable functionalities able to establish covalent bonds with GO. Furthermore, one of the most often used approach is mixing of monomers with GO, followed by monomer polymerization and GO reduction steps,[183–185] however, high possibility of toxic monomer residues presence within the final structure requires a number of time-consuming and costly purification steps, which decrease the feasibility of the scale-up processes. Direct mixing of the solution polymer with GO solutions to achieve uniform dispersion, followed by a reduction self-assembly of GO, is one of the approaches for the

synthesis of these materials. Yet, this method is characterized by use of solvents, contributing towards increasing content of Volatile Organic Compounds (VOCs) in the atmosphere.

As an alternative, the precursor material of this work, it is GO aqueous dispersion, which owing to its oxygen-containing functional groups allow it to disperse in aqueous media. In this way, polymers synthesized in a dispersed systems, specifically in aqueous media, could be an attractive material to be mixed with GO.[186] Emulsion polymerization is a potential technique leading to colloidal polymer particles dispersed in a continuous medium, most often water. One of the advantages to use emulsion polymers is that polymers are “product-by-process” whose microstructural features (molecular weight, monomer sequence distribution, particles size distribution, particle morphology, etc.) are mostly defined in the reactor.[187] Thus, the final properties of the polymer could be modified for different application perspectives. In this case, polymers will be specifically synthesized by emulsion polymerization in order to obtain waterborne polymers that could improve not only the CO_2 adsorption capacity of the 3D monoliths, but also the mechanical properties of them. Additional values of these polymers is that the particles can easily be functionalized on the surface during the synthesis by using small amount of functional monomers that contain hydrophilic moiety of choice, which finished distributed on the colloidal particle surface. This provides an easy way of functionalization of the 3D graphene-based materials upon introduction of the polymer particles within the structure. In fact, surface modification of 3D graphene materials in order to generate CO_2-philic groups is a critical perspective of this PhD Thesis. Finally, and not less important is that emulsion polymerization process is industrially relevant and environmentally friendly that use water as a solvent, and this process is with the lowest carbon footprint between the industrial polymerization processes as recently demonstrated by life cycle assessment study of coatings for metal surfaces.[188] The low price of these colloidal particles is worth mentioning, too.

1.5. Polymerization in dispersed media

1.5.1. Emulsion polymerization

Polymerization processes are required for the production of synthetic organic polymers. Inexpensive production and multiple properties have been the main reasons for the development of synthetic polymers. We find polymers in our daily life on the field of packages, agriculture, medicine, textile, electronic, etc. As a data production example, the global production of polymer resins and fibbers increased from 2 metric tons (Mt) in 1950 to 380 Mt in 2015.[189] Well-known problems, such as the accumulation of plastics in landfills or in natural environment, are the consequence of this large-scale production and non-biodegradable feature. Therefore, the manufacture of polymers, in terms of synthesis, transportation, application and decomposition, is a growing concern and in this way, they started to be oriented into the direction of environmentally friendly solution. For example, approaches to reduce VOCs and to safer production involve the replacement of solventborne polymers by waterborne polymeric dispersions.

Emulsion polymerization is the leading industrial technique to synthesize waterborne polymer dispersions, e.g. colloidal organic particles, in the range from 50 to 1000 nm, dispersed in aqueous medium. This product is commonly called latex. In this technique, monomers with limited water solubility are dispersed in water and polymerized by free radical polymerization (FRP). Materials obtained by emulsion polymerization, after drying or as dispersions, are employed in a wide range of applications. Polymer dispersions are used, for example, in synthetic rubber, paints, coatings, adhesives, leather treatment, additives for construction materials, etc.[190]

This technique presents several advantages over bulk or solution free-radical polymerizations. In bulk polymerization, for example, the principal advantage is that a very pure

polymer is obtained at a high production rate per unit volume of the reactor as the only constituents of the formulation are monomers and the initiator or catalyst (Figure 1.8.A). However, the difficulty of the polymerization heat control or removal because of the high viscosity of the system associated with the high concentration of polymer makes this technique less attractive. For reducing the drawbacks of bulk polymerization, the process can be carried out in solution where the reaction results in a soluble polymer in the chosen solvent (Figure 1.8.B).[191] The presence of the solvent lowers the monomer concentration and assists in heat removal and control, consequently, the thermal control is much easier if the monomer is polymerized in solution. Nevertheless, the main limitation is dealing with an environmentally unfriendly solvent, as solvent recovery and removal steps from the polymer are needed, as well as when applied from solution, this process contributes to huge VOC quantities released in the atmosphere.

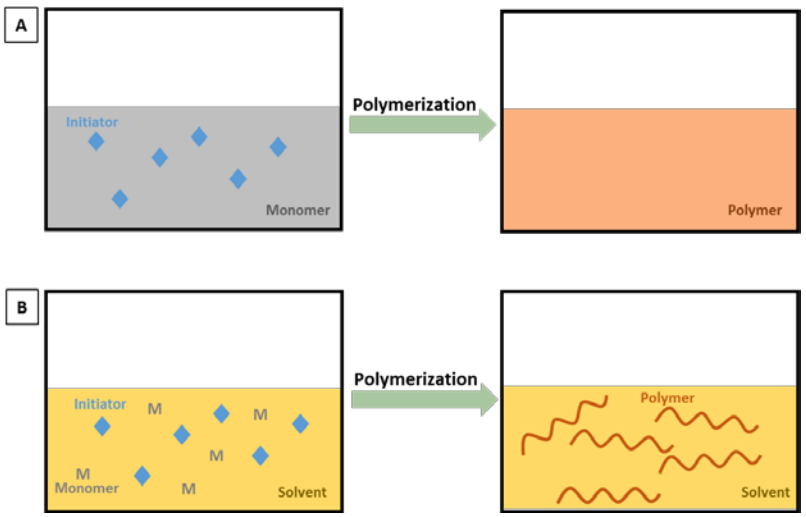

Figure 1.8. Schematic representation of bulk (A) and solution (B) polymerizations before and after radical polymerization reaction.

Instead, in emulsion polymerization in aqueous medium, the toxic organic solvents are replaced by water, and hence, the polymerization process is more environmentally friendly and also safer for the workers because combustive solvents are avoid in the formulation. On the other hand, the continuous aqueous medium decreases the viscosity of the dispersion (as it also the solvent does for solution systems) which allows easier stirring of the reaction mixture and good heat transfer. Besides, the high specific heat of water facilitates the temperature control of the system and reduces the chance of a thermal runaway. Finally, compared to bulk or solution polymerizations, emulsion polymerization is characteristic for the unique feature associated to the isolation or compartmentalization of the growing radicals within the polymer particles. As the growing radicals are confined in different polymer particles, they have no choice to terminate between them and therefore, they are allowed to grow for longer times until a second radical enters to the particle (in the absence of chain transfer reactions). Furthermore, the decrease of the radical termination reactions results in an increase in the total radical concentration, and thus, the polymerization rate. Therefore, radical compartmentalization within polymer particles let to the simultaneous increase in the polymerization rate and the molecular weights, feature quite unique for this polymerization process.

As it is mentioned above, emulsion polymerization is a heterogeneous FRP process, i.e. the sequential addition of vinyl monomer(s) to an active centre, which normally starts from an emulsion of monomer droplets stabilized with surfactant or emulsifier, leading to a dispersion of polymer particles. In this way, the basic formulation is composed of at least one monomer, surfactant, a radical initiator, and water. Besides, crosslinkers or chain transfer agents (CTA) can be used to control the molecular weight of the polymer. Generally, more than one monomers are polymerized, based on for example on functional groups and glass transition temperature (T_g) to

achieve a product with desirable properties. The principal monomers polymerized by this process are (meth)acrylic, vinyl acetate, styrene-acrylics, and styrene-butadiene copolymers.

Emulsion polymerizations are mostly carried out in semibatch or semicontinuous mode where a fraction of the reactants is gradually added to the reaction mixture. In this way, in semibatch process, the heat generation rate and many features such as the copolymer composition, particle size distribution, molecular weight distribution, and particle morphology can be controlled. Although batch emulsion polymerization is not regularly used, it is convenient to discuss first for the easier understanding of the polymerization technique.

1.5.1.1. Batch emulsion polymerization

The first hypothesis for a scientific description of batch emulsion polymerization mechanism was proposed by W. D. Harkins in 1947,[192] and over decades of carefully study, a complete definition of the mechanisms result in emulsion polymerization systems was established.[193–195] They suggested that a typical batch emulsion polymerization reaction contains three different intervals (Interval I, II and III). The batch emulsion polymerization process is schematically illustrated in Figure 1.9.[196,197] Before the reaction starts, a mixture of monomer, emulsifier and water is placed in the reactor (Figure 1.9.A). In most formulations, the amount of monomer and surfactant exceed the amount needed to saturate the aqueous phase. In this way, large droplets of monomer are formed that are stabilized by the surfactant adsorbed on their surface. On the other hand, there is still enough amount of surfactant for both to cover the monomer droplets and to saturate the aqueous phase, so the excess of surfactant let to the formation of micelles that are swollen with monomer. It is important to point out that the monomer and surfactant partitioning between the phases are in thermodynamic equilibrium, so the

monomer and surfactant molecules will continuously diffuse across the different phases during the polymerization to maintain the equilibrium.

Interval I or nucleation stage starts when the initiator is added to the reactor. (Figure 1.9.I). In general, water-soluble initiators are used that form radicals in water phase, when they are heated or undergo redox reactions. In this initiation, radicals are too hydrophilic to enter directly to the organic phase; therefore, they first react with monomers dissolved in the aqueous phase, forming oligoradicals. Once the oligoradical becomes hydrophobic enough, after the addition of some monomer units to the growing chain, they are able to enter into the micelles. The hydrophobic oligoradicals can unlikely enter monomer droplets as the monomer droplets surface area is roughly 3 orders of magnitude smaller than that of the micelles. The process of radical entrance into micelles is known as heterogeneous nucleation, in which the polymer particles are formed. Inside the particles, the oligoradical grows fast, forming a polymer chains. On the other hand, oligoradicals that do not enter into micelles they will continue growing in the aqueous phase until they reach a critical length and become insoluble in water. In this way, they precipitate and become stabilized by surfactant molecules nucleating new polymer particles by homogeneous nucleation. Both nucleation types are operative during emulsion polymerization, but depending on the conditions one of them may be dominating. For example, homogeneous nucleation can be pronounced if there are no micelles in the system at low amount of emulsifier or using monomers with relatively high solubility in water.

The newly formed polymer particles become the principal polymerization loci. Thus, as the monomer is consumed in the polymerization, the monomer molecules from the monomer droplets diffuse through the aqueous phase to the polymer particles to maintain equilibrium. Due to the continuous monomer diffusion to the polymerization loci and polymerization reaction, the polymer particles grow and the newly formed surface area is stabilized by surfactants. Most of

the surfactant is in the form of micelles, and therefore, some micelles are consumed to stabilize the growing particles. Furthermore, in case of surfactants with slow diffusion rate, they might not be able to diffuse fast and stabilize the generated surface area, and therefore, the small polymer particles (known as precursors particles) become stable after coagulation leading to bigger particles (coagulative nucleation).[198]

In the course of interval I, the number of polymer particles increases while the number of micelles decreases until all the micelles are consumed. This moment is considered to be the end of Interval I. Unless coagulation occurs, the number of particles in the reaction mixture remains constant during the rest of the batch process.

In interval II, the system is constituted of monomer droplets and growing polymer particles (Figure 1.9.II). As monomer is consumed inside the growing particles, new molecules are needed for the polymerization that are provided by diffusion from monomer droplets through the aqueous phase. During this interval, the concentration of the monomers in the particles reaches a maximum value and, thus, the polymerization rate is roughly constant and usually maximum. Due to the polymerization and monomer transport, after some time, the monomer droplets disappear marking the end of interval II.

After disappearance of monomer droplets, interval III commences, where the system contains only monomer-swollen polymer particles. In interval III, as the polymerization continue inside the polymer particles, the concentration of monomer decreases continuously, since no other monomer can diffuse through the aqueous phase, consequently, also the polymerization rate gradually decreases until all the monomer is consumed. The final product is polymer particles dispersed in aqueous phase (Figure 1.9.III).

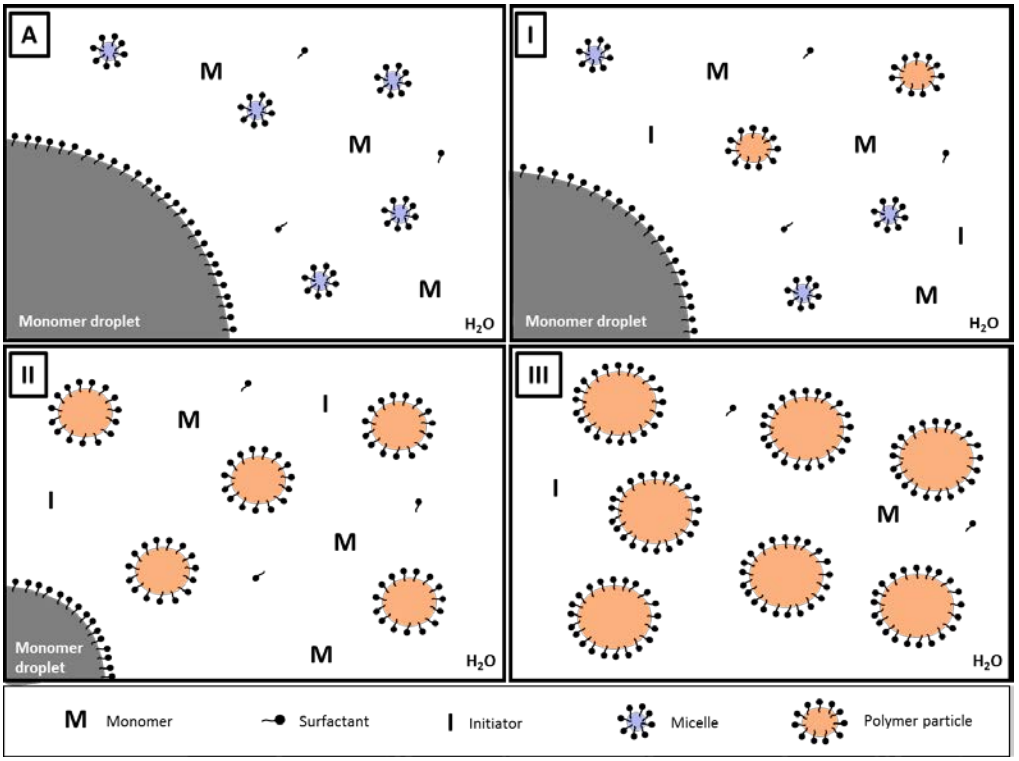

Figure 1.9. Schematic representation of different intervals I-III of batch emulsion polymerization process.

1.5.1.2. Semibatch emulsion polymerization

The description of Harkins is based on batch conditions, however, most of industrial processes are carried out under semibatch or semicontinuous reactors in which monomer is gradually added to the reaction mixture, sometimes with initiator, surfactant and water. The particle nucleation is the most variable event in emulsion polymerization and it is often controlled by starting the polymerization from pre-synthesized small polymer particles (seed). This process is called seeded semibatch emulsion polymerization where the polymer seed is firstly charged into the reactor and after the initiation of the system, the rest of components are fed.

Besides, semibatch emulsion polymerization let a better security control due to the low monomer concentration in the reaction mixture at any time (in batch conditions the concentration of monomers is generally high) and better control of the final latex properties, i.e. a higher process flexibility. The main properties of the latexes are largely determined during polymerization process, such as molecular weight of the polymer, chemical composition, particle morphology, and particle size distribution. For example, as the monomers react as they enter to the system, this allows to the synthesis of copolymers with homogeneous composition from monomers with distinct reactivity ratios.[199]

Finally, it is worth noting that the versatility of 3D graphene-polymer structures prepared throughout this project is owed to the wide range of polymers that may be incorporated in the monolithic structures, including highly hydrophobic ones, for which otherwise use of solvents is inevitable. In addition, latex technology permits introduction of various functionalities and specific microstructural features onto the polymer particles in a relatively easy way during polymer synthesis by emulsion polymerization.

1.6. Main motivation and objectives

The era of energy demand will continue increasing in the next decades, and as a consequence, the emissions of pollutant greenhouse gases, especially CO_2. Thus, there is a great interest in the development of efficient and cost effective CO_2 adsorbent materials to be applied in post-combustion capture technology.

One of the most promising strategy to take advantages of the unique properties of those individual graphene sheets in application perspective is the assembly of 2D graphene nanolayers

into a macroscopic 3D monolithic structure. Furthermore, it has more advantages, including the improved textural properties such as hierarchical structure, surface area and porosity.

On the other hand, the development of graphene-polymer composites modifies the surface chemistry of the 3D structures, and in this way, it could enhance the adsorption capacity and selectivity towards CO_2. Emulsion polymers give the opportunity to produce structures with tuneable characteristics and specific properties during reaction.

The objective of this PhD Thesis is to make a detail study of the synthesis and characterization of 3D graphene-polymer composite monolithic materials for selective CO_2 capture. GO nanosheets and polymer nanoparticles were used as building blocks and the self-assembly was induced by chemical reduction reaction. Variables such as reduction conditions, mass ratios, and polymer microstructure are used to study their influence in textural properties, adsorption capacities, and selectivity towards CO_2 gas over N_2. An environmentally friendly procedure is exclusively followed in water, low energy and quite versatile method, where scale-up procedures are viable.

1.7. Thesis outline

In **Chapter 2**, the investigation of reduction conditions how affect the resulting neat 3D graphene-base structures in terms of textural properties and adsorption performance is presented. Different amounts of reducing agent and reduction temperatures were employed for the synthesis of the 3D monolithic adsorbents. This knowledge allows producing monoliths with optimal properties.

Chapter 3 is dedicated to the synthesis of functionalized 3D graphene-polymer composites with the aim to enhance the CO_2 adsorption performance. Polymer particles functionalized with different types and amounts of functional monomers were synthesized and incorporated to the 3D graphene-based skeleton. The influence of such functionalized groups in the resulting adsorption capacities of the composites is studied.

Chapter 4 is devoted to the analysis and improvement of the selectivity of CO_2 over N_2 gas of the 3D adsorbents. The importance of the selectivity in terms of capture cost compared to the adsorption capacity is highlighted.

In **Chapter 5**, crosslinked polymer particles were synthesized by emulsion polymerization and incorporated to the 3D materials. The microstructure of the polymer particles plays an important role in CO_2 adsorption performance.

The knowledge gained in these fundamental studies was applied in **Chapter 6** for the scale-up synthesis of the 3D composite adsorbents. Monoliths were synthesized 6 times bigger compared to the references monoliths, as a way to analyse the scale-up feasibility for future post-combustion capture application.

In **Chapter 7**, the most relevant conclusions of this PhD Thesis are summarized.

The detailed description of the characterization techniques is given in Appendix I (General characterization methods).

1.8. References

(1) Zhong, W.; Haigh, J. D. The Greenhouse Effect and Carbon Dioxide. *Weather* **2013**, *68* (4), 100–105.

(2) Anderson, T. R.; Hawkins, E.; Jones, P. D. CO2, the Greenhouse Effect and Global Warming: From the Pioneering Work of Arrhenius and Callendar to Today's Earth System Models. *Endeavour* **2016**, *40* (3), 178–187.

(3) Stillman, J. H. Heat Waves, the New Normal: Summertime Temperature Extremes Will Impact Animals, Ecosystems, and Human Communities. *Physiology* **2019**, *34* (2), 86–100.

(4) Kerr, A. R.; Focus, N.; Kerr, A. R. Global Warming Is Changing the World. *Sci* **2007**, *316*, 188–190.

(5) Papalexiou, S. M.; Montanari, A. Global and Regional Increase of Precipitation Extremes Under Global Warming. *Water Resour. Res.* **2019**, *55* (6), 4901–4914.

(6) Stark, J. S.; Peltzer, E. T.; Kline, D. I.; Queirós, A. M.; Cox, T. E.; Headley, K.; Barry, J.; Gazeau, F.; Runcie, J. W.; Widdicombe, S.; et al. Free Ocean CO 2 Enrichment (FOCE) Experiments: Scientific and Technical Recommendations for Future in Situ Ocean Acidification Projects. *Prog. Oceanogr.* **2019**, *172* (December 2018), 89–107.

(7) Höök, M.; Tang, X. Depletion of Fossil Fuels and Anthropogenic Climate Change-A Review. *Energy Policy* **2013**, *52*, 797–809.

(8) World Bank Data (2015) https://data.worldbank.org/indicator/EG.USE.COMM.FO.ZS.

(9) Lee, S. Y.; Park, S. J. A Review on Solid Adsorbents for Carbon Dioxide Capture. *J. Ind. Eng. Chem.* **2015**, *23*, 1–11.

(10) Summary., I. T.; Shukla, P. R.; Skea, J.; Slade, R.; Diemen, R. van; Haughey, E.; Malley, J.; Pathak, M.; Pereira, J. P. *Foreword Technical and Preface*; 2019.

(11) *IPCC, 2014: Climate Change 2014: Synthesis Report. Contribution of Working Groups I, II and III to the Fifth Assessment Report of the Intergovernmental Panel on Climate Change*; Geneva, Switzerland, 2014; Vol. 9781107025.

(12) Delbeke, J.; Runge-Metzger, A.; Slingenberg, Y.; Werksman, J. The Paris Agreement. *Towar. a Clim. Eur. Curbing Trend* **2019**, 24–45.

(13) Jacobson, M. Z. Review of Solutions to Global Warming, Air Pollution, and Energy Security. *Energy Environ. Sci.* **2009**, *2* (2), 148–173.

(14) Pacesila, M.; Burcea, S. G.; Colesca, S. E. Analysis of Renewable Energies in European Union. *Renew. Sustain. Energy Rev.* **2016**, *56*, 156–170.

(15) Sari, A.; Akkaya, M. Contribution of Renewable Energy Potential to Sustainable Employment. *Procedia - Soc. Behav. Sci.* **2016**, *229*, 316–325.

(16) Evans, A.; Strezov, V.; Evans, T. J. Assessment of Sustainability Indicators for Renewable Energy Technologies. *Renew. Sustain. Energy Rev.* **2009**, *13* (5), 1082–1088.

(17) Arutyunov, V. S.; Lisichkin, G. V. Energy Resources of the 21st Century: Problems and Forecasts. Can Renewable Energy Sources Replace Fossil Fuels? *Russ. Chem. Rev.* **2017**, *86* (8), 777–804.

(18) Stangeland, A.; Foundation, T. B. Why CO 2 Capture and Storage (CCS) Is an Important Strategy to Reduce Global CO 2 Emissions. *Renew. Energy* **2007**, No. 1, 1–8.

(19) Leung, D. Y. C.; Caramanna, G.; Maroto-Valer, M. M. An Overview of Current Status of Carbon Dioxide Capture and Storage Technologies. *Renew. Sustain. Energy Rev.* **2014**, *39*, 426–443.

(20) *Carbon Dioxide Utilization: Closing the Carbon Cycle*, First.; A., P. S. . E. A. Q. . K., Ed.; Elsevier, 2015.

(21) Murdock, C. R.; Didas, S. A.; Jones, C. W. Direct Capture of CO 2 from Ambient Air. *Chem. Rev.* **2016**, *116*, 11840–11876.

(22) Didas, S. A.; Choi, S.; Chaikittisilp, W.; Jones, C. W. Amine − Oxide Hybrid Materials for CO 2 Capture from Ambient Air. *Acc. Chem. Res.* **2015**, *48*, 2680–2687.

(23) Chao, C.; Deng, Y.; Dewil, R.; Baeyens, J.; Fan, X. Post-Combustion Carbon Capture. *Renew. Sustain. Energy Rev.* **2021**, *138* (October 2020), 110490.

(24) D'Alessandro, D. M.; Smit, B.; Long, J. R. Carbon Dioxide Capture: Prospects for New Materials. *Angew. Chemie - Int. Ed.* **2010**, *49* (35), 6058–6082.

(25) Liu, J.; Baeyens, J.; Deng, Y.; Tan, T.; Zhang, H. The Chemical CO2 Capture by Carbonation-Decarbonation Cycles. *J. Environ. Manage.* **2020**, *260* (October 2019), 110054.

(26) Pardemann, R.; Meyer, B. Pre-Combustion Carbon Capture. *Handb. Clean Energy Syst.* **2015**, 1–28.

(27) Toftegaard, M. B.; Brix, J.; Jensen, P. A.; Glarborg, P.; Jensen, A. D. Oxy-Fuel

Combustion of Solid Fuels. *Prog. Energy Combust. Sci.* **2010**, *36* (5), 581–625.

(28) Scheffknecht, G.; Al-Makhadmeh, L.; Schnell, U.; Maier, J. Oxy-Fuel Coal Combustion-A Review of the Current State-of-the-Art. *Int. J. Greenh. Gas Control* **2011**, *5* (SUPPL. 1), 16–35.

(29) Liang, Y.; Harrison, D. P.; Gupta, R. P.; Green, D. A.; McMichael, W. J. Carbon Dioxide Capture Using Dry Sodium-Based Sorbents. *Energy and Fuels* **2004**, *18* (2), 569–575.

(30) Romeo, L. M.; Abanades, J. C.; Escosa, J. M.; Paño, J.; Giménez, A.; Sánchez-Biezma, A.; Ballesteros, J. C. Oxyfuel Carbonation/Calcination Cycle for Low Cost CO2capture in Existing Power Plants. *Energy Convers. Manag.* **2008**, *49* (10), 2809–2814.

(31) Thiruvenkatachari, R.; Su, S.; An, H.; Yu, X. X. Post Combustion CO2capture by Carbon Fibre Monolithic Adsorbents. *Prog. Energy Combust. Sci.* **2009**, *35* (5), 438–455.

(32) Bhown, A. S.; Freeman, B. C. Analysis and Status of Post-Combustion Carbon Dioxide Capture Technologies. *Environ. Sci. Technol.* **2011**, *45* (20), 8624–8632.

(33) Pires, J. C. M.; Martins, F. G.; Alvim-Ferraz, M. C. M.; Simões, M. Recent Developments on Carbon Capture and Storage: An Overview. *Chem. Eng. Res. Des.* **2011**, *89* (9), 1446–1460.

(34) Song, C.; Liu, Q.; Ji, N.; Deng, S.; Zhao, J.; Li, Y.; Song, Y. Alternative Pathways for e Ffi Cient CO 2 Capture by Hybrid Processes — A Review. **2018**, *82* (July 2017), 215–231.

(35) Rubin, E. S.; Mantripragada, H.; Marks, A.; Versteeg, P.; Kitchin, J. The Outlook for Improved Carbon Capture Technology. *Prog. Energy Combust. Sci.* **2012**, *38* (5), 630–671.

(36) Rubin, E. S.; Chen, C.; Rao, A. B. Cost and Performance of Fossil Fuel Power Plants with CO2 Capture and Storage. *Energy Policy* **2007**, *35* (9), 4444–4454.

(37) Thitakamol, B.; Veawab, A.; Aroonwilas, A. Environmental Impacts of Absorption-Based CO2 Capture Unit for Post-Combustion Treatment of Flue Gas from Coal-Fired Power Plant. *Int. J. Greenh. Gas Control* **2007**, *1* (3), 318–342.

(38) Wang, M.; Lawal, A.; Stephenson, P.; Sidders, J.; Ramshaw, C. Post-Combustion CO2 Capture with Chemical Absorption: A State-of-the-Art Review. *Chem. Eng. Res. Des.* **2011**, *89* (9), 1609–1624.

(39) Herzog, H. An Introduction to CO2 Separation and Capture Technologies. *MIT Energy Lab.* **1999**, 1–8.

(40) Olajire, A. A. CO2capture and Separation Technologies for End-of-Pipe Applications - A Review. *Energy* **2010**, *35* (6), 2610–2628.

(41) Rao, A. B.; Rubin, E. S. A Technical, Economic, and Environmental Assessment of Amine-Based CO 2Capture Technology for Power Plant Greenhouse Gas Control. *Environ. Sci. Technol.* **2002**, *36* (20), 4467–4475.

(42) Iglesias, R. S. Carbon Capture and Storage: How Green Can Black Be? *Science (80-.).* **2009**, *325* (September), 1647–1652.

(43) Yang, H.; Xu, Z.; Fan, M.; Gupta, R.; Slimane, R. B.; Bland, A. E.; Wright, I. Progress in Carbon Dioxide Separation and Capture: A Review. *J. Environ. Sci.* **2008**, *20* (1), 14–27.

(44) Gouedard, C.; Picq, D.; Launay, F.; Carrette, P. L. Amine Degradation in CO 2 Capture. I. A Review. *Int. J. Greenh. Gas Control* **2012**, *10*, 244–270.

(45) Strazisar, B. R.; Anderson, R. R.; White, C. M. Degradation Pathways for Monoethanolamine in a CO2 Capture Facility. *Energy and Fuels* **2003**, *17* (4), 1034–1039.

(46) Aaron, D.; Tsouris, C. Separation of CO2from Flue Gas: A Review. *Sep. Sci. Technol.* **2005**, *40* (1–3), 321–348.

(47) Rochelle, G. T. Thermal Degradation of Amines for CO2 Capture. *Curr. Opin. Chem. Eng.* **2012**, *1* (2), 183–190.

(48) Ahmed, R.; Liu, G.; Yousaf, B.; Abbas, Q.; Ullah, H.; Ali, M. U. Recent Advances in Carbon-Based Renewable Adsorbent for Selective Carbon Dioxide Capture and Separation-A Review. *J. Clean. Prod.* **2020**, *242*, 118409.

(49) Bernardo, P.; Drioli, E.; Golemme, G. Membrane Gas Separation : A Review / State of the Art. *Ind. Eng. Chem. Res.* **2009**, *48* (10), 4638–4663.

(50) Brunetti, A.; Scura, F.; Barbieri, G.; Drioli, E. Membrane Technologies for CO2separation. *J. Memb. Sci.* **2010**, *359* (1–2), 115–125.

(51) Powell, C. E.; Qiao, G. G. Polymeric CO2/N2gas Separation Membranes for the Capture of Carbon Dioxide from Power Plant Flue Gases. *J. Memb. Sci.* **2006**, *279* (1–2), 1–49.

(52) Luis, P.; Van Gerven, T.; Van Der Bruggen, B. Recent Developments in Membrane-Based Technologies for CO 2 Capture. *Prog. Energy Combust. Sci.* **2012**, *38* (3), 419–448.

(53) Hart, A.; Gnanendran, N. Cryogenic CO2 Capture in Natural Gas. *Energy Procedia* **2009**, *1* (1), 697–706.

(54) Meisen, A.; Shuai, X. Research and Development Issues in CO2 Capture. *Energy Convers. Manag.* **1997**, *38* (SUPPL. 1), 37–42.

(55) Tuinier, M. J.; Hamers, H. P.; Van Sint Annaland, M. Techno-Economic Evaluation of Cryogenic CO2 Capture-A Comparison with Absorption and Membrane Technology. *Int. J. Greenh. Gas Control* **2011**, *5* (6), 1559–1565.

(56) Adánez, J.; De Diego, L. F.; García-Labiano, F.; Gayán, P.; Abad, A.; Palacios, J. M. Selection of Oxygen Carriers for Chemical-Looping Combustion. *Energy and Fuels* **2004**, *18* (2), 371–377.

(57) Naqvi, R.; Bolland, O. Multi-Stage Chemical Looping Combustion (CLC) for Combined Cycles with CO2capture. *Int. J. Greenh. Gas Control* **2007**, *1* (1), 19–30.

(58) Zafar, Q.; Mattisson, T.; Gevert, B. Integrated Hydrogen and Power Production with CO2capture Using Chemical-Looping Reforming-Redox Reactivity of Particles of CuO, Mn2O3, NiO, and Fe2O3using SiO2as a Support. *Ind. Eng. Chem. Res.* **2005**, *44* (10), 3485–3496.

(59) Hossain, M. M.; de Lasa, H. I. Chemical-Looping Combustion (CLC) for Inherent CO2 Separations-a Review. *Chem. Eng. Sci.* **2008**, *63* (18), 4433–4451.

(60) Harter, R. D. Adsorption Phenomena. *Adsorpt. phenomena.* **1986**, 17–161.

(61) Ben-Mansour, R.; Habib, M. A.; Bamidele, O. E.; Basha, M.; Qasem, N. A. A.; Peedikakkal, A.; Laoui, T.; Ali, M. Carbon Capture by Physical Adsorption: Materials, Experimental Investigations and Numerical Modeling and Simulations - A Review. *Appl. Energy* **2016**, *161*, 225–255.

(62) Yu, C.-H.; Huang, C.-H.; Tan, C.-S. A Review of CO2 Capture by Absorption and Adsorption. *Aerosol Air Qual. Res.* **2012**, *12* (5), 745–769.

(63) Samanta, A.; Zhao, A.; Shimizu, G. K. H.; Sarkar, P.; Gupta, R. Post-Combustion CO 2 Capture Using Solid Sorbents: A Review. *Ind. Eng. Chem. Res.* **2012**, *51* (4), 1438–1463.

(64) Choi, S.; Drese, J. H.; Jones, C. W. Adsorbent Materials for Carbon Dioxide Capture from Large Anthropogenic Point Sources. *ChemSusChem* **2009**, *2* (9), 796–854.

(65) Wang, Q.; Luo, J.; Zhong, Z.; Borgna, A. CO2 Capture by Solid Adsorbents and Their Applications: Current Status and New Trends. *Energy Environ. Sci.* **2011**, *4* (1), 42–55.

(66) Gray, M. L.; Champagne, K. J.; Fauth, D.; Baltrus, J. P.; Pennline, H. Performance of Immobilized Tertiary Amine Solid Sorbents for the Capture of Carbon Dioxide. *Int. J. Greenh. Gas Control* **2008**, *2* (1), 3–8.

(67) PRAUSNITZ, A. L. M. and J. M. Thermodynamics of Mixed-Gas Adsorption. *A.1.Ch.E. J.* **1965**, *11* (1), 121–126.

(68) Lima, E. C.; Gomes, A. A.; Tran, H. N. Comparison of the Nonlinear and Linear Forms of the van't Hoff Equation for Calculation of Adsorption Thermodynamic Parameters ($\Delta S°$ and $\Delta H°$). *J. Mol. Liq.* **2020**, *311*, 113315.

(69) Bae, J. S.; Bhatia, S. K. High-Pressure Adsorption of Methane and Carbon Dioxide on Coal. *Energy and Fuels* **2006**, *20* (6), 2599–2607.

(70) Zhao, R.; Liu, L.; Zhao, L.; Deng, S.; Li, S.; Zhang, Y. A Comprehensive Performance Evaluation of Temperature Swing Adsorption for Post-Combustion Carbon Dioxide Capture. *Renew. Sustain. Energy Rev.* **2019**, *114* (July), 109285.

(71) Seshan, K. Pressure Swing Adsorption. *Appl. Catal.* **1989**, *46* (1), 180.

(72) Radosz, M.; Hu, X.; Krutkramelis, K.; Shen, Y. Flue-Gas Carbon Capture on Carbonaceous Sorbents: Toward a Low-Cost Multifunctional Carbon Filter for "Green" Energy Producers. *Ind. Eng. Chem. Res.* **2008**, *47* (10), 3783–3794.

(73) Van Der Vaart, R.; Huiskes, C.; Bosch, H.; Reith, T. Single and Mixed Gas Adsorption Equilibria of Carbon Dioxide/Methane on Activated Carbon. *Adsorption* **2000**, *6* (4), 311–323.

(74) Maroto-Valer, M. M.; Tang, Z.; Zhang, Y. CO2 Capture by Activated and Impregnated Anthracites. *Fuel Process. Technol.* **2005**, *86* (14–15), 1487–1502.

(75) Na, B. K.; Koo, K. K.; Eum, H. M.; Lee, H.; Song, H. K. CO2 Recovery from Flue Gas by PSA Process Using Activated Carbon. *Korean J. Chem. Eng.* **2001**, *18* (2), 220–227.

(76) Wang, Y.; Zhou, Y.; Liu, C.; Zhou, L. Comparative Studies of CO2 and CH4 Sorption on Activated Carbon in Presence of Water. *Colloids Surfaces A Physicochem. Eng. Asp.* **2008**, *322* (1–3), 14–18.

(77) Chue, K. T.; Kim, J. N.; Yoo, Y. J.; Cho, S. H.; Yang, R. T. Comparison of Activated Carbon and Zeolite 13X for CO2 Recovery from Flue Gas by Pressure Swing Adsorption. *Ind. Eng. Chem. Res.* **1995**, *34* (2), 591–598.

(78) Kikkinides, E. S.; Yang, R. T.; Cho, S. H. Concentration and Recovery of CO2 from Flue Gas by Pressure Swing Adsorption. *Ind. Eng. Chem. Res.* **1993**, *32* (11), 2714–2720.

(79) Bae, T. H.; Hudson, M. R.; Mason, J. A.; Queen, W. L.; Dutton, J. J.; Sumida, K.; Micklash, K. J.; Kaye, S. S.; Brown, C. M.; Long, J. R. Evaluation of Cation-Exchanged Zeolite Adsorbents for Post-Combustion Carbon Dioxide Capture. *Energy Environ. Sci.* **2013**, *6* (1), 128–138.

(80) Choudhary, V. R.; Mayadevi, S. Sorption Isotherms of Methane, Ethane, Ethylene, and Carbon Dioxide on ALPO-5 and SAPO-5. *Langmuir* **1996**, *12* (4), 980–986.

(81) Damjanović, L.; Auroux, A. *Determination of Acid/Base Properties by Temperature Programmed Desorption (TPD) and Adsorption Calorimetry*; 2010.

(82) Harlick, P. J. E.; Tezel, F. H. An Experimental Adsorbent Screening Study for CO2 Removal from N2. *Microporous Mesoporous Mater.* **2004**, *76* (1–3), 71–79.

(83) Kamiuto, K.; Abe, S. Effect of Desorption Temperature on CO2 Adsorption Equilibria of the Honeycomb Zeolite Beds. *Appl. Energy* **2002**, *72* (3–4), 555–564.

(84) Franchi, R. S.; Harlick, P. J. E.; Sayari, A. Applications of Pore-Expanded Mesoporous Silica. 2. Development of a High-Capacity, Water-Tolerant Adsorbent for CO2. *Ind. Eng. Chem. Res.* **2005**, *44* (21), 8007–8013.

(85) Llewellyn, P. L.; Bourrelly, S.; Serre, C.; Vimont, A.; Daturi, M.; Hamon, L.; Weireld, G. De; Chang, J.; Hong, D.; Hwang, Y. K.; et al. High Uptakes of CO 2 and CH 4 in Mesoporous Metal s Organic Frameworks MIL-100 and MIL-101. **2008**, No. 18, 7245–7250.

(86) Maina, J. W.; Pozo-Gonzalo, C.; Kong, L.; Schütz, J.; Hill, M.; Dumée, L. F. Metal Organic Framework Based Catalysts for CO2 Conversion. *Mater. Horizons* **2017**, *4* (3), 345–361.

(87) Jung, J. Y.; Karadas, F.; Zulfiqar, S.; Deniz, E.; Aparicio, S.; Atilhan, M.; Yavuz, C. T.; Han, S. M. Limitations and High Pressure Behavior of MOF-5 for CO2 Capture. *Phys. Chem. Chem. Phys.* **2013**, *15* (34), 14319–14327.

(88) Ma, Y.; McCarthy, M. C.; Yu, J.; Balbuena, P. B.; Li, J.-R.; Jeong, H.-K.; Sculley, J.; Zhou, H.-C. Carbon Dioxide Capture-Related Gas Adsorption and Separation in Metal-Organic Frameworks. *Coord. Chem. Rev.* **2011**, *255* (15–16), 1791–1823.

(89) Cooper, A. I. Conjugated Microporous Polymers. *Adv. Mater.* **2009**, *21* (12), 1291–1295.

(90) Lukose, B.; Kuc, A.; Heine, T. The Structure of Layered Covalent-Organic Frameworks. *Chem. - A Eur. J.* **2011**, *17* (8), 2388–2392.

(91) Zeng, Y.; Zou, R.; Zhao, Y. Covalent Organic Frameworks for CO2capture. *Adv. Mater.* **2016**, *28* (15), 2855–2873.

(92) Xu, S.; Luo, Y.; Tan, B. Recent Development of Hypercrosslinked Microporous Organic Polymers. *Macromol. Rapid Commun.* **2013**, *34*, 471–484.

(93) Babarao, R.; Dai, S.; Jiang, D. E. Functionalizing Porous Aromatic Frameworks with

Polar Organic Groups for High-Capacity and Selective CO2 Separation: A Molecular Simulation Study. *Langmuir* **2011**, *27* (7), 3451–3460.

(94) Karadas, F.; Yavuz, C. T.; Zul, S.; Aparicio, S.; Stucky, G. D.; Atilhan, M. CO2 Adsorption Studies on Hydroxy Metal Carbonates M (CO 3) x (OH) y (M = Zn , Zn À Mg , Mg , Mg À Cu , Cu , Ni , and Pb) at High Pressures up to 175 Bar. *Langmuir* **2011**, *27* (17), 10642–10647.

(95) Zulfiqar, S.; Sarwar, M. I.; Mecerreyes, D. Polymeric Ionic Liquids for CO2 Capture and Separation: Potential, Progress and Challenges. *Polym. Chem.* **2015**, *6* (36), 6435–6451.

(96) D'Alessandro, D. M.; McDonald, T. Toward Carbon Dioxide Capture Using Nanoporous Materials. *Pure Appl. Chem.* **2011**, *83* (1), 57–66.

(97) Kenarsari, S. D.; Yang, D.; Jiang, G.; Zhang, S.; Wang, J.; Russell, A. G.; Wei, Q.; Fan, M. Review of Recent Advances in Carbon Dioxide Separation and Capture. *RSC Adv.* **2013**, *3* (45), 22739–22773.

(98) Novoselov, K. S.; Geim, A. K.; Morozov, S. V.; Jiang, D.; Zhang, Y.; Dubonos, S. V.; Grigorieva, I. V.; Firsov, A. A. Electric Field in Atomically Thin Carbon Films. *Science (80-.).* **2004**, *306* (5696), 666–669.

(99) Sun, Z.; Fang, S.; Hu, Y. H. 3D Graphene Materials: From Understanding to Design and Synthesis Control. *Chem. Rev.* **2020**, *120* (18), 10336–10453.

(100) Allen, M. J.; Tung, V. C.; Kaner, R. B. Honeycomb Carbon: A Review of Graphene. *Chem. Rev.* **2010**, *110* (1), 132–145.

(101) Novoselov, K. S.; Fal'Ko, V. I.; Colombo, L.; Gellert, P. R.; Schwab, M. G.; Kim, K. A Roadmap for Graphene. *Nature* **2012**, *490* (7419), 192–200.

(102) Neto, A. H. C.; Guinea, F.; Peres, N. M. R.; Novoselov, K. S.; Geim, A. K. The Electronic Properties of Graphene. *Rev. Mod. Phys.* **2009**, *81* (1).

(103) Orlita, M.; Faugeras, C.; Plochocka, P.; Neugebauer, P.; Martinez, G.; Maude, D. K.; Barra, A. L.; Sprinkle, M.; Berger, C.; De Heer, W. A.; et al. Approaching the Dirac Point in High-Mobility Multilayer Epitaxial Graphene. *Phys. Rev. Lett.* **2008**, *101* (26), 1–4.

(104) Lee, C.; Wei, X.; Kysar, J. W.; Hone, J. Measurement of the Elastic Properties and Intrinsic Strength of Monolayer Graphene. *Science (80-.).* **2008**, *321* (July), 385–388.

(105) Eric Pop , Vikas Varshney, and A. K. R. Thermal Properties of Graphene: Fundamentals and Applications. *MRS Bull.* **2012**, *37* (12), 1273–1281.

(106) Teweldebrhan, D.; Lau, C. N.; Ghosh, S.; Balandin, A. A.; Bao, W.; Calizo, I.; Miao, F. Superior Thermal Conductivity of Single-Layer Graphene. *Nano Lett.* **2008**, *8* (3), 902–907.

(107) Zhu, Y.; Murali, S.; Cai, W.; Li, X.; Suk, J. W.; Potts, J. R.; Ruoff, R. S. Graphene and Graphene Oxide: Synthesis, Properties, and Applications. *Adv. Mater.* **2010**, *22* (35), 3906–3924.

(108) Stoller, M. D.; Park, S.; Zhu, Y.; An, J.; Ruoff, R. S. Graphene-Based Ultracapacitors. *Am. Chem. Soc.* **2008**, *8* (10), 3498–3502.

(109) Chua, C. K.; Pumera, M. Chemical Reduction of Graphene Oxide: A Synthetic Chemistry Viewpoint. *Chem. Soc. Rev.* **2014**, *43* (1), 291–312.

(110) Hummers, W. S.; Offeman, R. E. Preparation of Graphitic Oxide. *J. Am. Chem. Soc.* **1958**, *80* (6), 1339.

(111) Stankovich, S.; Dikin, D. A.; Piner, R. D.; Kohlhaas, K. A.; Kleinhammes, A.; Jia, Y.; Wu, Y.; Nguyen, S. B. T.; Ruoff, R. S. Synthesis of Graphene-Based Nanosheets via Chemical Reduction of Exfoliated Graphite Oxide. *Carbon N. Y.* **2007**, *45* (7), 1558–1565.

(112) Guo, J.; Morris, J. R.; Ihm, Y.; Contescu, C. I.; Gallego, N. C.; Duscher, G.; Pennycook, S. J.; Chisholm, M. F. Topological Defects: Origin of Nanopores and Enhanced Adsorption Performance in Nanoporous Carbon. *Small* **2012**, *8* (21), 3283–3288.

(113) Liu, C.; Yu, Z.; Neff, D.; Zhamu, A.; Jang, B. Z. Graphene-Based Supercapacitor with an Ultrahigh Energy Density. *Nano Lett.* **2010**, *10* (12), 4863–4868.

(114) Georgakilas, V. Addition of Organic Groups through Reactions with Oxygen Species of Graphene Oxide. *Funct. Graphene* **2014**, *1th ed.*, 59–94.

(115) Soliman, A. B.; Haikal, R. R.; Hassan, Y. S.; Alkordi, M. H. The Potential of a Graphene-Supported Porous-Organic Polymer (POP) for CO2 Electrocatalytic Reduction. *Chem. Commun.* **2016**, *52* (81), 12032–12035.

(116) Three-Dimensional Grahene Structure, and Preparation Method Thereof. US20140370262A1. 2014.

(117) GRAPHENE-BASED MATERIALS. US20150259212A1.Pdf. 2015.

(118) Method For Manufacturing Graphene Based Materials. US20180190979A1.Pdf, 2018.

(119) Graphene-Based Materials. US9738527B2. 2017.

(120) Union, I.; Pure, O. F.; Chemistry, A. INTERNATIONAL UNION OF PURE COMMISSION ON COLLOID AND SURFACE CHEMISTRY INCLUDING CATALYSIS * REPORTING PHYSISORPTION DATA FOR GAS / SOLID SYSTEMS with Special Reference to the Determination of Surface Area and Porosity. **1985**, *57* (4), 603–619.

(121) Thommes, M.; Kaneko, K.; Neimark, A. V.; Olivier, J. P.; Rodriguez-Reinoso, F.; Rouquerol, J.; Sing, K. S. W. Physisorption of Gases, with Special Reference to the Evaluation of Surface Area and Pore Size Distribution (IUPAC Technical Report). *Pure Appl. Chem.* **2015**, *87* (9–10), 1051–1069.

(122) Rethinasabapathy, M.; Kang, S.-M.; Jang, S.-C.; Huh, Y. S. Three-Dimensional Porous Graphene Materials for Environmental Applications. *Carbon Lett.* **2017**, *22* (1).

(123) Truong, S.; Tien, H.; Rinaldi, A.; Nguyen, N. P. V; Fan, Z.; Minh, H. Colloids and Surfaces A : Physicochemical and Engineering Aspects Morphology Control and Thermal Stability of Binderless-Graphene Aerogels from Graphite for Energy Storage Applications. *Colloids Surfaces A Physicochem. Eng. Asp.* **2012**, *414*, 352–358.

(124) Chem, J. M. High-Rate Capacitive Performance of Graphene Aerogel with a Superhigh C / O. **2012**, 23186–23193.

(125) Pei, S.; Cheng, H. M. The Reduction of Graphene Oxide. *Carbon N. Y.* **2012**, *50* (9), 3210–3228.

(126) Hydrogel, S. G. Self-Assembled Graphene Hydrogel via a One-Step Hydrothermal Process. *4* (7), 4324–4330.

(127) Pei, S.; Cheng, H. M. The Reduction of Graphene Oxide. *Carbon N. Y.* **2012**, *50* (9), 3210–3228.

(128) Chen, W.; Yan, L. In Situ Self-Assembly of Mild Chemical Reduction Graphene for Three-Dimensional Architectures. *Nanoscale* **2011**, *3* (8), 3132–3137. https://doi.org/10.1039/c1nr10355e.

(129) Park, S.; An, J.; Potts, J. R.; Velamakanni, A.; Murali, S.; Ruoff, R. S. Hydrazine-Reduction of Graphite- and Graphene Oxide. *Carbon N. Y.* **2011**, *49* (9), 3019–3023.

(130) Ren, P. G.; Yan, D. X.; Ji, X.; Chen, T.; Li, Z. M. Temperature Dependence of Grapheme Oxide Reduced by Hydrazine Hydrate. *Nanotechnology* **2011**, *22* (5).

(131) Zhu, P.; Shen, M.; Xiao, S.; Zhang, D. Experimental Study on the Reducibility of Graphene Oxide by Hydrazine Hydrate. *Phys. B Condens. Matter* **2011**, *406* (3), 498–502.

(132) Guardia, L.; Paredes, J. I.; Solı, P.; Tasco, J. M. D. Vitamin C Is an Ideal Substitute for

Hydrazine in the Reduction of Graphene Oxide Suspensions ´ N. **2010**, 6426–6432.

(133) De Silva, K. K. H.; Huang, H. H.; Joshi, R. K.; Yoshimura, M. Chemical Reduction of Graphene Oxide Using Green Reductants. *Carbon N. Y.* **2017**, *119*, 190–199.

(134) Gao, J.; Liu, F.; Liu, Y.; Ma, N.; Wang, Z.; Zhang, X. Environment-Friendly Method to Produce Graphene That Employs Vitamin C and Amino Acid. *Chem. Mater.* **2010**, *22* (7), 2213–2218.

(135) Ghosh, T. K.; Sadhukhan, S.; Rana, D.; Bhattacharyya, A.; Chattopadhyay, D.; Chakraborty, M. Green Approaches to Synthesize Reduced Graphene Oxide and Assessment of Its Electrical Properties. *Nano-Structures and Nano-Objects* **2019**, *19*, 100362.

(136) Zhang, J.; Yang, H.; Shen, G.; Cheng, P.; Zhang, J.; Guo, S. Reduction of Graphene Oxide Vial-Ascorbic Acid. *Chem. Commun.* **2010**, *46* (7), 1112–1114.

(137) Fang, Q.; Shen, Y.; Chen, B. Synthesis, Decoration and Properties of Three-Dimensional Graphene-Based Macrostructures: A Review. *Chem. Eng. J.* **2015**, *264*, 753–771.

(138) Worsley, M. A.; Olson, T. Y.; Lee, J. R. I.; Willey, T. M.; Nielsen, M. H.; Roberts, S. K.; Pauzauskie, P. J.; Biener, J.; Satcher, J. H.; Baumann, T. F. High Surface Area, Sp2-Cross-Linked Three-Dimensional Graphene Monoliths. *J. Phys. Chem. Lett.* **2011**, *2* (8), 921–925.

(139) Adhikari, B.; Biswas, A.; Banerjee, A. Graphene Oxide-Based Hydrogels to Make Metal Nanoparticle-Containing Reduced Graphene Oxide-Based Functional Hybrid Hydrogels. *ACS Appl. Mater. Interfaces* **2012**, *4* (10), 5472–5482.

(140) Sui, Z. Y.; Cui, Y.; Zhu, J. H.; Han, B. H. Preparation of Three-Dimensional Graphene Oxide-Polyethylenimine Porous Materials as Dye and Gas Adsorbents. *ACS Appl. Mater. Interfaces* **2013**, *5* (18), 9172–9179.

(141) Sun, H.; Xu, Z.; Gao, C. Multifunctional, Ultra-Flyweight, Synergistically Assembled Carbon Aerogels. *Adv. Mater.* **2013**, *25* (18), 2554–2560.

(142) Sheng, K.; Sun, Y.; Li, C.; Yuan, W.; Shi, G. Ultrahigh-Rate Supercapacitors Based on Eletrochemically Reduced Graphene Oxide for Ac Line-Filtering. *Sci. Rep.* **2012**, *2*, 3–7.

(143) Liu, F.; Seo, T. K. A Controllable Self-Assembly Method for Large-Scale Synthesis of Craphene Sponges and Free-Standing Craphene Films. *Adv. Funct. Mater.* **2010**, *20* (12), 1930–1936.

(144) Yorgun, S.; Yildiz, D. Preparation and Characterization of Activated Carbons from Paulownia Wood by Chemical Activation with H3PO4. *J. Taiwan Inst. Chem. Eng.* **2015**,

53, 122–131.

(145) Lillo-Ródenas, M. A.; Cazorla-Amorós, D.; Linares-Solano, A. Understanding Chemical Reactions between Carbons and NaOH and KOH: An Insight into the Chemical Activation Mechanism. *Carbon N. Y.* **2003**, *41* (2), 267–275.

(146) Srinivas, G.; Burress, J.; Yildirim, T. Graphene Oxide Derived Carbons (GODCs): Synthesis and Gas Adsorption Properties. *Energy Environ. Sci.* **2012**, *5* (4), 6453–6459.

(147) Benítez, A.; Caballero, A.; Morales, J.; Hassoun, J.; Rodríguez-Castellón, E.; Canales-Vázquez, J. Physical Activation of Graphene: An Effective, Simple and Clean Procedure for Obtaining Microporous Graphene for High-Performance Li/S Batteries. *Nano Res.* **2019**, *12* (4), 759–766.

(148) Ma, M.; Ying, H.; Cao, F.; Wang, Q.; Ai, N. Adsorption of Congo Red on Mesoporous Activated Carbon Prepared by CO2 Physical Activation. *Chinese J. Chem. Eng.* **2020**.

(149) Marsh, H., F. R.-R. *Activated Carbon*; Elsevier: London, 2006.

(150) Yun, S.; Lee, H.; Lee, W. E.; Park, H. S. Multiscale Textured, Ultralight Graphene Monoliths for Enhanced CO2 and SO2 Adsorption Capacity. *Fuel* **2016**, *174*, 36–42.

(151) Liu, S.; Peng, W.; Sun, H.; Wang, S. Physical and Chemical Activation of Reduced Graphene Oxide for Enhanced Adsorption and Catalytic Oxidation. *Nanoscale* **2014**, *6* (2), 766–771.

(152) Prauchner, M. J.; Rodríguez-Reinoso, F. Chemical versus Physical Activation of Coconut Shell: A Comparative Study. *Microporous Mesoporous Mater.* **2012**, *152*, 163–171.

(153) Le, N. H.; Mahesh, K.; Tiwari, R. N.; Timilsina, R.; Tiwari, J. N.; Kim, K. S.; Kemp, K. C. Reduced Graphene Oxide-Based Hydrogels for the Efficient Capture of Dye Pollutants from Aqueous Solutions. *Carbon N. Y.* **2013**, *56*, 173–182.

(154) Guo, C. X.; Lu, Z. S.; Lei, Y.; Li, C. M. Ionic Liquid-Graphene Composite for Ultratrace Explosive Trinitrotoluene Detection. *Electrochem. commun.* **2010**, *12* (9), 1237–1240.

(155) Gao, H.; Sun, Y.; Zhou, J.; Xu, R.; Duan, H. Mussel-Inspired Synthesis of Polydopamine-Functionalized Graphene Hydrogel as Reusable Adsorbents for Water Purification. *ACS Appl. Mater. Interfaces* **2013**, *5* (2), 425–432.

(156) Rodriguez-Couto, S.; Arzac, A.; Leal, G. P.; Tomovska, R. Reduced Graphene Oxide Hydrogels and Xerogels Provide Efficient Platforms for Immobilization and Laccase Production by Trametes Pubescens. *Biotechnol. J.* **2014**, *9* (4), 578–584.

(157) Ormategui, N.; Veloso, A.; Leal, G. P.; Rodriguez-Couto, S.; Tomovska, R. Design of Stable and Powerful Nanobiocatalysts, Based on Enzyme Laccase Immobilized on Self-Assembled 3D Graphene/Polymer Composite Hydrogels. *ACS Appl. Mater. Interfaces* **2015**, *7* (25), 14104–14112.

(158) He, K.; Chen, G.; Zeng, G.; Chen, A.; Huang, Z.; Shi, J.; Huang, T.; Peng, M.; Hu, L. Three-Dimensional Graphene Supported Catalysts for Organic Dyes Degradation. *Appl. Catal. B Environ.* **2018**, *228* (December 2017), 19–28.

(159) Wang, H.; Yuan, X.; Zeng, G.; Wu, Y.; Liu, Y.; Jiang, Q.; Gu, S. Three Dimensional Graphene Based Materials: Synthesis and Applications from Energy Storage and Conversion to Electrochemical Sensor and Environmental Remediation. *Adv. Colloid Interface Sci.* **2015**, *221*, 41–59.

(160) Cao, X.; Yin, Z.; Zhang, H. Three-Dimensional Graphene Materials: Preparation, Structures and Application in Supercapacitors. *Energy Environ. Sci.* **2014**, *7* (6), 1850–1865.

(161) Yang, Z.; Chabi, S.; Xia, Y.; Zhu, Y. Preparation of 3D Graphene-Based Architectures and Their Applications in Supercapacitors. *Prog. Nat. Sci. Mater. Int.* **2015**, *25* (6), 554–562.

(162) Dong, X.; Wang, X.; Wang, L.; Song, H.; Zhang, H.; Huang, W.; Chen, P. 3D Graphene Foam as a Monolithic and Macroporous Carbon Electrode for Electrochemical Sensing. *ACS Appl. Mater. Interfaces* **2012**, *4* (6), 3129–3133.

(163) Spasevska, D.; Daniloska, V.; Leal, G. P.; Gilev, J. B.; Tomovska, R. Reactive Emulsion Mixing as a Novel Pathway toward Water-Borne Reduced Graphene Oxide/Polymer Composites. *RSC Adv.* **2014**, *4* (47), 24477–24483.

(164) Ormategui, N.; Veloso, A.; Leal, G. P.; Rodriguez-Couto, S.; Tomovska, R. Design of Stable and Powerful Nanobiocatalysts, Based on Enzyme Laccase Immobilized on Self-Assembled 3D Graphene/Polymer Composite Hydrogels. *ACS Appl. Mater. Interfaces* **2015**, *7* (25), 14104–14112.

(165) Politakos, N.; Cantador, L. S.; Cecilia, J. A.; Barbarin, I.; Tomovska, R. Co2 Capture by Reduced Graphene Oxide Monoliths with Incorporated Ceo2 Grafted with Functionalized Polymer Brushes. *Appl. Sci.* **2021**, *11* (23).

(166) Nelson, M. R.; Borkman, R. F. Ab Initio Calculations on CO2 Binding to Carbonyl Groups. *J. Phys. Chem.* **1998**, *102*, 7860–7863.

(167) Zhang, Q.; Xu, X.; Fisher, T. S.; Xiong, G. Mechanically Robust Honeycomb Graphene Aerogel Multifunctional Polymer Composites. *Carbon N. Y.* **2015**, *93*, 659–670.

(168) Szczęśniak, B.; Choma, J.; Jaroniec, M. Gas Adsorption Properties of Graphene-Based

Materials. *Adv. Colloid Interface Sci.* **2017**, *243*, 46–59.

(169) Saha, D.; Kienbaum, M. J. Role of Oxygen, Nitrogen and Sulfur Functionalities on the Surface of Nanoporous Carbons in CO2 Adsorption: A Critical Review. *Microporous Mesoporous Mater.* **2019**, *287* (May), 29–55.

(170) Oschatz, M.; Antonietti, M. A Search for Selectivity to Enable CO2 Capture with Porous Adsorbents. *Energy Environ. Sci.* **2018**, *11* (1), 57–70.

(171) Deng, W.; Fang, Q.; Zhou, X.; Cao, H.; Liu, Z. Hydrothermal Self-Assembly of Graphene Foams with Controllable Pore Size. *RSC Adv.* **2016**, *6* (25), 20843–20849.

(172) Wickramaratne, N. P.; Jaroniec, M. Activated Carbon Spheres for CO2 Adsorption. *ACS Appl. Mater. Interfaces* **2013**, *5* (5), 1849–1855.

(173) Seredych, M.; Jagiello, J.; Bandosz, T. J. Complexity of CO2 Adsorption on Nanoporous Sulfur-Doped Carbons - Is Surface Chemistry an Important Factor? *Carbon N. Y.* **2014**, *74*, 207–217.

(174) Meconi, G. M.; Tomovska, R.; Zangi, R. Adsorption of CO 2 Gas on Graphene-Polymer Composites. *J. CO2 Util.* **2019**, *32* (March), 92–105.

(175) Christian Kemp, K.; Chandra, V.; Saleh, M.; Kim, K. S. Reversible CO2 Adsorption by an Activated Nitrogen Doped Graphene/Polyaniline Material. *Nanotechnology* **2013**, *24* (23).

(176) Liu, F. Q.; Wang, L. L.; Li, G. H.; Li, W.; Li, C. Q. Hierarchically Structured Graphene Coupled Microporous Organic Polymers for Superior CO 2 Capture. *ACS Appl. Mater. Interfaces* **2017**, *9*, 33997–34004.

(177) Seema, H.; Kemp, K. C.; Le, N. H.; Park, S. W.; Chandra, V.; Lee, J. W.; Kim, K. S. Highly Selective CO2 Capture by S-Doped Microporous Carbon Materials. *Carbon N. Y.* **2014**, *66*, 320–326.

(178) Seredych, M.; Rodríguez-Castellón, E.; Bandosz, T. J. Alterations of S-Doped Porous Carbon-RGO Composites Surface Features upon CO2 Adsorption at Ambient Conditions. *Carbon N. Y.* **2016**, *107*, 501–509.

(179) Chandra, V.; Yu, S. U.; Kim, S. H.; Yoon, Y. S.; Kim, D. Y.; Kwon, A. H.; Meyyappan, M.; Kim, K. S. Highly Selective CO2 Capture on N-Doped Carbon Produced by Chemical Activation of Polypyrrole Functionalized Graphene Sheets. *Chem. Commun.* **2012**, *48* (5), 735–737.

(180) Szczęśniak, B.; Osuchowski, Ł.; Choma, J.; Jaroniec, M. Highly Porous Carbons Obtained by Activation of Polypyrrole/Reduced Graphene Oxide as Effective Adsorbents

for CO2, H2 and C6H6. *J. Porous Mater.* **2018**, *25* (2), 621–627.

(181) Sudeep, P. M.; Narayanan, T. N.; Ganesan, A.; Shaijumon, M. M.; Yang, H.; Ozden, S.; Patra, P. K.; Pasquali, M.; Vajtai, R.; Ganguli, S.; et al. Covalently Interconnected Three-Dimensional Graphene Oxide Solids. *ACS Nano* **2013**, *7* (8), 7034–7040.

(182) Hsan, N.; Dutta, P. K.; Kumar, S.; Bera, R.; Das, N. Chitosan Grafted Graphene Oxide Aerogel: Synthesis, Characterization and Carbon Dioxide Capture Study. *Int. J. Biol. Macromol.* **2019**, *125*, 300–306.

(183) Bai, H.; Sheng, K.; Zhang, P.; Li, C.; Shi, G. Graphene Oxide/Conducting Polymer Composite Hydrogels. *J. Mater. Chem.* **2011**, *21* (46), 18653–18658.

(184) Liu, R.; Liang, S.; Tang, X. Z.; Yan, D.; Li, X.; Yu, Z. Z. Tough and Highly Stretchable Graphene Oxide/Polyacrylamide Nanocomposite Hydrogels. *J. Mater. Chem.* **2012**, *22* (28), 14160–14167.

(185) Zhang, E.; Wang, T.; Lian, C.; Sun, W.; Liu, X.; Tong, Z. Robust and Thermo-Response Graphene-PNIPAm Hybrid Hydrogels Reinforced by Hectorite Clay. *Carbon N. Y.* **2013**, *62*, 117–126.

(186) Arzac, A.; Leal, G. P.; Carlos, J.; Cal, D.; Tomovska, R. Water-Borne Polymer / Graphene Nanocomposites. *201600315*, 1–30.

(187) Asua, J. M. *Polymer Reaction Engineering*; Oxford: Blackwell, 2007.

(188) Industry, C. Carbon Footprint Study for Industrial Coatings Applied on a Metal Substrate Focus on Powder Coatings DSM Presents Carbon Footprint Study for Industrial Metal Coatings and Takes next Step towards a Sustainable. *31* (0).

(189) Geyer, R.; Jambeck, J. R.; Law, K. L. Production , Use , and Fate of All Plastics Ever Made. *Sci. Adv.* **2017**, *3*, 25–29.

(190) Asua, J. M. *Polimeric Dispersions: Principles and Applications*; 1997.

(191) D., M. A. V. . J. Bulk and Solution Processes. In *Handbook of Polymer Synthesis, Characterization, and Processing*; John Wiley & Sons, Inc., 2013.

(192) Harkins, W. D. A General Theory of the Mechanism of Emulsion Polymerization. *J. Am. Chem. Soc.* **1947**, *69* (6), 1428–1444.

(193) Thickett, S. C.; Gilbert, R. G. Emulsion Polymerization : State of the Art in Kinetics and Mechanisms. *Polymer (Guildf).* **2007**, *48* (24), 6965–6991.

(194) J. C. de la Cal; J. R. Leiza; J. M. Asua; A. Butte; Morbidelli, G. S. M. Handbook of Polymer

Reaction Engineering // Emulsion Polymerization; 2005; pp 249–322.

(195) José, M. A. Emulsion Polymerization: From Fundamental Mechanisms to Process Developments. *J. Polym. Sci. Part A Polym. Chem.* **2004**, *42* (5), 1025–1041.

(196) Meyer, T.; Keurentjes, J. *Handbook of Polymer Reaction Engineering*; Wiley-VCH Verlag GmbH & Co.KGaA: Weinheim, Germany, 2005.

(197) Asua, J. M. *Polymeric Dispersions: Principles and Applications*; 1997.

(198) Lichti, G.; Gilbert, R. G.; Napper, D. H. The Mechanisms of Latex Particle Formation and Growth in the Emulsion Polymerization of Styrene Using the Surfactant Sodium Dodecyl Sulfate. *J. Polym. Sci. Polym. Chem. Ed.* **1983**, *21*, 269–291.

(199) Arzamendi, G.; Asua, J. M. Monomer Addition Policies for Copolymer Composition Control in Semicontinuous Emulsion Copolymerization. *J. Appl. Polym. Sci.* **1989**, *38* (11), 2019–2036.

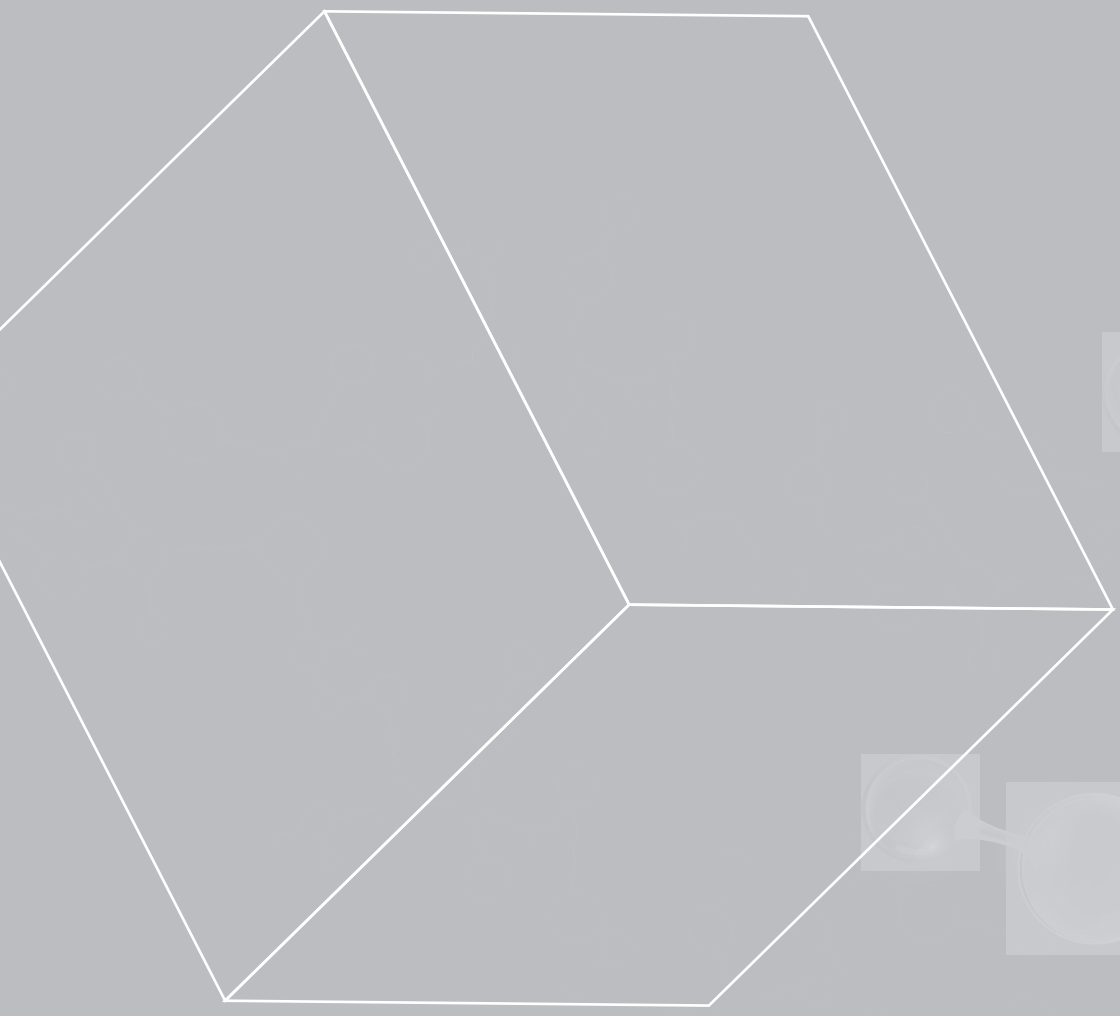

CHAPTER 2

Neat rGO monoliths: effect of synthesis conditions on properties and adsorption performance

Chapter 2. Neat rGO monoliths: effect of synthesis conditions on properties and adsorption performance

2.1. Introduction

As explained in the literature survey in Chapter 1, 3D graphene-based monolithic structures are of particular interest for CO_2 adsorption in post-combustion capture process. In fact, more advantages for efficient CO_2 capture will be gained if an easy way to produce solid sorbents in monolithic appearance is developed. Namely, the monoliths usually present a lower pressure drop of the gas flue, in comparison to that of an equivalent particulate system,[1–3] and a fast mass transport due to a high bed porosity and unique pore structure consisting of an interconnected 3D network of pores.[4,5] The monoliths also offer a substantially easier handling than do powders and improved structural and chemical uniformity.[6] Nevertheless, the synthesis of carbon-based or graphene-based monoliths is energy intensive, applying a few steps of an extremely high temperature treatment, or pre- or post-synthesis activation processes to increase the capacity to capture CO_2.

In this chapter, we propose an easy (one-step), low-cost (self-assembly), and environmentally friendly technique (aqueous-based) with a reduced carbon footprint (mild conditions) for the synthesis of graphene-based monolithic materials to capture CO_2. The method is based on a reduction-induced self-assembly process of GO nanoplatelets in aqueous dispersion at relatively mild temperatures (45-90 °C) to create hierarchical porous structures within macroscopic monoliths, the size of which depends on the amount of materials used for the

synthesis and on the reduction conditions. The GO reduction was performed by ascorbic acid (AsA), which has been considered as a green approach. Additionally, by varying the reduction parameters, a range of different monoliths with different porous structures and levels of functionalization, and subsequently, different performances for CO_2 capture, was developed. On the other hand, the addition of a small amount of polymer particles to the graphene-based skeleton was analyzed in terms of adsorption-desorption cycles.

2.2. Experimental part

2.2.1. Materials

Aqueous dispersion of graphene oxide (GO) sheets of 4 mg/mL (Graphenea) was used as supplied, with a monolayer content > 95 %, a pH range between 2.2-2.5 and particle size < 10μm. The elemental analysis of the GO showed: C (49-56 %), O (41-50 %), S (2-3 %), H (1-2 %), and N (0-1 %). For chemical reduction of GO L-ascorbic acid (AsA, ≥99 %, Sigma-Aldrich) was used. Technical grade monomers methyl methacrylate (MMA, Quimidroga) and glycidyl methacrylate (GMA, Sigma-Aldrich) were used without purification. Sodium dodecyl sulfate (SDS, Sigma-Aldrich), potassium persulfate (KPS, ≥99 %, Sigma-Aldrich) and sodium bicarbonate ($NaHCO_3$, Sigma-Aldrich) were used as received. Deionized water was used as polymerization media.

2.2.2. Synthesis procedures

2.2.2.1. Synthesis of polymer dispersion

The epoxy-functionalized polymethyl methacrylate latex was synthesized by means of batch emulsion polymerization of a monomer mixture made of glycidyl methacrylate/methyl

methacrylate (GMA/MMA) in a ratio of 10/90 wt%. The formulation employed for the synthesis is shown in Table 2.1. The reaction was performed in a 250 mL glass reactor equipped with a stainless-steel anchor-type stirrer, a reflux condenser, a thermocouple, a sampling tube, and a nitrogen inlet. The reactor´s temperature was managed by an automatic control system (Camille TG, Biotage). The monomer mixture and aqueous solution of SDS and $NaHCO_3$ were added to the reactor. The mixture was degassed by nitrogen bubbling, constantly stirring at 200 rpm, while heating to 70 ºC. Once the desired reaction temperature was reached, an aqueous thermal initiator (KPS) solution was added in one shot. After that, the system was left to polymerize batchwise during 90 min. As a result, a latex with a final solids content of 20 % were prepared with an overall conversion of 99 % and an average polymer particle diameter of 70 nm.

Table 2.1. Formulation employed for the synthesis of GMA-MMA latex.

	MMA (g)	**GMA (g)**	**SDS (g)**	**$NaHCO_3$ (g)**	**KPS (g)**	**H_2O (g)**
Reactor	32.4	3.6	1.08	0.9	-	136
Shot	-	-	-	-	0.18	8

2.2.2.2. Synthesis of 3D neat graphene-based monolith

Initially, 40 mL of GO aqueous dispersion was sonicated using Hielscher Sonicator-UIS250v (amplitude of 70 % and energy pulsed at 0.5 Hz, Hielscher Ultrasonics GmbH, Teltow, Germany) at 25 °C for 1 h. The dispersion was then transferred into a flask and left stirring for 2.5 h at 80 °C. After 2.5 h, pre-treated GO dispersion was left to cool to room temperature. After that, the reducing agent, AsA, was added to the dispersion and stirred for 0.5 h for the purpose of homogenization. Subsequently, the homogeneous mixture of GO/AsA was placed in the oven and left at a given temperature (45, 60, and 90 °C) for the formation of the monolithic hydrogel. At 90 °C, the structure was formed in less than 2 h, at 60 °C the process needed 4 h, and at 45

°C, more than 10 h. However, all the procedures were done for 12 h for comparison. Once the sample was removed from the oven, the formed hydrogel monolith was washed or purified by a dialysis process in water to remove the extra AsA and reduction products. The progress of the cleaning process was followed by conductivity measurements of the water solution. The end of the dialysis process was considered when conductivity values were lower than 10 µS/cm. The yield of GO transformed to a monolith was estimated gravimetrically to be in a range of 91 to 95 %, at different AsA amounts and temperatures. Finally, the wet monolith was dried by freeze-drying technique using Telstar LyoQuest 55 at -49 °C and 0.2 mbar for three days to remove the adsorbed water. In Figure 2.1, the straightforward experimental procedure of the 3D neat rGO monolithic material is schematically described.

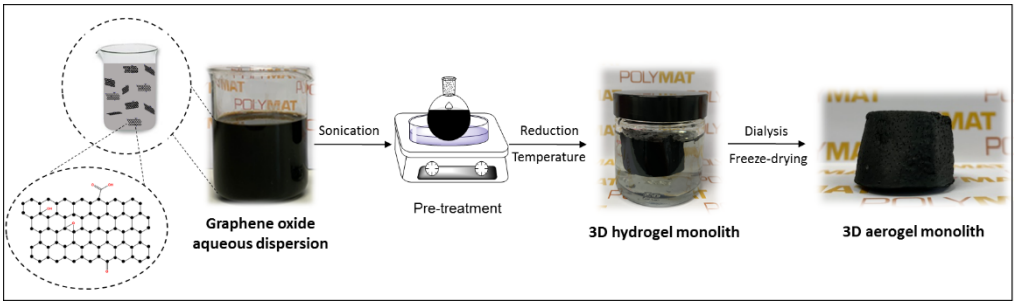

Figure 2.1. Schematic representation of the synthesis of the 3D rGO monolith.

A portfolio of monoliths was prepared by varying different reduction parameters in order to study the influence of these parameters on the morphology, thermal properties, textural properties, and CO_2 adsorption capacities. The altered parameters included (a) reduction temperature (45, 60 and 90 ºC), and (b) ratio between GO to AsA by weight (1:0.5, 1:1, and 1:2). Table 2.2 summarizes the nomenclature of the materials, the reaction conditions and density values.

Table 2.2. Nomenclature of the monoliths, synthesis conditions, and density values.

Material	Temperature (°C)	GO/AsA wt ratio	Density (g/cm^3)
M45_1	45	1:1	0.0035
M60_0.5	60	1:0.5	0.0042
M60_1	60	1:1	0.0051
M60_2	60	1:2	0.0071
M90_0.5	90	1:0.5	0.0061
M90_1	90	1:1	0.0106
M90_2	90	1:2	0.0093

Figure 2.2 presents photos of the monoliths at different reduction temperatures at same GO/AsA weight ratio, and a 5-cent coin is shown as a size comparison. Clearly, the reduction temperature influences the monoliths size, and subsequently, the textural properties.

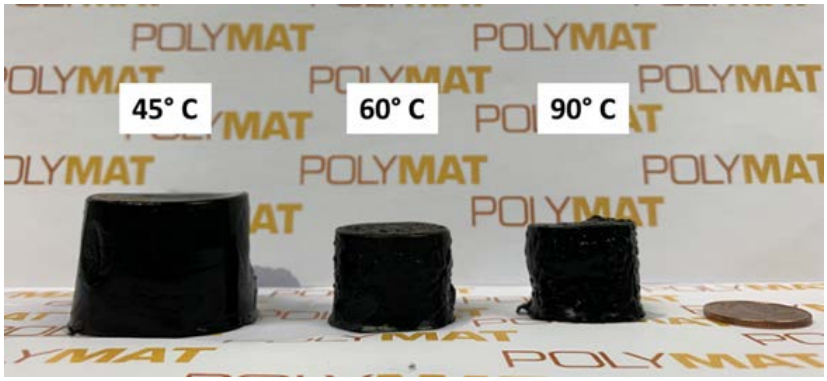

Figure 2.2. Picture of monoliths synthesized at different reduction temperatures (45, 60, and 90 °C) at a GO:AsA ratio of 1:1. The 5-cent coin is added as a size comparison.

2.2.2.3. Synthesis of 3D graphene-based polymer composite monolith

In the synthesis of the rGO/polymer composite monolith, instead of the aqueous dispersion of GO, an aqueous dispersion of GO and polymer nanoparticles was used. After the pre-treatment of GO (sonication and heat at 80 °C), but prior to the addition of AsA, the polymer and GO were left mixing and interacting for 2 h at room temperature. After the addition of AsA (GO:AsA 1:0.5) the reduction process was performed at 90 °C. The composite monolith was then cleaned by dialysis process and dried by freeze-drying process, as explained previously. Figure 2.3. presents the preparation route of the 3D graphene-based polymer composite structure.

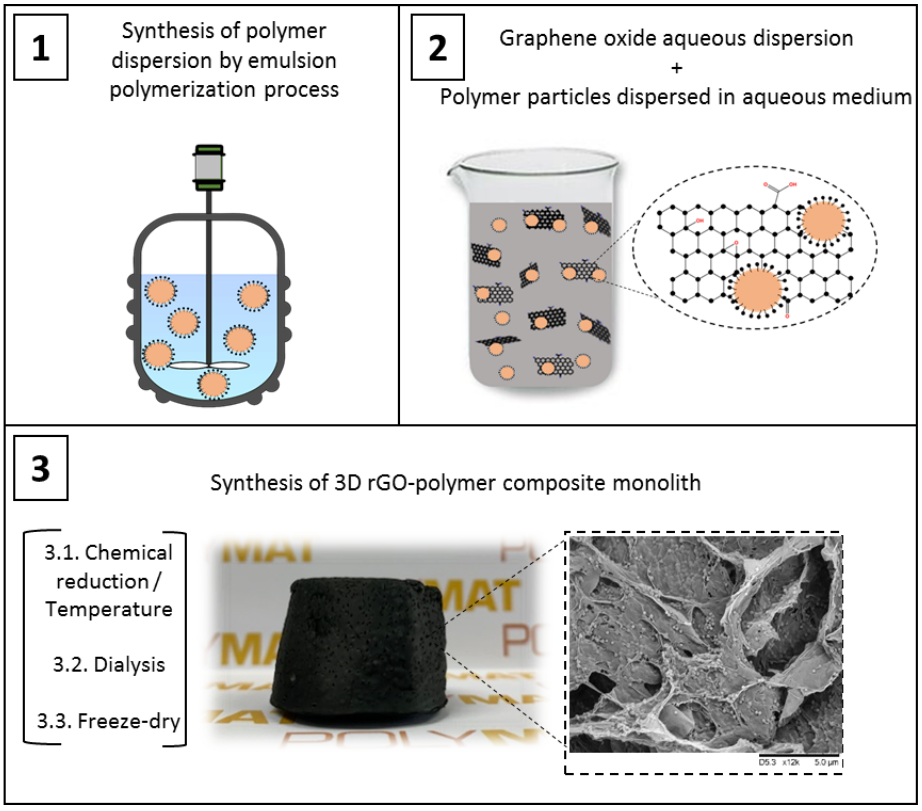

Figure 2.3. Schematic representation of the synthesis of the 3D rGO-polymer composite monolith.

2.2.3. Characterization

In terms of polymer characterization, conversion of the monomer and solids content were calculated gravimetrically. The z-average particle size (dz) of the polymer particles was measured by dynamic light scattering (DLS). The detailed description of the latex characterization methods is given in Section I.1 of Appendix I.

On the other hand, regarding the characterization of the 3D structures, the chemical reduction process was follow by solid-state ^{13}C-NMR in a Bruker 400 AVANCE III WB spectrometer. Thermogravimetric analysis were performed using a TGA500 (TA Instruments) to estimate the amount of residual oxygen-containing functional groups and to study the thermal stability of the 3D monolithic composites. The density of monolithic structures was determined from the ratio of the volume and mass of a rectangular sample (10 mm x 10 mm x 3 mm). From each monolith, at least five samples were prepared, and the densities presented in Table 2.2 are the average of the five measurements. The surface morphology of the structures was examined using a scanning electron microscopy (SEM). The porous texture of the monoliths was characterized by means of N_2 adsorption-desorption isotherm at -196 °C in a Micromeritics ASAP 2020 apparatus. Detailed information of these characterization methods is given in Section I.2 of Appendix I.

The materials´ CO_2 and N_2 gas adsorption capacities were measured from their isotherms, measured using a Micromeritics ASAP 20220 (i.e. volumetrically) at 25 °C. The CO_2/N_2 selectivity was calculated by the ideal adsorbed solution theory (IAST) using only data for the pure-component adsorption equilibria at the same temperature (25 °C) and on the same adsorbent. The respective partial pressures of the components for these calculations were taken from the composition of flue gas from a coal-fired power plant, which contains approximately 15

% CO_2 and 85 % N_2. Detailed information of these gas adsorption measurements is given in Section I.3 of Appendix I.

2.3. Results and discussion

2.3.1. Morphological and textural characteristics of 3D neat graphene-based monolithic structures

Graphene-based monoliths were synthesized by chemical reduction of GO aqueous dispersion using AsA as reducing agent at different temperatures (45, 60, and 90 ºC) and at different weight ratios between GO and AsA (1:0.5, 1:1, and 1:2). The reduction parameters play an important role because they determine the degree and rate of the GO reduction process, which subsequently determines the rate of the self-assembly of rGO sheets and their structure. It is well known that GO platelets contain epoxy (-COC-), hydroxyl (-OH), carbonyl (-CO) and carboxyl (-COOH) groups that are eliminated during reduction process,[7] turning the GO platelets into rGO platelets with a significantly more hydrophobic character. In this way, the interface tension between GO platelets and the aqueous phase and the surface energy of GO platelets in the dispersion increase significantly, resulting in rGO self-organization towards the minimization of the interface between both phases. This process results in the formation of monolithic structures with a porous hierarchical morphology. The 3D monoliths are an ultra-low-density material, as is shown in Table 2.2, with a density in the range of 0.0035-0.0106 g/cm^3. The monoliths synthesized at higher temperatures and AsA amounts exhibit an increased in the density value, indicating that under such conditions, the materials are more compact due to a faster association process, as it can be appreciated in Figure 2.2.

Solid-state ^{13}C-NMR was used to study how the temperature variation influences the chemical structure of the resulting rGO material in the reduction process. In Figure 2.4, the results obtained from solid-state ^{13}C-NMR of the initial GO platelets and monolithic rGOs synthesizes at 45, 60, and 90 ºC are presented.

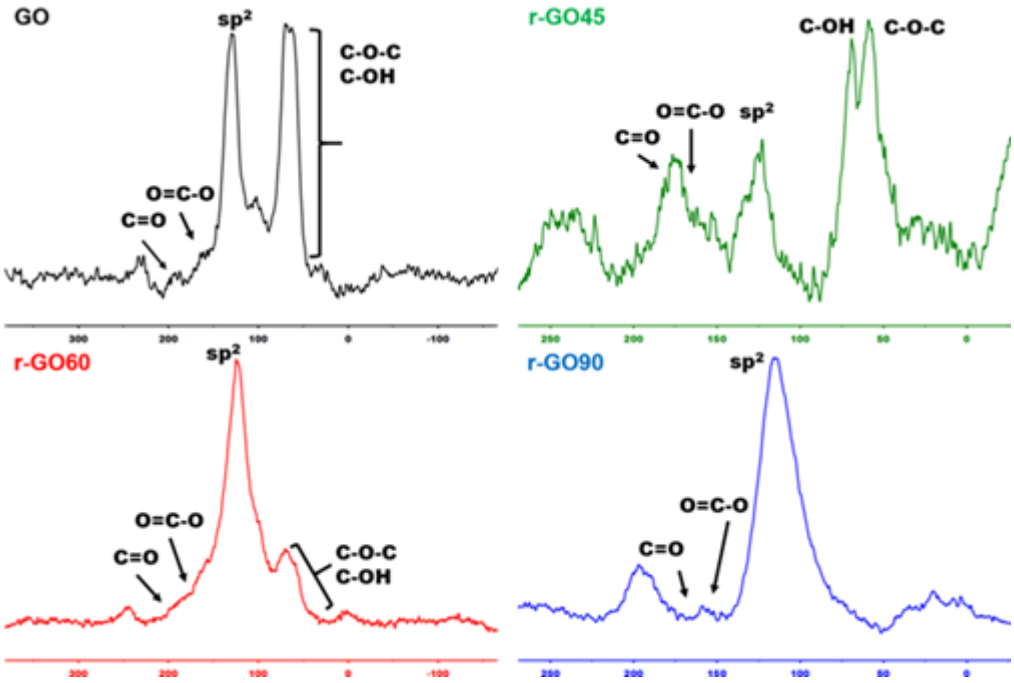

Figure 2.4. Solid state ^{13}C-NMR of monoliths produced at different temperatures (45, 60, and 90 °C) at GO:AsA (1:1) in comparison to that of initial GO.

From the spectra, the ratios of the areas of characteristic peaks of sp^2 C (carbon from C=C) and sp^3 C (carbon from C-O) were calculated and they are presented in Table 2.3 for the different reduction conditions (temperature and AsA amount).

Table 2.3. Ratio of sp^2 to sp^3 carbon, calculated from ^{13}C-NMR spectra of graphene monoliths obtained at different temperatures (GO:AsA 1:1) and with different AsA quantities (at 60 ºC).

Sample	Temperature (°C) (GO/AsA = 1:1)	Ratio sp^2 C /sp^3 C	Sample	Ratio GO/AsA (T = 60 °C)	Ratio sp^2 C /sp^3 C
M45_1	45	0.60	**M60_0.5**	1:0.5	1.96
M60_1	60	4.60	**M60_1**	1:1	4.6
M90_1	90	16.7	**M60_2**	1:2	10.0

Table 2.3 reveals that reduction performed at higher temperatures with the same quantity of AsA results in a more efficient recuperation of the graphene aromatic structure and a higher loss of oxygen-containing functionalities; therefore, the sp^2 C/sp^3 C ratio is higher. Likely, this is the result of a faster chemical reduction by AsA at the increased temperature and the simultaneous thermal reduction. A similar effect was observed for reductions performed at a higher amount of the reducing agent at a constant temperature of 60 ºC.

A more quantitative evaluation of the amount of the residual oxygen-containing functional groups present on the surface of porous monoliths was obtained by thermogravimetric analysis (TGA), as shown in Figure 2.5.

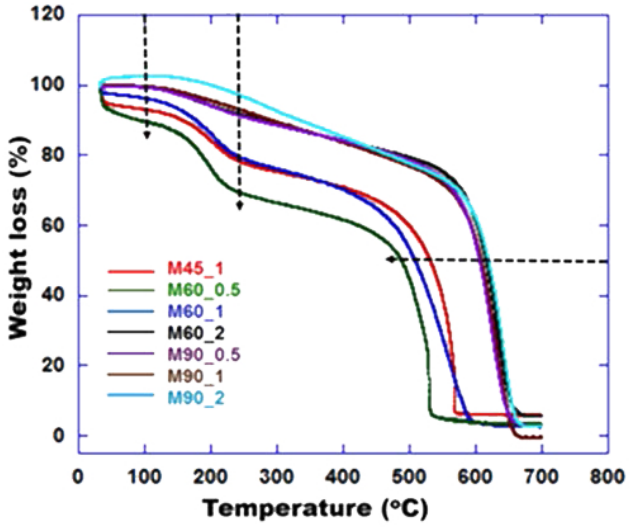

Figure 2.5. TGA thermographs of graphene-based monoliths prepared under different reduction conditions.

Figure 2.5 shows that the monoliths were degraded in two main steps, the first region from 100 °C until 225 ºC is assigned to the loss of the residual oxygen-containing functional groups from the surface of the porous monoliths. The weight loss in the first degradation step until 225 ºC was calculated and it is presented in Table 2.4. It was considered that this loss corresponds to the content of oxygen functionalities in each of the resulting monoliths.

Table 2.4. Degradation temperatures and corresponding weight loss obtained from TGA curves of the monoliths.

Material	Weight loss from 100 ºC until 225 ºC (% O- functionality)	2nd degradation temperature range (ºC)	Weight loss during 2nd degradation step (%)
M45_1	20.3	428-571	62.5
M60_0.5	29.1	420-535	54.9
M60_1	18.2	400-602	66.7
M60_2	7.3	542-671	70.5
M90_0.5	8.1	498-664	75.1
M90_1	6.0	540-669	73.00
M90_2	1.8	557-675	69.1

TGA confirmed that the reduction performed at higher temperatures results in an important drop in the functionalization of the monoliths. Instead, the monoliths synthesized under milder conditions are highly functionalized (20-30 wt%). As may be observed from Figure 2.5 and Table 2.4, the second-degradation step of the monoliths prepared under milder conditions (M45_1, M60_0.5, and M60_1) started at lower temperatures (400-430 ºC), whereas the monoliths obtained at higher temperatures and AsA amounts started this decomposition at 500-560 ºC. The exact degradation temperatures and the corresponding weight loss for each monolith are also presented in Table 2.4. Most of the materials' weight was lost during the second decomposition step due to the burning of carbon structures in the presence of oxygen.[8] This result indicates that the structure of the monoliths obtained under mild conditions is loosely packed, therefore, less energy is necessary to burn it compared to monoliths obtained at higher temperatures and AsA quantities. On the other hand, the materials obtained at 90 ºC with different AsA amounts (M90_0.5, M90_1, and M90_2) exhibit a similar degradation trend. These results indicate that when reacting at higher temperatures, the role of the amount of AsA is not

significantly important for the structuring of the rGO platelets, even though it is important for the amount of residual oxygen-containing functionalities.

The structure and morphology of the 3D monolithic materials were analyzed by SEM characterization technique. In Figure 2.6, the SEM images of all materials are gathered, showing the effect of temperature and AsA amount on the morphology.

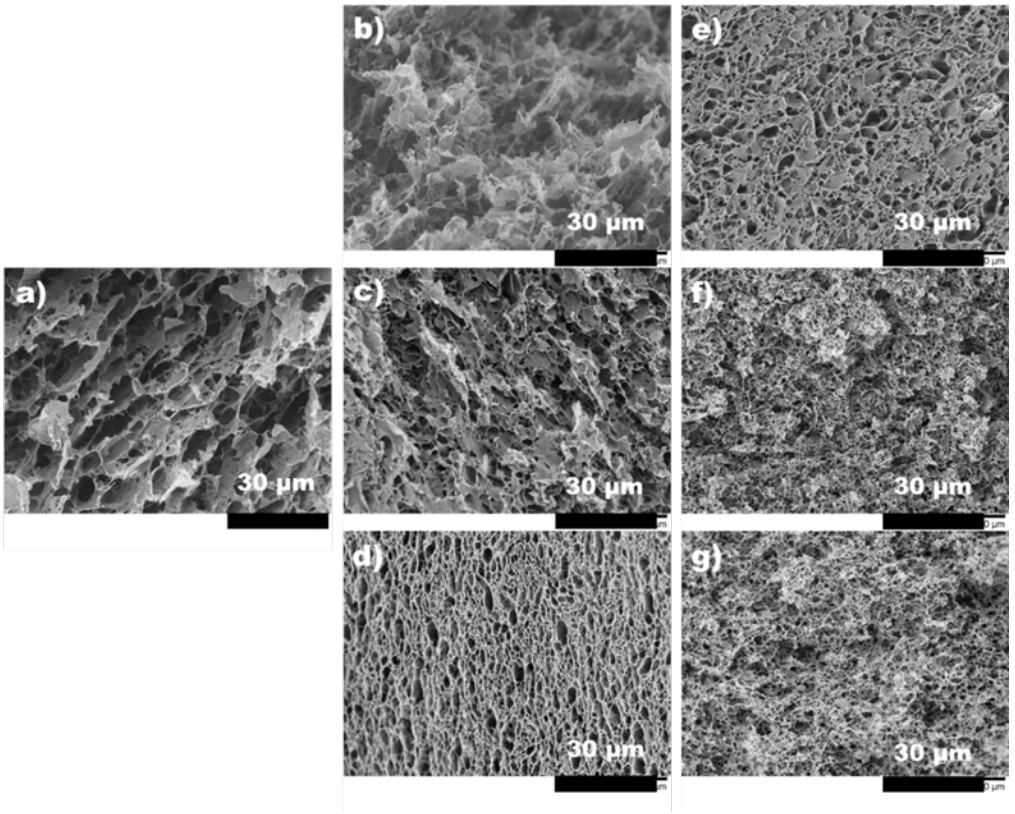

Figure 2.6. SEM images of monoliths obtained at different temperatures and GO:AsA ratios: a) M45_1, b) M60_0.5, c) M60_1, d) M60_2, e) M90_0.5, f) M90_1, and g) M90_2. In each line of the figure, the amount of AsA is constant; in each column of the figure, the temperature is constant. The scale bar is 30 µm.

In Figure 2.6, it can be seen that all monoliths present quite porous morphology, showing an inhomogeneous distribution of large macroscopic pores and a more homogeneous distribution of smaller pores. The increase in temperature from 45 °C to 60 ºC (Figure 2.6, a and c) results in an increase in the porosity, but in both cases, more loosely packed structures are formed. The further increase in temperature to 90 ºC results in a more compact structure (Figure 2.7 f), which is in agreement with TGA. The difference in the packing at different temperatures can also be observed in Figure 2.2, where the photos of the monoliths formed at 45, 60, and 90 ºC at a constant rGO/AsA (1:1) weight ratio are presented. It can be seen that the monolith synthesized at 90 ºC possesses a substantially lower volume than that obtained at 45 °C and 60 ºC.

On the other hand, the porous morphology is significantly influenced by the amount of AsA, thus, a low AsA amount yields a small number of larger pores (Figure 2.6, b and e for M60_0.5 and M90_0.5, respectively). The monolithic materials synthesized with higher amounts of AsA contain elevated numbers of smaller pores, and the graphene sheets are considerably more densely packed within the monoliths (Figure 2.6, d and g for M60_2 and M90_2, respectively).

Furthermore, N_2 adsorption-desorption experiments were carried out in order to obtain a deeper insight into the morphology and textural properties of the 3D monoliths. The adsorption-desorption isotherms are presented in Figure 2.7, whereas Table 2.5 provides information of the specific BET surface area (S_{BET}, m^2/g), total volume and area of the pores (V_{total}, cm^3/g, and A_{total}, m^2/g, respectively), volume of the micropores (V_{micro}, cm^3/g), and porosity (%). The % of porosity was calculated by A_{total}/S_{BET}.

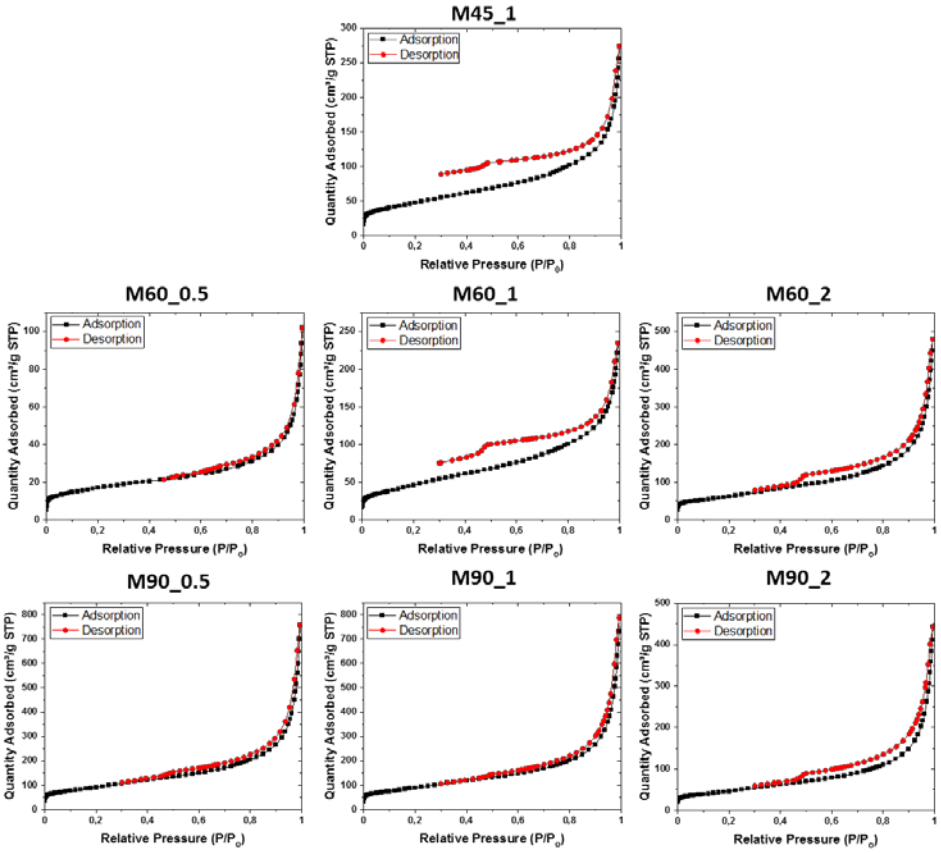

Figure 2.7. N_2 adsorption-desorption isotherms of monoliths obtained at different temperatures and AsA amounts.

Table 2.5. Textural properties of the monoliths obtained at different reaction temperatures and AsA amounts.

Material	S_{BET} (m^2/g)	V_{total} (cm^3/g)	V_{micro} (cm^3/g)	A_{total} (m^2/g)	Porosity (%)
M45_1	170	0.390	0.017	136	80
M60_0.5	60	0.142	0.013	37	62
M60_1	166	0.333	0.015	141	85
M60_2	220	0.709	0.016	208	95
M90_0.5	328	1.118	0.032	293	89
M90_1	319	1.162	0.030	291	91
M90_2	166	0.661	0.010	161	97

The shape of the N_2 adsorption/desorption isotherms in Figure 2.7 indicate a Type IV isotherm characteristic of mesoporous materials and Type H3 hysteresis that refers to aggregates of platelet-like particles forming slit-like pores.[9,10] The results in Table 2.5 reveal that increasing the reduction temperature raises the BET area from 170 m^2/g at 45 ºC up to 328 m^2/g at 90 ºC; therefore, a higher temperature produces structures that are more porous, likely due to the increased number of small pores (in accordance with the SEM images in Figure 2.6 a and f). Furthermore, the porosity increased from 80 to 97 %; and according to Table 2.5, both the total volume and area of pores are affected positively by the increased temperature. Comparing the monoliths synthesized at 60 ºC (M60_0.5, M60_1, and M60_22), when the amount of AsA is increased, an increase in the porosity of the material is also observed, in terms of BET area, total volume and area of the pores, and volume of the micropores (in concordance with the SEM images in Figure 2.6 a,c, and f).

The majority of the increased BET, in this case, represents the contribution from the total volume of the pores increase, as the volume of micropores is not affected importantly (Table 2.5). The only exception is M90_2 monolith, obtained at the highest temperature and with the highest AsA amount, which shows a larger porosity, as the total pore volume is quite high (0.661 cm^3/g) and BET (166 m^2/g) and volume of micropores (0.010 cm^3/g) decrease. This decrease in BET area indicates that M90_2 is a rather wrinkled bulk material, due to the highest temperature and AsA amount. On the contrary, the monolith M60_0.5, produced with the lowest amount of AsA at 60 °C, presents also a low BET and low volume of pores due to the slower reduction process.

From the pore size distributions presented in the next Figure 2.8 (micropores 21-27 %, mesopores 71-76 %, and macropores 2-3 %), it may be concluded that the distributions are not significantly affected by the reaction parameters. The results indicate the all the monoliths are mostly mesoporous materials.

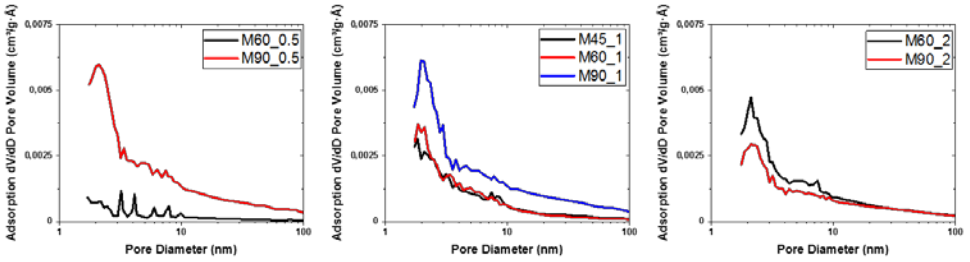

Figure 2.8. Pore volume distribution of the monoliths. Each figure presents the monolith obtained at different temperature at constant AsA content.

All the results discuss above show that the combination of reduction temperature and the amount of reducing agent is decisive for the structuring of the rGO platelets. The monoliths

present a hierarchical structure, which indicates that different self-assembly processes at different size scales of the respective building blocks are contributing toward the final structure formation. We believe that the micropores and the smaller mesopores are formed during the initial restacking of the platelets due to the reduction process and elimination of oxygen-containing functional groups because the individual rGO platelets are the smallest structural elements. The joining of these aggregates during further reduction forms the higher pore size (meso- and macropores), as is shown in the next Figure 2.9.

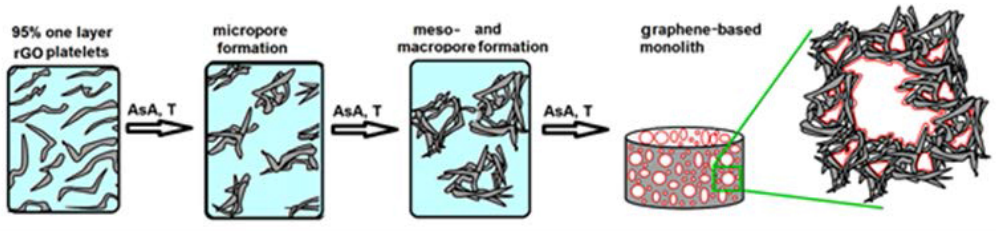

Figure 2.9. Proposed mechanism for the formation of the hierarchical porous structure of graphene-based monoliths.

In general, a higher temperature corresponds to faster reduction processes, which is favorable to produce a well-developed porous morphology and high BET area. However, this effect is limited, as at the highest values of temperature (in combination with the AsA content), the synthesized monoliths lose their porosity, and the self-assembly process results in the simple aggregation of the bulk-graphite-like material (M90_2 sample). On the other hand, milder temperatures with a low amount of reducing agent correspond to slower reduction processes affecting negatively to the self-assembly process, and so to the hierarchical porous morphology.

2.3.2. CO_2 adsorption performance of 3D monoliths

3D graphene-based monolithic structures were synthesized with the aim to use as CO_2 adsorbents in post-combustion process. In Figure 2.10 (a, b, and c), the CO_2 adsorption-desorption isotherms obtained at 25 °C of the monoliths synthesized under different reaction conditions are presented, whereas Figure 2.10.d shows a comparison graph of the CO_2 adsorption capacities obtained at 25 °C and 1 atm for all the materials.

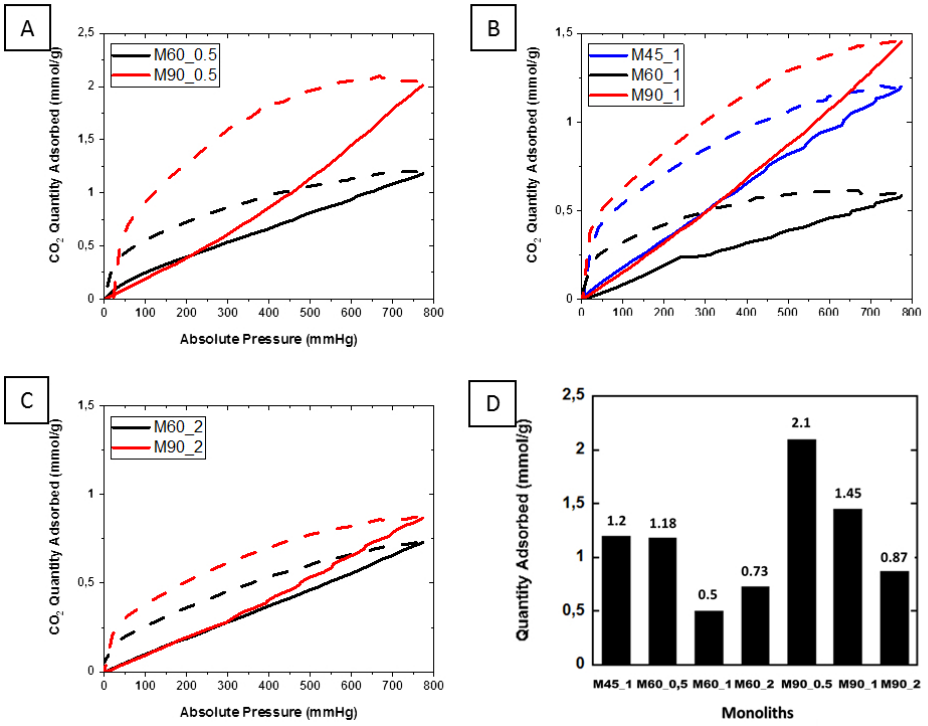

Figure 2.10. CO_2 adsorption (full line)-desorption (dashed line) isotherms of monoliths obtained at different temperatures and with (A) GO:AsA 1:0.5, (B) GO:AsA 1:1, and (C) GO:AsA 1:2. (D) A comparison graph of the CO_2 adsorption capacities of all the monoliths at 25 ºC and 1 atm.

In general, during adsorption, the monoliths act as molecular sieves that retain CO_2 molecules. From Figure 2.10a, b, and c, can be observed that the isotherms exhibited a large hysteresis loop within the whole pressure rang investigated. This means that during the desorption process the CO_2 was not released according to the thermodynamic equilibrium. One of the probable reasons may be the capillary condensation phenomenon, characteristic for solid adsorbents with mesopores.[9] Due to the capillary condensation phenomenon, the accumulated CO_2 molecules condense within the pores. Therefore, for desorption, a larger free energy difference is required to pull out CO_2 molecules from this denser interface than to attract them from a dilute ambient.[11] On the other hand, such a large hysteresis loop may be indication of a long pore size, in which more molecules become adsorbed that in turn increases the energy necessary to be desorbed in the reverse process.[12]

The CO_2 adsorption capacity is directly related to the textural properties. Thus, it can be observed that the monoliths with a higher CO_2 adsorption capacity (M90_0.5 and M90_1) are those that present a greater total porous area because of a stronger affinity between the carbon pores and CO_2 molecules. The highest CO_2 adsorption of 2.1 mmol/g is achieved for the M90_0.5 monolith, produced at 90 ºC and with a low AsA amount (GO/AsA 1:0.5). This result is not surprising, as M90_0.5 has the highest BET (328 m^2/g), as well as the highest total pore area (293 m^2/g) and a significant amount of remaining functionalization (8 %). The importance of either pore area or total volume of the pores for the CO_2 capture capacity is clear from the comparison of the adsorbed CO_2 amount by M45_1 of 1.2 mmol/g, which is twice that of M60_1 (0.5 mmol/g). Despite a very similar BET, and pore area of approximately 170 m^2/g and 140 m^2/g, respectively, M45_1 presents a higher total volume of the pores (0.390 cm^3/g vs 0.333 cm^3/g). The surprising result is that of the M60_0.5 monolith, because M60_0.5 presents the lowest BET and an inconsequential pore area (37 m^2/g), yet, exhibits a relatively high CO_2 adsorption of 1.18

mmol/g. As it has been demonstrated, the presence of heteroatoms, such as O, S, or P, increases the attraction of CO_2 to the solid sorbents,[13,14] because we think that the denser presence of oxygen-containing functionalities on the surface of M60_0.5 (29 wt%, Table 2.4) contributes importantly towards the increased CO_2 adsorption in this case. Considering this notion and defining the capacity of the monoliths to capture CO_2 as the interplay among the BET area, volume and area of the pores, and the level of functionalization, all the results presented in Figure 2.10.d may be explained. For example, M90_0.5 and M90_1 yield very similar porous structures (BET and porosity); however, M90_0.5 adsorbs approximately 30 % more CO_2, likely due to the higher level of functionalization (8 vs 6 %). On the other hand, M60_1 and M60_2 present similar CO_2 adsorptions, likely because of the higher BET of M60_2 compensating for the higher level of functionalization in M60_1. It is worth mentioning that the presented capacity for CO_2 capture was obtained with "as-received" monoliths, without any activation treatment that usually triple the adsorbed CO_2 quantity.[15–23] These activation processes are performed using bases and at extremely high temperatures (500-900 ºC), therefore, the amount of CO_2 released during production is tremendous.

The adsorbed amount by the series of different "as-received" monoliths at 25 ºC and 1 atm is within the range of 0.60 mmol/g to 2.10 mmol/g (Figure 2.10d). Compared to published data for CO_2 adsorption by similar carbon-based porous materials (Table 2.6), this result is one of the highest reported for untreated "as-received" materials.

Table 2.6. Comparison of the adsorption capacities of the monoliths from this work with similar reported materials.

Type of GO/C	Preparation	Activation	Conditions of CO_2 measurement	Adsorption capacity (mmol/g)	Ref.
rGO-monolith	Reduction at 45-90 ºC	None	298 K, 1 atm	0.60-2.10	This work
rGO-monolith	Hydrothermal carbonization glucose/GO 200 ºC	KOH/800 ºC	298 K, 1 atm	0.70 (no act) 3.00 (act)	15
rGO-3D	Hydrothermal 80-120 ºC	None	273 K, 1 atm	2.4	16
rGO-3D	Sonication HNO_3	500 ºC/ 30 min (N_2)	298 K, 1 atm	1.3	17
rGO-3D	Thermal reduction 250 ºC/30 min	CO_2 at 750, 850, & 950 °C	273 K, 1 atm	0.90 (no act) 3.36 (act)	18
GO-3D	Resorcinol, borax & glutaraldehyde	None	298 K, 1 atm	0.6	19
rGO	Hydrazine	None	298 K, 1 atm	0.5	20
rGO	Hydrazine 100 ºC	800 ºC	298 K, 1 atm	2.20 (act)	21
Graphene networks	300 ºC	TETA (introduced NH2 groups)	303 K, 1 atm	2.92	22
Active carbon	Carbonization of pine nut shell 500 ºC/1.5 h	KOH/500-900 ºC 0.5 to 2.5 h	298 K, 1 atm	5	23

According to the data shown in Table 2.6, the CO_2 adsorption capacity of similar "as-received" carbon-based porous materials under similar conditions is within the range of 0.7-0.9 mmol/g. A higher CO_2 adsorption of 2.4 mmol/g by the similar 3D rGO structure was presented by Sui and Han;[16] however, the value was determined at 0 ºC, and it is well known that with decreasing temperature, the CO_2 adsorption increases. A high-temperature treatment with KOH (500-900 ºC) likely activated the material and further increased the adsorption to a range of 3-5 mmol/g.[15,18,21,23] A graphene network synthesized at 300 ºC and post-modified by NH_2 groups presented a CO_2 adsorption of 2.92 mmol/g.[22] In conclusion, in addition to being synthesized with a low-energy process, the present monoliths present the highest CO_2 adsorption capacity when compared to that of similar non-treated materials.

Nevertheless, to have a relevant solid sorbent for CO_2 capture, in addition to a high capacity to capture CO_2, it is important that the monoliths not only show a high selectivity in the presence of N_2 (especially for the case of post-combustion capturing processes) but also to exhibit stability in cycle operations. To that aim, the M90_0.5 monolith, with the best performance for CO_2 capture, was selected for further experiments. Figure 2.11 shows a comparison of the single-component adsorption isotherms of CO_2 and N_2 in a pressure range of 5 to 772 mm Hg, presenting a significantly higher adsorption capacity for CO_2 over that of N_2 for the whole pressure range investigated.

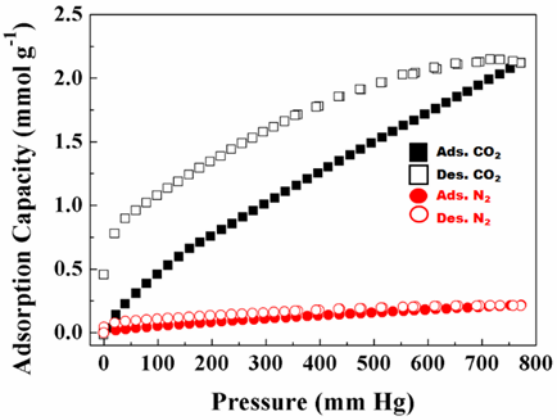

Figure 2.11. Comparison of the adsorption/desorption isotherms of CO_2 and N_2 captured by the M90_0.5 monolith at 25 ºC.

This effect is likely a consequence of the stronger CO_2 quadrupole moment, which after the appropriate adsorption onto a graphene surface, allows the clustering of CO_2 molecules by electrostatic interactions;[24] this enhancement does not happen with N_2 molecules because they have a quadrupole moment one-third that of CO_2. For the calculation of the selectivity of CO_2 over N_2, ideal adsorbed solution theory (IAST) was used, using the single-component adsorption isotherms of CO_2 and N_2 obtained at 25 ºC, modelled by Freundlich isotherm.[25] The fitting curves for CO_2 and N_2 and the parameters in the Freundlich isotherms are presented in Section II.1 of Appendix II. The limitations using low pressure, single gas adsorption measurements to calculate the selectivity is mainly because the adsorption equilibria for mixtures is considerably affected by heterogeneity of the adsorption surface, as the surface of our monoliths is. Furthermore, the predicted results from individual adsorption isotherms sometimes differ from the real measurements of gas mixtures because of kinetic flow conditions. Nevertheless, this method is widely used because of its simplicity and robustness.

At a total pressure of 772 mm Hg, the selectivity was found to be 53, which is considered above the threshold of a cost-efficient capture/separation process.[26] This selectivity is within the range of reported values for similar materials (29-162).[18,27]

The stability of the M90_0.5 monolith in cycle operation is presented in Figure 2.12. The monolith was exposed to 5 cycles of CO_2 adsorption-desorption processes, whereby CO_2 desorption was performed by a pressure swing.

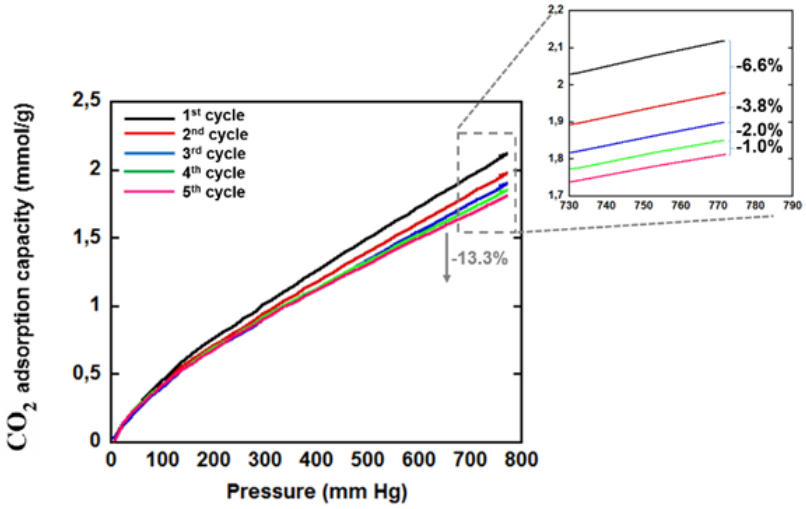

Figure 2.12. CO_2 adsorption isotherms for different cycles of the M90_0.5 monolith.

During this operation, no mass loss was noticed, showing the good mechanical stability of the monolith; however, after each cycle, the amount of captured CO_2 decreased. For example, in the second cycle, the adsorbed CO_2 is 6.6 % less than that in the first cycle, and in the third cycle, the value is 3.8 % less than in the second cycle, etc. In the fourth and fifth cycles, the percentage lost between the cycles is lower, which means that the monolith slowly stabilizes with

respect to CO_2 sorption. We thought that some small pores with walls made of very thin rGO platelets collapsed irreversibly after the first few desorption cycles because of a lack of mechanical stability when exposed to pressures as low as 5 mm Hg. A similar behavior has been reported for other porous materials used for CO_2 adsorption.[28–30] In Figure 2.13, the adsorption-desorption isotherms for the first and last (5th) cycles are shown, where except for the final adsorption, which is lower, there is no important difference noticed in the shape of the isotherms. This result indicates that the structure and the morphology are not affected significantly during the process cycles.

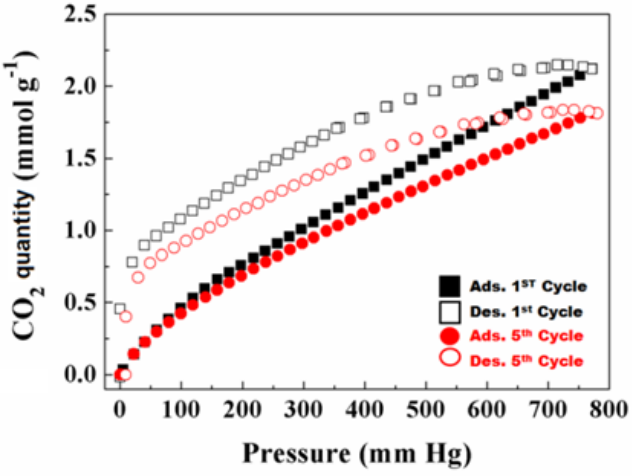

Figure 2.13. CO_2 adsorption/desorption isotherms of monolith M90_1 for first and last cycle of 5 cycles performed.

Previous experience has shown that the addition of a small amount of polymer nanoparticles to porous graphene-based structures improved the mechanical resistance.[31] Therefore, to check this possibility, a composite monolith was produced under the same conditions as M90_0.5 but in the presence of polymer nanoparticles made of poly(glycidyl methacrylate/methyl methacrylate) (MMA/GMA) with an average diameter of 70 nm, produced

by batch emulsion polymerization. 20 wt% polymer with respect to the initial amount of GO was added to the structure. The capacity to capture CO_2 by the composite monolith in five cycles is shown in Figure 2.14.

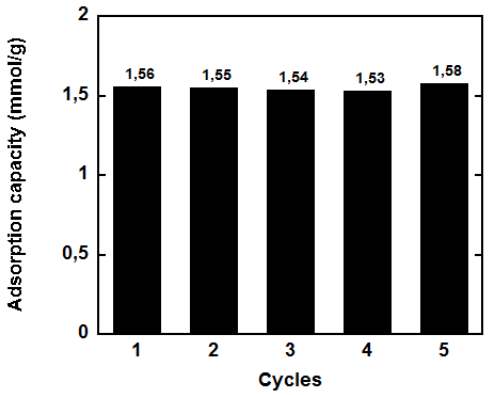

Figure 2.14. CO_2 adsorption capacity for 5 adsorption/desorption cycles of the M90_0.5 monolith containing polymer particles, measured at 25 ºC and 1 atm.

On the one hand, with the addition of polymer, the maximum CO_2 sorption capacity drops slightly from 2.1 to 1.55 mmol/g, and on the other hand, this value remains constant during the 5 cycles of adsorption-desorption. The drop in the capacity is probably a result of the change in porous morphology due to the polymer's presence in the composite monolith synthesis, which may provide mechanical stability to the monolith for cycling operation. Nevertheless, this result shows a possible route to stabilize rGO-based monoliths for cycle operation, which paves the way towards repeated use of the monoliths in selective CO_2 capture.

2.4. Conclusions

In this study, porous monolithic graphene-based materials for the capture of CO_2 were synthesized by a self-assembly process of GO. The variation in the reaction parameters, such as temperature and the amount of reducing agent (AsA), allowed for the synthesis of a portfolio of different monoliths.

The characterization performed by solid state ^{13}C-NMR, SEM, TGA, and BET analyses provided detailed information about the chemical structure and morphology that facilitated the comprehension of the self-assembly process. As a result, a mechanism for the creation of the monolithic porous structures was proposed and may be a basis for the process design to tailor the porous morphology and chemistry of the monoliths.

The efficiency of the monoliths as solid CO_2 sorbents was analysed and related to the chemical structure and morphology. That is, by maintaining mild synthesis conditions (low temperature and AsA concentration), the resulting monoliths were highly functionalized with low BET values. However, for some of these materials, the contribution of the pore volume to the BET was higher, which in combination with a high content of oxygen-containing functionalities resulted in a substantial CO_2 capture capacity. At a high temperature and with different AsA concentrations, the monolithic materials were more compact with very well-developed hierarchical porous structures and high porosities; these properties resulted in high BET areas with lower contents of oxygen-containing functionalities and higher CO_2 adsorptions. The best performance was obtained at 90 ºC and with the lowest AsA content, parameters that allowed a relatively high functionalization of 8 % (2.1 mmol/g). The monolith obtained under such conditions was further evaluated to determined the CO_2/N_2 selectivity and stability in cycle operation. A relatively high selectivity of 53 was obtained; however, in 5 adsorption-desorption cycles, this

monolith exhibited a slightly reduced capacity to capture CO_2. This behavior was explained by the possible collapse of small pores with thin walls under the process of desorption at very low pressures. A solution to improve the mechanical stability of the monoliths was proposed and included the addition of a small amount of polymer particles within the monolithic structure, which indeed yielded a stable operation during 5 cycles.

2.5. References

(1) Crittenden, B.; Patton, A.; Jouin, C.; Perera, S.; Tennison, S.; Echevarria, J. A. B. Carbon Monoliths: A Comparison with Granular Materials. *Adsorption* **2005**, *11* (1 SUPPL.), 537–541.

(2) Arami-Niya, A.; Rufford, T. E.; Zhu, Z. Activated Carbon Monoliths with Hierarchical Pore Structure from Tar Pitch and Coal Powder for the Adsorption of CO2, CH4 and N2. *Carbon N. Y.* **2016**, *103*, 115–124.

(3) Rezaei, F.; Mosca, A.; Webley, P.; Hedlund, J.; Xiao, P. Comparison of Traditional and Structured Adsorbents for Co2 Separation by Vacuum-Swing Adsorption. *Ind. Eng. Chem. Res.* **2010**, *49* (10), 4832–4841.

(4) Estevez, L.; Dua, R.; Bhandari, N.; Ramanujapuram, A.; Wang, P.; Giannelis, E. P. A Facile Approach for the Synthesis of Monolithic Hierarchical Porous Carbons-High Performance Materials for Amine Based CO2 Capture and Supercapacitor Electrode. *Energy Environ. Sci.* **2013**, *6* (6), 1785–1790.

(5) Akhtar, F.; Andersson, L.; Ogunwumi, S.; Hedin, N.; Bergström, L. Structuring Adsorbents and Catalysts by Processing of Porous Powders. *J. Eur. Ceram. Soc.* **2014**, *34* (7), 1643–1666.

(6) Yun, S.; Lee, H.; Lee, W. E.; Park, H. S. Multiscale Textured, Ultralight Graphene Monoliths for Enhanced CO2 and SO2 Adsorption Capacity. *Fuel* **2016**, *174*, 36–42.

(7) Zhang, J.; Yang, H.; Shen, G.; Cheng, P.; Zhang, J.; Guo, S. Reduction of Graphene Oxide Vial-Ascorbic Acid. *Chem. Commun.* **2010**, *46* (7), 1112–1114.

(8) Azizighannad, S.; Mitra, S. Stepwise Reduction of Graphene Oxide (GO) and Its Effects on Chemical and Colloidal Properties. *Sci. Rep.* **2018**, *8* (1), 1–8.

(9) Thommes, M.; Kaneko, K.; Neimark, A. V.; Olivier, J. P.; Rodriguez-Reinoso, F.;

Rouquerol, J.; Sing, K. S. W. Physisorption of Gases, with Special Reference to the Evaluation of Surface Area and Pore Size Distribution (IUPAC Technical Report). *Pure Appl. Chem.* **2015**, *87* (9–10), 1051–1069.

(10) Li, T.; Jiang, Z.; Xu, C.; Liu, B.; Liu, G.; Wang, P.; Li, X.; Chen, W.; Ning, C.; Wang, Z. Effect of Pore Structure on Shale Oil Accumulation in the Lower Third Member of the Shahejie Formation, Zhanhua Sag, Eastern China: Evidence from Gas Adsorption and Nuclear Magnetic Resonance. *Mar. Pet. Geol.* **2017**, *88*, 932–949.

(11) Dantas, S.; Struckhoff, K. C.; Thommes, M.; Neimark, A. V. Phase Behavior and Capillary Condensation Hysteresis of Carbon Dioxide in Mesopores. *Langmuir* **2019**, *35* (35), 11291–11298.

(12) Balderas Altamirano, M. A.; Cordero, S.; López-Esparza, R.; Pérez, E.; Gama Goicochea, A. Importance of Pore Length and Geometry in the Adsorption/Desorption Process: A Molecular Simulation Study. *Mol. Phys.* **2015**, *113* (23), 3849–3853.

(13) Alabadi, A.; Razzaque, S.; Yang, Y.; Chen, S.; Tan, B. Highly Porous Activated Carbon Materials from Carbonized Biomass with High CO2 Capturing Capacity. *Chem. Eng. J.* **2015**, *281*, 606–612.

(14) Abdelmoaty, Y. H.; Tessema, T. D.; Norouzi, N.; El-Kadri, O. M.; Turner, J. B. M. G.; El-Kaderi, H. M. Effective Approach for Increasing the Heteroatom Doping Levels of Porous Carbons for Superior CO2 Capture and Separation Performance. *ACS Appl. Mater. Interfaces* **2017**, *9* (41), 35802–35810.

(15) Martín-Jimeno, F. J.; Suárez-García, F.; Paredes, J. I.; Martínez-Alonso, A.; Tascón, J. M. D. Activated Carbon Xerogels with a Cellular Morphology Derived from Hydrothermally Carbonized Glucose-Graphene Oxide Hybrids and Their Performance towards CO2 and Dye Adsorption. *Carbon N. Y.* **2015**, *81* (1), 137–147.

(16) Sui, Z. Y.; Han, B. H. Effect of Surface Chemistry and Textural Properties on Carbon Dioxide Uptake in Hydrothermally Reduced Graphene Oxide. *Carbon N. Y.* **2015**, *82* (C), 590–598.

(17) Chowdhury, S.; Balasubramanian, R. Holey Graphene Frameworks for Highly Selective Post-Combustion Carbon Capture. *Sci. Rep.* **2016**, *6* (February), 1–10.

(18) Chowdhury, S.; Balasubramanian, R. Three-Dimensional Graphene-Based Porous Adsorbents for Postcombustion CO2 Capture. *Ind. Eng. Chem. Res.* **2016**, *55* (29), 7906–7916.

(19) Sudeep, P. M.; Narayanan, T. N.; Ganesan, A.; Shaijumon, M. M.; Yang, H.; Ozden, S.; Patra, P. K.; Pasquali, M.; Vajtai, R.; Ganguli, S.; et al. Covalently Interconnected Three-Dimensional Graphene Oxide Solids. *ACS Nano* **2013**, *7* (8), 7034–7040.

(20) Seema, H.; Kemp, K. C.; Le, N. H.; Park, S. W.; Chandra, V.; Lee, J. W.; Kim, K. S. Highly Selective CO2 Capture by S-Doped Microporous Carbon Materials. *Carbon N. Y.* **2014**, *66*, 320–326.

(21) Chowdhury, S.; Balasubramanian, R. Highly Efficient, Rapid and Selective CO2 Capture by Thermally Treated Graphene Nanosheets. *J. CO2 Util.* **2016**, *13*, 50–60.

(22) Gadipelli, S.; Lu, Y.; Skipper, N. T.; Yildirim, T.; Guo, Z. Design of Hyperporous Graphene Networks and Their Application in Solid-Amine Based Carbon Capture Systems. *J. Mater. Chem. A* **2017**, *5* (34), 17833–17840.

(23) Deng, S.; Wei, H.; Chen, T.; Wang, B.; Huang, J.; Yu, G. Superior CO2 Adsorption on Pine Nut Shell-Derived Activated Carbons and the Effective Micropores at Different Temperatures. *Chem. Eng. J.* **2014**, *253*, 46–54.

(24) Meconi, G. M.; Tomovska, R.; Zangi, R. Adsorption of CO 2 Gas on Graphene-Polymer Composites. *J. CO2 Util.* **2019**, *32* (March), 92–105.

(25) PRAUSNITZ, A. L. M. and J. M. Thermodynamics of Mixed-Gas Adsorption. *A.1.Ch.E. J.* **1965**, *11* (1), 121–126.

(26) Zhai, H. Advanced Membranes and Learning Scale Required for Cost-Effective Post-Combustion Carbon Capture Advanced Membranes and Learning Scale Required for Cost-Effective Post-Combustion Carbon Capture. *ISCIENCE* **2019**, *13*, 440–451. https://doi.org/10.1016/j.isci.2019.03.006.

(27) Pan, Y.; Xue, M.; Chen, M.; Fang, Q.; Zhu, L.; Valtchev, V.; Qiu, S. ZIF-Derived: In Situ Nitrogen Decorated Porous Carbons for CO2 Capture. *Inorg. Chem. Front.* **2016**, *3* (9), 1112–1118.

(28) Koushyar, H.; Alavi-Soltani, S.; Minaie, B.; Violette, M. Effects of Variation in Autoclave Pressure, Temperature, and Vacuum-Application Time on Porosity and Mechanical Properties of a Carbon Fiber/Epoxy Composite. *J. Compos. Mater.* **2012**, *46* (16), 1985–2004.

(29) Samanta, A.; Zhao, A.; Shimizu, G. K. H.; Sarkar, P.; Gupta, R. Post-Combustion CO 2 Capture Using Solid Sorbents: A Review. *Ind. Eng. Chem. Res.* **2012**, *51* (4), 1438–1463.

(30) Ben-Mansour, R.; Habib, M. A.; Bamidele, O. E.; Basha, M.; Qasem, N. A. A.; Peedikakkal, A.; Laoui, T.; Ali, M. Carbon Capture by Physical Adsorption: Materials, Experimental Investigations and Numerical Modeling and Simulations - A Review. *Appl. Energy* **2016**, *161*, 225–255.

(31) Ormategui, N.; Veloso, A.; Leal, G. P.; Rodriguez-couto, S.; Tomovska, R. Design of Stable and Powerful Nanobiocatalysts, Based on Enzyme Laccase Immobilized on Self-Assembled 3D Graphene/Polymer Composite Hydrogels. **2015**.

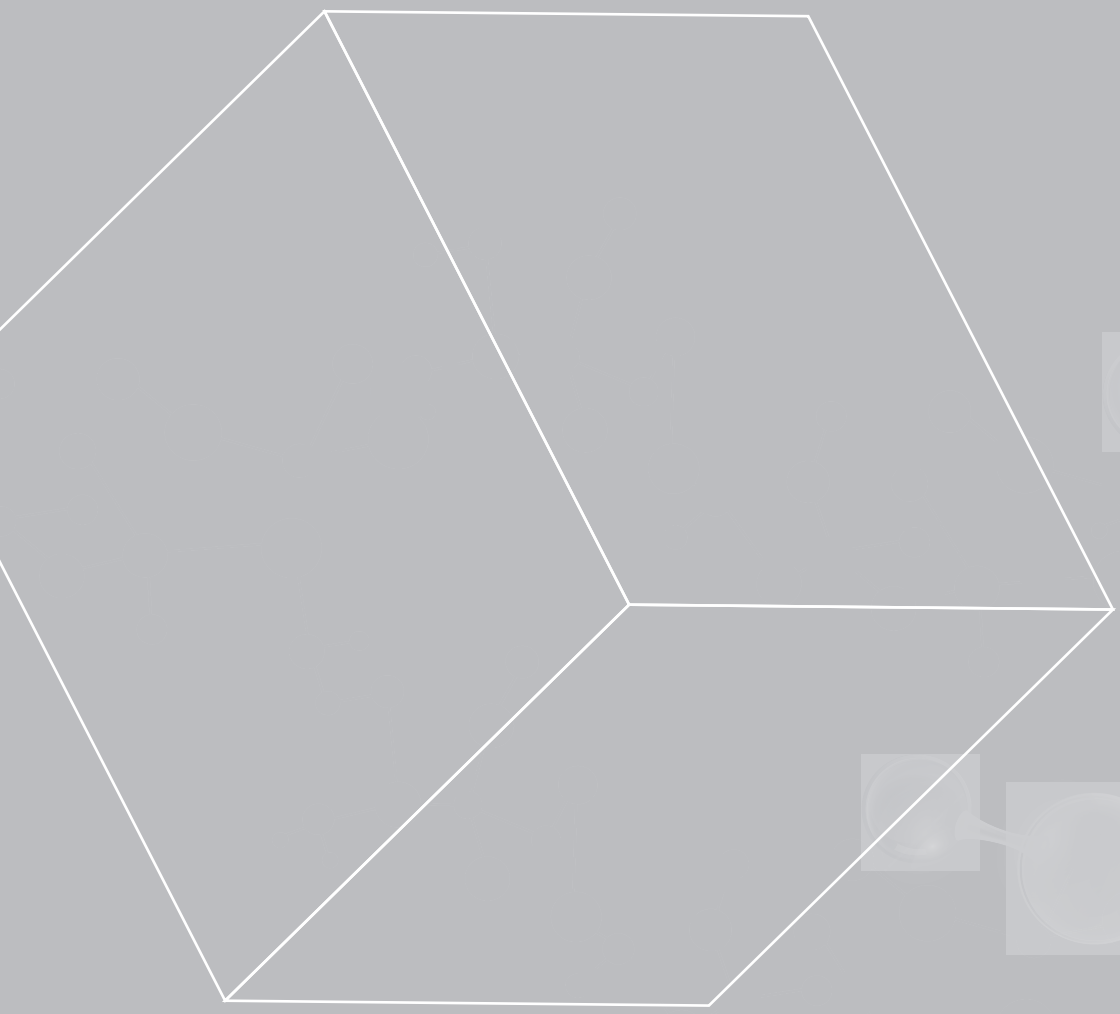

CHAPTER 3

Functionalized graphene-polymer monolithic structures for selective CO_2 capture

Chapter 3. Functionalized graphene-polymer monolithic structures for selective CO_2 capture

3.1. Introduction

In Chapter 2, the study of the influence of reduction conditions (amount of reducing agent and reduction temperature) in the final morphology, textural and adsorption properties of the 3D neat rGO monolithic structures was carried out. However, these materials showed a poor cycle stability in terms of CO_2 adsorption-desorption processes due to the possible collapse of small pores. Nevertheless, the addition of a small amount of polymer particles within the graphene-based skeleton improved the mechanical stability and yielded a stable cycle operation.

In this chapter, the addition of polymer particles in resulting properties is further studied due to, without any doubt, the incorporation of functionalized polymers to the 3D graphene-based structures provides multiple advantages. It has been demonstrated that functional groups containing heteroatoms, principally nitrogen, oxygen and sulphur, can promote the selective CO_2 adsorption with respect to the pristine graphene.[1–4] Even though the presence of these functional groups enhanced the performance of the composites for selective CO_2 capture,[5,6] the whole procedure to introduce heteroatoms on carbon surface or matrix requires high-energy synthesis or post-synthesis activation processes, as it is also mentioned in Chapter 1 and 2.[7] Although there are reports in which for the synthesis of 3D graphene-polymer structures activation or high energy-consuming methods were avoided, the CO_2 adsorption capacities were significantly lower.[8,9] In this study, we propose and develop an unique method of functionalization of graphene during the synthesis of self-assembled monolithic 3D graphene-polymer structures, performed

under mild conditions (45-90 °C) in aqueous solution, attaining competitive CO_2 adsorption capacity results.

Herein, by selecting two different functional monomers, sodium 4-vinylbenzensulfonate (NaSS) and 2-acrylamido-2-methyl-1-propanesulfonic acid (AMPS), either sulphur or sulphur and nitrogen containing functional groups were introduced onto polymer particles prior to composite synthesis. The chemical structures of NaSS and AMPS are presented in Figure 3.1. 1 % of NaSS and 1 % of AMPS were independently copolymerized with the main monomer methyl methacrylate (MMA). MMA polymer particles were selected due to their high T_g (about 105 °C),[10] which ensures that during drying process the particles would not lost the particle morphology and will not entirely covered the rGO surface. Namely, our previous (experimental and theoretical studies) results have shown that the CO_2 molecules have higher affinity towards the neat rGO surfaces than towards the polymers.[11] On the other hand, the addition of solution polymer containing 100 % of both NaSS and AMPS functional monomers is also studied.

In order to do so, GO aqueous dispersion was mixed with aqueous dispersions of functionalized polymer particles as precursor materials for creation of 3D composite structures, synthesized by self-assembly process driven by GO reduction. The schematic representation of the synthesis of the composites is presented in Figure 2.3 in Chapter 2. The effect of the functionalities on the textural properties of the 3D monolithic materials obtained under different synthesis conditions were studied and related to the performance for selective CO_2 capture. It is worth noting that this work provides different approach of functionalization of graphene that does not required complex reaction, catalyst or solvent use, nor increased temperature, as well as, no subsequent purifications steps of the functionalized graphene platelets are necessary.

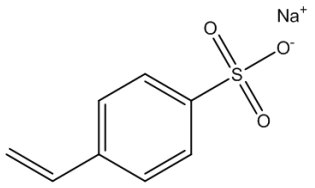

Sodium 4-vinylbenzensulfonate
(NaSS)

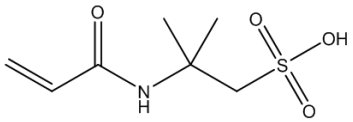

2-Acrylamido-2-methyl-1-propanesulfonic acid
(AMPS)

Figure 3.1. Chemical structures of NaSS and AMPS functional monomers.

3.2. Experimental part

3.2.1. Materials

As in Chapter 2, 40 mL of aqueous dispersion of graphene oxide (GO) sheets of 4 mg/mL (Graphenea) was used as supplied. For chemical GO reduction L-ascorbic acid (AsA, ≥99 %, Sigma- Aldrich) was used. Technical monomers methyl methacrylate (MMA, Quimidroga), sodium 4-vinylbenzensulfonate (NaSS, ≥90 %, Sigma-Aldrich), and 2-acrylamido-2-methyl-1-propanesulfonic acid (AMPS, 99 %, Sigma-Aldrich) were used without purification. *Tert*-Butyl hydroperoxide solution (TBHP, 70 wt % in H_2O, Sigma-Aldrich), potassium persulfate (KPS, ≥99 %, Sigma-Aldrich) and Dowfax 2A1 (Dow Chemical Company) were used as received. Deionized water was used as polymerization media. Tetrahydrofuran (GPC grade-THF, Scharlab) was used for the SEC measurement. Polystyrene (PS) and polyethylene glycol (PEG) standards (Polymer Laboratories, VARIAN) were used for the calibration of THF-based SEC and aqueous-based SEC, respectively. Silica carbide (Carborundum,VWR, Prolabo) particles with average sizes of 0.105, 0.500, and 1.190 mm were used in the pressure drop measurement.

3.2.2. Synthesis of polymers

3.2.2.1. Synthesis of functionalized polymer dispersions

NaSS and AMPS functional monomers (1 wt%) were independently copolymerized with the main monomer MMA (99 wt%) by seeded semibatch emulsion polymerization. The reactions were carried out under nitrogen flux in a glass reactor equipped with a reflux condenser, a stainless-steel stirrer, a sampling tube, a thermocouple and feeding inlet. The reactor's temperature was controlled through an automatic control system (Camile TG, Biotage).

The procedure was as follow: initially, a seed of 20 % solids content of MMA was produced by batch emulsion polymerization. MMA, emulsifier (Dowfax 2A1) and water were loaded in the reactor. The mixture was degassed by nitrogen bubbling, constantly stirring at 200 rpm, while heating to 70 °C. Once the desired reaction temperature was reached, an aqueous thermal initiator (KPS) solution was added in one shot. After that, the reaction mixture was let to react batchwise at 70 °C during 120 min. Finally, the reaction was kept at 70 °C for an additional 30 min to ensure complete monomer consumption. In the next step, the rest of the monomers, the aqueous solution of redox initiators (TBHP and AsA) and the emulsifier (Dowfax 2A1) were fed for 210 min in two independent streams. The formulations used for the synthesis of the latexes are shown in Table 3.1, where F1 and F2 correspond to the two different streams and F.M. abbreviation corresponds to functional monomer. With this methodology, two latexes with a final solids content of 30 % were prepared with functional monomers (NaSS and AMPS) content of 1 % weight-based to MMA. Comparing their chemical structures (Figure 3.1), both of them contain sulphur (S) atom, but AMPS functional monomer also contains nitrogen (N) atom.

Table 3.1. Formulation employed for the synthesis of both NaSS-MMA and AMPS-MMA latexes.

		Initial seed (g)	MMA (g)	F.M. (g)	Dowfax (g)	KPS (g)	AsA (g)	TBHP (g)	H_2O (g)
Batch	Seed		360		7.2	1.8			1440
Semi-batch	Initial charge	33.87	-	-	-	-	-	-	120
	F1	-	-	1.05	-	-	0.53	-	57.85
	F2	-	98.28	-	1.05	-	-	0.53	40

3.2.2.2. Synthesis of solution polymers

To obtain water-soluble homopolymers of NaSS and AMPS functional monomers, solution polymerization was performed. The reactions were carried out under nitrogen flux in a glass reactor. The functional monomer (10 g) and water (32 g) were loaded in the reactor and heat up to 70 °C. Once the desired reaction temperature was reached, an aqueous thermal initiator (KPS) solution (0.05 g KPS in 8 g water) was added in one shot. After that, the reaction mixture was let to react batchwise at 70 °C during 24 h obtaining a homopolymer with a final concentration of 20 %.

3.2.3. Synthesis of 3D rGO-polymer composites

The synthesis of 3D rGO-polymer composites were performed following the same route explained in Section 2.2.2.3 of Chapter 2. Shortly, 40 mL of GO aqueous dispersion was sonicated at 25 ºC for 1 h. The dispersion was then stirred for 2.5 h at 80 °C. Pre-treated GO dispersion was mixed with an appropriate amount of polymer nanoparticles dispersion (latex) for 2 h at room temperature. After that, the reducing agent AsA was added to the mixture and stirred for 0.5 h. Subsequently, the samples obtained were placed in the oven at different temperatures

overnight. The formed hydrogels monoliths were purified by the dialysis process, which was followed by measuring water conductivity. Finally, the wet monoliths were dried by freeze-drying for three days. In Figure 2.3 in Chapter 2, the straightforward experimental procedure of the 3D composites is schematically described.

Furthermore, to study the influence of different parameters and to optimize the synthesis, the reaction conditions were varied. Two different polymerization techniques were used, emulsion polymerization to obtain dispersed polymer particles and solution polymerization (water as solvent was used) to produce soluble polymer chains. The amount of polymer used is described as 10 wt% and 40 wt% based on the initial amount GO. The AsA to GO mass ratio was also varied based on the weight of GO, to be 1:1 or 1:0.5 (GO:AsA). Two reduction temperatures (45 °C and 90 °C) were used.

3.2.4. Characterization

In terms of polymer characterization, conversion of the MMA monomer and solids content were calculated gravimetrically. The z-average particle size (dz) of the polymer particles were measured by dynamic light scattering (DLS). The molar masses and distributions of the polymer particles were measured by THF-based size exclusion chromatography (SEC), and the molar masses of the solution polymers were measured via aqueous SEC. The conversions of NaSS and AMPS functional monomers in both emulsion polymerization and solution polymerization techniques were characterized by ^{1}H-Nuclear Magnetic Resonance (NMR). ^{1}H-NMR spectras were recorded in a Bruker AVANCE 400 MHz instrument. The conversion was determined on the evolution of the peaks corresponding to the vinyl protons of NaSS (δ, 6.2, 5.9 ppm) and AMPS (δ, 6.1, 5.6 ppm). The peak corresponding to deuterated dimethyl sulfoxide (DMSO, δ,

3.3 ppm) was used as internal reference. The detailed description of the latex characterization methods is given in Section I.1 of Appendix I.

On the other hand, regarding the characterization of the 3D structures, thermogravimetric analyses (TGA) were performed to estimate the amount of residual oxygen-containing functional groups within the monolithic structures and to study the thermal stability. The surface morphology of the structures was examined using a scanning electron microscopy (SEM) and transmission electron microscopy (TEM). The pressure drop of the 3D monolith was measured by Digitron 2080 (Sifam Instrument Limited). The porous texture of the monoliths was characterized by means of N_2 adsorption–desorption at –196 °C in a Micromeritics ASAP2020 apparatus. Detailed information of these characterization techniques is given in Section I.2 of Appendix I.

Finally, in terms of gas adsorption measurements, the materials´ CO_2 and N_2 gas adsorption capacities were measured from their isotherms, measured using a Micromeritics ASAP 20220 Analyzer. The selectivity of CO_2 over N_2 was calculated by the ideal adsorbed solution theory (IAST) using only data for the pure-component adsorption equilibria at the same temperature (25 °C) and on the same adsorbent. Detailed information of these gas adsorption measurements is given in Section I.3 of Appendix I.

3.3. Results and discussion

3.3.1. Characterization of the polymers

Using two functional monomers, NaSS and AMPS, four different polymer types were synthesized at high monomers' conversion. The characteristics of polymers are presented in Table 3.2. Two of them are nanoparticle dispersions, prepared by seeded semibatch emulsion

polymerization of MMA (99 wt%) and functional monomer (1 wt%). In both cases when either NaSS or AMPS functional monomers were employed, colloidally stable aqueous polymer dispersions of approximately 30 wt% solids content were obtained. In case of NaSS, the MMA particles were functionalized with sulfonate functional groups on the surface. Surprisingly, only 37 % of the NaSS was converted, which might be because of high water solubility of this functional monomer, while the polymerization proceed mainly within the hydrophobic polymer particles.[12] Linear polymer chains with average molar mass of 510.000 g/mol and high polydispersity (rather wide molar mass distribution) were produced. In case of AMPS, the particles were functionalized with both sulfonic acid and amide moieties, with average size slightly higher (255 nm) than NaSS particles, causing much lower average molar mass of the polymer chains. Taking into consideration that both reactions were performed at the same solids content and that the polymer particles are the main polymerization loci, there was fewer number of particles in the AMPS reaction, resulting in higher radical concentration per particle and lower molar masses polymer chains.

By aqueous solution polymerizations of both functional monomers, their homopolymers' aqueous solutions were produced at 20 % solid content. Much lower molar mass polymer chains in narrow distribution were produced. In this way, polymer chains rich in either sulfonate or combination of acrylamide and sulfonic acid groups were produced.

Table 3.2. Overall conversion, particle size and molecular weight distributions of the polymers.

Polymerization process	Monomers	MMA conversion (%)	FM conversion (%)	z-ave (nm)	Mw (g/mol)	PDI
Emulsion copolymerization	**NaSS/MMA**	98	37	221	510000	7.1
	AMPS/MMA	97	100	255	170000	6
Solution polymerization	**NaSS**	-	100	-	153300	2.0
	AMPS	-	95	-	103500	1.4

3.3.2. Morphology and textural characterization of 3D composites at different reduction conditions

The complex self-assembly hierarchical process of GO platelets occurred during their reduction to rGO, giving rise to three-dimensional graphene-based polymer monoliths. The mechanism of the process, previously detailed in Chapter 2, encompasses mixing of GO platelets and polymer particles aqueous dispersions resulting in formation of composite platelets by physico/chemical interactions between both types of materials, as it is shown in Figure 2.3 in Chapter 2. By the subsequent reduction of GO by AsA at increased temperature (45-90 °C), elimination of oxygen-containing functional groups (epoxy, hydroxyl, carbonyl and carboxyl groups) from GO happen, producing much more hydrophobic rGO platelets. Due to the significant rise of the surface energy in the dispersion, the reduced composite platelets self-assembled giving rise to the 3D structures, characterized by improved consistency, high porosity and monolithic appearance.

It was already determined in the literature survey, Chapter 1, and in Chapter 2, that multiple reaction parameters affect the self-assembly process, and subsequently, the

morphology, textural characteristics, and the adsorption performance, such as reducing agent amount, reduction temperature, and amount and type of polymer (functionalization). Those parameters were also studied in this chapter, because completely different functionalization of the polymer particles might affect the self-assembly process and the characteristics of the composite monoliths. For that purpose, two reduction reaction temperatures (45 °C and 90 °C), two different reducing agent (AsA) concentrations (GO:AsA mass ratio 1:1 and GO:AsA 1:0.5) and two different polymer contents (10 % and 40 % with respect to GO mass) were studied. The reaction temperature and the amount of AsA affect the velocity of the reduction process and the residual oxygen functionalities, and hence, the self-assembly process and CO_2 uptake capacity. Table 3.3 presents all the 3D monolithic neat and composite materials, produced at two different temperatures (45 °C and 90 °C), constant AsA concentration (GO:AsA mass ratio 1:1), with both NaSS and AMPS functionalized polymer particles in two concentration (10 or 40 wt%). In the nomenclature of the materials, first number represents the reduction temperature, followed by the functional monomer used, and finished with the quantity of the polymer.

Table 3.3. Amount of residual oxygen functionalities and textural properties of different monoliths obtained at GO:AsA mass ratio 1:1.

Material	% O-functionality	S_{BET} (m^2/g)	V_{total} (cm^3/g)	V_{micro} (cm^3/g)	% Micropores	Reduction ratio GO/rGO
45_Blank	13.7	160	0.289	0.008	2.7	0.20
45_NaSS_10	12.8	185	0.184	0.035	18.8	0.21
45_NaSS_40	10.7	143	0.176	0.019	10.9	0.21
45_AMPS_10	12.9	170	0.170	0.032	19.1	0.21
45_AMPS_40	10.6	118	0.152	0.016	10.5	0.21
90_Blank	3.1	299	1.359	0.001<	0.1	0.04
90_NaSS_10	3.6	199	0.337	0.016	4.9	0.05
90_NaSS_40	3.2	177	0.313	0.011	3.6	0.05
90_AMPS_10	3.8	207	0.348	0.016	4.6	0.05
90_AMPS_40	3.1	117	0.206	0.001	0.6	0.06

A quantitative evaluation of the amount of oxygen groups present on the surface of the resulting monolith materials was obtained by TGA. Figure 3.2 shows the thermographs of all materials, including the thermal degradation curve of initial GO. The first observed weight drop until 100 °C is related to the humidity, the second weight drop within a range of 100-225 °C corresponds to the loss of the residual oxygen-containing functional groups from rGO platelets, and finally, in the third region, between 300 °C and 400 °C, the weight drop was assigned to the polymer degradation. The amount of residual oxygen functional groups calculated from the respective thermographs, as well as, the reduction ratios of GO to rGO are presented in Table 3.3. The reduction temperature affected importantly the reduction ratio, which drop from 0.2 at 45 ºC to 0.04 at 90 ºC. Nevertheless, the reduction ratios demonstrate that the presence of polymer and its quantity did not have any effect on the reduction process. It is worth mentioning

that the reduction ratio of initial GO was 0.8, which means that the reduction was significant at all conditions studied.

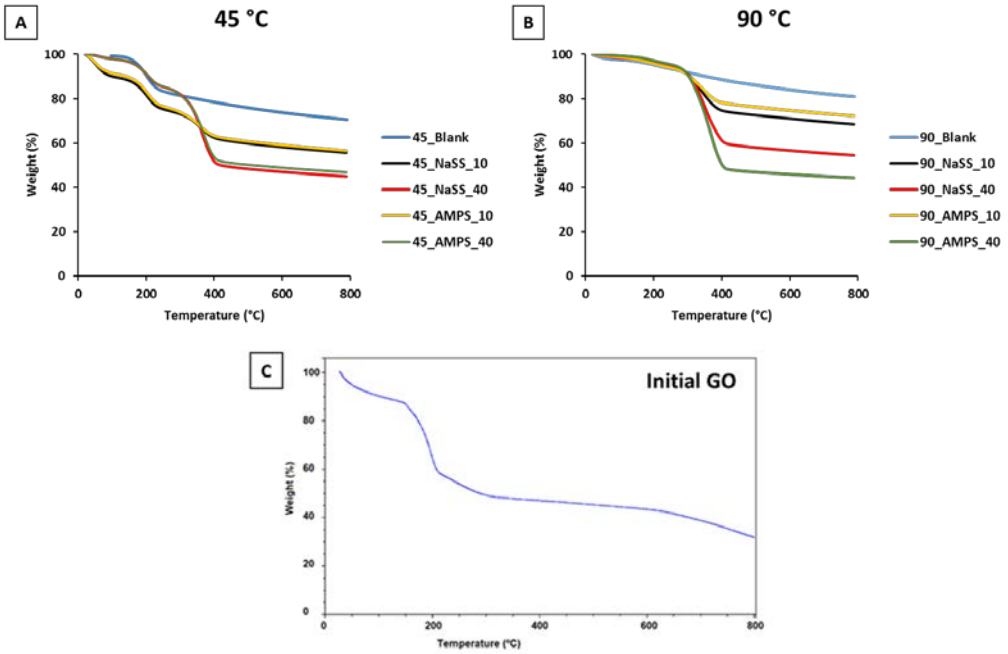

Figure 3.2. TGA thermographs for monoliths synthesized at 45 °C (A) and 90 °C (B); and initial GO (C).

When the reduction was performed at higher temperatures, a significant decay in the functionalization of the rGO within the 3D structures was obtained. The monoliths prepared under milder conditions (45 °C) were highly functionalized containing oxygen functional groups quantity between 10 and 13 wt% of the total amount of the material, whereas these prepared at 90 °C contain around 3 wt%. Added polymer quantity affected the thermal stability, whereas the polymer type did not have any effect on the composite thermal stability, which is not surprising having in mind that 99 % of the polymer added in both type of materials was 99 % MMA.

To obtain details on the porous structure of the monoliths, textural characterization was performed by determining the N_2 adsorption-desorption isotherms. The adsorption-desorption isotherms are presented in Figure 3.3, and the data acquired for each of the monoliths are presented in Table 3.3. The % of micropores, in Table 3.3, corresponds to V_{micro}/V_{total}.

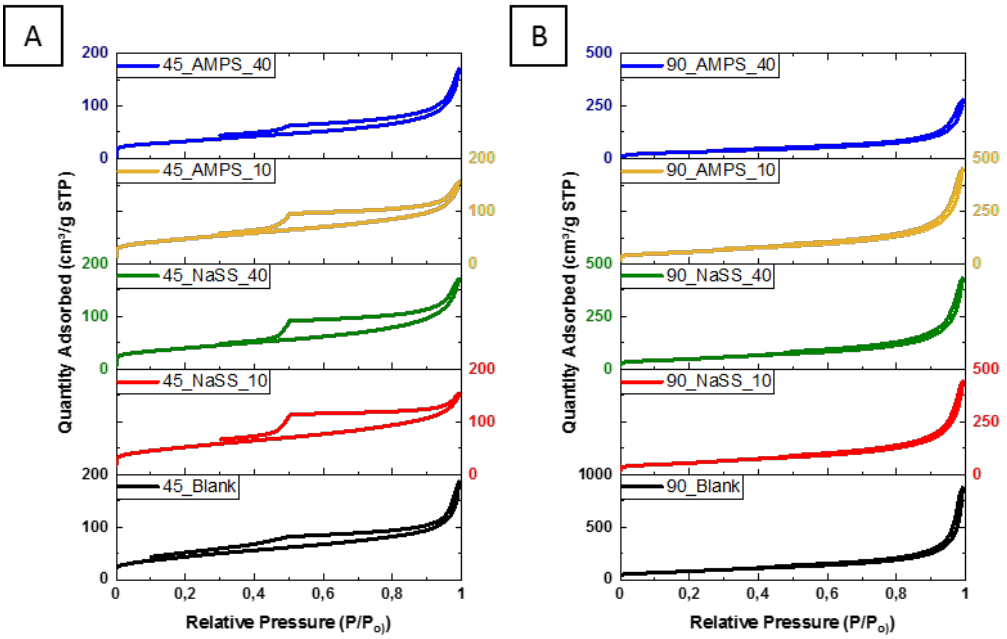

Figure 3.3. N_2 adsorption-desorption isotherms for monoliths synthesized at 45 °C (A) and 90 °C (B).

The specific BET surface area was found to be in a range of 120–300 m^2/g and was influenced significantly by the reduction temperature, i.e., for higher reduction temperatures, the same material type has a higher BET surface area. For example, for the blank monoliths, the BET surface area increased from 160 m^2/g when produced at 45 °C to 299 m^2/g when produced at 90 °C. As we demonstrated previously, and observed in this part, too, the monolithic materials synthesized at 90 °C are considerably more densely packed. The higher reduction energy makes

faster the elimination of oxygen functional groups increasing the driving force for the creation of the monoliths, resulting in more compact structures. In fact, it can be observed in TGA thermographs shown in Figure 3.2, that materials synthesized at 90 °C needed more thermal energy to degrade, i.e. they present higher thermal stability, than the monoliths synthesized at 45 °C.

The volume of the micropores and their contribution to the overall porous structure (%) is larger for the monoliths synthesized under mild conditions, at 45 °C, nevertheless, the total volume of the pores decreases indicating less porous materials. This behaviour was also observed as general for composite monoliths, as it can be seen in Figure 3.4, where the pore size distribution curves of the monoliths are shown.

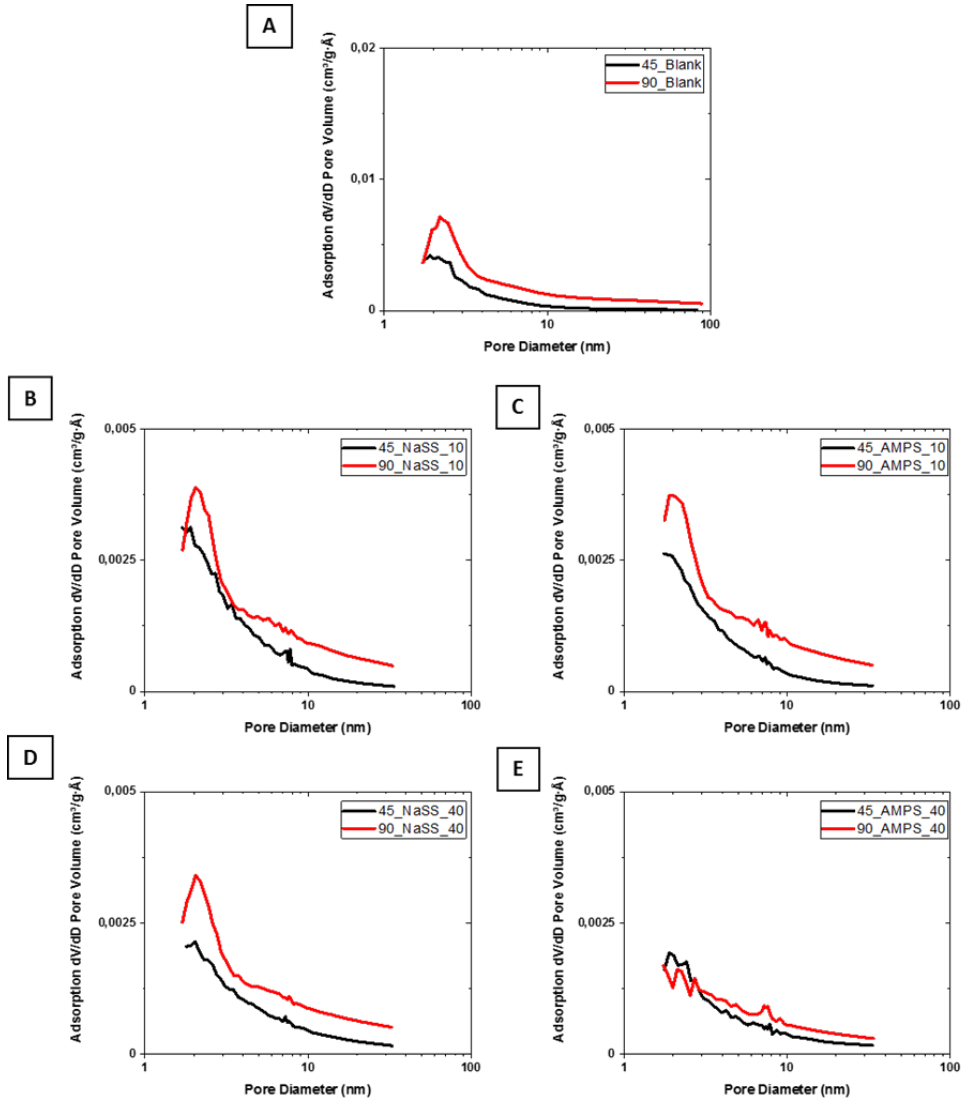

Figure 3.4. Pore size distributions from adsorption isotherms for blank and composites monoliths. 45_Blank and 90_Blank materials correspond to A graph. NaSS-based materials correspond to B and D graphs and AMPS-based materials to C and E graphs.

The faster elimination of oxygen groups at higher temperature results in higher free energy difference thus, the aggregation of the rGO layers occurs faster, giving rise to more compact platelets. As we consider that the micropores are formed at this instance, the materials produced at higher temperatures would have less micropore fraction, as we observed. Therefore, the total volume of micropores for 45_Blank is 0.008 cm^3/g, and in the case of 90_Blank is 0.001< cm^3/g (Table 3.3). This means that their contribution to the porous morphology is very low, thus, even increased, they did not affected importantly the overall porosity of the monoliths.

Furthermore, the addition of polymer particles plays an important role in the final porous morphology. The addition of polymer particles increased the contribution of micropores to the overall porous structure, independently on reduction temperature. It is thought that once the particles are attached to the surface of the GO platelets, their mobility and their hydrophilic character changed affecting the hierarchical self-assembly process, and hence, the resulting 3D morphology. Generally, porosity is decreased with the addition of polymer particles in higher amount (40 %). The polymer particles between the aggregated platelets actuated as spacers preventing their complete aggregation, therefore forming higher quantity of micropores than in a case of the blanks. Similar behaviours have been reported previously, where the addition of different polymers to the 3D graphene aerogels also decreases the BET surface area due to the formation of different micro morphologies.[13,14] However, when a higher amount of polymer particles is added, the volume of the spacers between the platelets increases, decreasing the micropores' volume. Besides, at 40 % polymer particles, the resulting rGO layers are heavier and more hydrophilic, so the driving force is reduced and the self-assembly process changes with respect to the blank materials.

The structure and morphology of the monoliths was observed by SEM and TEM techniques. The SEM images of 45_Blank and 90_Blank are presented in Figure 3.5.

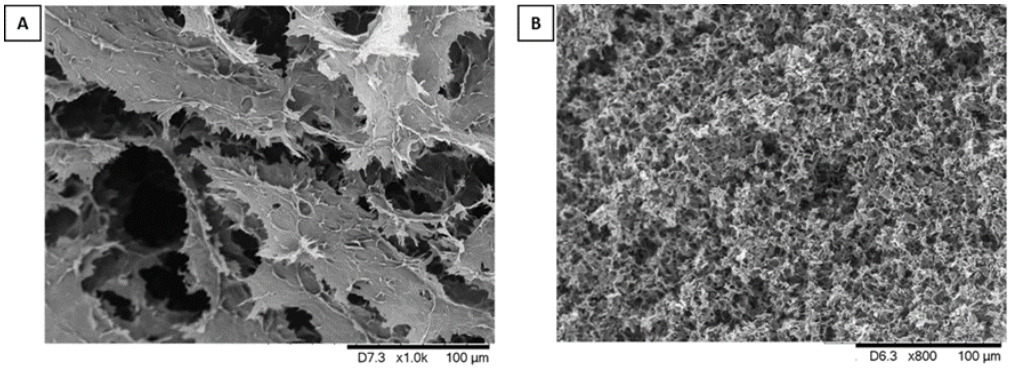

Figure 3.5. SEM images of 45_Blank (A) and 90_Blank (B) at 100 µm scale bar.

In Figure 3.5, it can be seen that both 3D structures present a porous morphology. The 90_Blank has a higher porosity made of a multiple small pores, and higher compactness compared to 45_Blank, in concordance with the textural properties. In Figure 3.6, SEM images at different magnifications for 45_AMPS_40 and 90_AMPS_40 composites are presented.

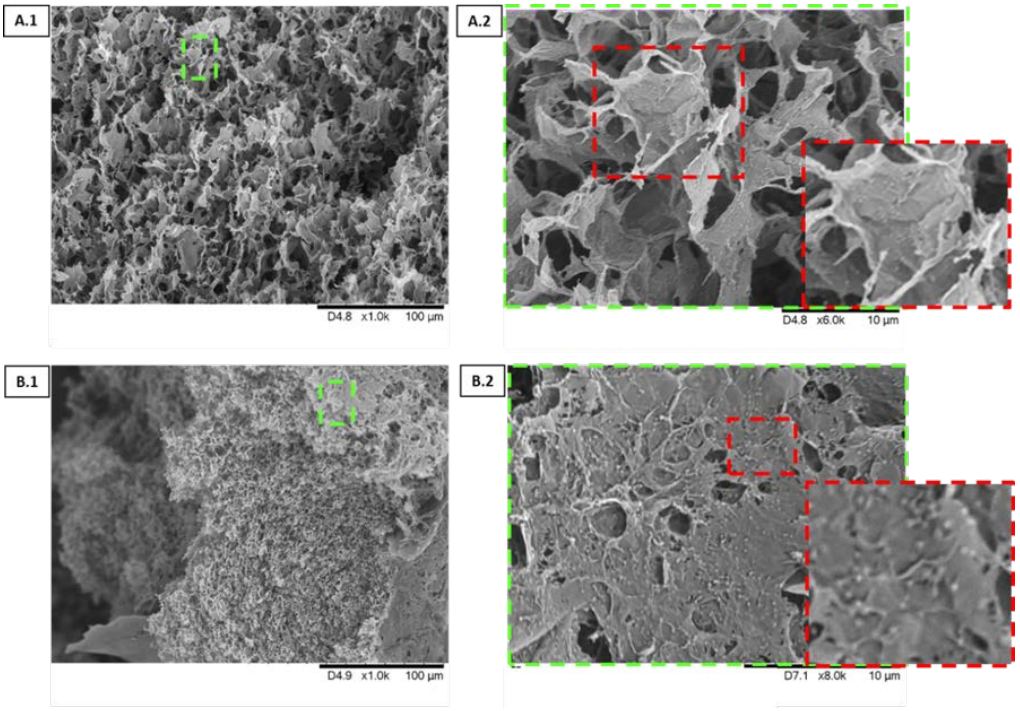

Figure 3.6. SEM images of 45_AMPS_40 (A.1 and A.2) and 90_AMPS_40 (B.1 and B.2) at 100 and 10 µm scale bars. In the insets of (A.2 and B.2), enlarged view of one segment decorated with polymer particles is shown.

In Figure 3.6, it can be observed that after the addition of polymer particles at micrometre level increased number of smaller size pores are formed than in the blanks, more pronounced at increased temperature. In both A.2 and B.2 enlarged SEM images, the well-distributed polymer particles in rGO platelets are perceived. Figure 3.7 shows the SEM images for the remaining composites, presenting similar morphologies as observed in Figure 3.6.

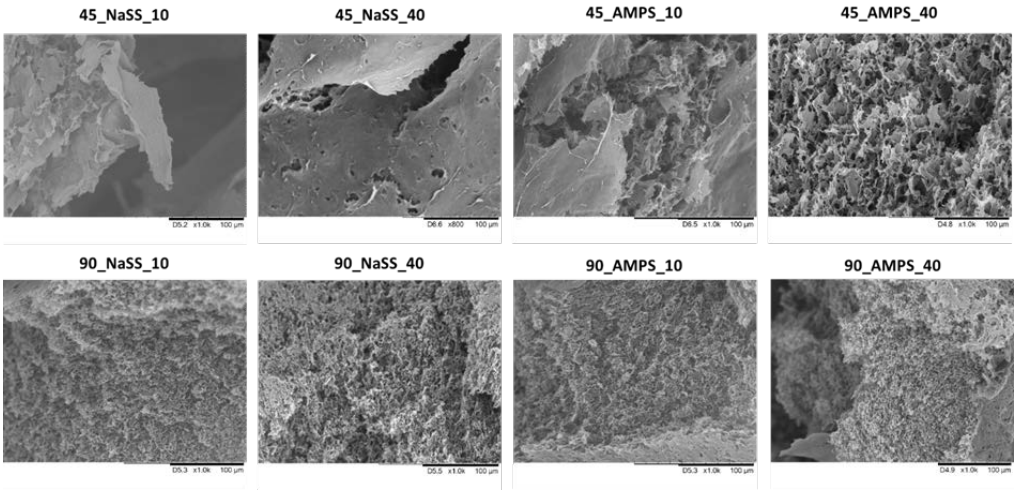

Figure 3.7. SEM images of different composites synthesized by the addition of functionalized polymer particles. The scale bar in each image is 100 µm.

In Figure 3.8, TEM images of 90_Blank, 90_NaSS_40, and 90_AMPS_40 are shown, obtained by embedding the monolith within epoxy resin. The thin graphene based walls forming the porous structures can be observed in all monoliths, whereas white polymeric particles anchored onto graphene walls can be seen only in the composite structures (Figure 3.8, B and C). There is no any relevant difference observed between NaSS-MMA and AMPS-MMA polymer particles.

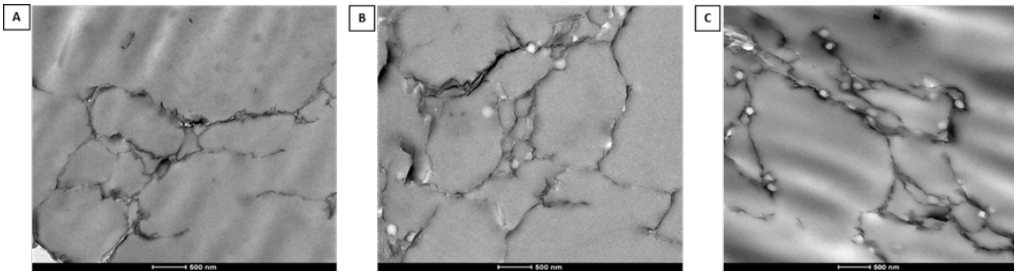

Figure 3.8. TEM images of 90_Blank (A), 90_NaSS_40 (B), and 90_AMPS_40 (C) at 500 nm scale bar.

One of the advantage of monolithic materials with respect to their powder form counterparts is that they induce much lower pressure drop in continuous operation. This was checked on an example of two selected monoliths (45_Blank and 90_Blank), and the results are placed in Figure 3.9. As the monoliths cannot be easily convert into powder, due to incredible strength of the graphene structure, we compared the pressure drop of the monoliths with that of standard powder materials made of SiC in three different particle sizes.

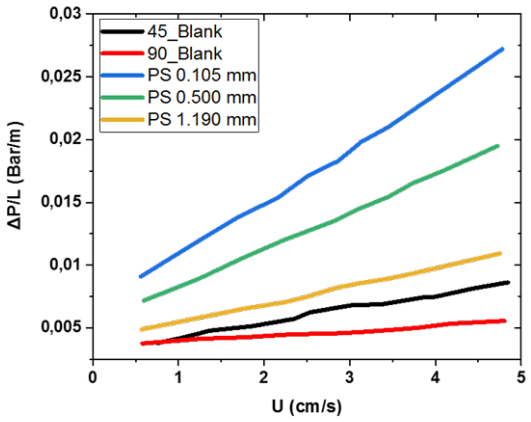

Figure 3.9. Pressure drop of 45_Blank and 90_Blank monoliths compared with SiC powder materials with 0.105, 0.500, and 1.190 mm particle sizes.

From Figure 3.9, it can be observed that both 45_Blank and 90_Blank monoliths present lower pressure drop even from the SiC powder with the highest particle size. The pressure drop is lower at different linear velocities compared to a powder material with different particle sizes. On the other hand, 90_Blank induced lower pressure drop, which was not significantly affected by the increase of a linear air velocity.

The next series of monoliths was synthesized under the same conditions as the previous one, except the amount of AsA reducing agent, which was lowered to a half (GO:AsA mass ratio 1:0.5). The same polymer types were used (NaSS-MMA and AMPS-MMA), added in 10 wt% amount based on GO. This polymer amount was chosen for further investigations, as it provided the most promising result in terms of amount of oxygen functionalities, textural properties such as total volume of the pores and the volume of the micropores. Consistently, a term "1/2" was added in the samples nomenclature, referring to a quantity of AsA with a respect to the previous series of monoliths. Figure 3.10 shows the TGA thermographs for each monolith, presenting similar degradation behaviour as the monoliths obtained at higher AsA concentration.

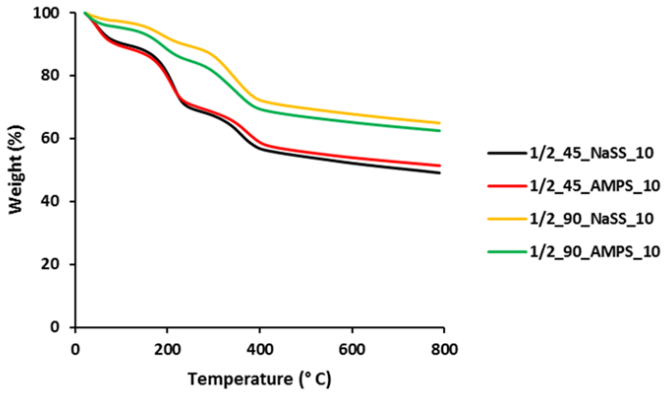

Figure 3.10. TGA thermographs for 1/2_45_NaSS_10, 1/2_45_AMPS_10, 1/2_90_NaSS_10, and 1/2_90_AMPS_10 composites.

In Table 3.4, the amount of residual oxygen groups and the textural properties of the four monoliths produced in this case are shown (1/2_45_NaSS_10, 1/2_45_AMPS_10, 1/2_90_NaSS_10, and 1/2_90_AMPS_10). The N_2 adsorption-desorption isotherms are presented in Figure 3.11.

Table 3.4. Amount of residual oxygen functionalities and textural properties of monoliths obtained with lower AsA amount (GO:AsA 1:0.5).

Material	% O-functionality	S_{BET} (m^2/g)	V_{total} (cm^3/g)	V_{micro} (cm^3/g)	% Micro.
1/2_45_NaSS_10	17.2	60	0.13	0.005	3.8
1/2_45_AMPS_10	16.1	72	0.074	0.012	16.3
1/2_90_NaSS_10	6.8	288	0.435	0.028	6.4
1/2_90_AMPS_10	9.2	215	0.297	0.027	9.1

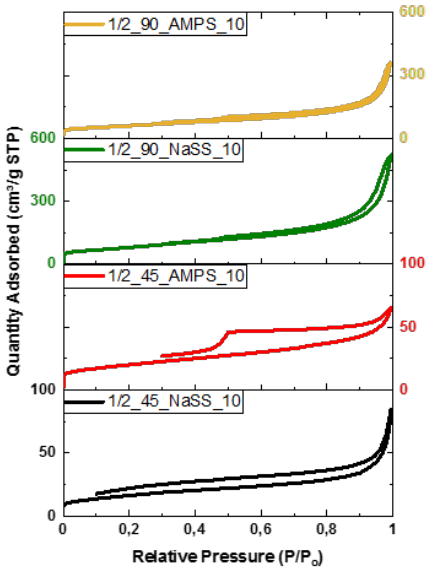

Figure 3.11. N_2 adsorption-desorption isotherms for 1/2_45_NaSS_10, 1/2_45_AMPS_10, 1/2_90_NaSS_10, and 1/2_90_AMPS_10 composites.

Table 3.4 shows that by decreasing the AsA concentration, there is an increase in the residual amount of oxygen-containing functional groups than in case of monoliths obtained with

higher AsA amount (Table 3.3). For example, 45_NaSS_10 (Table 3.3) and 1/2_45_NaSS_10 (Table 3.4) have 12.8 and 17.2, % O-functionality, respectively, likely due to slower reduction process. Even though the same general tendency is observed, here the textural properties are affected more importantly by the reduction temperature than in case of higher AsA quantity. Consequently, a fourfold increased BET area was achieved when the temperature was increased from 45 °C to 90 °C for both polymer types, without significant effect on the other textural properties. The reduction process is simultaneously determined by both parameters temperature and reducing agent quantity, and in conditions of low temperature and low AsA quantity, the driving force for monolith formation is very weak, which is the case of 1/2 AsA and 45 °C. Therefore, the temperature increase to 90 °C induced much stronger effect. Nevertheless, oppositely than previously observed in Chapter 2, here the amount of micropores increased at higher reduction temperatures, which is likely result on this interplay between both parameters temperature and quantity of AsA.

Figure 3.12 shows the SEM images for the composite monoliths synthesized with lower AsA amount, presenting the same observation already discussed. The monoliths obtained with lower AsA amount contain increased quantity of smaller pores than the monoliths produced at higher AsA concentration, effect that is more pronounced at increased temperature.

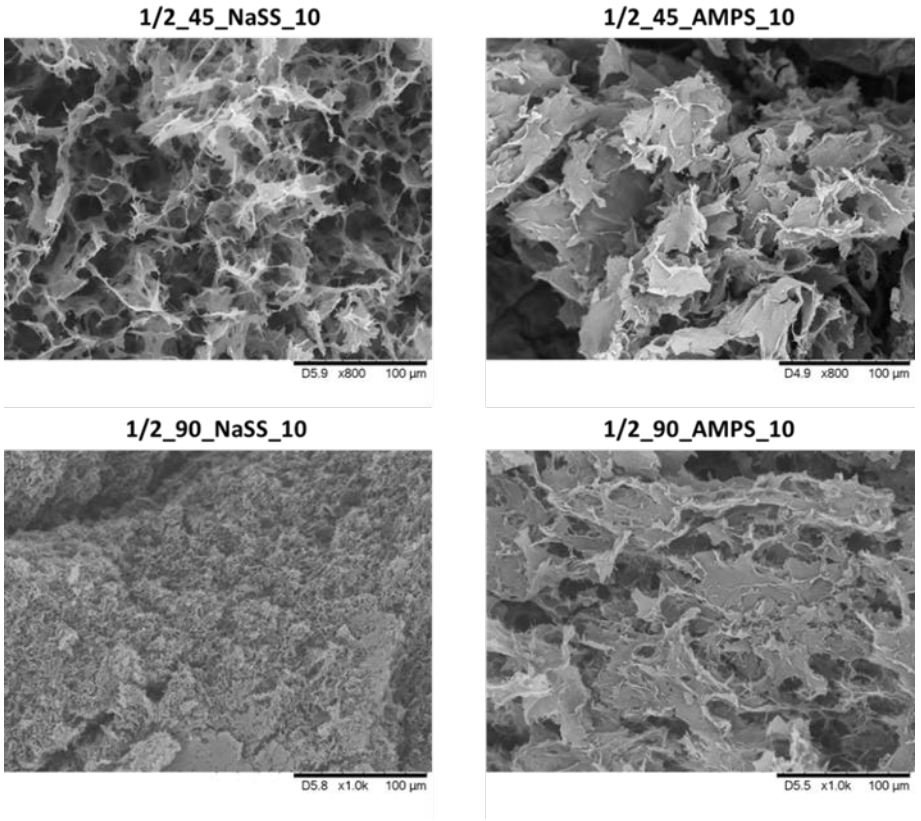

Figure 3.12. SEM images for 1/2_45_NaSS_10, 1/2_45_AMPS_10, 1/2_90_NaSS_10, and 1/2_90_AMPS_10 composites. The scale bar in each image is 100 µm.

The final series of monoliths were prepared using fundamentally different approach than previously. Namely, instead of hard polymer particles dispersion, herein the polymer chains aqueous solution was combined with GO dispersion prior to monolith synthesis. The polymer solutions were prepared by polymerizing exclusively the functional monomers NaSS and AMPS, giving rise to polymer chains rich in functional groups containing S and N atoms, to study their effect on the CO_2 adsorption performance. In the monolith nomenclature a "*S*" is added, referring to solution polymer. Reduction conditions of 90 °C, GO:AsA 1:0.5, and polymer amount (10 wt%)

were selected, as these conditions provided the most promising results, by means of oxygen functionalities, BET surface areas, total volume of pores, and total volume of micropores of the resulting monoliths. In Table 3.5, the textural properties obtained for S_90_NaSS_10 and S_90_AMPS_10 are shown. The N_2 adsorption-desorption isotherms are presented in Figure 3.13.

Table 3.5. Amount of residual oxygen functionalities and textural properties of different composites obtained by addition of solution polymers.

Material	% O-functionality	S_{BET} (m^2/g)	V_{total} (cm^3/g)	V_{micro} (cm^3/g)	% Micro.
S_90_NaSS_10	13.4	183	0.292	0.014	4.8
S_90_AMPS_10	8.5	207	0.296	0.02	6.6

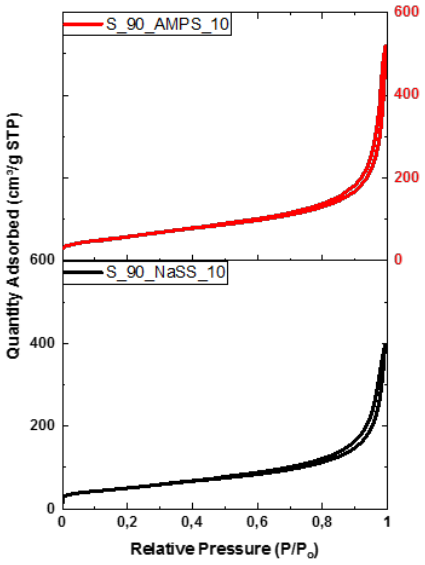

Figure 3.13. N_2 adsorption-desorption isotherms for S_90_NaSS_10 and S_90_AMPS_10 composites.

Even though the synthesis procedure was fundamentally different, compared with Table 3.4, there is no significant effect on remaining oxygen functionality content, BET area and porosity of the monoliths. This is likely because the monoliths are actually build of rGO platelets and polymer is only a surface modifier. Nevertheless, the microporosity was affected, as addition of the solution polymers resulted in drop of the microporosity. This fact actually demonstrates our hypothesis that the polymer particles actuated as spacers and contributed towards development of more micropores, because the drop in microporosity here is likely effect of lack of these spacers. Namely, polymer chains were directly distributed over rGO platelets and such composite sheets could be easily stacked more tightly.

Figure 3.14 shows the thermographs for both samples, in which it can be observed that the decomposition process is different from that of the monoliths synthesized with polymer particles. These rGO monoliths, covered with either polyNaSS or polyAMPS, degraded gradually with increasing temperatures, indicating more homogeneous composition, where the monolith containing polyNaSS was more thermally stable.

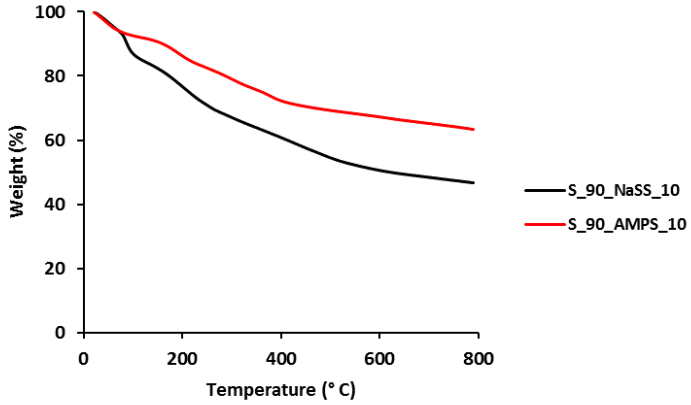

Figure 3.14. TGA thermographs for S_90_NaSS_10 and S_90_AMPS_10 composites.

Figure 3.15.A and B, show the SEM images of S_90_NaSS_10 and S_90_AMPS_10, respectively. Although decomposition of materials was different in comparison to polymer particles containing monoliths, they presented similar porous structures when compared with the analogous monoliths obtained with polymer particles at 90 °C and 10 wt% polymer quantity (Figure 3.12). TEM images presented in Figure 3.15.C and D, on the other hand, present clear lack of polymer particles and the polymer presence is not so obvious. It rather appears as white small structures covering the grey rGO platelets.

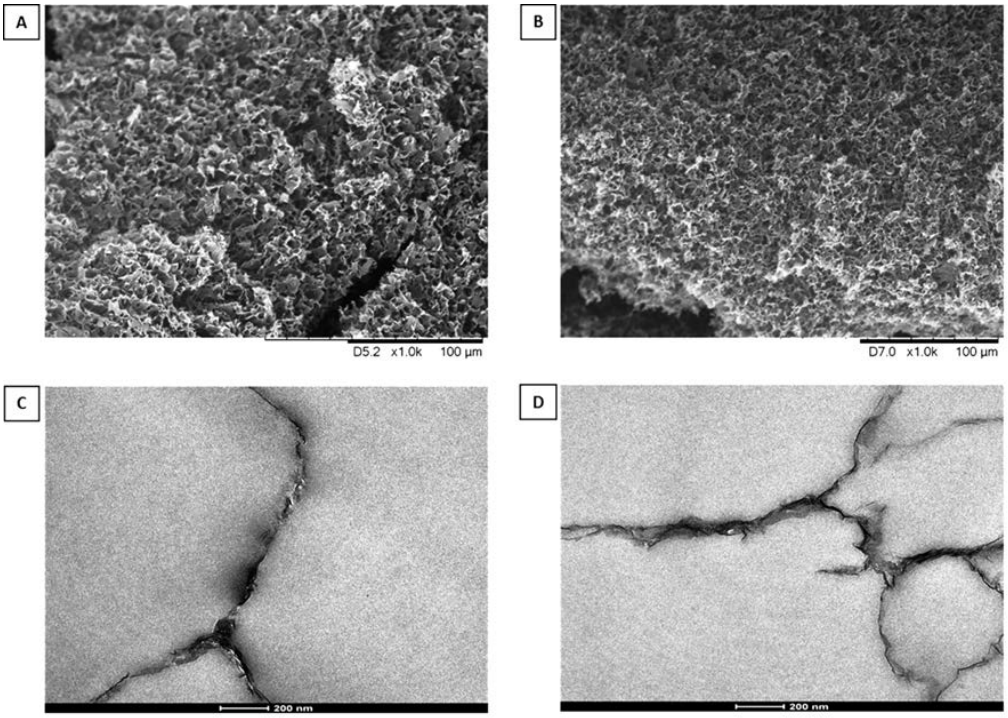

Figure 3.15. SEM and TEM images of both S_90_NaSS_10 (A and C) and S_90_AMPS_10 (B and D) composites synthesized. The scale bar is 100 µm and 200 nm for SEM and TEM, respectively.

3.3.3. Adsorption performance of 3D composites

3.3.3.1. CO_2 capture

The CO_2 adsorption performance of graphene-based polymer porous monolithic materials was studied at 25 °C and 1 atm. For that, CO_2 adsorption-desorption isotherms were measured at 25 °C for each sample discussed above, and all the isotherms are presented in Figure 3.16-3.19.

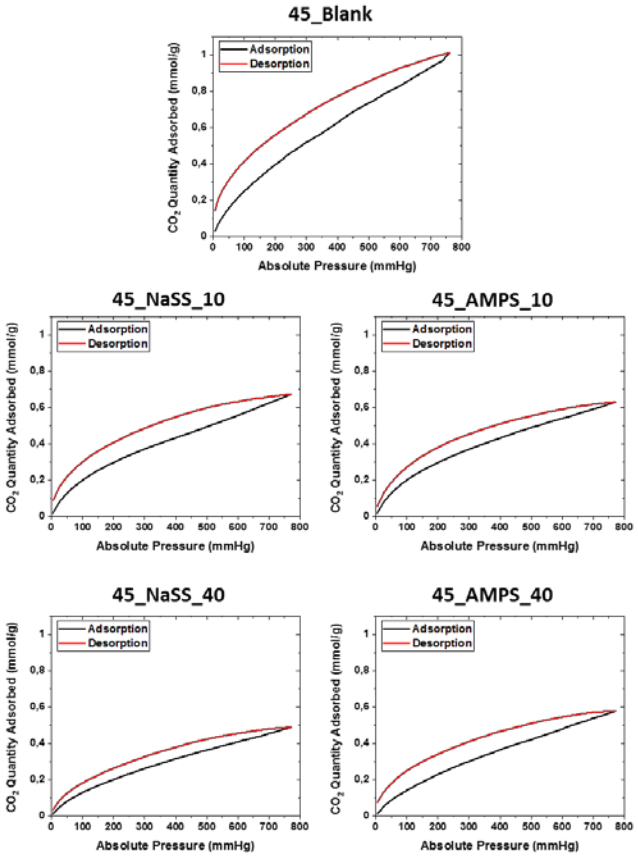

Figure 3.16. CO_2 adsorption-desorption isotherms for monoliths synthesized at 45 °C and GO:AsA mass ratio 1:1 using polymer particles.

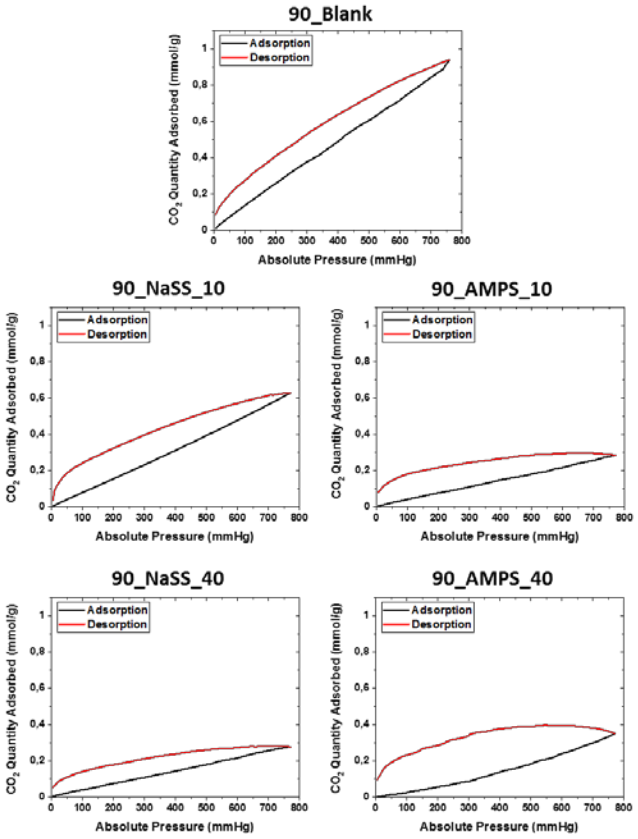

Figure 3.17. CO_2 adsorption-desorption isotherms for monoliths synthesized at 90 °C and GO:AsA mass ratio 1:1 using polymer particles.

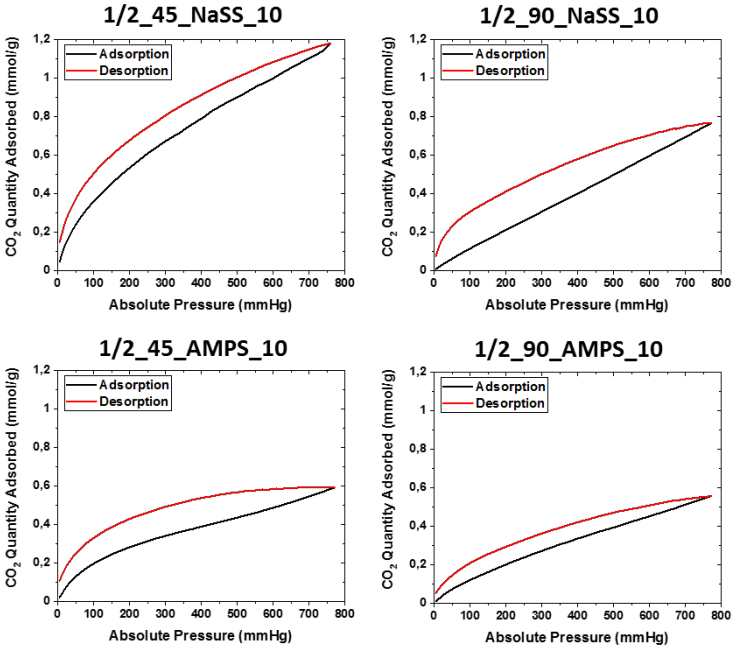

Figure 3.18. CO_2 adsorption-desorption isotherms for monoliths synthesized at 45 °C and 90 °C and GO:AsA mass ratio 1:0.5 using polymer particles.

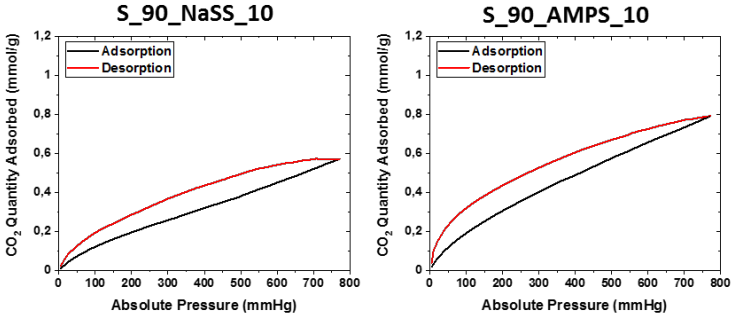

Figure 3.19. CO_2 adsorption-desorption isotherms for monoliths synthesized at 90 °C and GO:AsA mass ratio 1:0.5 using solution polymers.

In the first set of monoliths, the effect of the reaction temperature (45 °C and 90 °C), type of polymer (NaSS-MMA and AMPS-MMA), and amount of polymer (10 and 40 wt% based on GO) affected the morphological and textural properties, especially at high polymer content, and hence, high impact on CO_2 capture is expected. The quantity of AsA was kept constant for all the cases (GO:AsA mass ratio 1:1). In Table 3.6, the CO_2 adsorption capacities obtained at 25 °C and 1 atm are presented, followed by a graph in which BET areas and CO_2 adsorption are plotted (Figure 3.20).

Table 3.6. CO_2 adsorption capacities of different monoliths.

Material	CO_2 adsorption (mmol/g)
45_Blank	1.01
45_NaSS_10	0.67
45_NaSS_40	0.49
45_AMPS_10	0.63
45_AMPS_40	0.58
90_Blank	0.94
90_NaSS_10	0.63
90_NaSS_40	0.28
90_AMPS_10	0.28
90_AMPS_40	0.35

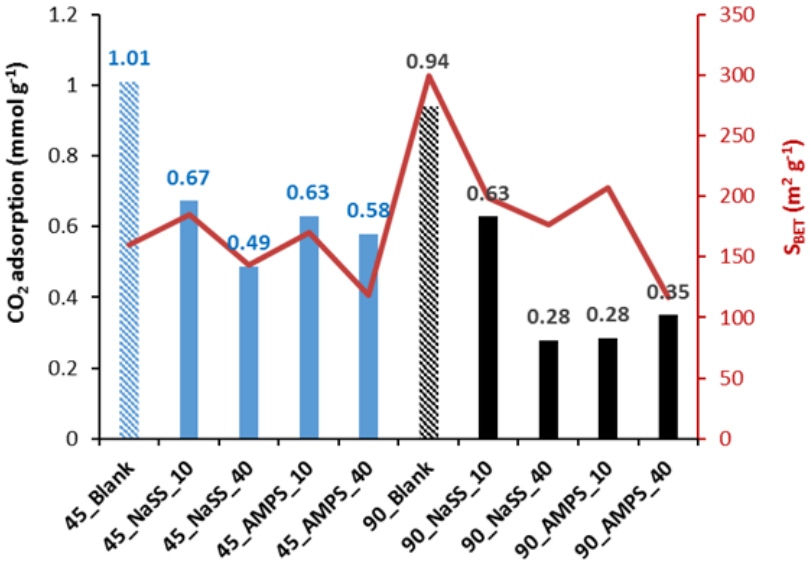

Figure 3.20. CO_2 adsorption capacities and specific surface areas (S_{BET}) for the composite monoliths synthesized with constant AsA concentration (GO:ASA mass ratio 1:1). Blue and black bars correspond to CO_2 adsorption capacities of materials synthesized at 45 °C and 90 °C, respectively.

The comparison of CO_2 adsorption of the blank materials shows that, although 90_Blank has almost a twice value in BET area than 45_Blank (Table 3.3), they adsorb similarly, 0.94 mmol/g and 1.01 mmol/g, respectively. These results indicate that the CO_2 gas at 25 °C and 1 atm did not cover the total available surface area in accordance to the claim that the surface area is essentially prevailing factor at high pressures.[15] Other studies reported that even though the materials have higher BET surface areas, they present lower CO_2 adsorption capacitates, because other factors such as oxygen groups and pore size also play important roles.[16] 45_Blank has higher fraction of residual oxygen groups and of micropores (Table 3.3), hence, it seems that these characteristics have a predominant effect over the CO_2 adsorption than the high BET area of 90_Blank at low pressures.

In general terms, higher adsorption capacities are achieved when 3D materials are synthesized at 45 °C. Based on the data obtained in Table 3.3, these materials present lower BET surface area, nevertheless, they have higher amount of oxygen functionalities and higher amount of micropores per unit area. In all the composite monoliths, synthesized either at 45 °C or at 90 °C, the addition of polymer particles to the 3D structures decreases the CO_2 adsorption capacity with respect to the corresponding blank material. This is surprising for composites with 10 wt% polymer particles, for which even though the BET area decreased, there is an increase in both residual functionalities and micropores fractions. Few factors can contribute to this behaviour: (i) addition of less adsorptive material to a high adsorptive one (the neat polymers NaSS-MMA and AMPS-MMA polymers adsorbed only 0.17 and 0.16 mmol/g, respectively); (ii) possible interactions between polymer-rGO through H-bonding, which makes not available the oxygen groups for interactions with CO_2; and (iii) the changes in textural properties.

In composites with 40 wt% polymer particles, all important parameters dropped by the polymer addition, including oxygen functionalities, BET area, total volume of the pores, and micropores fraction, which may be additional reason for lower adsorption capacity. Interestingly, in the composites synthesized at 45 °C, there is a concordance in the trends of the BET area and CO_2 adsorption (Figure 3.20), as well as in the amount of the oxygen functionalities (Table 3.3). CO_2 adsorption was enhanced for materials with higher BET area and higher relative fraction of residual oxygen groups. Nevertheless, according to Figure 3.20, the trends of BET area and CO_2 adsorption variations are different for the materials synthesized at 90 °C.

On the other hand, in NaSS-MMA systems higher adsorption capacities are achieved compare to AMPS-MMA system when 10 wt% of polymer particles are added independently on reduction temperature. Although in both cases 1 wt% of functional monomer was used, in case

of NaSS, only the 37 % was converted. Taking into consideration the textural properties and the oxygen groups fraction shown in Table 3.3, which very similar for all the composite monoliths with 10 % polymer produced at the same temperature, the observed adsorption increase in this case is caused by the NaSS functionalities, which a part of sulfonate contains aromatic ring able to establish π-π interactions with CO_2. When 40 wt% of polymer particles are added, the CO_2 adsorption dropped even further with respect to both neat rGO and 10 % composite monoliths, probably due to the lower BET area and lower relative fraction of oxygen functionalities.

When the AsA quantity was decreased (GO:AsA mass ratio 1:0.5), the composite monoliths in general presented higher quantity of oxygen functionalities and higher BET area and micropore fraction (Table 3.4), providing expectation for improved capacity of CO_2 adsorption. In Table 3.7, the CO_2 adsorption capacities obtained at 25 °C and 1 atm are presented.

Table 3.7. CO_2 adsorption capacities of different samples with lower AsA amount.

Material	CO_2 adsorption (mmol/g)
1/2_45_NaSS_10	1.18
1/2_45_AMPS_10	0.59
1/2_90_NaSS_10	0.76
1/2_90_AMPS_10	0.55

Certainly, the decrease in the reducing agent quantity provided to the materials better characteristics for the CO_2 capture, as it was enhanced for almost all the materials (except 1/2_45_AMPS_10). Similarly, a higher CO_2 adsorption was achieved for materials synthesized at 45 °C. Actually, at present conditions, and in case of NaSS functionalization, the adsorption

capacity was improved for first time behind that of the blank materials, in case of 1/2_45_NaSS_10. This material as shown in Table 3.4, has worst textural properties than all other materials, including low BET area (60 m^2/g) and only 3.8 % of microporosity, but it has the highest fraction of oxygen functionalities, which likely are distributed over much smaller BET area, creating densely functionalized surface, appropriate for CO_2 capture.

Taking into consideration that handling of the blank monoliths is difficult and that they presented instability in cycle operations with respect to composite monoliths (Chapter 2), this result is a step forward toward practical application.

Finally, the effect of the polymer microstructure by addition of soluble polymer chains to the composite monoliths on CO_2 adsorption capacity was studied. In Table 3.8, the CO_2 adsorption capacities obtained at 25 °C and 1 atm are presented for S_90_NaSS_10 and S_90_AMPS_10 monoliths.

Table 3.8. CO_2 adsorption capacities of S_90_NaSS_10 and S_90_AMPS_10 monoliths.

Material	CO_2 adsorption (mmol/g)
S_90_NaSS_10	0.57
S_90_AMPS_10	0.79

In Table 3.8, it can be seen that the CO_2 adsorption was in similar range as for other composite materials, even though the much denser functionalization provided with the polyNaSS and polyAMPS was expected to enhance it. In the case of polyAMPS-based system, higher adsorption capacity was obtained than for polyNaSS, 0.79 and 0.57 mmol/g, respectively. This

is likely due to double functionalization introduced by AMPS, supported with slightly higher micropores fraction.

3.3.3.2. Selectivity

The selectivity toward CO_2 over N_2 plays an important role on the application perspective in post-combustion capturing technology. In fact, flue gas stream from power plants contains approximately 15 % CO_2 and 85 % N_2. Table 3.9 shows N_2 adsorption capacities at 25 °C and 1 atm for all the monoliths synthesized. In Table 3.10, the CO_2/N_2 selectivity is shown, calculated by IAST method, using the single-component adsorption isotherms of CO_2 and N_2 obtained at 25 °C, modelled by Freundlich isotherm. The fitting curves for CO_2 and N_2 and the parameters in the Freundlich isotherms are presented in Section II.2 of Appendix II.

Table 3.9. N_2 adsorption capacities at 25 °C and 1 atm for all the monoliths synthesized.

GO:AsA 1:1		**GO:AsA 1:0.5**		**GO:AsA 1:0.5 / Solution polymer**	
Material	N_2 adsorption (mmol/g)	Material	N_2 adsorption (mmol/g)	Material	N_2 adsorption (mmol/g)
45_Blank	0.064	**1/2_45_NaSS_10**	0.059	**S_90_NaSS_10**	0.060
45_NaSS_10	0.076	**1/2_45_AMPS_10**	0.067	**S_90_AMPS_10**	0.080
45_NaSS_40	0.056	**1/2_90_NaSS_10**	0.065		
45_AMPS_10	0.072	**1/2_90_AMPS_10**	0.058		
45_AMPS_40	0.064				
90_Blank	0.061				
90_NaSS_10	0.069				
90_NaSS_40	0.031				
90_AMPS_10	0.033				
90_AMPS_40	0.038				

Table 3.10. Selectivity values for all 3D monoliths.

GO:AsA 1:1		GO:AsA 1:0.5		GO:AsA 1:0.5 / Solution polymer	
Material	Selectivity	Material	Selectivity	Material	Selectivity
45_Blank	90	**1/2_45_NaSS_10**	93	**S_90_NaSS_10**	52
45_NaSS_10	51	**1/2_45_AMPS_10**	50	**S_90_AMPS_10**	57
45_NaSS_40	52	**1/2_90_NaSS_10**	66		
45_AMPS_10	53	**1/2_90_AMPS_10**	56		
45_AMPS_40	53				
90_Blank	86				
90_NaSS_10	49				
90_NaSS_40	48				
90_AMPS_10	45				
90_AMPS_40	44				

In Table 3.10, the selectivity values of the 3D monoliths vary from 41 to 93, depending on the characteristics of the monoliths obtained under different reaction conditions. All the monoliths present relatively high selectivity, which for carbon-based materials was explained to be a result of the quadrupole moment of CO_2. It allows clustering of CO_2 molecules, effect not present during N_2 adsorption.[11] The highest selectivity value of 93, was obtained for the material 1/2_45_NaSS_10, which also presented the highest CO_2 adsorption capacity of 1.18 mmol/g obtained in this work. Along with the excellent stability in cycle operation of these materials demonstrated in our previous chapter, and the possibility for temperature or pressure swing regeneration, without any doubt, this material present solid opportunity for practical application. In a relatively recent work, Ho et al.[17] established a direct relationship between the cost of CO_2 capture and the intrinsic adsorbent characteristics (selectivity and capture capacity) for a fuel gas with a composition CO_2/N_2 of 10/90. Evaluating the 1/2_45_NaSS_10 solid sorbent according to it, the projected costs would be of 35 USD per ton of CO_2, which in comparison to

the current commercial technology with roughly 58.30 USD per metric ton of CO_2,[18,19] presents suitability to replace costly liquid amine scrubbing or cryogenic distillation.

3.4. Conclusions

In this work, functionalized graphene-based porous 3D monolithic structures were developed and the properties were characterized and related to CO_2 adsorption performance. The monoliths were synthesized by self-assembly of rGO-polymer platelets. The rGO platelets were previously decorated by functionalized MMA polymer particles using functional monomers, NaSS to provide sulfonate functionality and AMPS to provide both sulfonic acid and amide functionalities. Moreover, aqueous solution homopolymers of NaSS and AMPS were synthesized too, and distributed over the rGO platelets, to check the effect of heavily functionalized polymer chains on the synthesis and performance of these materials. The reduction parameters, such as AsA reducing agent amount (GO:AsA mass ratio 1:1 and 1:0.5) and reduction temperature (45 °C and 90 °C) were varied and their influence on the materials characteristics was studied, as well as the type of functionalization, morphology, and amount of the polymers (10 % or 40 % with respect to GO).

The materials synthesized at higher temperature and AsA presented a lower fraction of residual oxygen groups onto rGO surface, higher BET area, higher total volume of the pores and lower amount of micropores. Addition of functionalized polymer particles enlarged the amount of micropores, because the particles acted as spacers between the rGO platelets, effect that was not observed when solution polymers were used. It was observed that sulfonate functionalities in NaSS are quite favourable for the CO_2 adsorption. An increase of the fraction of residual oxygen functionalities could be observed by decreasing the amount of AsA during the GO

reduction. Nevertheless, an augmentation of the BET area, total volume of pores and even the microporosity was noticed only for material produced at higher temperature (90 °C). Probably the combination of low temperature and low AsA concentration did not provide sufficient driving force for rGO self-assembly process, resulting in not well-developed textural characteristics of the monoliths.

By studying the performance of these monoliths for selective CO_2 capture, it was found that all the parameters studied affected it synergistically. An interplay between the fraction of residual oxygen-containing functional groups, textural properties and the type and amount of polymers onto the monolithic materials determine the selective CO_2 adsorption capacity over that of N_2. In most of the cases, lower adsorption capacities are obtained for composites than for blank materials due to the higher affinity of graphene than of polymers toward CO_2. This means, in case of similar fraction of functionalities between materials, the increasing BET area would mean that the density of the functional groups will be lower, so the CO_2 adsorption dropped. This happens when small quantity of polymer was added (10 %) with respect to the neat rGO. When higher quantity of polymer was added (40 %), BET area decreased but as well the fraction of functionalities with respect to these of neat rGO and 10 % composites, making the functionality density even lower, therefore the CO_2 adsorption decreased even further. However, the best performance by means of high capacity and selectivity was obtained for composite monolith prepared with lower amount of AsA at lower temperature (1/2_45_NaSS_10). CO_2 uptake of 1.18 mmol/g, and a selectivity over N_2 of 93 were attained, which was attributed to the dense functionalization.

Beside development of monolithic 3D materials with very good combination of CO_2 adsorption and selectivity over N_2, the high potential for practical application is based on the simplicity, low cost and energy consumption methodology for their synthesis. Additional value of

the present work is the facile, versatile and elegant way of graphene functionalization that does not required complex organic reaction, catalyst or solvent use, nor high temperatures.

3.5. References

(1) Nelson, M. R.; Borkman, R. F. Ab Initio Calculations on CO2 Binding to Carbonyl Groups. *J. Phys. Chem.* **1998**, *102*, 7860–7863.

(2) Saha, D.; Kienbaum, M. J. Role of Oxygen, Nitrogen and Sulfur Functionalities on the Surface of Nanoporous Carbons in CO2 Adsorption: A Critical Review. *Microporous Mesoporous Mater.* **2019**, *287* (May), 29–55.

(3) Christian Kemp, K.; Chandra, V.; Saleh, M.; Kim, K. S. Reversible CO2 Adsorption by an Activated Nitrogen Doped Graphene/Polyaniline Material. *Nanotechnology* **2013**, *24* (23).

(4) Liu, F. Q.; Wang, L. L.; Li, G. H.; Li, W.; Li, C. Q. Hierarchically Structured Graphene Coupled Microporous Organic Polymers for Superior CO2 Capture. *ACS Appl. Mater. Interfaces* **2017**, *9* (39), 33997–34004.

(5) Park, J.; Cho, S. Y.; Jung, M.; Lee, K.; Nah, Y. C.; Attia, N. F.; Oh, H. Efficient Synthetic Approach for Nanoporous Adsorbents Capable of Pre-and Post-Combustion CO2capture and Selective Gas Separation. *J. CO2 Util.* **2021**, *45* (November 2020), 101404.

(6) Ghosh, S.; Sevilla, M.; Fuertes, A. B.; Andreoli, E.; Ho, J.; Barron, A. R. Defining a Performance Map of Porous Carbon Sorbents for High-Pressure Carbon Dioxide Uptake and Carbon Dioxide-Methane Selectivity. *J. Mater. Chem. A* **2016**, *4* (38), 14739–14751.

(7) Kamran, U.; Park, S. J. Chemically Modified Carbonaceous Adsorbents for Enhanced CO2 Capture: A Review. *J. Clean. Prod.* **2021**, *290*, 125776.

(8) Sudeep, P. M.; Narayanan, T. N.; Ganesan, A.; Shaijumon, M. M.; Yang, H.; Ozden, S.; Patra, P. K.; Pasquali, M.; Vajtai, R.; Ganguli, S.; et al. Covalently Interconnected Three-Dimensional Graphene Oxide Solids. *ACS Nano* **2013**, *7* (8), 7034–7040.

(9) Hsan, N.; Dutta, P. K.; Kumar, S.; Bera, R.; Das, N. Chitosan Grafted Graphene Oxide Aerogel: Synthesis, Characterization and Carbon Dioxide Capture Study. *Int. J. Biol. Macromol.* **2019**, *125*, 300–306.

(10) Brandrup, J.; Immergnt, E. H. *Polymer Handbook*, 3rd ed.; Wiley: New York, 1989.

(11) Meconi, G. M.; Tomovska, R.; Zangi, R. Adsorption of CO 2 Gas on Graphene-Polymer Composites. *J. CO2 Util.* **2019**, *32* (March), 92–105.

(12) J.C. de la Cal, J.R. Leiza, J.M. Asua, A. Butte, G. Storti, M. M. Handbook of Polymer Reaction Engineering; Wiley-VCH, 2005; pp 249–322.

(13) Ji, C. C.; Xu, M. W.; Bao, S. J.; Cai, C. J.; Lu, Z. J.; Chai, H.; Yang, F.; Wei, H. Self-Assembly of Three-Dimensional Interconnected Graphene-Based Aerogels and Its Application in Supercapacitors. *J. Colloid Interface Sci.* **2013**, *407*, 416–424.

(14) Öner, E.; Öztürk, A.; Yurtcan, A. B. Utilization of the Graphene Aerogel as PEM Fuel Cell Catalyst Support: Effect of Polypyrrole (PPy) and Polydimethylsiloxane (PDMS) Addition. *Int. J. Hydrogen Energy* **2020**, *45* (60), 34818–34836.

(15) Singh, G.; Ramadass, K.; Lee, J. M.; Ismail, I. S.; Singh, M.; Bansal, V.; Yang, J. H.; Vinu, A. Convenient Design of Porous and Heteroatom Self-Doped Carbons for CO2 Capture. *Microporous Mesoporous Mater.* **2019**, *287* (April), 1–8.

(16) Sui, Z. Y.; Han, B. H. Effect of Surface Chemistry and Textural Properties on Carbon Dioxide Uptake in Hydrothermally Reduced Graphene Oxide. *Carbon N. Y.* **2015**, *82* (C), 590–598.

(17) Ho, M. T.; Allinson, G. W.; Wiley, D. E. Reducing the Cost of CO2 Capture from Flue Gases Using Pressure Swing Adsorption. *Ind. Eng. Chem. Res.* **2008**, *47* (14), 4883–4890.

(18) Web Page. https://scitechdaily.com/cheaper-carbon-capture-is-on-the-way-marathon-research-effort-drives-down-cost/ (accessed Feb 22, 2022).

(19) Jiang, Y.; Mathias, P. M.; Freeman, C. J.; Swisher, J. A.; Zheng, R. F.; Whyatt, G. A.; Heldebrant, D. J. Techno-Economic Comparison of Various Process Configurations for Post-Combustion Carbon Capture Using a Single-Component Water-Lean Solvent. *Int. J. Greenh. Gas Control* **2021**, *106* (January), 103279.

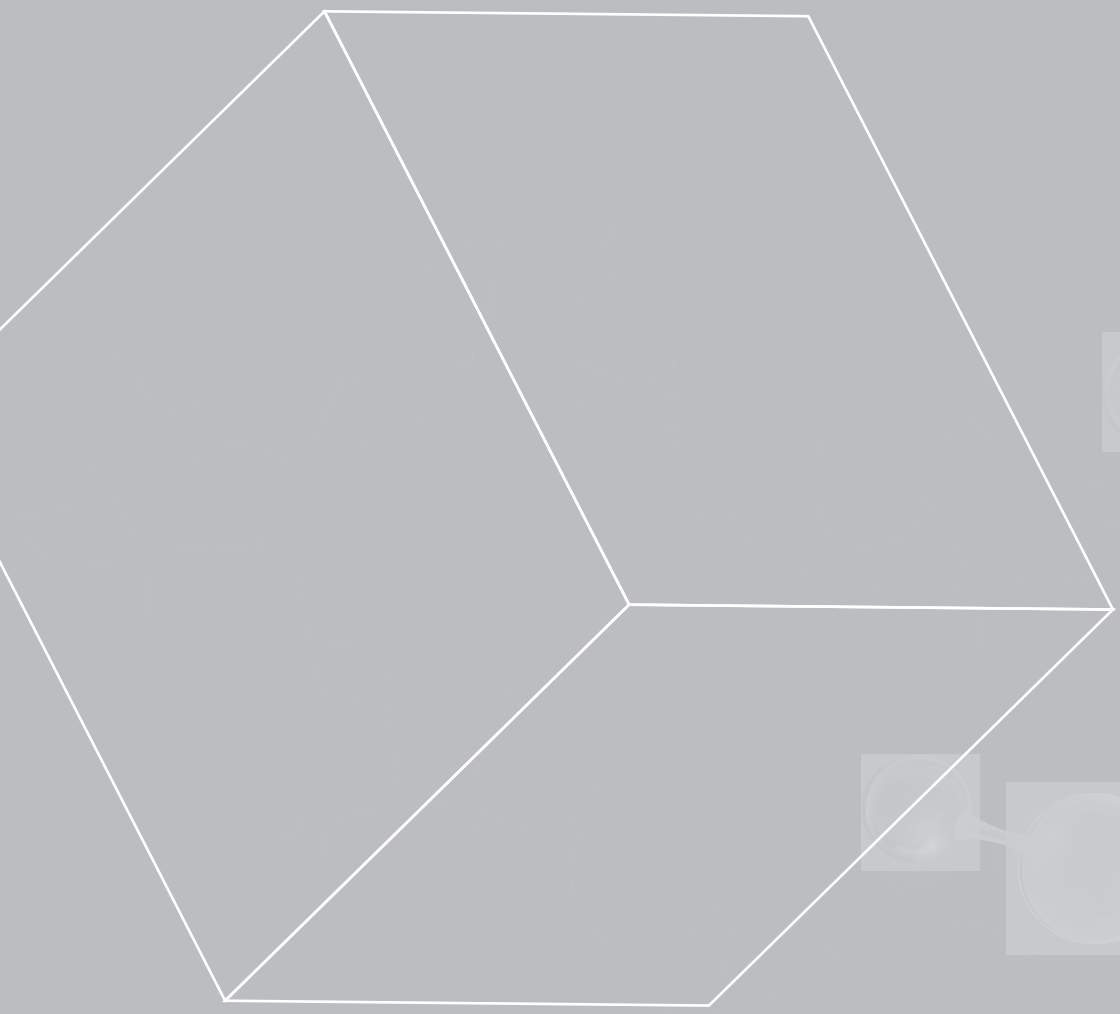

CHAPTER 4

Introducing and understanding of outstanding CO_2/N_2 selectivity in 3D graphene-polymer monoliths

Chapter 4. Introducing and understanding of outstanding CO_2/N_2 selectivity in 3D graphene/polymer monoliths

4.1. Introduction

In Chapter 3, the study of addition of functionalized polymer particles and solution polymers to the graphene-based skeleton at different reduction conditions and related to CO_2 adsorption performance was carried out. Two different functional monomers were used, NaSS and AMPS, to provide both sulfonic acid and amide functionalities. It was found that all the parameters studied (reduction temperature, amount of reducing agent, and amount and type of polymer) affected the CO_2 capture synergistically. Namely, an interplay between the fraction of residual oxygen-containing functional groups, textural properties, and type and amount of polymer onto the graphene-based monolith determine the selective CO_2 adsorption over that of N_2.

Nevertheless, although important CO_2 adsorption capacity is one of the most desirable parameter, a high selectivity of the material to adsorb CO_2 over N_2, O_2 or CH_4 plays just as or even more important role.[1] The separation of CO_2 from N_2 is of upmost importance but still highly challenging, as the post combustion flue gas mixture generally comprises 3-15 % CO_2 and more than 70 % N_2.[2] While the enhancement of the CO_2 adsorption capacity has been a focus of numerous works, the selectivity was investigated as a side effect, turning it into a current application bottleneck,[3] due to often low CO_2 selectivity of the porous adsorbents over other gasses (N_2, O_2, H_2O, …).[4,5] Searching for adsorbents that will provide the base for cost-efficient

carbon capture technology under post-combustion conditions, the both adsorption capacity and CO_2/N_2 selectivity have created a dilemma which will affect more importantly the process costs. E. Willey and co-workers have calculated the capture costs per ton of CO_2 avoided, as shown in Figure 4.1.[6] The figure shows that increasing CO_2 capture capacity affects less the costs than the improved selectivity. Therefore, by rising the capacity from 1 to 4 mmol/g decreases the costs for about 5 US$/t, whereas, if the selectivity CO_2/N_2 is augmented from 50 to 500, the costs dropped by 12 US$/t. By selectivity increasing, higher is the purity of the captured gas, independently on the regeneration pressure ratio. Therefore, one potential strategy to make the CO_2 capture in post-combustion mode economically viable is to increase the selectivity over N_2.

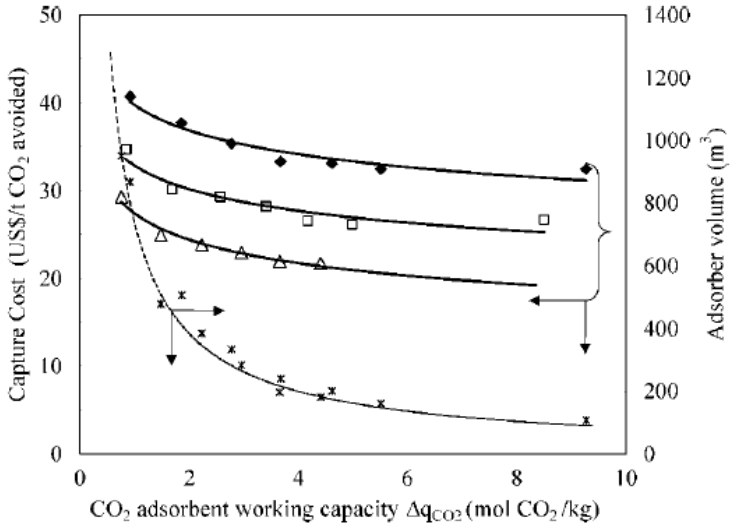

Figure 4.1. Effect on CO_2 capture cost (—) and total adsorber volume (---) of CO_2 adsorbent working capacity at three CO_2/N_2 selectivities: 50 (♦), 100 (□), and 500 (Δ), at 85 % CO_2 recovery. Reprinted with permission from Ind. Eng. Chem. Res. 2008, 47, 14, 4883–4890. Copyright 2008 American Chemical Society.

Different strategies have been proposed to enhance the selectivity of CO_2 over N_2, mostly emphasized on the idea to increase the CO_2 adsorption capacity creating "CO_2-philic" spots. These approaches focused on the control of the textural properties by creating narrow microporosity that will interact rather with CO_2 than with N_2 gas, or on the incorporation of heteroatoms-doped adsorbent that will increase the electrostatic interaction with CO_2 molecules.[7–14] In most of the cases, a higher CO_2 adsorption capacity was achieved, but not always a higher selectivity performance. On the other hand, reaching lower N_2 adsorption along to higher CO_2 adsorption can be a power approach towards CO_2/N_2 selective CCS technology. Few theoretical and experimental studied the "N_2-phobic" context, pointing out that it is crucial to achieve high selectivity.[15–17] They highlight the importance of the hierarchical pore structuring, claiming that adsorbents with well-defined small mesopores disrupt and reduce N_2 adsorption.

In order to make our carbon capturing technology based on self-assembly graphene closer to practical application, in this chapter, we altered the synthesis procedure towards augmentation of the fraction of oxygen functionalities and the content of the small mesopores within the monolithic structure. According our original procedure for synthesis of 3D rGO monoliths, the GO dispersion was kept at 80 °C for 2.5 h as a pre-treatment step, to homogenize the GO platelets prior to subject them to reduction process that induce self-assembly of the reduced platelets and formation of the monoliths (Figure 4.2). Taking into consideration that during this step certain quantity of oxygen functionalities from GO are lost and some restacking of the platelets occurred, this result on one hand in decreasing the driving force for monoliths formation and on the other hand, it negatively affects the fraction of oxygen functionalities. Therefore, in the present work the pre-treatment step was intentionally avoided.

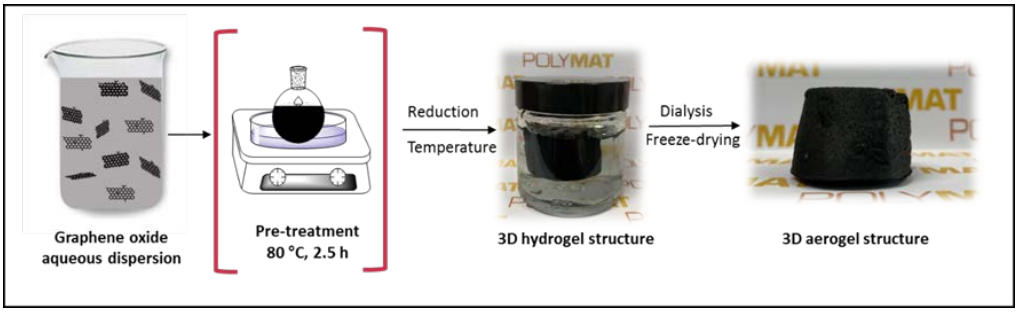

Figure 4.2. Schematic representation of the synthesis of the 3D rGO monolith.

4.2. Experimental part

4.2.1. Materials

As in previous chapters, 40 mL graphene oxide (GO) aqueous dispersion with concentration of 4 mg/mL was purchased from Graphenea. L-Ascorbic acid (AsA, ≥99 %, Sigma-Aldrich) was used for chemical reduction of GO. Technical monomers methyl methacrylate (MMA, Quimidroga), 2-Acrylamido-2-methyl-1-propanesulfonic acid (AMPS, 99 %, Sigma-Aldrich), and sodium 4-vinylbenzensulfonate (NaSS, ≥90 %, Sigma-Aldrich) were used without purification. Dowfax 2A1 (Dow Chemical Company), potassium persulfate (KPS, ≥99 %, Sigma-Aldrich), and Tert-Butyl hydroperoxide solution (TBHP, 70 wt% in H2O, Sigma-Aldrich) were used as received. Deionized water was used in all the polymerization reactions.

4.2.2. Synthesis of functionalized polymer dispersions

The synthesis procedure was explained in previous Chapter 3 (Section 3.2.2.1). Shortly, two types of polymer dispersions were synthesized by seeded semibatch emulsion polymerization process. Two different functional monomers, either sodium 4-vinylbenzensulfonate (NaSS) or 2-Acrylamido-2-methyl-1-propanesulfonic acid (AMPS) in small

amount (1% wt based to main monomer MMA) were independently copolymerized with the main monomer MMA. The reactions were carried out under nitrogen flux in a glass reactor fitted with a stainless-steel stirrer, a reflux condenser, a thermocouple, a sampling tube, and a feeding inlet. The reaction temperature was controlled by an automatic control system (Camile TG, Biotage). The formulation employed for the synthesis is presented in Table 3.1 in Chapter 3. Two colloidally stable polymer particle dispersions were obtained of approximately 30 wt% solids contents. ^{1}H-NMR was used to measure the incorporations of both non-volatile monomers NaSS and AMPS, showing that NaSS was incorporated only 37 % onto MMA particles, whereas almost all added AMPS was incorporated (100 %). The main monomer MMA was converted completely to polymer, as determined gravimetrically. The chemical structures of NaSS and AMPS are presented in Figure 3.1 in Chapter 3. As a results, NaSS-MMA and AMPS-MMA latexes with final solids content of 30 % and average polymer particles of 221 and 255 nm were prepared for NaSS-MMA and AMPS-MMA, respectively.

4.2.3. Synthesis of 3D neat rGO and composite monoliths

3D rGO-polymer composite monoliths were synthesized by the same procedure as neat rGO structure, except that prior to reduction process, the GO dispersions (pre-treated and non-treated) were mixed with functionalized MMA polymer particle dispersions for 2 h at room temperature. During this period, the polymer particles were adsorbed onto GO platelets. Afterwards, AsA was added to the composite dispersions (GO:AsA 1:1 weight ratio) and stirred for 0.5 h. Then, the dispersions were placed in an oven at different temperatures overnight (45, 60, and 90 °C) to induce the reduction process, producing the composite monolithic hydrogel structures. All the quantity of polymer used was incorporated in the structures, as confirmed by gravimetrical analysis of the residual water after formation of the monolith. Subsequently, the hydrogel was cleaned and dried similarly as the neat rGO monoliths, explained previously. The

straightforward experimental procedure of the 3D monolithic composed of rGO and polymer particles is schematically described in Figure 2.3 in Chapter 2.

4.2.4. Characterization

In terms of polymer characterization, conversion of the monomers and solids content were calculated gravimetrically. The z-average particle size (dz) of the polymer particles were measured by dynamic light scattering (DLS). The conversion of NaSS and AMPS functional monomers in both emulsion polymerization and solution polymerization techniques was characterized by ^{1}H-Nuclear Magnetic Resonance (NMR). 1H-NMR spectras were recorded in a Bruker AVANCE 400 MHz instrument. The conversion was determined on the evolution of the peaks corresponding to the vinyl protons of NaSS (δ, 6.2, 5.9 ppm) and AMPS (δ, 6.1, 5.6 ppm). The peak corresponding to deuterated dimethyl sulfoxide (DMSO, δ, 3.3 ppm) was used as internal reference. The detailed description of the latex characterization methods is given in Section I.1 of Appendix I.

On the other hand, regarding the characterization of the 3D structures, thermogravimetric analyses (TGA) were performed to estimate the amount of residual oxygen-containing functional groups within the monolithic structures and to study the thermal stability. The surface morphology of the structures was examined using a scanning electron microscopy (SEM). The porous texture of the monoliths was characterized by means of N_2 adsorption–desorption at –196 °C in a Micromeritics ASAP2020 apparatus. X-ray photoelectron spectroscopy (XPS) was used to study the surface chemical states of composing elements of monoliths. The surface roughness of both 3D monoliths and rGO layers were analysed by means of atomic force microscope (AFM). Detailed information of these characterization techniques is given in Section I.2 of Appendix I.

Finally, CO_2 and N_2 gas adsorption capacities were measured from their isotherms, measured using a Micromeritics ASAP 20220 Analyzer. The selectivity of CO_2 over N_2 was calculated by the ideal adsorbed solution theory (IAST) using only data for the pure-component adsorption equilibria at the same temperature (25 °C) and on the same adsorbent. Detailed information of these gas adsorption measurements is given in Section I.3 of Appendix I.

4.3. Results and discussion

4.3.1. Characteristics of 3D neat monoliths

The neat graphene and graphene-polymer composite monolithic structures were synthesized by a chemical reduction of GO platelets in aqueous dispersion, in absence or presence of polymer colloids, respectively. The reduction process was performed at different reduction temperatures (45, 60, and 90 °C), at constant GO:AsA mass ratio of 1:1, in two different procedures with and without pre-treatment of GO aqueous dispersion (2.5 h at 80 ºC).

Six monolithic structures made of neat rGO were prepared, the nomenclature of which is 45_Blank_80, 60_Blank_80, and 90_Blank_80 with the pre-treatment step, where the first number refers to reduction temperature and the last number to the pre-treatment temperature. The nomenclature of the monoliths obtained without the pre-treatment is 45_Blank, 60_Blank, and 90_Blank. The characteristics of the monoliths are presented in Table 4.1.

Table 4.1. Amount of the residual oxygen-containing functional groups and textural properties of 3D neat rGO structures.

Material	% O-functionality	S_{BET} (m^2/g)	V_{total} (cm^3/g)	V_{micro} (cm^3/g)	% Micro
45_Blank_80	14	160	0.289	0.008	2.7
45_Blank	17	137	0.161	0.021	13.3
60_Blank_80	9	172	0.653	0.001<	0.2
60_Blank	12	146	0.240	0.007	2.9
90_Blank_80	3	299	1.359	0.001<	0.1
90_Blank	5	214	0.354	0.015	4.3

The formation mechanism of the 3D structures was explained in Chapter 2. Shortly, the synthesis consists of reaction induced self-assembly of rGO platelets in aqueous dispersion. For composite monoliths, polymer particle aqueous dispersion is added to the GO dispersion. Initially, GO platelets are amphiphilic and form a colloidal dispersion in water. After reduction, their hydrophobicity increased substantially, inducing their incomplete aggregation and formation of one monolithic structure in which all the solids presented in the dispersions (including polymer particles) are incorporated. The monolithic structures are swelled with water, forming a kind of hydrogels, which after freeze-drying gave rise to hydrophobic, highly porous, 3D monoliths, made either of neat rGO or rGO/polymer composites. The driving force for this process is the sudden rise of the surface energy in the dispersion after GO reduction. Therefore, if the GO dispersions are subjected to 80 °C pre-treatment, the loss of the oxygen functionalities and partial rGO restacking occurred, increasing the hydrophobicity of the initial GO platelets and lowering the driving force for monoliths formation. We expected that by avoiding of the pre-treatment a higher driving force would be created that contributes to formation of more compact structures richer in residual oxygen functionalities and small mesopores. Moreover, the carbon footprint of the synthesis process would decrease further.

The thermal stability and the amount of residual oxygen functionality groups of neat monoliths were determined by TGA analysis. The TGA graphs are presented in Figure 4.3.

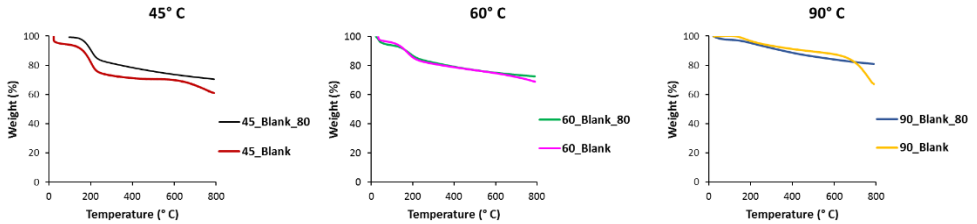

Figure 4.3. TGA thermographs of 45_Blank_80, 45_Blank, 60_Blank_80, 60_Blank, 90_Blank_80, and 90_Blank samples.

The weight loss of all curves occurred in three steps, in which the first weight decay until 100 °C is related to the humidity and the second weight drop, between 100 and 225 °C, corresponds to the loss of the residual oxygen functionalities, and the last lost is assigned to the graphenic structure. According to Figure 4.3, at increasing reduction temperature more compact structures were formed due to a faster self-assembly process. From the TGA curves, the amount calculated from the weight loss occurring in a range of 100-225 °C was considered a fraction of oxygen-containing functional groups, as shown in Table 4.1. This fraction decreases in the monoliths produced at higher reduction temperatures. On the other hand, when materials were pre-treated at 80 °C prior to the reduction process, the fraction of oxygen functionalities is much lower than in the respective materials produced by avoiding the pre-treatment, e.g. 14 % versus 17 % for 45 ºC reduction temperature, respectively. This confirms the hypothesis that by avoiding the pre-treatment, a denser functionalization of rGO platelets within the resulting monoliths is achieved.

The textural properties and porous structure of the monoliths was developed from N_2 adsorption-desorption isotherms, shown in Figure 4.4. It can be observed that all the isotherms are of type IV, typical for mesoporous materials.[18]

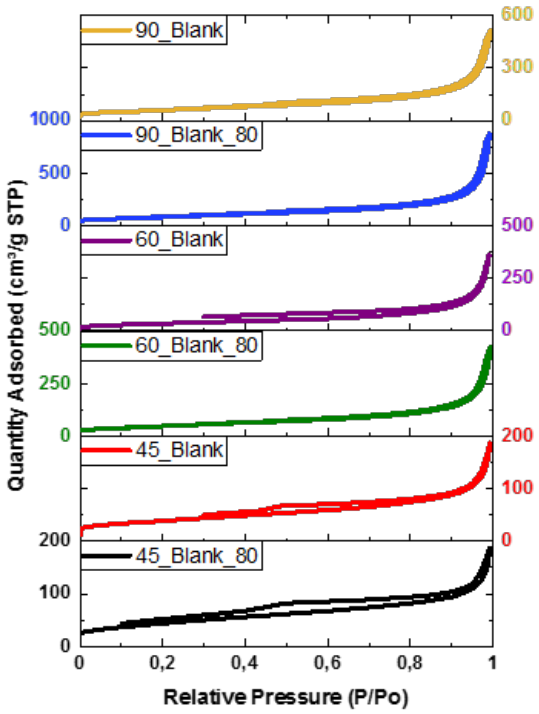

Figure 4.4. N_2 adsorption-desorption isotherms of 45_Blank_80, 45_Blank, 60_Blank_80, 60_Blank, 90_Blank_80, and 90_Blank materials.

According to the textural characteristics presented in Table 4.1, the monoliths produced at higher temperatures present larger specific surface areas and total volume of the pores, reaching maximum surface area of 299 m^2/g and pore volume of 1.359 cm^3/g (90_Blank_80). It

is clear that the pre-treated platelets allowed development of higher surface area and total pore volume, with very minor fraction of micropores, whereas without pre-treatment the monoliths are less porous, but the micropores fraction is higher. It is possible that the microporosity is increased due to more oxidized surface of the non-pretreated platelets, preventing complete restacking of the platelets during self-assembly. The decrease in BET surface area indicates that during the pre-treatment in the initial restacking of the GO platelets large number of small mesopores are formed. Taking into account that without pre-treatment higher fraction of oxygen functionalities are distributed throughout lower available BET area, the monoliths are much more densely functionalized. According to previous Chapter 3, such characteristic of the monoliths has shown to be quite favourable for the selective CO_2/N_2 capture at ambient conditions (1 atm and 25 ºC), at which the interplay between BET surface area and fraction of oxygen functionalities are decisive and the porous texture did not affect significantly.

The structure and morphology of the monolithic materials were characterized by SEM technique, and the images are gathered in Figure 4.5.

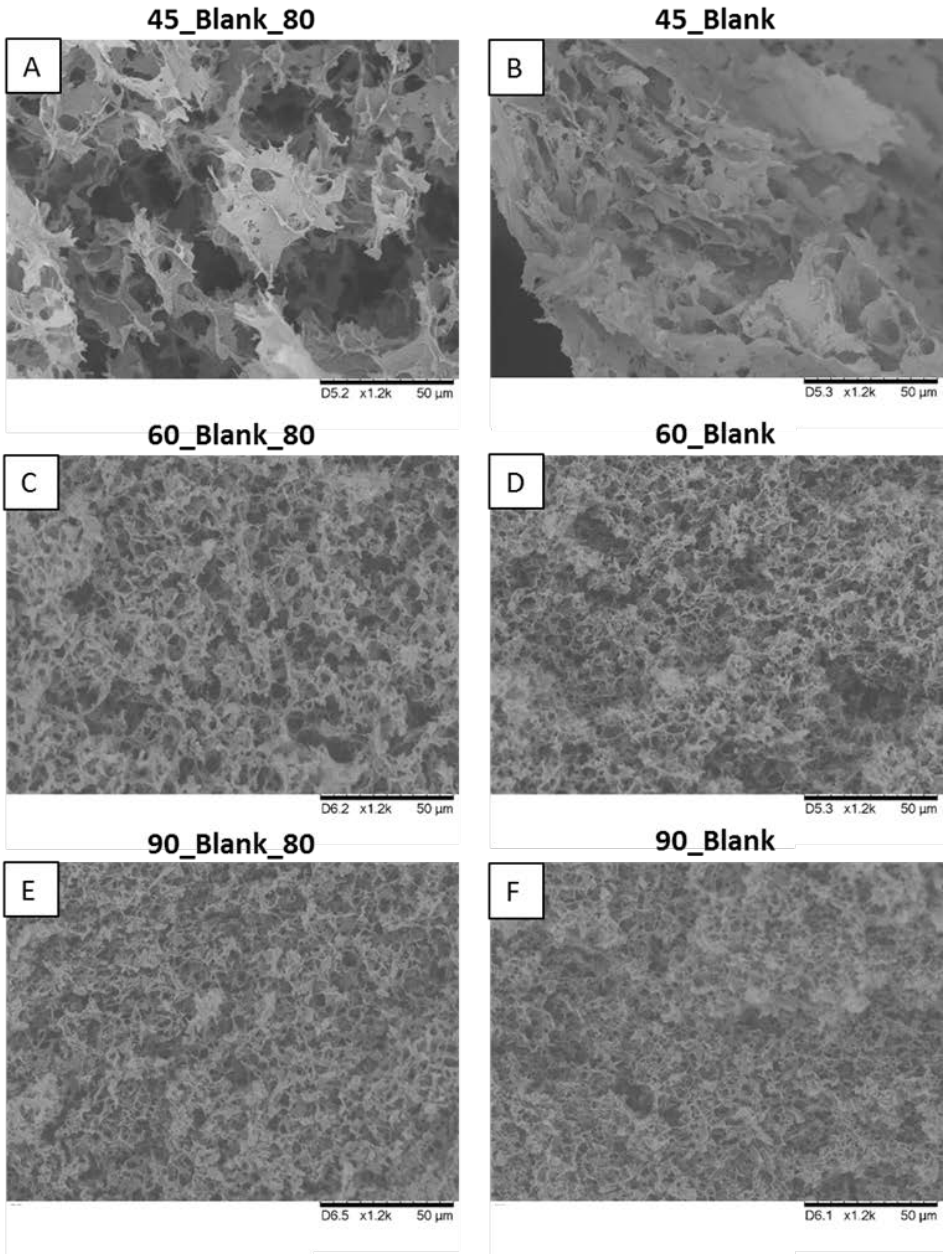

Figure 4.5. SEM images of 45_Blank_80 (A), 45_Blank (B), 60_Blank_80 (C), 60_Blank (D), 90_Blank_80 (E), and 90_Blank (F) at 50 µm scale bar.

According to SEM images in Figure 4.5, all monoliths present a porous structure, however, monoliths synthesized at higher reduction temperatures (90_Blank_80 (E) and 90_Blank (F)) are more closely packed (higher number of lower size pores) and present a higher porosity in concordance to the larger BET surface areas (Table 4.1). In fact, materials formed at 90 °C present a lower overall volume than those obtained at milder temperatures for the same material mass, i.e. they are more compact. On the other hand, there are no observable differences in the SEM images between the structures synthesized with or without pre-treatment.

The CO_2/N_2 selectivity of the monoliths was calculated by IAST method from the single-component adsorption isotherms according to Freundlich's model. The CO_2 and N_2 individual adsorption-desorption isotherms obtained at 1 atm and 25 °C are presented in Figure 4.6., and the fitting curves for CO_2 and N_2 and the parameters in the Freundlich isotherms are presented in Section II.3 of Appendix II.

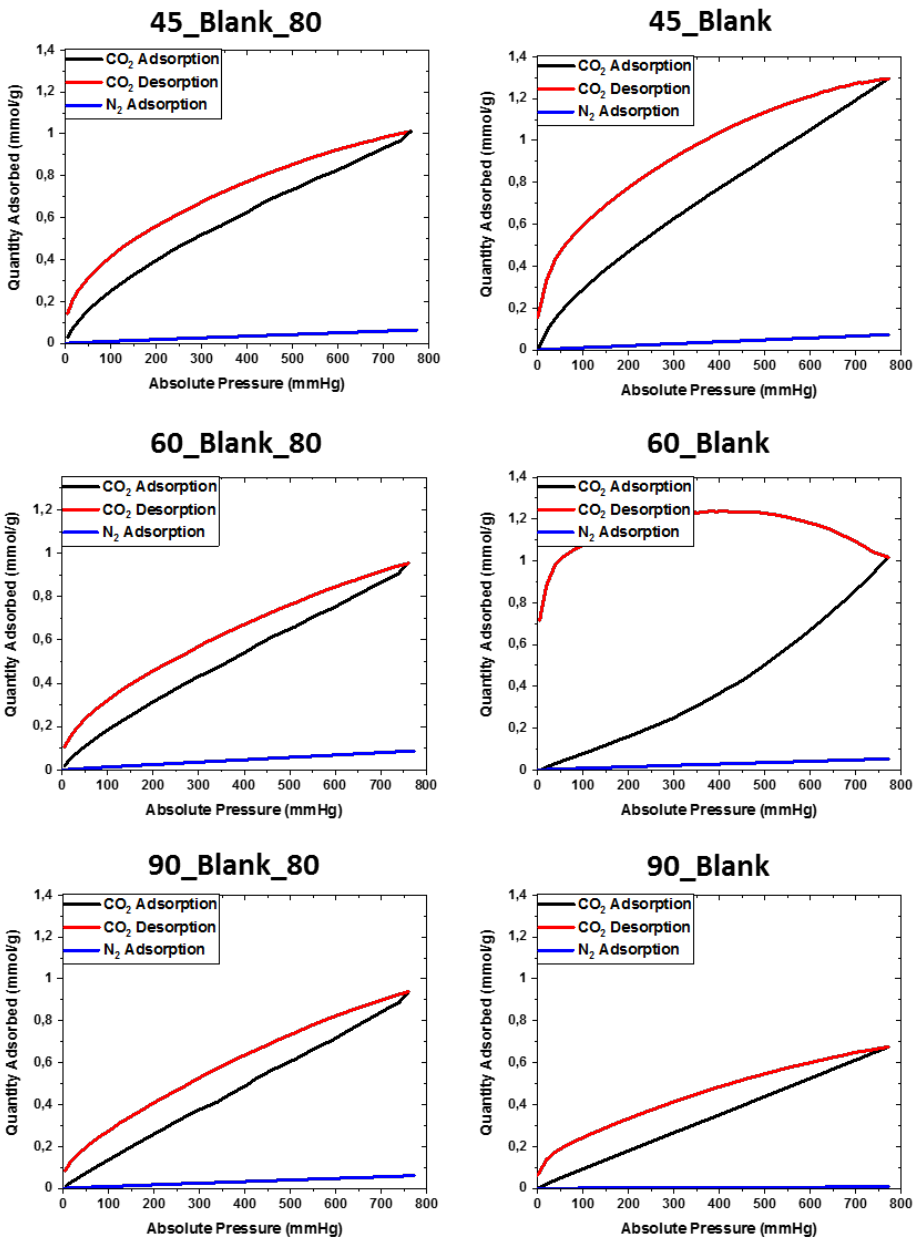

Figure 4.6. CO_2 adsorption-desorption and N_2 adsorption isotherms for 3D rGO monoliths.

In Table 4.2, and in Figure 4.7, CO_2 and N_2 adsorption capacities at 1 atm and 25 °C and IAST selectivity for each of these neat monoliths are presented.

Table 4.2. CO_2 and N_2 adsorption capacities and selectivity values for 3D neat rGO monoliths.

Material	CO_2 adsorption (mmol/g)	N_2 adsorption (mmol/g)	Selectivity
45_Blank_80	1.01	0.064	90
45_Blank	1.29	0.073	106
60_Blank_80	0.95	0.088	62
60_Blank	1.02	0.053	85
90_Blank_80	0.94	0.061	86
90_Blank	0.67	0.008	470

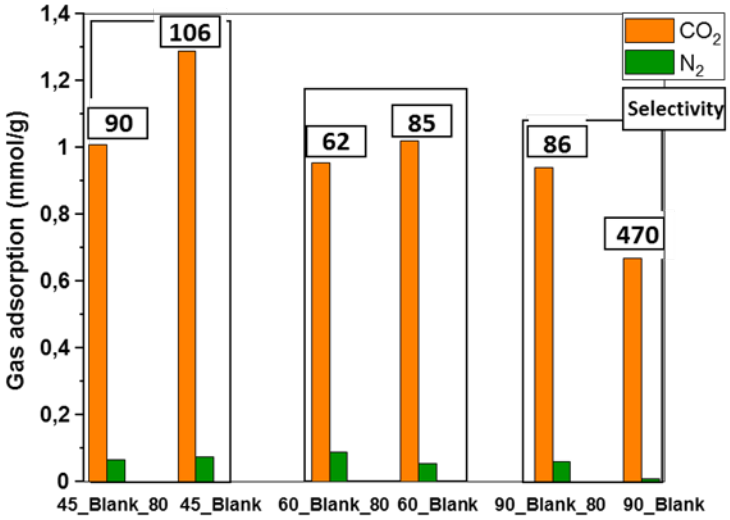

Figure 4.7. Comparison of CO_2 and N_2 adsorption, and CO_2/N_2 selectivity of neat rGO monoliths produced at 45, 60, and 90 °C with and without pre-treatment.

Figure 4.7 reveals that the neat rGO monoliths synthesized at 45 ºC and 60 ºC by avoiding the pre-treatment adsorbed higher CO_2 quantity than pre-treated monoliths, and consequently improved selectivity was attained (the selectivity is denoted in a black square frame over each adsorption bar in Figure 4.7). Nevertheless, for the monolith prepared at 90 ºC, both CO_2 and N_2 adsorptions were decreased when the pre-treatment was avoided. Likely, this is a consequence of important decrease of surface area when the pre-treatment was avoided, along with insignificant enhancement of the functionalization. However, this monolith (90_Blank) has shown to be almost completely N_2-phobic. Consequently, largely amplified CO_2/N_2 selectivity from 86 in pre-treated to 470 in non-treated monolith was achieved. This results confirms the findings obtained from the theoretical studies of the selectivity in C-based porous materials, which claimed that excellent selectivity cannot be attained only by improving the CO_2 adsorption capacity, but N_2-phobicity have to be gained, too.[15,16] To the best of the author's knowledge, this value is maximum selectivity achieved by carbon-based monolithic structures at the conditions studied. Table 4.3 shows reported results on CO_2/N_2 selectivity for similar carbon-based materials, which are at least a third of the presented value.

Table 4.3. Summary of some carbon-based adsorbents with their textural properties, CO_2 adsorption capacities, and CO_2/N_2 selectivity properties.

Material	BET (m^2/g)	CO_2 capacity (1 atm, 298 K), mmol/g	Selectivity CO_2/N_2 (0.15/0.85), 298 K	Ref.
H-BINAM	776	4.12	102	9
MPC-700	1930	5.18	153	9
mJUC160-900	940	3.5	29	19
a-NDC6	-	4.3	34	20
GPN-800	484	2.19	43	21
HGF-II	497	1.4	70	22
a-RGO-950	1316	1.06	162	23

4.3.2. Characteristics of 3D composite monoliths

Chapter 2 has shown that the neat rGO structures are not stable and lost mass in cyclic operations, which was resolved by addition of functionalized polymer particles (20 wt%) into the structures. In order to study how the addition of functionalized polymer particles affects the textural properties and adsorption characteristics when the pre-treatment step was avoided, herein a portfolio of 3D graphene-polymer composites were synthesized without the 80 °C pre-treatment, using NaSS-functionalized MMA and AMPS-functionalized MMA polymer particles. Furthermore, two different amount of polymer particles were used, 10 wt% and 40 wt% based on GO quantity, and the monoliths were produced at three different reduction temperatures (45, 60, and 90 °C) at constant amount of reducing agent (GO:AsA mass ratio 1:1). Table 4.4 presents the characteristics of the 3D rGO-polymer composite monoliths, which were compared with these of the counterpart monoliths synthesized at 45 °C and 90 °C from the pre-treated GO, reported in Chapter 3. In the nomenclature of the composite monoliths, the first number refers to the reduction temperature, followed by the functional monomer used, and finished with the polymer fraction.

Table 4.4. Amount of the residual oxygen-containing functional groups and textural properties of 3D rGO-polymer monolithic structures synthesized by avoiding the pre-treatment of GO dispersion at 80 ºC prior to reduction. In brackets, the results of the previously reported 3D rGO-polymer structures synthesized by using the pre-treatment step are also presented (Chapter 3).

Material[a]	% O-functionality	S_{BET} (m^2/g)	V_{total} (cm^3/g)	V_{micro} (cm^3/g)	% Micro
45_NaSS_10	24 (12.8)	147 (185)	0.151 (0.184)	0.026 (0.035)	17.1(18.8)
45_NaSS_40	19 (10.7)	98 (143)	0.150 (0.176)	0.011 (0.019)	7.1 (10.9)
45_AMPS_10	24 (12.9)	80 (170)	0.114 (0.170)	0.013 (0.032)	11.8(19.1)
45_AMPS_40	16 (10.6)	112 (118)	0.108 (0.152)	0.021 (0.016)	19.6(10.5)
60_NaSS_10	11	157	0.247	0.012	4.9
60_NaSS_40	11	131	0.223	0.008	3.7
60_AMPS_10	16	158	0.214	0.017	8.1
60_AMPS_40	9	127	0.213	0.009	4.3
90_NaSS_10	2 (3.6)	246 (199)	0.426 (0.337)	0.012 (0.016)	2.9 (4.9)
90_NaSS_40	5 (3.2)	181 (177)	0.324 (0.313)	0.012 (0.011)	3.6 (3.6)
90_AMPS_10	6 (3.8)	210 (207)	0.360 (0.348)	0.014 (0.016)	3.9 (4.6)
90_AMPS_40	4 (3.1)	162 (117)	0.282 (0.206)	0.011 (0.001)	4.0 (0.6)

[a]*Nomenclature of the samples: reduction T_type of F.M. (NaSS or AMPS) copolymerized with MMA_weight % of the polymer (10 or 40)*

According to the TGA thermographs shown in Figure 4.8, the composites present similar thermal degradation behaviour as the blanks, except one additional degradation step at about 300-400 °C assigned to the degradation of the polymers. This step is obviously higher for the composites containing 40 % polymer than these with 10 %.

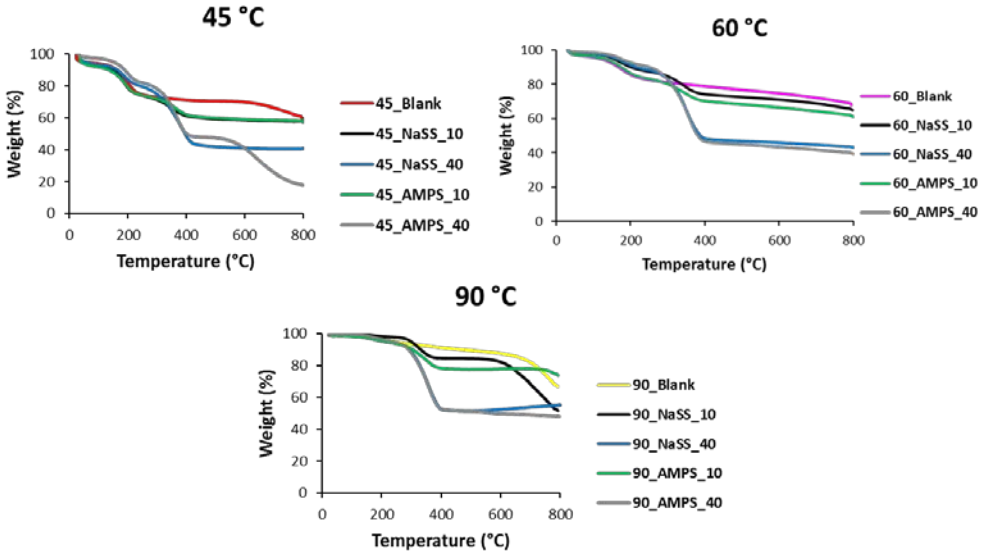

Figure 4.8. TGA thermographs of blanks and composites samples.

The fraction of oxygen functionalities calculated from the TGA degradation curves, shown in Table 4.4, is lower in the monoliths obtained at higher reduction temperatures. Compared to the values of Chapter 3 of these composites produced following the procedure that include the pre-treatment of GO dispersion (shown in brackets in Table 4.4), avoiding this step ensures much higher fraction of oxygen functionalities incorporated onto the graphenic surface of the monoliths, although the difference is smaller at higher reduction temperature (90 ºC).

The N_2 adsorption-desorption isotherms of the composite monoliths are shown in Figure 4.9. The textural properties of the composite monoliths are presented in Table 4.4.

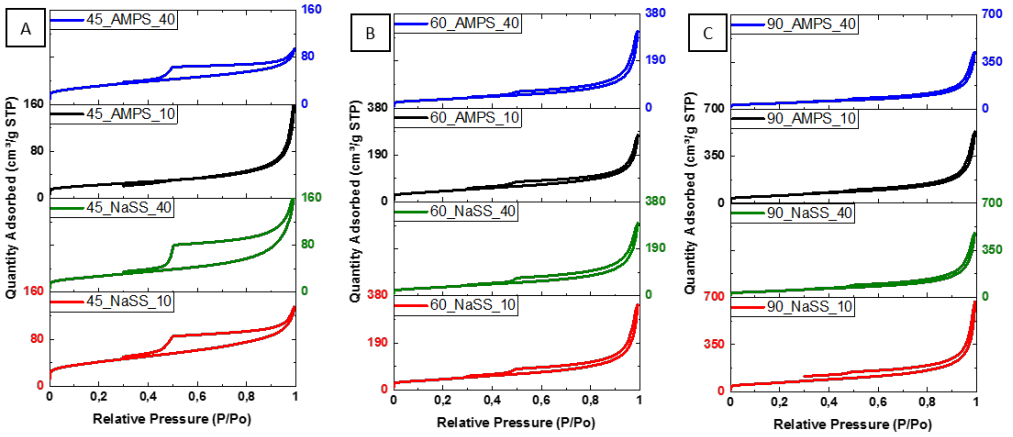

Figure 4.9. N_2 adsorption-desorption isotherms for composites synthesized at 45 °C (A), at 60 °C (B), and 90 °C (C).

BET surface area was importantly affected by the reduction temperature, giving rise to more compact and simultaneously more porous composites when produced at higher temperature due to higher total pore volume. For example, the BET surface area increased from 147 m^2/g in the monolith 45_NaSS_10, to 157 m^2/g in 60_NaSS_10, and to 246 m^2/g in 90_NaSS_10, which trend was followed by all other monoliths. Monoliths synthesized at higher reduction temperatures are more densely pack composed of a higher number of smaller pores, the volume of which increases with temperature from around 0.1 cm^3/g in composites synthesized at 45 °C, to 0.2 cm^3/g at 60 °C, and up to 0.4 cm^3/g at 90 °C. In terms of volume of micropores and their contribution to the overall porous structure (% Micro), monoliths synthesized at 45 °C had lower volume of micropores, without much difference between composites synthesized at 60 °C or 90 °C.

The BET surface area, in most of the cases, decreases with the addition of particles in the structure compared to the blank materials (Table 4.1). In the synthesis procedure, polymer

particles were attached to the GO layers, and therefore, the hydrophobicity and the mobility of the layers changed, and consequently the self-assembly process is affected, giving place to a lower total volume of pores. According to Chapter 3, the addition of polymer particles in most of the cases increases the contribution of micropores (% Micro) to the overall porous structure, as polymer particles act like spacers between the aggregated rGO layers avoiding their total stacking. This effect was far weaker when the pre-treatment step was skipped (Table 4.4). Likely, less initial aggregation of the GO platelets prior to the polymer addition and reduction process produced fewer micropores.

The CO_2 and N_2 adsorption-desorption curves measured at 25 °C and 1 atm are presented in Figure 4.10-4.12, whereas the capturing performances of the monoliths are presented in Table 4.5 and in Figure 4.13, where it is compared with the adsorption performance reported previously for monoliths produced with the pre-treatment in Chapter 3 (composite monoliths prepared at 45 ºC and 90 ºC).

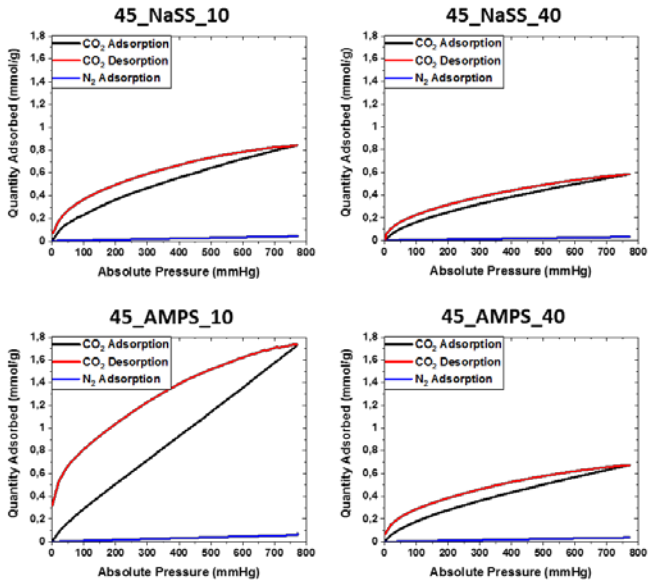

Figure 4.10. CO_2 adsorption-desorption and N_2 adsorption isotherms for composites synthesized at 45 °C.

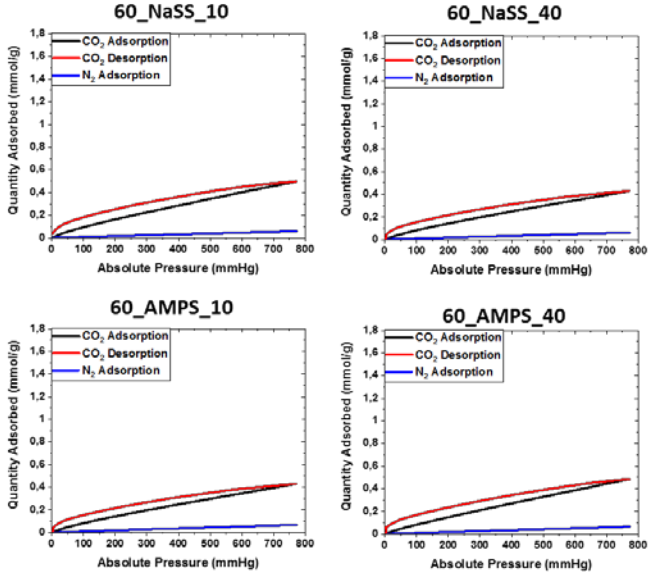

Figure 4.11. CO_2 adsorption-desorption and N_2 adsorption isotherms for composites synthesized at 60 °C.

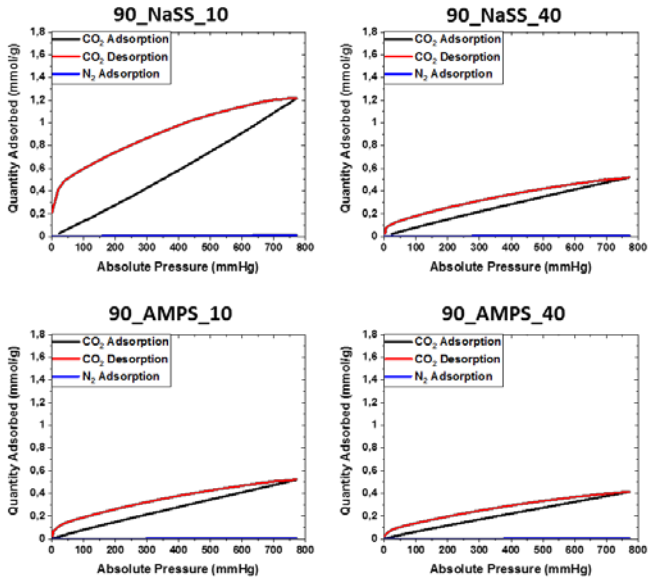

Figure 4.12. CO_2 adsorption-desorption and N_2 adsorption isotherms for composites synthesized at 90 °C.

Table 4.5. CO_2 and N_2 adsorption capacities and selectivity values for 3D rGO composites. In brackets, the results of the previously reported 3D rGO-polymer structures synthesized by using the pre-treatment step are also presented (Chapter 3).

Material[a]	CO_2 adsorption (mmol/g)	N_2 adsorption (mmol/g)	Selectivity
45_NaSS_10	0.84 (0.67)	0.044 (0.076)	119 (51)
45_NaSS_40	0.59 (0.49)	0.032 (0.056)	113 (52)
45_AMPS_10	1.73 (0.67)	0.059 (0.072)	156 (53)
45_AMPS_40	0.68 (0.58)	0.038 (0.064)	108 (53)
60_NaSS_10	0.5	0.060	51
60_NaSS_40	0.43	0.063	42
60_AMPS_10	0.59	0.068	50
60_AMPS_40	0.49	0.065	52
90_NaSS_10	1.21 (0.63)	0.011 (0.069)	621 (49)
90_NaSS_40	0.52 (0.28)	0.006 (0.031)	471 (48)
90_AMPS_10	0.52 (0.28)	0.006 (0.033)	527 (45)
90_AMPS_40	0.42 (0.35)	0.005 (0.038)	496 (44)

[a]*Nomenclature of the samples:*
Reduction T[a] _Type of F.M. (NaSS or AMPS) copolymerized with MMA_Weight % of the polymer (10 or 40)

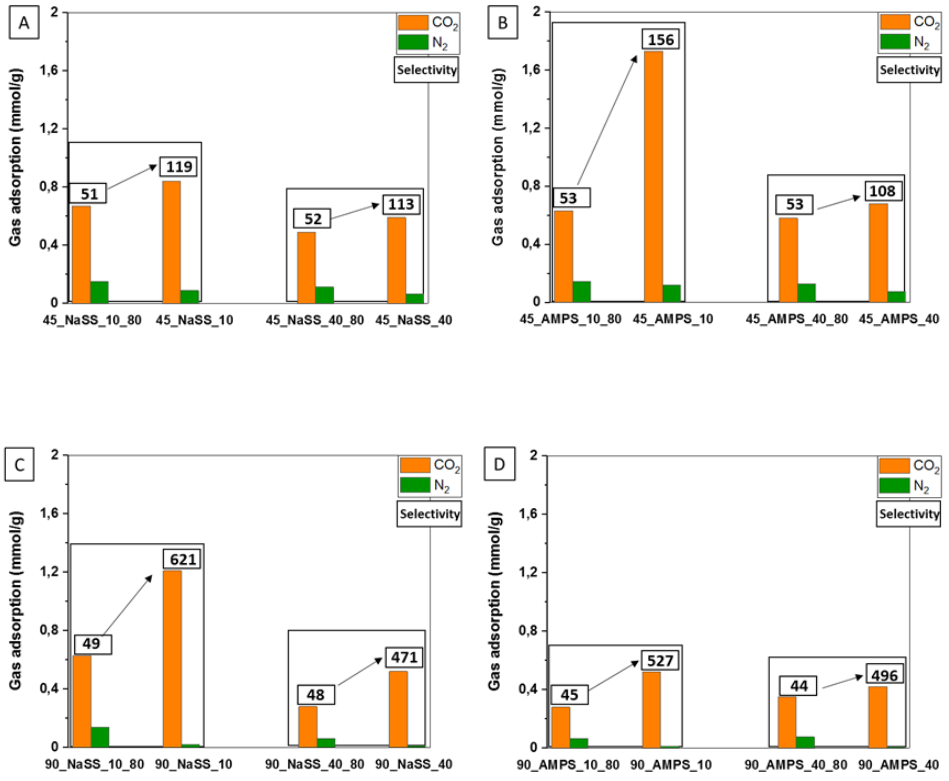

Figure 4.13. Comparison of CO_2 and N_2 adsorption, and CO_2/N_2 selectivity of composite monoliths produced at 45 °C (A and B) and 90 °C (C and D) with and without pre-treatment. The 80 number in the formulation corresponds to monoliths synthesized with the pre-treatment step (Chapter 3).

In general, the addition of functionalized polymer particles did not improve the adsorption capacities compare to the blank materials, except in few cases for 45_AMPS_10 and 90_NaSS_10, for which higher CO_2 adsorption of 1.73 and 1.21 mmol/g, respectively, were achieved (Table 4.5). N_2 adsorption decreased with polymer addition and decreased significantly in the monoliths obtained at high reduction temperature (90 °C). Avoiding the pre-treatment step

results in more homogeneous characteristics with less difference between the different materials' performance.

The CO_2/N_2 selectivity was calculated using IAST method, as already explained, and the results are also presented in Table 4.5 and Figure 4.13. The fitting curves for CO_2 and N_2 and the parameters on the Freundlich isotherm are presented in Section II.3 of Appendix II. Therefore, the addition of functionalized polymer particles in most of the monoliths did not influenced significantly the CO_2 adsorption (with exception of 45_AMPS_10 and 90_NaSS_10), but did affected the CO_2/N_2 selectivity in the composites synthesized at 45 °C and 90 °C. Regarding to the polymer quantity, the addition of 10 % polymer presented better textural and adsorption properties in terms of CO_2 uptake and higher selectivity than monoliths with 40 % polymer fraction. According to Figure 4.13, the monoliths produced without pre-treatment present increased CO_2 adsorption than in the pre-treated monoliths, which probably is a consequence of increased fraction of oxygen residual functionalities, which are distributed over lower surface areas, resulting in denser functionalization. On the other hand, the N_2 adsorption decreased for all non-pre-treated monoliths. These effects are higher for monoliths produced at higher temperatures, resulting in significant increasing of the CO_2/N_2 selectivity to extraordinary values in a range of 471 to 621. The monoliths with the 40 % polymer, when they are compared with monoliths with the 10 %, generally present lower N_2 adsorptions, nevertheless, the CO_2 adsorption is also much lower, thus, the selectivity slightly dropped, too. The monoliths produced at 60 ºC did not follow the observed trends and the CO_2 and N_2 adsorption and selectivity were not affected importantly by the production process (Figure 4.14).

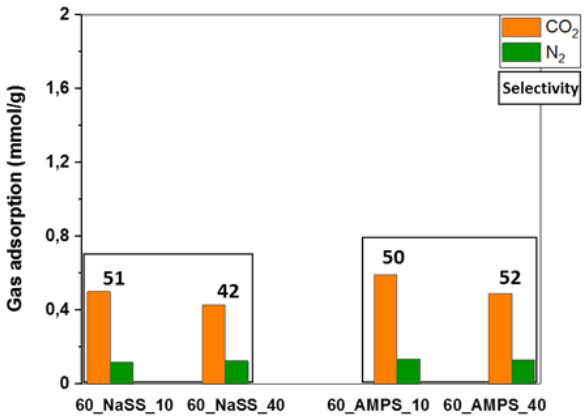

Figure 4.14. Adsorption performance of composites synthesized at 60 °C, without available comparison with pre-treated materials.

The highest selectivity value of 621 under the conditions studied was achieved by 90_NaSS_10, for which BET surface area was increased by avoiding the pre-treatment, whereas the oxygen functionality fraction was lower. Besides that, the CO_2 adsorption was duplicated from 0.63 to 1.21 mmol/g, and N_2 adsorption dropped from 0.069 to 0.011 mmol/g, turning the material into greatly N_2-phobic by avoiding of the pre-treatment step. Apparently, the interplay between both adsorption characteristics contributes to the best selectivity achieved, rising from 49 with the pre-treatment to 621 when it was avoided. The selectivity was thirteen fold increased and is far higher than any reported value for C-based porous adsorbents, and between the highest reported (Table 4.3). Taking into account that the behaviour of this monolith was opposite than previously observed, it is clear that there are additional characteristics that affect this behaviour, which we will try to explain latter.

4.3.3. Understanding of selectivity

All the monoliths produced at 90 ºC without the pre-treatment presented more than one order of magnitude improved selectivity. Comparison of the characteristics of these monoliths, presented in Table 4.4, did not show important differences in the characteristics that might indicate the reason behind such a jump of the CO_2/N_2 selectivity. In order to shed a bit of light of this issue we have tried to obtain more detailed characterization of the surface of the monoliths. According to the literature, well-defined small mesopores, more or less between 3-7 nm, disrupt and reduce N_2 adsorption.[15,16] In Figure 4.15 and Figure 4.16 the pore size distributions of the blank and composite monoliths, respectively, are presented where it can be observed that there is no well-defined small mesopores in that size region that could justify the observed differences. Furthermore, the pore size distributions of the composites synthesized with the pre-treatment step, Figure 3.4 in Chapter 3, and without the pre-treatment (Figure 4.16) do not show any significant differences.

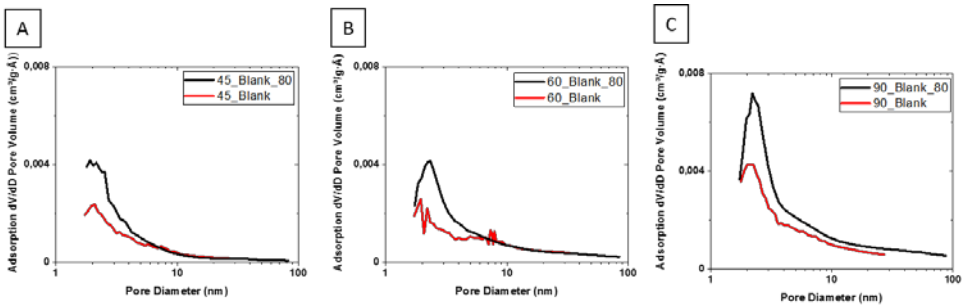

Figure 4.15. Pore size distributions of the blank materials synthesized at 45 °C (A), 60 °C (B), and 90 °C (C).

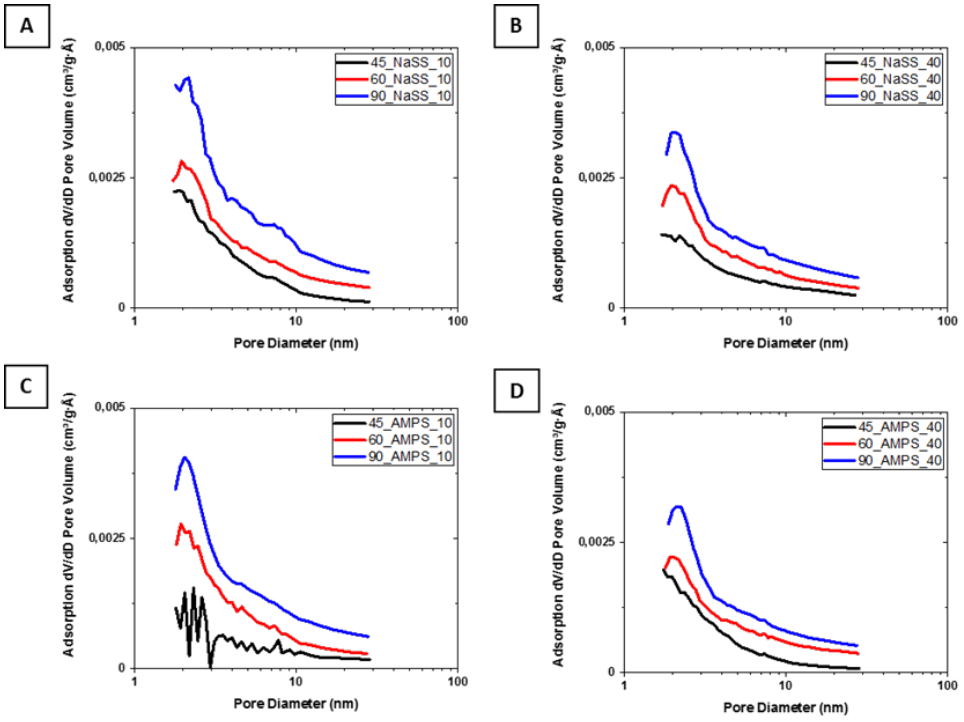

Figure 4.16. Pore size distributions of the composite materials synthesized at different temperatures for NaSS_10 (A), NaSS_40 (B), AMPS_10 (C), and AMPS_40 (D) without pre-treatment step.

In order to go further in the N_2 adsorption understanding, the surface chemistry of the monoliths focused on blank materials was profoundly studied, using XPS. Namely, by TGA the whole oxidized quantity was determined, and probably some of the functional groups might be buried within the structures, in which case they would not contribute to the adsorption process. In Figure 4.17, the survey scan spectra of all samples are presented, in which mostly the presence of carbon and oxygen are identified.

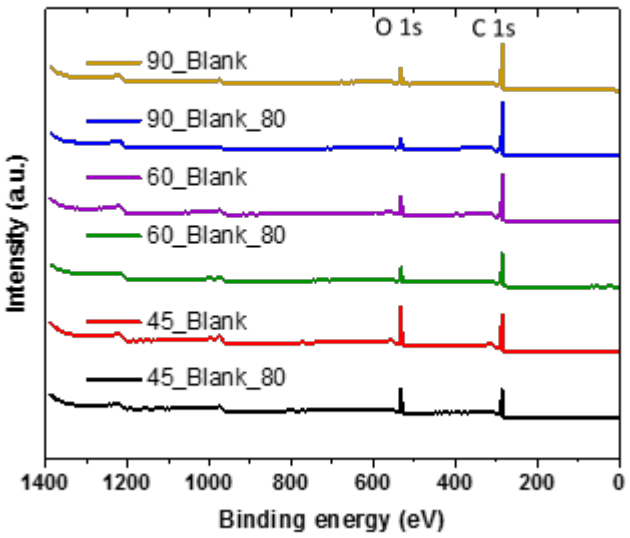

Figure 4.17. XPS survey spectra of 45_Blank_80, 45_Blank, 60_Blank_80, 60_Blank, 90_Blank_80, and 90_Blank materials.

Figure 4.18 shows the high-resolution XPS spectra of C 1s region for different monoliths, in which the de-convoluted peaks are assigned to the chemical moieties according to the binding energy of the peaks. It is clear that all the monoliths made of neat rGO present the same peaks at 284.6 eV, 287.0 eV, and 288.6 eV, which binding energies correspond to C-C, C-O, and C=O or O-C=O. Even though their fraction is affected by the reduction temperature and by the procedure of synthesis (with or without pre-treatment step), the differences are rather negligible, as shown in Table 4.6.

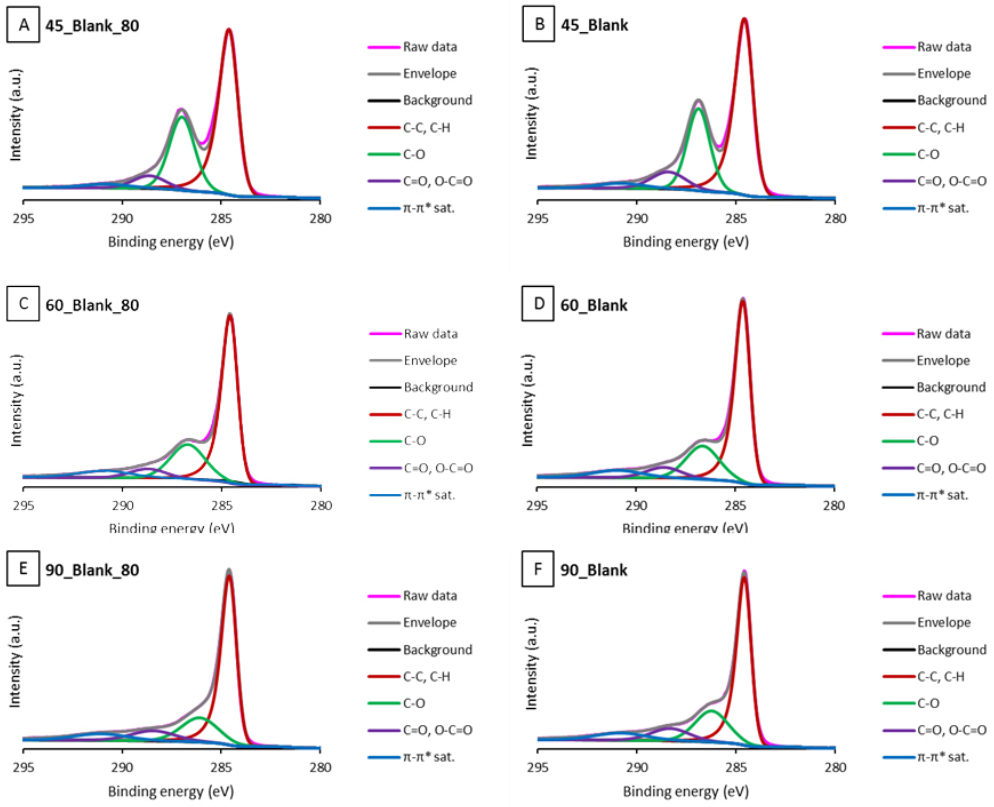

Figure 4.18. High-resolution C 1s XPS spectra of (A) 45_Blank_80, (B) 45_Blank, (C) 60_Blank_80, (D) 60_Blank, (E) 90_Blank_80, and (F) 90_Blank.

Table 4.6 presents the exact position of the peaks and the corresponding binding energies, as well as the assignment of the peaks and relative fraction of each of the functional groups within the respective monoliths. The trace quantities of N and Si observed in the samples are not shown in Table 4.6. The concentrations of both C and O show that in all cases the monoliths produced by avoiding the pre-treatment have more oxidized surfaces, thus, they are richer in oxygen functional groups. Moreover, the XPS spectra shows that there is π-π

interactions established between the individual graphene sheets, the quantity of which increased in the structures produced at higher temperatures.

Table 4.6. XPS data for 45_Blank_80, 45_Blank, 60_Blank_80, 60_Blank, 90_Blank_80, and 90_Blank.

Sample	Cycle	Groups	Biding energy (eV)	Conc. %	Conc. %
45_Blank_80	C	C-C, C-H	284.6	39.9	74.0
		C-O	287.0	25.5	
		C=O, O-C=O	288.6	5.7	
		π-π* sat.	290.8	2.5	
		π-π* sat.	293.9	0.3	
	O	O-C=O, C=O	531.2	3.2	23.5
		C-OH	532.8	19.3	
		C-O-C	535.0	0.9	
45_Blank	C	C-C, C-H	284.6	39.1	74.6
		C-O	286.9	24.1	
		C=O, O-C=O	288.4	7.6	
		π-π* sat.	290.8	3.1	
		π-π* sat.	293.8	0.7	
	O	O-C=O, C=O	531.2	2.1	24.7
		C-OH	532.9	21.7	
		C-O-C	535.1	0.9	
60_Blank_80	C	C-C, C-H	284.6	44.9	80.4
		C-O	286.7	21.7	
		C=O, O-C=O	288.7	6.3	
		π-π* sat.	290.9	6.0	
		π-π* sat.	294.0	1.6	
	O	O-C=O, C=O	531.2	2.5	17.9
		C-OH	532.8	14.5	
		C-O-C	535.6	0.9	
60_Blank	C	C-C, C-H	284.6	47.3	83.1

		C-O	286.7	20.4	
		C=O, O-C=O	288.6	7.1	
		π-π* sat.	290.9	6.4	
		π-π* sat.	293.9	1.9	
	O	O-C=O, C=O	531.3	3.3	
		C-OH	532.9	11.0	15.2
		C-O-C	535.3	0.9	
90_Blank_80	C	C-C, C-H	284.6	50.1	
		C-O	286.1	18.7	
		C=O, O-C=O	288.4	9.1	87.3
		π-π* sat.	291.1	7.6	
		π-π* sat.	294.1	1.7	
	O	O-C=O, C=O	531.5	3.9	
		C-OH	533.2	6.8	11.7
		C-O-C	535.6	1.0	
90_Blank	C	C-C, C-H	284.6	44.2	
		C-O	286.2	20.4	
		C=O, O-C=O	288.3	9.1	82.6
		π-π* sat.	290.8	7.1	
		π-π* sat.	293.9	1.7	
	O	O-C=O, C=O	531.4	4.8	
		C-OH	533.1	9.7	15.8
		C-O-C	535.4	1.4	

The concentration of C and O in the monoliths presented in Table 4.6 demonstrates that certainly the reduction temperature affects in the oxygen-containing moieties, as already observed by TGA measurements. By increasing the reduction temperature from 45 °C to 90 °C, the quantity of residual functional groups in the monoliths decreases, i.e., there is greater recuperation of the sp^2 hybridized carbons in monoliths synthesized at higher temperatures. The pre-treated GO resulted in less functionalization than the monoliths produced from non-pre-

treated GO, except the monoliths synthesized at 60 ºC for which the effect is just opposite. Except that the surface was more oxidized, there was no significant variation of the relative quantities of different oxygen functional groups that might contribute to the increased N_2-phobicity observed in the monoliths produced without pre-treatment.

Beside the functionalized surface, the interaction with CO_2 and N_2 molecules can be eventually be affected by the surface morphology. To obtain more details on the surface morphology of the monoliths, or with other word, to check how the pre-treatment affects the GO morphology, AFM was used to survey the surface. For that aim, the couple of monoliths obtained either with or without pre-treatment that presented the highest difference in CO_2/N_2 selectivity, 90_Blank_80 and 90_Blank were selected for analysis. The AFM height images of both are shown in Figure 4.19.

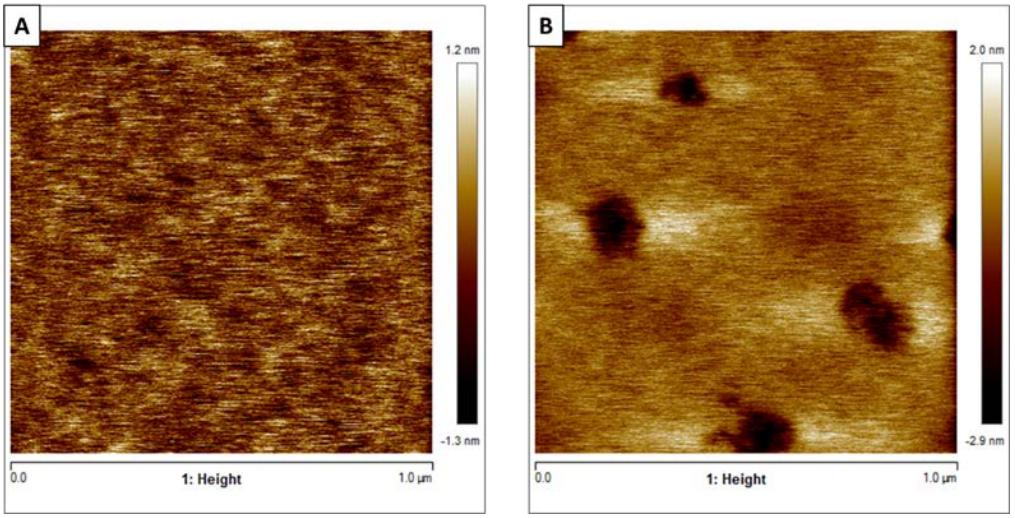

Figure 4.19. AFM images for pre-treated 90_Blank_80 (A) and non-treated 90_Blank (B) 3D structures.

Indeed, Figure 4.19 shows that there is important difference in the surface morphology of the pre-treated (Figure 4.19A) and non-treated (Figure 4.19B), as the former seems to be much less rough (according to the nm scale along the image). Moreover, it possesses higher number of smaller pores (the darker structures) than the monolith obtained without pre-treatment, shown in Figure 4.19B, in accordance to the results presented in Table 4.1. These images are neither conclusive why the non-treated monoliths are more selective. Taking into account that actually the rGO walls that create the porous structure of the monoliths provide the area for interactions with the gasses, it was thought that the roughness of the walls can affect the preference for the gas to be adsorbed. Nevertheless, the images shown in Figure 4.19 are not clear enough to measure the surface roughness. As well, the presence of pores may affect the results.

Furthermore, it was decided to study how the pre-treatment process at 80 ºC affects the morphology of the rGO platelets, that afterwards formed the structure. For that aim, GO dispersions original and pre-treated were chemically reduced at room temperature. Increasing temperature was avoided, as it will produced the monolith structure formation. In Figures 4.20A-D, AFM images of rGO layers are presented at different magnifications. The main difference between the pre-treated and not-treated is that the last have brighter surface, indicating stiffer material. The stiffness is likely induced by the oxygen functional groups, which are denser on the non-treated material.

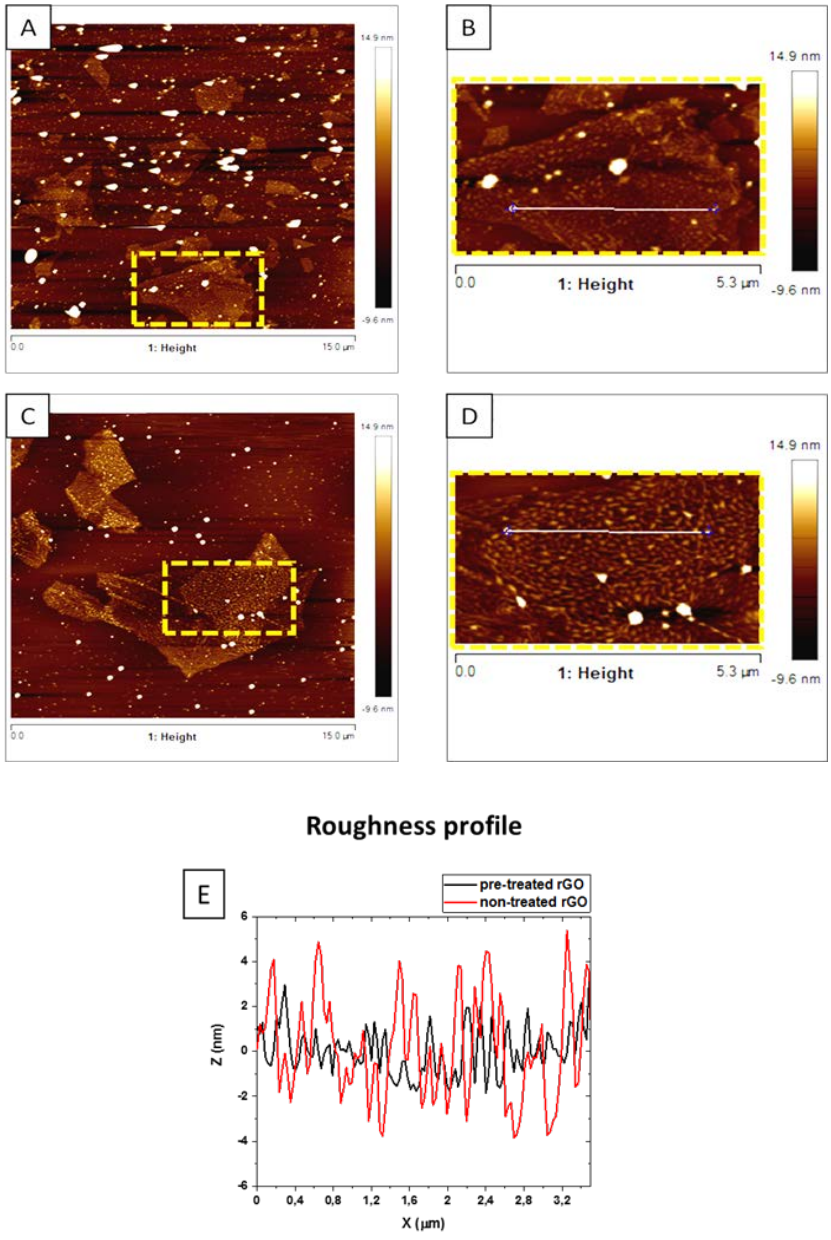

Figure 4.20. AFM images for pre-treated rGO (A and B) and non-treated rGO (C and D). The surface roughness profile is plotted in Figure E, obtained throughout the white line from enlarged images B and D.

Figure 4.20E presents the roughness profiles for both pre-treated and non-pre-treated platelets. The surface roughness profile of both type of platelets was determined along the white lines shown in Figure 4.20B and D. As in the Figure 4.20E can be observed, the non-treated rGO (red profile line in Figure 4.20E) is much more wrinkled than the pre-treated rGO, which presented flatter surface. As this analysis is rather random, we have performed it in multiple images and in each image in multiple points, obtaining always the same output, the non-treated platelets are rougher than the treated ones. In Figures 4.21 to 4.23, some of these images are show, presenting the same observed tendency.

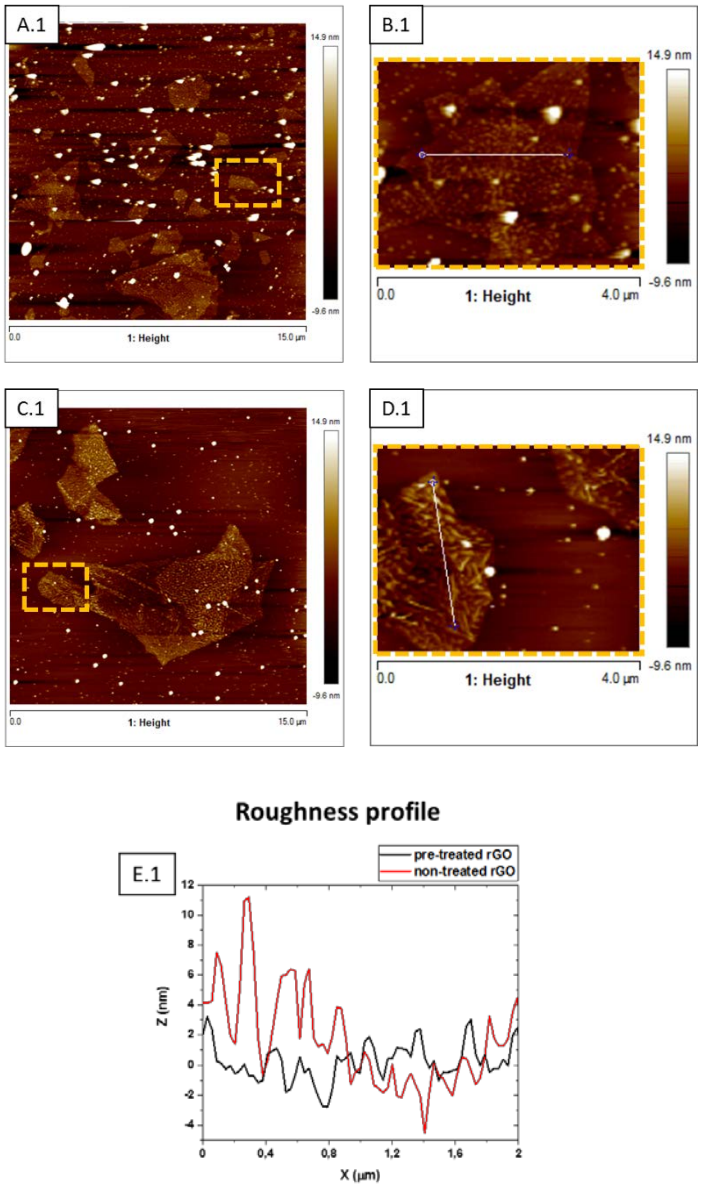

Figure 4.21. AFM images for pre-treated GO (A .1 and B.1) and non-treated rGO (C.1 and D.1). The surface roughness profile is plotted in Figure E, obtained throughout the white line from enlarged images B.1 and D.1.

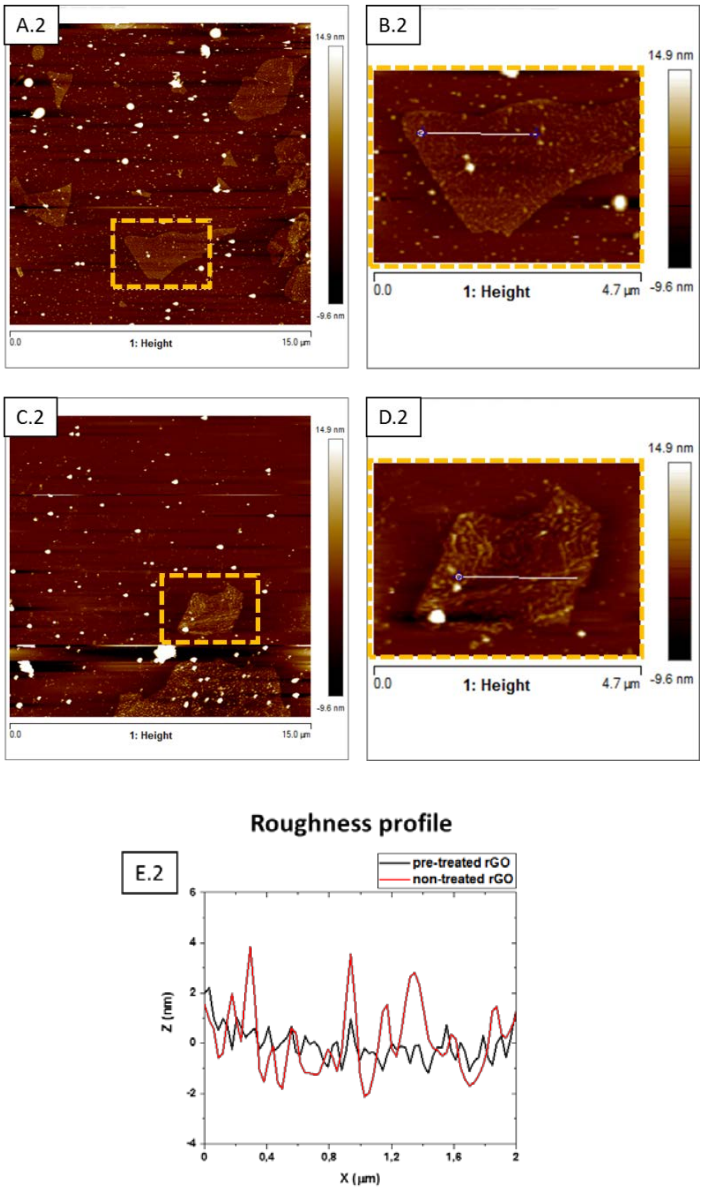

Figure 4.22. AFM images for pre-treated GO (A .2 and B.2) and non-treated rGO (C.2 and D.2). The surface roughness profile is plotted in Figure E, obtained throughout the white line from enlarged images B.2 and D.2.

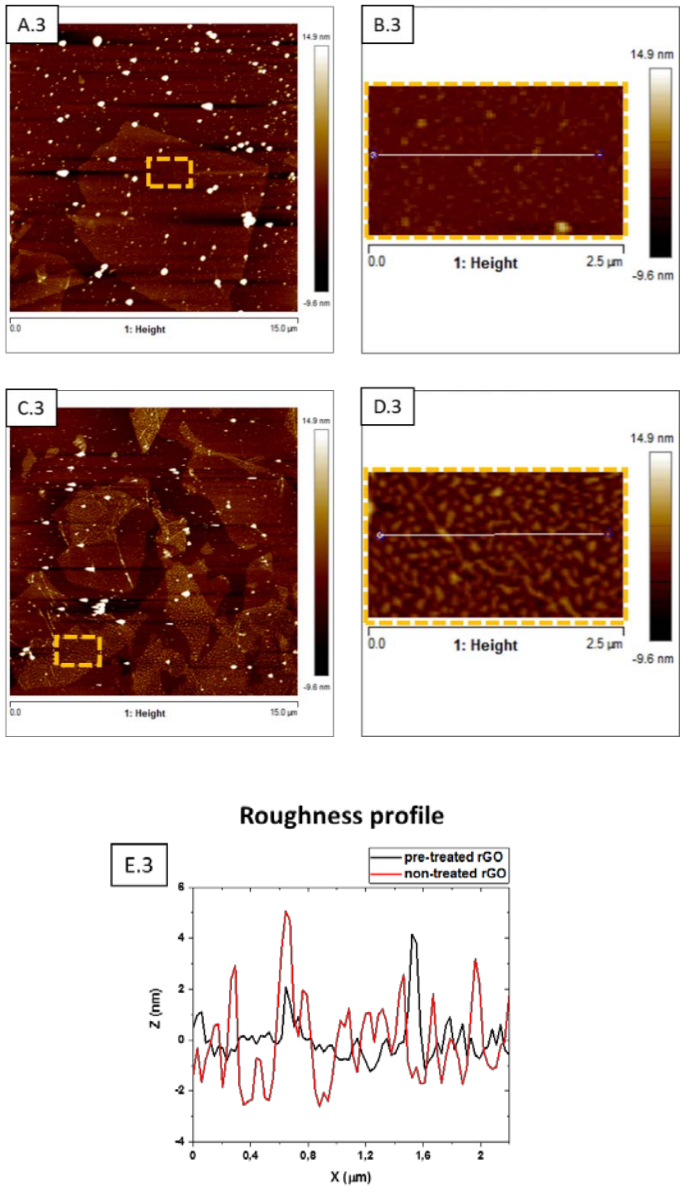

Figure 4.23. AFM images for pre-treated GO (A .3 and B.3) and non-treated rGO (C.3 and D.3). The surface roughness profile is plotted in Figure E, obtained throughout the white line from enlarged images B.3 and D.3.

These results are in accordance with previously reported findings that increase in surface roughness of large graphene and GO platelets is related with increased oxidation.[24] Moreover, the wrinkled graphene structures obtained by surface treatment of graphene using KOH, has been associated with increased adsorption sites for hydrophobic pollutants adsorption.[25] Similar treatments with strong acids or bases of the graphene have been used often to chemically activate the graphene sheets, often followed by thermal activation at high temperatures that usually managed to improve the CO_2 capture.[26,27] Nevertheless, to the best of authors knowledge, the increasing of the wrinkling and roughness of the platelets (of carbon-based nanomaterials in general) has not been related with the applied activation treatment and subsequently with the adsorption performance.

Considering that the N_2 adsorption quantities (Figures 4.7 and 4.13) were much higher on the pre-treated materials, and that the density of surface oxidation affected rather CO_2 adsorption than that of N_2, one may conclude that the flatter graphenic surface provides better platform for N_2 adsorption. Likely, rougher and irregular is the surface, as these produced by avoiding the pre-treatment, less N_2-philic material is produced.

It has been demonstrated that the wrinkles are intrinsic structuration encountered onto graphene platelets, created by the total free energy minimization,[28] which has been intensified by thermal treatment that induced folding of the platelets.[25,29] These outcomes explains well the behaviour of the present monoliths. Namely, when produced by chemical reduction performed at 90 ºC from non-treated GO, the monoliths are likely even more rough and wrinkled than these presented in Figures 4.20-4.23, due to the higher temperature applied, which corresponds to the impressive enhancement of CO_2/N_2 selectivity, observed for all monoliths (neat and composite) produced at 90 ºC.

The topic of CO_2 adsorption by carbon-based materials has been a standpoint from the first signs of climate change, which is mostly based on the understanding of the adsorbate-adsorbent interactions with the aim to identify the adsorption keys, and synthesized an adsorbent that fulfil the requirements to be implemented in CCS. However, CCS post-combustion CO_2 capture requires adsorbents with high selectivity of CO_2 over N_2, and there is a lack information in the reported literature about N_2-phobic spot that could not only increases the adsorption performance but also decreases the capture cost. Thus, this work opens a new point of view of N_2-philicity in carbon-based monolithic structures based on the surface roughness of the graphene layers.

4.4. Conclusions

In this study, porous monolithic CO_2 adsorbents were prepared, based on 3D graphene and graphene-polymer structures, for potential use in CCS post-combustion technology. The monolithic materials were synthesized by combined chemical and thermal reduction of single-layer GO platelets in aqueous dispersions, performed at 45, 60 and 90 ºC. During this process, the rGO and rGO-polymer flakes were self-assembled, building the 3D porous monoliths. The main aim of this work was, by manipulation of the synthesis procedure, to rise the CO_2/N_2 selectivity, as important parameter that affects significantly the costs of the CCS process. The selectivity elevation was projected through increase of the fraction of the oxygen functional groups and that of the small mesopores within the rGO-based monoliths.

Certainly, the modified synthesis procedure induced rise of the fraction of oxygen functionalities and increase of the microporosity, resulting in higher CO_2 and lower N_2 adsorption capacities in most of the monoliths. This effect was huge for the monoliths produced at the

highest temperature (90 ºC), resulting in rise of CO_2/N_2 selectivity to values of 470–621, which is more than one order of magnitude higher than the monoliths produced without modification of the synthesis method. Moreover, the selectivity values achieved in this work are far higher than all the reported values for carbon based nanomaterial adsorbents to the best of authors' knowledge. The rise of the CO_2 adsorption was attributed to the increase of the functionalization while decreasing the BET area, resulting in densely functionalized surface. Nevertheless, the experimental results have shown that the observed changes in the characteristics of the monoliths produced with the modified synthesis method could not explained the rise of N_2-phobicity.

The attempts to obtain deeper understanding on the issue have revealed that by modified synthesis procedure, the surface morphology of the graphene platelets was impacted, producing rougher and more wrinkled surface, which likely induce less N_2 adsorption. On the other hand, the highly wrinkled and densely functionalized surface of the monoliths likely offered more adsorption sites to CO_2 molecules, resulting in the outstanding selectivity attained. The production temperature affects even more the winking and folding of graphene platelets, which explains the excellent results obtained at 90 ºC.

To the best of the authors' knowledge, this is the first study that associates the increasing of wrinkling and roughness of the platelets (or carbon-based nanomaterials in general) with N_2-phobicity and selectivity of CO_2 adsorbents. It offers new viewpoints for improvement of the selectivity of C-based nanomaterials adsorbents for application in post-combustion CCS.

4.5. References

(1) Park, J.; Cho, S. Y.; Jung, M.; Lee, K.; Nah, Y. C.; Attia, N. F.; Oh, H. Efficient Synthetic Approach for Nanoporous Adsorbents Capable of Pre-and Post-Combustion CO2capture and Selective Gas Separation. *J. CO2 Util.* **2021**, *45* (December 2020), 101404.

(2) Qiao, Z.; Wang, Z.; Zhang, C.; Yuan, S.; Zhu, Y.; Wang, J. PVAm–PIP/PS Composite Membrane with High Performance for CO2/N2 Separation. *AIChE J.* **2012**, *59* (4), 215–228.

(3) Oschatz, M.; Antonietti, M. A Search for Selectivity to Enable CO2 Capture with Porous Adsorbents. *Energy Environ. Sci.* **2018**, *11* (1), 57–70.

(4) Zhao, Y.; Liu, X.; Han, Y. Microporous Carbonaceous Adsorbents for CO2 Separation via Selective Adsorption. *RSC Adv.* **2015**, *5* (38), 30310–30330.

(5) Belmabkhout, Y.; Guillerm, V.; Eddaoudi, M. Low Concentration CO2 Capture Using Physical Adsorbents: Are Metal-Organic Frameworks Becoming the New Benchmark Materials? *Chem. Eng. J.* **2016**, *296*, 386–397.

(6) Ho, M. T.; Allinson, G. W.; Wiley, D. E. Reducing the Cost of CO2 Capture from Flue Gases Using Pressure Swing Adsorption. *Ind. Eng. Chem. Res.* **2008**, *47* (14), 4883–4890.

(7) Ma, X.; Su, C.; Liu, B.; Wu, Q.; Zhou, K.; Zeng, Z.; Li, L. Heteroatom-Doped Porous Carbons Exhibit Superior CO2 Capture and CO2/N2 Selectivity: Understanding the Contribution of Functional Groups and Pore Structure. *Sep. Purif. Technol.* **2021**, *259* (September), 118065.

(8) Liang, W.; Liu, Z.; Peng, J.; Zhou, X.; Wang, X.; Li, Z. Enhanced CO 2 Adsorption and CO 2 /N 2 /CH 4 Selectivity of Novel Carbon Composites CPDA@A-Cs. *Energy and Fuels* **2019**, *33* (1), 493–502.

(9) Alabadi, A. A.; Abbood, H. A.; Dawood, A. S.; Tan, B. Ultrahigh-CO2 Adsorption Capacity and CO2/N2 Selectivity by Nitrogen-Doped Porous Activated Carbon Monolith. *Bull. Chem. Soc. Jpn.* **2020**, *93* (3), 421–426.

(10) Wu, Y.; Wang, J.; Muhammad, Y.; Subhan, S.; Zhang, Y.; Ling, Y.; Li, J.; Zhao, Z.; Zhao, Z. Pyrrolic N-Enriched Carbon Fabricated from Dopamine-Melamine via Fast Mechanochemical Copolymerization for Highly Selective Separation of CO2 from CO2/N2. *Chem. Eng. J.* **2018**, *349*, 92–100.

(11) Ning, H.; Yang, Z.; Wang, D.; Meng, Z.; Li, Y.; Ju, X.; Wang, C. Graphene-Based Semi-Coke Porous Carbon with N-Rich Hierarchical Sandwich-like Structure for Efficient

Separation of CO2/N2. *Microporous Mesoporous Mater.* **2021**, *311* (October 2020), 110700.

(12) Li, Q.; Liu, S.; Wang, L.; Chen, F.; Shao, J.; Hu, X. Efficient Nitrogen Doped Porous Carbonaceous CO2 Adsorbents Based on Lotus Leaf. *J. Environ. Sci. (China)* **2021**, *103*, 268–278.

(13) Yue, L.; Rao, L.; Wang, L.; An, L.; Hou, C.; Ma, C.; Dacosta, H.; Hu, X. *Efficient CO2 Adsorption on Nitrogen-Doped Porous Carbons Derived from d -Glucose*; 2018; Vol. 32.

(14) An, L.; Liu, S.; Wang, L.; Wu, J.; Wu, Z.; Ma, C.; Yu, Q.; Hu, X. *Novel Nitrogen-Doped Porous Carbons Derived from Graphene for Effective CO 2 Capture*; 2019; Vol. 58.

(15) Wang, S.; Zhang, Z.; Dai, S.; Jiang, D. E. Insights into CO2/N2Selectivity in Porous Carbons from Deep Learning. *ACS Mater. Lett.* **2019**, *1* (5), 558–563.

(16) Wang, S.; Li, Y.; Dai, S.; Jiang, D. en. Prediction by Convolutional Neural Networks of CO2/N2 Selectivity in Porous Carbons from N2 Adsorption Isotherm at 77 K. *Angew. Chemie - Int. Ed.* **2020**, *59* (44), 19645–19648.

(17) Lee, J. H.; Lee, H. J.; Lim, S. Y.; Kim, B. G.; Choi, J. W. Combined CO2-Philicity and Ordered Mesoporosity for Highly Selective CO2 Capture at High Temperatures. *J. Am. Chem. Soc.* **2015**, *137* (22), 7210–7216.

(18) Orr, P. A. W. C. *Analytical Methods in Fine Particle Technology*; Micromeritics, 1997.

(19) Pan, Y.; Xue, M.; Chen, M.; Fang, Q.; Zhu, L.; Valtchev, V.; Qiu, S. ZIF-Derived: In Situ Nitrogen Decorated Porous Carbons for CO2 Capture. *Inorg. Chem. Front.* **2016**, *3* (9), 1112–1118.

(20) Chandra, V.; Yu, S. U.; Kim, S. H.; Yoon, Y. S.; Kim, D. Y.; Kwon, A. H.; Meyyappan, M.; Kim, K. S. Highly Selective CO2 Capture on N-Doped Carbon Produced by Chemical Activation of Polypyrrole Functionalized Graphene Sheets. *Chem. Commun.* **2012**, *48* (5), 735–737.

(21) Chowdhury, S.; Balasubramanian, R. Highly Efficient, Rapid and Selective CO2 Capture by Thermally Treated Graphene Nanosheets. *J. CO2 Util.* **2016**, *13*, 50–60.

(22) Chowdhury, S.; Balasubramanian, R. Holey Graphene Frameworks for Highly Selective Post-Combustion Carbon Capture. *Sci. Rep.* **2016**, *6* (December 2015), 1–10.

(23) Chowdhury, S.; Balasubramanian, R. Three-Dimensional Graphene-Based Porous Adsorbents for Postcombustion CO2 Capture. *Ind. Eng. Chem. Res.* **2016**, *55* (29), 7906–7916.

(24) Peng, E.; Todorova, N.; Yarovsky, I. Effects of Size and Functionalization on the Structure and Properties of Graphene Oxide Nanoflakes: An in Silico Investigation. *ACS Omega* **2018**, *3* (9), 11497–11503.

(25) Wang, J.; Chen, B.; Xing, B. Wrinkles and Folds of Activated Graphene Nanosheets as Fast and Efficient Adsorptive Sites for Hydrophobic Organic Contaminants. *Environ. Sci. Technol.* **2016**, *50* (7), 3798–3808.

(26) Vargas, D. P.; Balsamo, M.; Giraldo, L.; Erto, A.; Lancia, A.; Moreno-Piraján, J. C. Equilibrium and Dynamic CO2 Adsorption on Activated Carbon Honeycomb Monoliths. *Ind. Eng. Chem. Res.* **2016**, *55* (29), 7898–7905.

(27) Ma, X.; Li, Y.; Cao, M.; Hu, C. A Novel Activating Strategy to Achieve Highly Porous Carbon Monoliths for CO2 Capture. *J. Mater. Chem. A* **2014**, *2* (13), 4819–4826.

(28) Meyer, J. C.; Geim, A. K.; Katsnelson, M. I.; Novoselov, K. S.; Booth, T. J.; Roth, S. The Structure of Suspended Graphene Sheets. *Nature* **2007**, *446* (7131), 60–63.

(29) Wei, Y.; Wu, J.; Yin, H.; Shi, X.; Yang, R.; Dresselhaus, M. The Nature of Strength Enhancement and Weakening by Pentagong-Heptagon Defects in Graphene. *Nat. Mater.* **2012**, *11* (9), 759–763.

(30) J.C. de la Cal, J.R. Leiza, J.M. Asua, A. Butte, G. Storti, M. M. Handbook of Polymer Reaction Engineering; Wiley-VCH, 2005; pp 249–322.

(31) Ji, C. C.; Xu, M. W.; Bao, S. J.; Cai, C. J.; Lu, Z. J.; Chai, H.; Yang, F.; Wei, H. Self-Assembly of Three-Dimensional Interconnected Graphene-Based Aerogels and Its Application in Supercapacitors. *J. Colloid Interface Sci.* **2013**, *407*, 416–424.

(32) Öner, E.; Öztürk, A.; Yurtcan, A. B. Utilization of the Graphene Aerogel as PEM Fuel Cell Catalyst Support: Effect of Polypyrrole (PPy) and Polydimethylsiloxane (PDMS) Addition. *Int. J. Hydrogen Energy* **2020**, *45* (60), 34818–34836.

(33) Singh, G.; Ramadass, K.; Lee, J. M.; Ismail, I. S.; Singh, M.; Bansal, V.; Yang, J. H.; Vinu, A. Convenient Design of Porous and Heteroatom Self-Doped Carbons for CO2 Capture. *Microporous Mesoporous Mater.* **2019**, *287* (April), 1–8.

(34) Sui, Z. Y.; Han, B. H. Effect of Surface Chemistry and Textural Properties on Carbon Dioxide Uptake in Hydrothermally Reduced Graphene Oxide. *Carbon N. Y.* **2015**, *82* (C), 590–598.

(35) Meconi, G. M.; Tomovska, R.; Zangi, R. Adsorption of CO 2 Gas on Graphene-Polymer Composites. *J. CO2 Util.* **2019**, *32* (March), 92–105.

(36) Ho, M. T.; Allinson, G. W.; Wiley, D. E. Reducing the Cost of CO2 Capture from Flue

Gases Using Pressure Swing Adsorption. *Ind. Eng. Chem. Res.* **2008**, *47* (14), 4883–4890.

(37) Web Page. https://scitechdaily.com/cheaper-carbon-capture-is-on-the-way-marathon-research-effort-drives-down-cost/ (accessed Feb 22, 2022).

(38) Jiang, Y.; Mathias, P. M.; Freeman, C. J.; Swisher, J. A.; Zheng, R. F.; Whyatt, G. A.; Heldebrant, D. J. Techno-Economic Comparison of Various Process Configurations for Post-Combustion Carbon Capture Using a Single-Component Water-Lean Solvent. *Int. J. Greenh. Gas Control* **2021**, *106* (January), 103279.

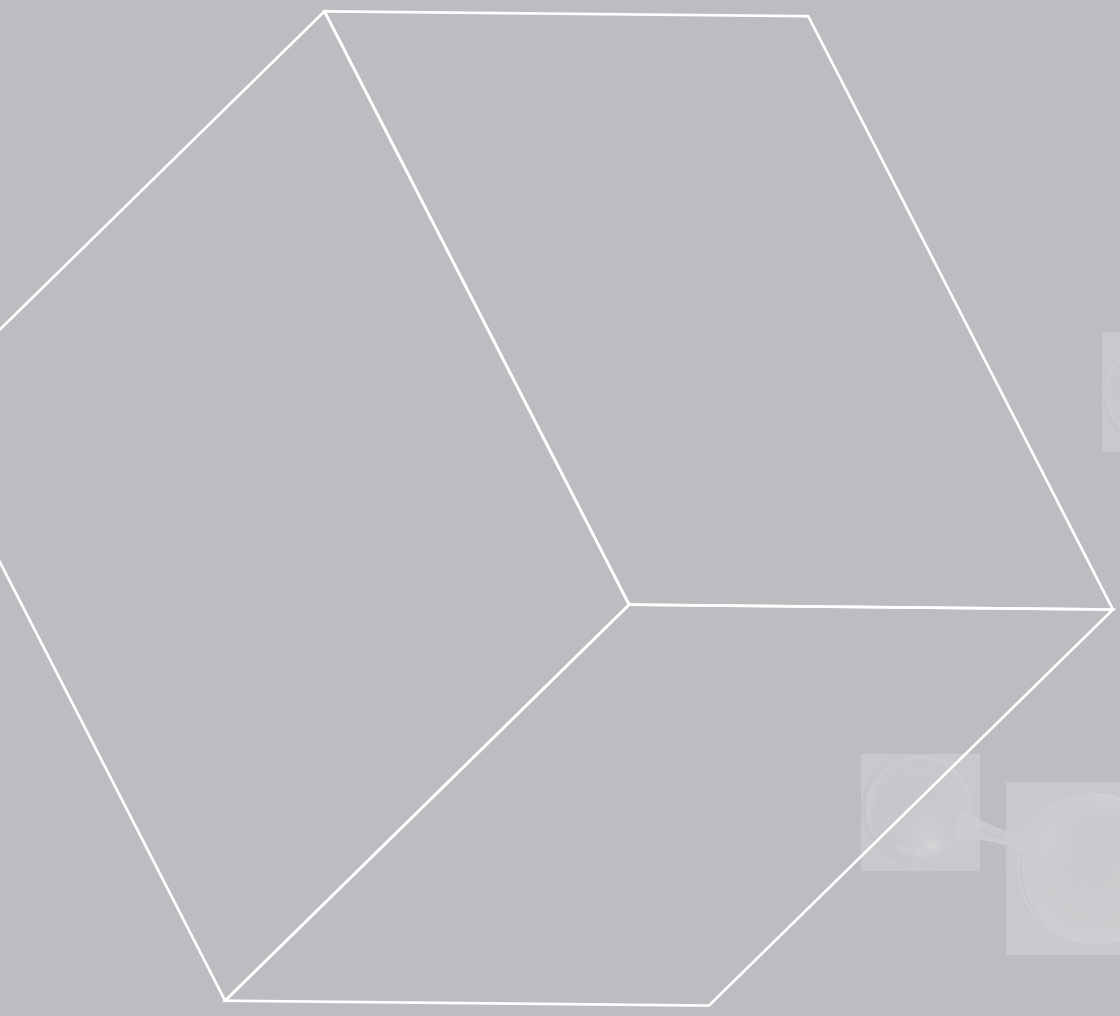

CHAPTER 5

Tailoring of textural properties of 3D composite monoliths made of graphene and highly crosslinked polymer particles towards improved CO_2 sorption

Chapter 5. Tailoring of textural properties of 3D composite monoliths made of graphene and highly crosslinked polymer particles towards improved CO_2 sorption

5.1. Introduction

Chapter 3 and Chapter 4 were devoted to the study of the influence of the addition of functionalized polymer particles to the 3D graphene skeleton how impacts on the morphology and textural properties, and on adsorption performance. Nevertheless, as explained in the literature survey in Chapter 1, apart from affinity-based separation, size exclusion or molecular sieving mechanism is another alternative to enhance the combination between the adsorbate, CO_2 gas, and adsorbent, 3D monolith. This mechanism based on the idea that CO_2 gas molecules with the size larger than the width of the pores of the 3D adsorbent are refused, whereas gas molecules with smaller size than the pores are adsorbed making the fractionation possible.[1] However, the critical limitation of 3D carbon-based adsorbents is the appropriate control over the pore size and pore size distribution, especially in the micropore and small mesopores size regions, which may be dominant for CO_2 adsorption.[2]

As a consequence, the interest in porous organic polymers (POPs) as alternative CO_2 adsorbents, is growing rapidly, due to their proper control of pore width and permanent porosity that make them promising materials for adsorption performance by molecular sieve effect.[3] Mostly, the permanent porosity proceed from wide chemical crosslinks between polymer chains

that prevent their complete collapsing, achieving a porous state.[4] To date, a range of different POPs has emerged, such as polymers of intrinsic microporosity, covalent triazine frameworks, and hypercrosslinked porous polymers.[5,6] For example, hypercrosslinked porous polymers are mainly prepared via Friedel-Crafts alkylation routes, result in surface areas up to 2090 m^2/g.[7] Nevertheless, one of the disadvantages of microporous organic polymers is the diffusion limitation of the adsorbing gas due to the small pores. The diffusion will be very slow when the pore size is similar to the kinetic diameter of the CO_2 molecule.[8] Besides, in most of the cases, the synthetic approaches are environmentally unfriendly as high temperature are required, noble-metal catalysts, and the use of organic solvents.[9]

In this chapter, in order to take advantages and to overcome the drawbacks of both 3D graphene-based structures and crosslinked polymers, hybrid structures made of 3D graphene-crosslinked polymer were synthesized. Due to the consistent mesoporous textural properties and high surface area, functionalized surface rich in oxygen functional groups, and relatively high CO_2 adsorption, the 3D graphene-based monolithic materials provide an excellent 3D adsorption platform. On the other hand, crosslinked polymers will increase further the available surface area by providing micro- and mesoporosity induced by stable covalent crosslinked structure. Moreover, to avoid high-energy consuming processes and the use of volatile organic compounds in the synthesis of crosslinked polymers, polymerization in aqueous dispersed media was employed.

5.2. Experimental part

5.2.1. Materials

Graphene oxide aqueous dispersion (GO) of 4 mg/mL was used as supplied from Graphenea. L-Ascorbic acid (AsA, ≥99%, Sigma-Aldrich) was used as chemical reducer. Technical monomers methyl methacrylate (MMA, Quimidroga), and divinylbenezene (DVB, 80 % mixture of isomers, Alfa Aesar) were used without purification. Potassium persulfate (KPS, ≥99 %, Sigma-Aldrich), sodium dodecyl sulfate (SDS, Sigma-Aldrich), and sodium bicarbonate ($NaHCO_3$, Sigma-Aldrich) were used as received. In all polymerization reactions, deionized water was used.

5.2.2. Synthesis of crosslinked polymer particles

Different degree of crosslinked MMA polymer particles were synthesized by seeded semibatch emulsion polymerization process. DVB monomer was used as a crosslinker (0.2 mol%, 2 mol% and 4 mol% with respect to MMA). The reactions were carried out in glass reactor equipped with a nitrogen inlet, a reflux condenser, a thermocouple, a sampling tube, and a stainless steel anchor-type stirrer. The reaction temperature was managed by an automatic control system (Camille TG, Biotage).

The recipe used for the synthesis of the latexes is shown in Table 5.1 (for 0.2 mol% DVB). First, a seed with 20 % solid content of MMA was synthesized by batch emulsion polymerization. A pre-emulsion was prepared by mixing MMA into aqueous solution of surfactant (SDS) and buffer ($NaHCO_3$), and loaded in the reactor, followed by addition of water soluble initiator (KPS). The reaction mixture was let to react for 2 h. Afterwards, the monomer mixture (MMA and DVB), emulsifier (SDS), buffer ($NaHCO_3$), and initiator (KPS) aqueous solution were fed for 3 h in two

independent streams (F1 and F2, see Table 5.1). At the end of the feeding, the reaction mixture was allowed to react for 30 min batchwise to ensure complete monomer consumption. The reactions were carried out under N_2 atmosphere at 70 °C and under stirring with 200 rpm. With this procedure, latexes with final solids content of 30 % were prepared.

Table 5.1. Formulation employed for the synthesis of the Blank and 0.2 mol% DVB containing latexes.

Material		Seed (g)	MMA (g)	DVB (g)	SDS (g)	KPS (g)	$NaHCO_3$ (g)	H_2O (g)
Seed		-	80	-	1.6	0.4	0.4	320
Blank MMA	Inital charge	20.8	-	-	0.085	0.078	-	32.1
	F1	-	117	-	1.43	-	0.65	205
	F2	-	-	-	-	0.275	-	11.6
0.2% MMA-DVB	Inital charge	20.8	-	-	0.085	0.078	-	32.1
	F1	-	117	0.32	1.43	-	0.65	205
	F2	-	-	-	-	0.275	-	11.6

5.2.3. Synthesis of 3D rGO/polymer hybrid structures

The synthesis of the 3D rGO/polymer hybrid structures was based on the previously explained method. First, 40 mL of GO aqueous dispersion was sonicated at 25 °C for 1 h. Then, the dispersion was stirred for 2.5 h at 80 °C. Pre-treated GO aqueous dispersion was mixed with the proper amount of latex for 2 h at room temperature to obtain polymer content of 10 % and 40 % in the hybrid structures. Subsequently, AsA reducing agent was added (GO:AsA mass ratio 1:0.5) and stirred for 0.5 h. The sample was then placed in the oven at 90 °C overnight, which resulted in formation of monolithic structures in which all the solids placed in the initial dispersion (polymer and rGO) were incorporated. The monolithic hydrogels were purified by a dialysis using

deionized water. The conductivity of the residual water was by measuring water conductivity until value was lower than 10 µS/cm. Finally, the hydrogel was dried by freeze-drying technique.

5.2.4. Characterization

In terms of polymer characterization, conversion of the monomer and solids content were calculated gravimetrically. The z-average particle size (dz) of the polymer particle was measured by dynamic light scattering (DLS). The gel content (GC %) of the polymer was measured by means of latex centrifugation in THF for 24 h at 4 °C and 15000 rpm conditions. The molar masses of the soluble fractions obtained by centrifugation were measured using size exclusion chromatography (SEC) in THF. On the other hand, crosslinking degree or crosslinking density of the polymer particles were related to the capacity of particles swelling in toluene ($g_{toluene}$ / $g_{polymer}$). The strategy to analyse the swell capacity of the particles was the same described by Morton et al,[10] and by gas chromatograph (GC) the amount of toluene swollen by polymer particles was calculated. The detailed description of the latex characterization methods is given in Section I.1 of Appendix I.

On the other hand, regarding the characterization of the 3D structures, thermogravimetric analysis (TGA) were performed to estimate the amount of residual oxygen-containing functional groups and to study the thermal stability of the 3D monolithic composites. The surface morphology of the structures was examined using a SEM and TEM techniques. The porous texture of the monoliths was characterized by means of N_2 adsorption-desorption isotherm at -196 °C in a Micromeritics ASAP 2020 apparatus. Detailed information of these characterization methods is given in Section I.2 of Appendix I.

The materials´ CO_2 and N_2 gas adsorption capacities were measured from their isotherms, measured using a Micromeritics ASAP 20220 Analyzer (i.e. volumetrically) at 1 atm and 25 °C. Detailed information of these gas adsorption measurement is given in Section I.3 of Appendix I.

5.3. Results and discussion

5.3.1. Characteristics of polymer particles

Four different polymer particle dispersions were synthesized with an aim of studying the influence of the crosslinking degree over the BET surface area on CO_2 capture capacity of the final hybrid monoliths. MMA was copolimerized by free radical emulsion polymerization technique with different molar fraction of DVB crosslinker: 0 mol% (denoted as Blank MMA), 0.2 mol% (0.2 % DVB-MMA), 2 mol% (2 % DVB-MMA), and 4 mol% (4 % DVB-MMA). The final MMA conversion, particle size, fraction of polymer insoluble in THF solvent (gel content, GC %), molar mass of the soluble polymer fraction, and the particles swelling in toluene of the different polymers are shown in Table 5.2.

Table 5.2. Characteristics of the polymers.

Material	MMA conversion %	z-average particle size (nm)	GC %	sol Mw (kg/mol)	Đ	Particles swelling
Blank MMA	97.2	181	0	438	2.5	0.14
0.2 % DVB-MMA	99.4	198	76	239	2.8	0.12
2 % DVB-MMA	98.1	204	88	59	1.7	0.086
4 % DVB-MMA	97.5	169	85	2	1.1	0.067

In Table 5.2, it can be seen that high MMA conversion was obtained in all cases, resulting in polymer particle aqueous dispersion (latex) with average particle size in a range of 170-200 nm. There was no gel formed in case of neat MMA polymerization (Blank MMA), because of a lack of extractable hydrogens in MMA units, but as well because the disproportionation is predominant termination mechanism of MMA growing chains.[11] By addition of DVB even in such small quantity as 0.2 mol%, 76 % of the polymer was insoluble likely due to crosslinking of the MMA chains induced by DVB. Moreover, by increasing the DVB fraction the gel content was raised up to almost 90 % in 2% DVB-MMA and 4% DVB-MMA polymers. The molar masses of the soluble part decreased by the increasing gel fraction due to incorporation of higher molar mass chains into the gel. The swelling degree shows that by introducing DVB the polymer swelled less solvent, probably because the created crosslinks between the polymer chains decreased their mobility and created a structure that is more compact. Further drop of the swelling degree with the increasing DVB fraction in the polymer is an indication of increased density of the crosslinked points. This fact perfectly explain that, 2% and 4% DVB-MMA latexes have similar gel content, although there is a drop in the swelling degree, which indicates that the crosslinking degree was raised for higher amounts of DVB and that the distance between the crosslink points is lesser in 4% DVB-MMA.

In Figure 5.1, the N_2 adsorption-desorption isotherms are presented, and in Figure 5.2, the pore size distributions are showed for each polymer particle, where the left graphs correspond to dV/dD curve, in which the contribution of smaller pores are pronounced, while the right graphs correspond to dV/dlogD representing the contribution of larger pores.[12] In Table 5.3, the textural properties (BET specific surface area, S_{BET} (m^2/g), total volume of the pores (V_{total}, cm^3/g), area of the micropores (A_{micro}, cm^2/g), and volume of the micropores (V_{micro}, cm^3/g)), and CO_2 adsorption (mmol/g) of the crosslinked freeze-dried polymer particles are presented.

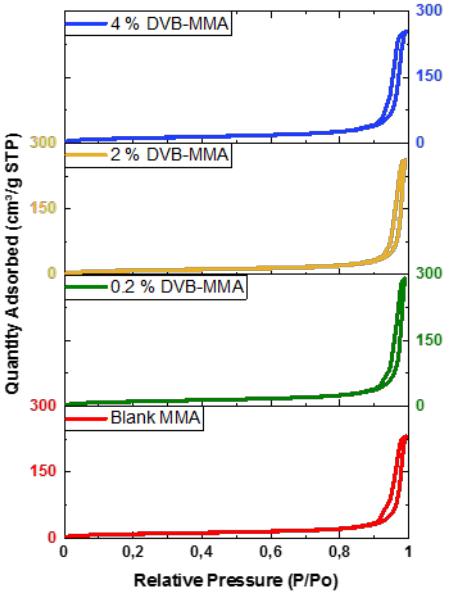

Figure 5.1. N_2 adsorption-desorption isotherms for each polymer particle.

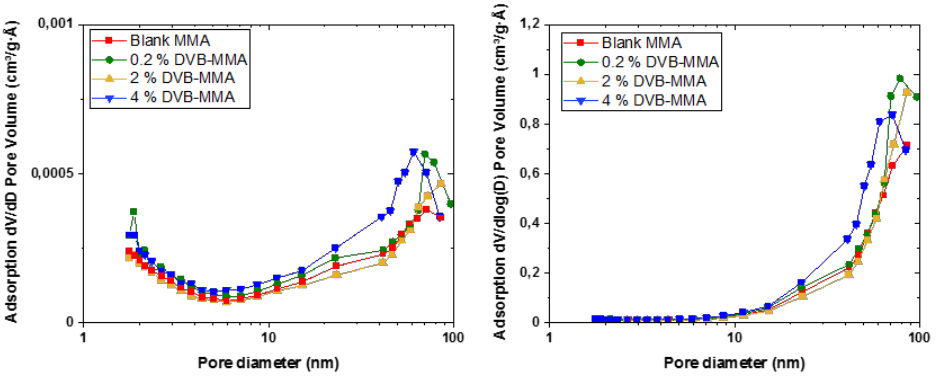

Figure 5.2. Pore size distributions for each polymer particle.

Table 5.3. Textural properties determined from N_2 adsorption-desorption isotherms at -196 ºC and CO_2 adsorption capacities of the polymer particles at 25 ºC and 1 atm.

Material	S_{BET} (m^2/g)	V_{total} (cm^3/g)	A_{micro} (cm^2/g)	V_{micro} (cm^3/g)	CO_2 adsorption (mmol/g)
Blank MMA	34	0.358	< 0.001	< 0.001	0.3
0.2% DVB–MMA	41	0.442	0.860	0.001	0.31
2% DVB-MMA	33	0.405	3.264	0.001	0.31
4% DVB-MMA	42	0.394	5.793	0.002	0.32

MMA was copolymerized with DVB to control the textural properties in terms of microporosity of the polymers particles that could improve the adsorption performance of the resulting monolithic materials. Table 5.3 shows that Blank MMA with 0 % addition of DVB did not present microporosity, due to the more compact packing of the disordered and entanglements of the macromolecular chains. Instead, polymer particles containing DVB present higher surface areas, amount of the total volume of the pores, area of micropores and volume of micropores due to the developed pore structure. The pores are developed due to decreased mobility and packing of the crosslinked chains. By increasing the DVB content, the crosslinked density increased too, as shown by the swelling degree (Table 5.2), due to lower chain length between two crosslinked points, resulting in smaller pores and consequently more developed microporosity, as it is shown in Table 5.3. However, if the volume of micropores is compared with the total pore volume, it might be seen that it is negligible, which is rather strange if one take into account that the polymers containing DVB are more than 80 % crosslinked. Likely, the mesoporous fraction was also increased with the crosslinking density, resulting in similar contribution of the micropores to the porous structure.

To obtain deeper insight to this issue, pore size distributions, presented in Figure 5.2 were studied. Figure 5.2 shows that the fraction of micropores and small mesopores ranging between 1.5–5 nm is similar in all the materials, however the crosslinking introduced by addition of DVB contributed to the augment of the fraction of pores with average diameter at 2 nm, especially for 0.2 and 4 % DVB. The fractions of larger mesopores (20-50 nm) and macropores (50-100 nm) are more significantly different. By increasing the DVB content and crosslinking degree in the polymers, this fraction is larger and is shifted towards smaller size pores, likely due to decreasing the distance between the crosslinked points. Taking into account that MMA free radical emulsion polymerization is characterized by production of large molar masses,[13] which according to Table 5.2 are about 400.000 Da (for Blank MMA), apparently the fraction of meso- and macro pores were significantly raised.

The CO_2 adsorption by these polymer particles is in the range of similar materials.[14] The textural properties did not affected the adsorption capacity significantly, even though slight increase with enhancing the porosity was observed. The CO_2 adsorption–desorption isotherms obtained at 25 ºC and up to 1 bar, presented in Figure 5.3, show linear increase of the adsorbed CO_2 quantity with pressure and large hysteresis loop. The desorption process is much more energy demanding, indicating more stable binding of the CO_2 molecules, which need more energy to desorb, i.e. the gas is not released to the extent corresponding to the thermodynamic equilibrium value. Moreover, the textural properties of the materials may also have contribution to this behaviour, on one hand by the capillary condensation process occurring within the micro- and mesopores and on the other, the specific shape of these pores. According to the chemistry of the polymers, no chemisorption is expected to occur. On the other hand, as the same behaviour is observed in the Blank MMA polymer particles, it is clear indication that the MMA chemistry is responsible for the possible stronger CO_2 binding. It has been demonstrated

theoretically that the ether and ester oxygen in main polymer backbone or in the pending functionalities introduced strong CO_2-philicity through specific binding that are sufficiently large to be important even at room temperature.[15] Bonded in such way, CO_2 molecules would need higher energy for desorption than the purely physisorbed CO_2 molecules by van der Walls interactions, which can explain the large hysteresis observed in CO_2 adsorption-desorption isotherms in Figure 5.3.

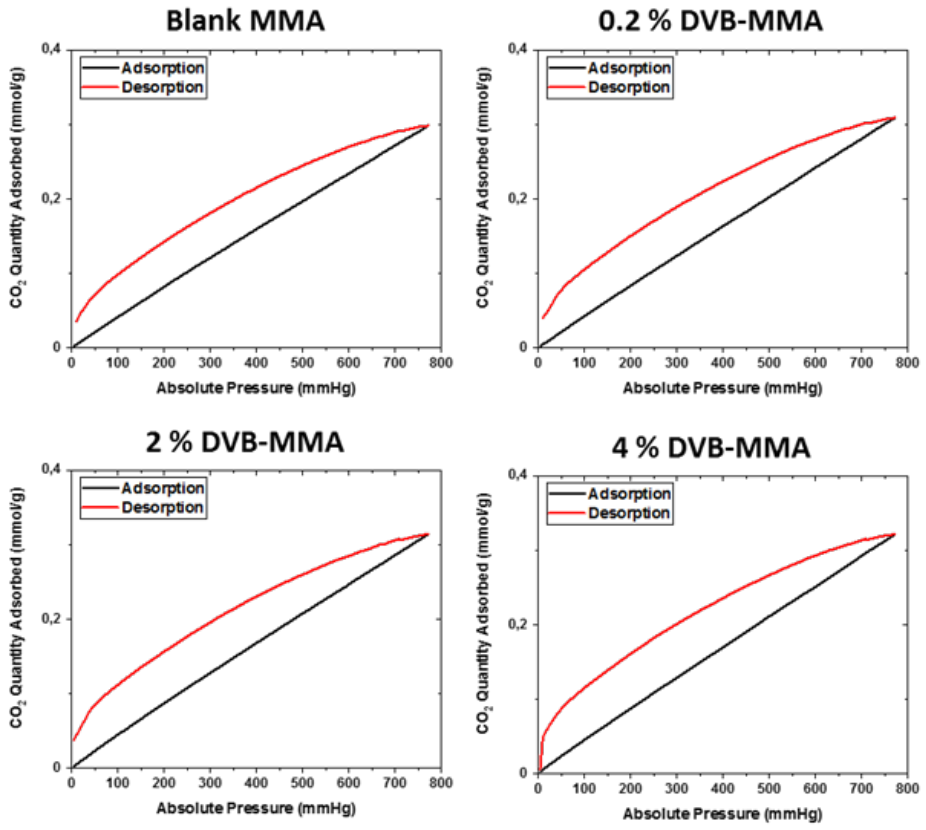

Figure 5.3. CO_2 adsorption-desorption isotherms at 25 °C and 1 atm for each polymer.

5.3.2. Characteristics of 3D monolith structures

To produce the hybrid monoliths, GO aqueous dispersion was mixed with appropriate amount of polymer particles dispersions (10 % and 40 % polymer fraction based on the neat GO weight), during which process the polymer particles are adsorbed onto the GO platelets.[16] Afterwards, the chemical reduction eliminates the oxygen-containing functional groups of GO, and consequently, the hydrophobic character of the reduced graphene oxide (rGO) results in their self-assembly attaining 3D rGO-polymer monolithic structures. For comparison, neat rGO structure was produced, too, by reduction of pure GO aqueous dispersion without addition of polymer particles.

Each of these hybrid materials was analyzed by TGA, to study the thermal properties and to determine the residual amount of oxygen-containing functional groups. In Figure 5.4, the resulting thermographs are shown.

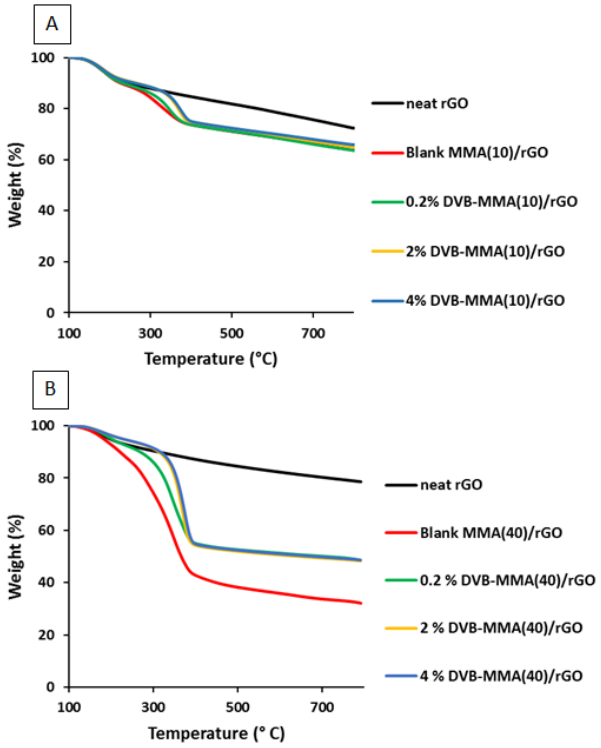

Figure 5.4. TGA thermographs of: (A) monoliths with 10 % polymer; and (B) monoliths with 40 % polymer. In both graphs neat rGO monolith was added for comparison.

The first weight loss between 100 °C and 225 °C observed for all the materials, including neat rGO, corresponds to the residual oxygen-containing functional groups. The second weight loss region, between 300 °C and 400 °C, was attributed to the degradation of the polymer. The fraction of the residual oxygen groups for all materials is shown in Table 5.4. On the other hand, TGA curves revealed that the addition of polymer particles dropped the thermal stability, which effect was fewer in case of crosslinked particles. In fact, the monoliths with a higher crosslinking density (2% and 4% DVB-MMA/rGO with addition of both 10 and 40 wt% polymer particles) have

a slightly improved thermal stability compared to the hybrid Blank MMA/rGO structures. In both cases, the thermal degradation was postponed for about 100 ºC when crosslinked MMA/DVB particles were added in the structure in comparison to Blank MMA particles. This enhancement at higher amount of DVB may be due to the aromatic nature of the DVB that increases the onset temperature of degradation,[17] but mostly this effect is due to the crosslinked structure of the polymer, which when more compact would need more energy for the degradation.

The morphological structure of the monoliths was characterized by SEM. In Figure 5.5, SEM images of monoliths containing 10 % and 40 % Blank MMA, 10 % and 40 % crosslinked MMA polymer particles with 0.2 % DVB, and that of neat rGO are presented, whereas the monoliths with higher quantity of DVB are shown in Figure 5.6. The SEM images reveal highly porous morphology of all monoliths.

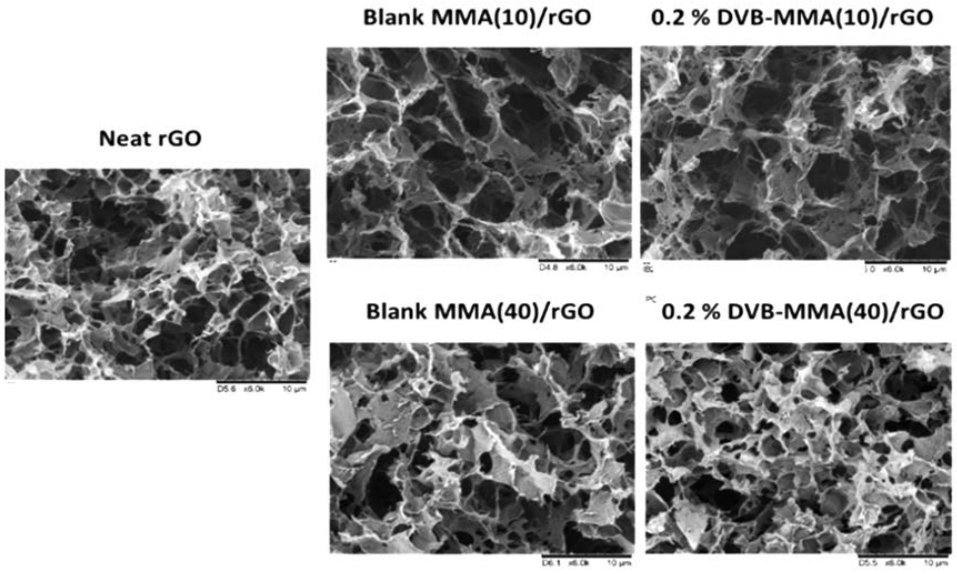

Figure 5.5. SEM images of monoliths containing 10 % and 40 % Blank MMA, 10 % and 40 % crosslinked MMA polymers with 0.2 % DVB, and that of neat rGO (the scale bar in all images is 10 μm).

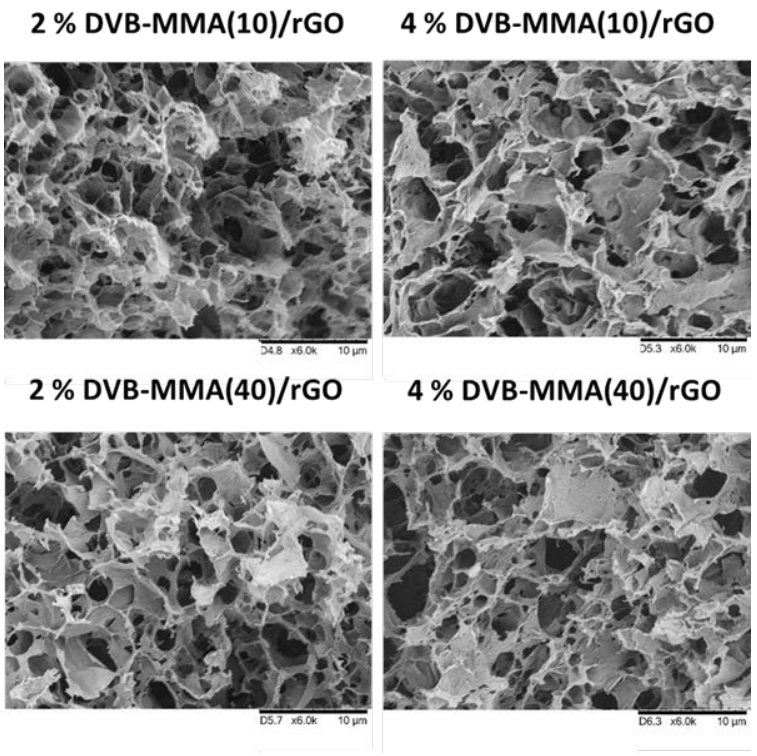

Figure 5.6. SEM images of monoliths containing 10 % and 40 % crosslinked MMA polymers with 2 and 4 % DVB.

Figures 5.5 and 5.6 clearly show that the addition of polymer in different quantity and with different crosslinking density did not affect significantly the final morphological structure. All the monoliths present a very similar porous morphological skeleton. Furthermore, TEM analysis were performed and the images obtained for neat rGO and 2 % DVB-MMA(10)/rGO are shown in Figure 5.7.

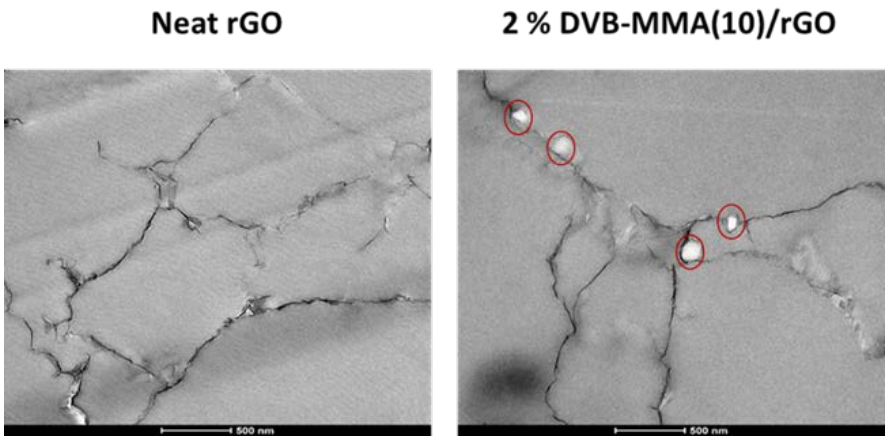

Figure 5.7. TEM images of neat rGO and 2 % DVB-MMA(10)/rGO materials. Polymer particles are marked in red.

In Figure 5.7, thin rGO layers can be clearly seen in both images, whereas white polymer particles marked in red are attached and distributed onto rGO platelets in the 2 % DVB-MMA(10)/rGO composite.

To get deeper insights in the textural properties of the monolithic structures, the N_2 adsorption-desorption isotherms were determined and presented in Figures 5.8A and B.

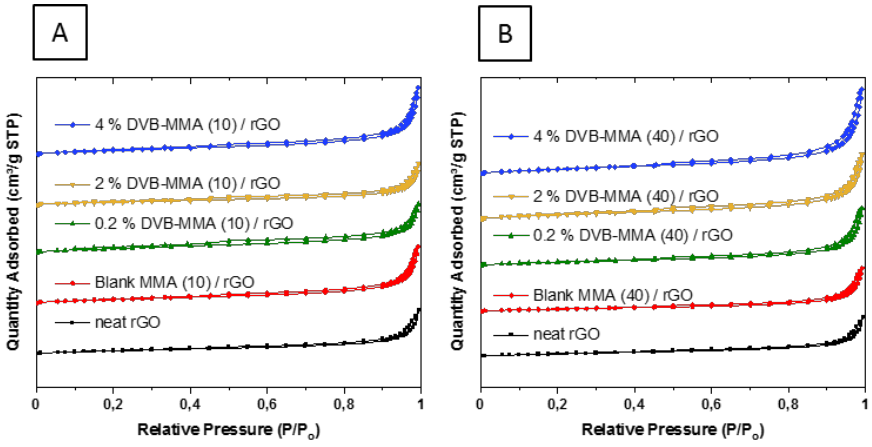

Figure 5.8. N_2 adsorption-desorption isotherms for neat rGO and composites with the addition of 10 wt% polymer particles (A) and 40 wt% polymer particles (B).

According to Figures 5.8A and B all the isotherms are of type IV, characteristic of mesoporous materials.[18] The addition of polymer particles either 10 or 40 wt% did not altered the type of the isotherms, which is in accordance to the SEM images (Figure 5.5 and Figure 5.6).

In Figure 5.9A and B, the pore size distributions are shown, where it can be observed that, in most of the cases the composites were composed of a higher volume of pores than the neat rGO monolith.

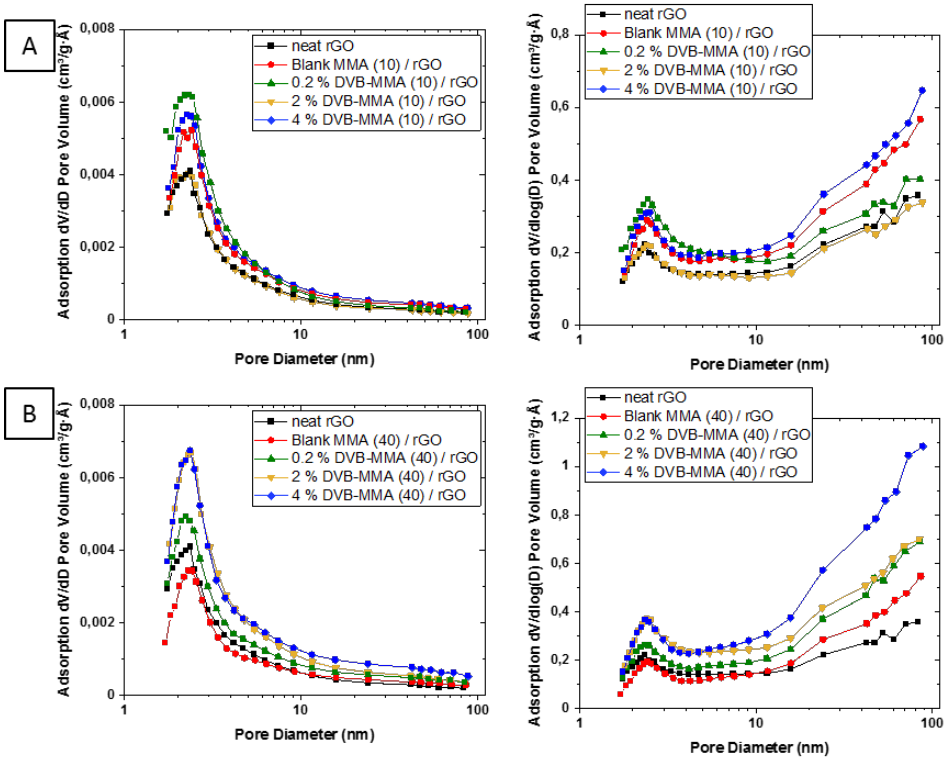

Figure 5.9. Pore size distributions for neat rGO and composites with the addition of 10 wt% polymer particles (A) and 40 wt% polymer particles (B).

On one hand, the fraction of small mesopores in a range of 2-4 nm, increased by addition of 10 % and 40 % Blank MMA, and crosslinked particles, likely due to the spacer effect of the particles that prevent the complete rGO platelets stacking, as observed previously in Chapter 3. However, in case of 40 % polymer addition, the crosslinked particles induced further augmentation of the fraction of small mesopores, as well as of the larger ones and the macropores, effect probably induced by the crosslinked structure of particles, observed in the pore size distribution in Figure 5.2.

In Table 5.4, the fraction of the residual oxygen-containing functional groups determined from TGA curves, textural properties and CO_2 adsorption capacities are presented for neat rGO and the composite monoliths.

Table 5.4. Fraction of the residual oxygen-containing functional groups. Textural properties of the 3D monolithic structures determined from the adsorption desorption isotherms at -196 ºC and CO_2 adsorption capacities determined at 25 ºC and 1 atm.

Material	% O-functionality	S_{BET} (m^2/g)	V_{total} (cm^3/g)	A_{micro} (cm^2/g)	V_{micro} (cm^3/g)	Micro (%)	CO_2 adsorption (mmol/g)
Neat rGO	9.8	169	0.524	4.2	< 0.001	0.2	0.87
Blank MMA(10)/rGO	9.1	218	0.664	20.8	0.0059	0.9	1.06
0.2 % DVB-MMA(10)/rGO	9.5	265	0.59	25.2	0.0083	1.4	1.08
2 % DVB-MMA(10)/rGO	8.2	172	0.453	29.5	0.0093	2.1	0.96
4 % DVB-MMA(10)/rGO	8.4	236	0.759	31.2	0.0091	1.2	1.17
Blank MMA(40)/rGO	10.5	155	0.545	25.4	0.0092	1.7	0.67
0.2 % DVB-MMA(40)/rGO	6.9	214	0.732	23.3	0.0057	0.8	0.84
2 % DVB-MMA(40)/rGO	4.9	283	0.852	27.1	0.008	0.9	1.38
4 % DVB-MMA(40)/rGO	4.9	297	1.103	37.4	0.0107	1	1.01

The fraction of oxygen functionalities within rGO were around 10 % for 10 % polymer added, and about 7 % for 40 % with decreasing tendency in case of crosslinked particles. Taking into account that in case of 40 % polymer, less graphenic materials is present, even though the relative quantity of oxygen functionalities is lower, the functionalization level is similar.

The textural properties developed from the N_2 adsorption-desorption isotherms are shown in Table 5.4. As predicted, higher BET specific surface areas were obtained within composites structures compared to the neat rGO, which is oppositely than obtained in all previous studies with not-crosslinked polymer particles. This is a consequence of interplay between two effects. While polymer particles acted as spacers between individual rGO platelets, preventing their complete stacking during self-assembly process and contribute to formation of the microporous structure, their crosslinked morphology and internal porous structure contributed to the overall porosity of the composites. Considering the total volume of the pores, almost all composite monoliths presented higher porosity than the neat rGO structure. As mentioned, this is for first time to attain higher porosity by addition of polymer particles to the neat rGO structure, especially when 40 % polymer was introduced within the structures, which according to our previous works affected negatively the textural properties and capture capacity. As the main difference with the previous chapters is the particle crosslinking, the observed effect of increased porosity is clear effect of the crosslinked polymer chains within the particles. The fraction of micropores is higher for all composites than the neat rGO, nevertheless the effect is fewer in case of 40 % polymer. Probably much higher quantity of polymer particles spacers between the rGO platelets resulted in formation of less micro- and small mesopores. The particle diameter in a range of 170–200 nm between individual graphene sheets apparently created larger meso- and macropores.

In Figure 5.10, the CO_2 adsorption-desorption isotherms for 3D monolithic structures measured at 25 °C and up to 1 atm are presented. What is curious is that when 10 % crosslinked particles are introduced within the structures, the CO_2 adsorption-desorption isotherm behaviour is similar to that of polymer particles shown in Figure 5.3, indicating that the polymer particles within the composite structure have direct contact with CO_2 molecules and affect the adsorption. Oppositely, when 40 % particles are introduced into the composites, the CO_2 adsorption-

desorption behaviour is similar to that of neat rGO material. Despite much higher presence of polymer particles, probably they are included between the platelets that act as a barrier and hinder the direct contact between polymer and CO_2.

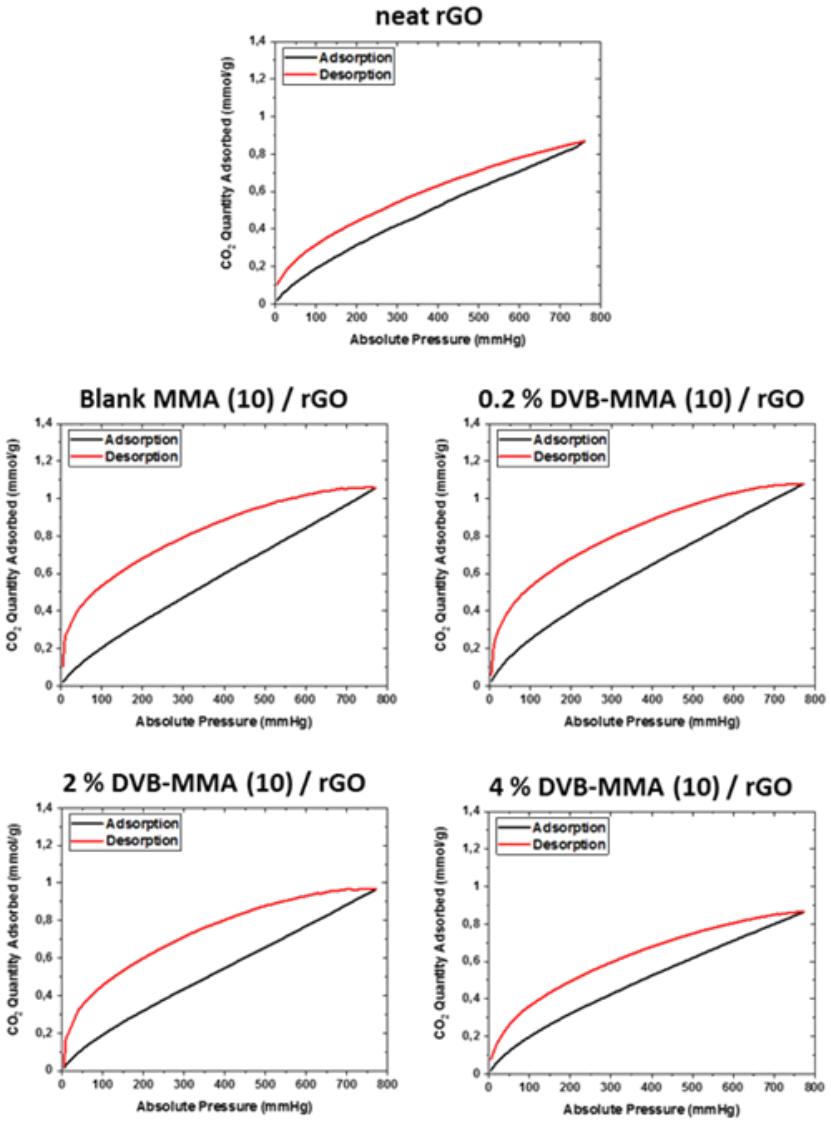

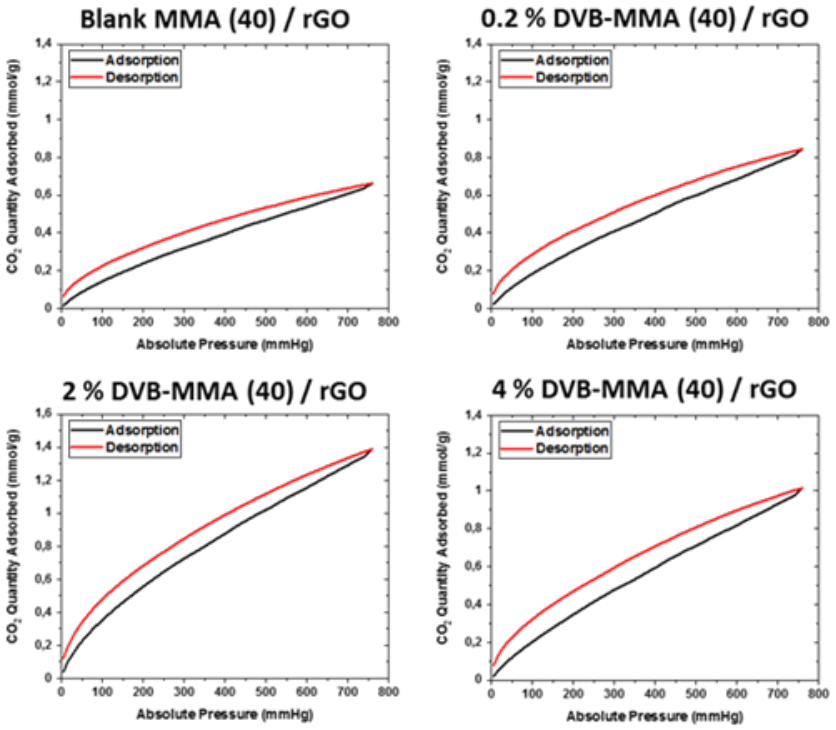

Figure 5.10. CO_2 adsorption-desorption isotherms at 25 °C and 1 atm for 3D monolithic structures.

CO_2 adsorption capacities of the monoliths are presented in Table 5.4 and in Figure 5.11. When 10 wt% addition of polymer was used, in all the cases the CO_2 adsorption improved with respect to the neat rGO monolith, obtaining the highest CO_2 adsorption of 1.17 mmol/g, with the highest crosslinked polymer particle, 4 % DVB-MMA(10)/rGO. The adsorption seems to be very similar, probably due to similar chemistry and textural properties of the composites containing 10 % polymer and the introduced crosslinking does not have important effect.

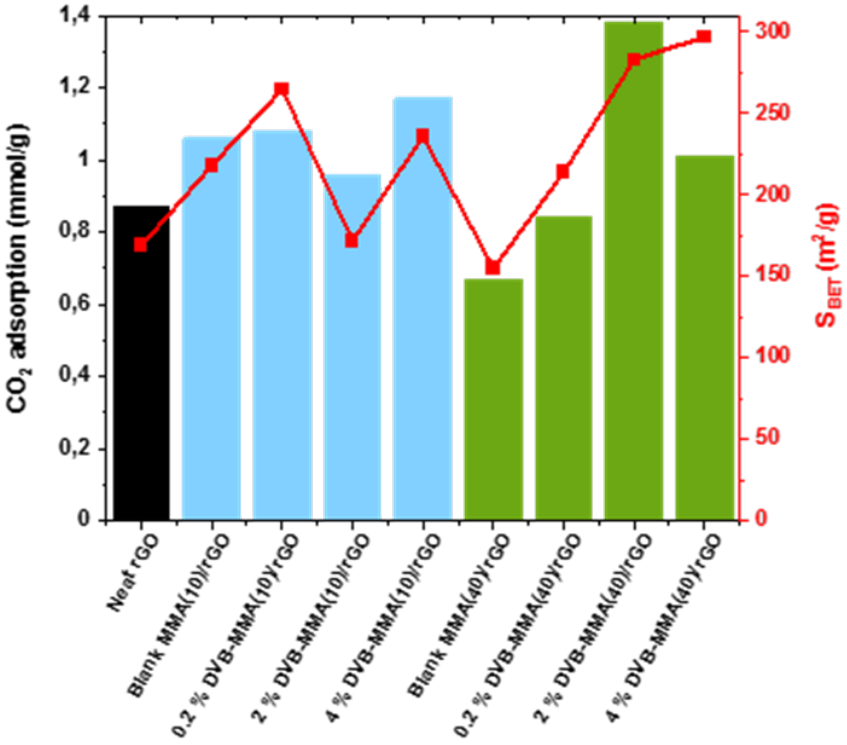

Figure 5.11. CO_2 adsorption capacity and BET surface area of the different 3D monolithic structures. Black bars correspond to neat rGO structure, blue bars to monoliths with the 10 % addition of polymer particles, and green bars to monoliths with the 40 % addition of polymer particles.

In contrast, at 40 wt% addition, the CO_2 adsorption performance increased with respect to neat rGO just in case of higher amounts of DVB, whereas the crosslinking of the particles was favorable to CO_2 adsorption with respect to Blank MMA(40)/rGO. The 2 % DVB-MMA(40)/rGO and 4 % DVB-MMA(40)/rGO structures presented 1.38 and 1.01 mmol/g of CO_2 uptake, respectively, which is the highest adsorption achieved so far when so much polymer was introduced within the composites, according to our previous studies when non-crosslinked

particles were used. Likely, the important augmentation of BET surface area from about 155 for the Blank MMA(40)/rGO to almost 300 m^2/g (the highest achieved in rGO/polymer composite monoliths) have the main decisive effect on the observed CO_2 uptake rise. It is worth noting that the contribution of microporosity to BET is the lowest, which define the 40 % composites as highly mesoporous material and as such very favorable for CO_2 capture under the studied conditions. Moreover, taking into consideration that the quantity of rGO is less than 60 % and that there is still decent fraction of oxygen functional groups, the graphene surface that in majority has the direct contact with CO_2 is actually densely functionalized, which according to our previous experience is the most important parameter determining the CO_2 adsorption capacity.

Therefore, the textural properties of the 3D composites can be improved further by increasing the contribution of all pore types, from micro, meso- up to macropores by changing the amount and type of crosslinked polymer particles. In this way, an excellent control of the microstructure of the graphene-based composite materials was achieved, a task that is still challenging when we speak about the carbonaceous porous absorbents.[2] This meet the requirements and widen the application possibilities of these materials for capture of CO_2 at different conditions and implementation of this technology in different processes.

5.4. Conclusions

The main aim of this work is to improve the control of the textural properties of 3D rGO/polymer composite monoliths and to increase their BET surface area towards enhanced CO_2 adsorption. The approach was based on the synthesis of MMA crosslinked polymer particles with different density and to study the effect of the porous structure and the fraction of micro- and mesopores and how it affects the CO_2 uptake. For that, four different particles were produced by emulsion co-polymerization of MMA with different amounts of crosslinker DVB, and they were added to the 3D structures at two different amounts (10 wt% and 40 wt%). The monoliths were synthesized by a simple mixing of the GO platelets and the polymer particles in aqueous dispersion, which after addition of reducing agent and reduction temperature, were self-assembled into composite monolithic, porous structures.

The crosslinked polymer particles with a higher DVB amount presented denser crosslinking and shorter distance between the crosslinking points, resulting in an increase of the BET specific surface area, total volume of the pores, and area and volume of micro- and mesopores.

Beside augmentation of the fraction of micro- and meso-pores in the structures by addition of 10 wt% particles, there was no important differences observed in the chemistry (oxygen functional groups quantity on rGO) and BET surface area, resulting in rather similar affinity towards CO_2 of around 1 mmol/g, independently of the microstructure of the polymer particles (crosslinked or not).

Nevertheless, in case of 40 % polymer particles, the textural properties were importantly affected, the porosity was increased by augmentation of all pore types, resulting in significant

rise of the BET surface area. The rGO surface was more densely functionalized, too, all together causing an augmentation of the CO_2 uptake.

Because of the proper control of the microstructure of the polymer particles, the characteristics of the 3D graphene-polymer monoliths can be tailored by a simple procedure resulting in competitive CO_2 adsorption capacities for practical application. The advantages of the crosslinked polymer particles synthesized by emulsion polymerization are in their synthetic routes, monomer diversity, scalable technology, and potential low cost.

5.5. References

(1) Saha, D.; Kienbaum, M. J. Role of Oxygen, Nitrogen and Sulfur Functionalities on the Surface of Nanoporous Carbons in CO2 Adsorption: A Critical Review. *Microporous Mesoporous Mater.* **2019**, *287*, 29–55.

(2) Deng, W.; Fang, Q.; Zhou, X.; Cao, H.; Liu, Z. Hydrothermal Self-Assembly of Graphene Foams with Controllable Pore Size. *RSC Adv.* **2016**, *6* (25), 20843–20849.

(3) Gao, H.; Li, Q.; Ren, S. Progress on CO2 Capture by Porous Organic Polymers. *Curr. Opin. Green Sustain. Chem.* **2019**, *16*, 33–38.

(4) Wood, C. D.; Bien, T.; Trewin, A.; Hongjun, N.; Bradshaw, D.; Rosseinsky, M. J.; Khimyak, Y. Z.; Campbell, N. L.; Kirk, R.; Stöckel, E.; et al. Hydrogen Storage in Microporous Hypercrosslinked Organic Polymer Networks. *Chem. Mater.* **2007**, *19* (8), 2034–2048.

(5) Zou, L.; Sun, Y.; Che, S.; Yang, X.; Wang, X.; Bosch, M.; Wang, Q.; Li, H.; Smith, M.; Yuan, S.; et al. Porous Organic Polymers for Post-Combustion Carbon Capture. *Adv. Mater.* **2017**, *29* (37).

(6) Bhanja, P.; Modak, A.; Bhaumik, A. Porous Organic Polymers for CO2 Storage and Conversion Reactions. *ChemCatChem* **2019**, *11* (1), 244–257.

(7) Ahn, J. H.; Jang, J. E.; Oh, C. G.; Ihm, S. K.; Cortez, J.; Sherrington, D. C. Rapid Generation and Control of Microporosity, Bimodal Pore Size Distribution, and Surface Area in Davankov-Type Hyper-Cross-Linked Resins. *Macromolecules* **2006**, *39* (2), 627–632.

(8) Xu, C.; Hedin, N. Microporous Adsorbents for CO2 Capture - A Case for Microporous Polymers? *Mater. Today* **2014**, *17* (8), 397–403.

(9) Ji, G.; Yang, Z.; Zhang, H.; Zhao, Y.; Yu, B.; Ma, Z.; Liu, Z. Hierarchically Mesoporous o -Hydroxyazobenzene Polymers: Synthesis and Their Applications in CO 2 Capture and Conversion. *Angew. Chemie* **2016**, *128* (33), 9837–9841.

(10) Morton, M.; Kaizerman, S.; Altier, M. W. Swelling of Latex Particles. *Rubber Chem. Technol.* **1959**, *32* (3), 814–824.

(11) González, I.; Asua, J. M.; Leiza, J. R. The Role of Methyl Methacrylate on Branching and Gel Formation in the Emulsion Copolymerization of BA/MMA. *Polymer (Guildf).* **2007**, *48* (9), 2542–2547.

(12) Liu, K.; Ostadhassan, M. The Impact of Pore Size Distribution Data Presentation Format on Pore Structure Interpretation of Shales. *Adv. Geo-Energy Res.* **2019**, *3* (2), 187–197.

(13) Gardon, J. L. Emulsion Polymerization. II. Review of Experimental Data in the Context of the Revised Smith-Ewart Theory. *J. Polym. Sci. Part A.1* **1968**, *6*, 643–664.

(14) Zulfiqar, S.; Awan, S.; Karadas, F.; Atilhan, M.; Yavuz, C. T.; Sarwar, M. I. Amidoxime Porous Polymers for CO2 Capture. *RSC Adv.* **2013**, *3* (38), 17203–17213.

(15) Kilic, S.; Michalik, S.; Wang, Y.; Johnson, J. K.; Enick, R. M.; Beckman, E. J. Phase Behavior of Oxygen-Containing Polymers in CO2. *Macromolecules* **2007**, *40* (4), 1332–1341.

(16) Ormategui, N.; Veloso, A.; Leal, G. P.; Rodriguez-Couto, S.; Tomovska, R. Design of Stable and Powerful Nanobiocatalysts, Based on Enzyme Laccase Immobilized on Self-Assembled 3D Graphene/Polymer Composite Hydrogels. *ACS Appl. Mater. Interfaces* **2015**, *7* (25), 14104–14112.

(17) Uhl, F. M.; Levchik, G. F.; Levchik, S. V.; Dick, C.; Liggat, J. J.; Snape, C. E.; Wilkie, C. A. Thermal Stability of Cross-Linked Polymers: Methyl Methacrylate with Divinylbenzene and Styrene with Dimethacrylates. *Polym. Degrad. Stab.* **2001**, *71* (2), 317–325.

(18) Orr, P. *Analytical Methods in Fine Particle Technology*; 1997.

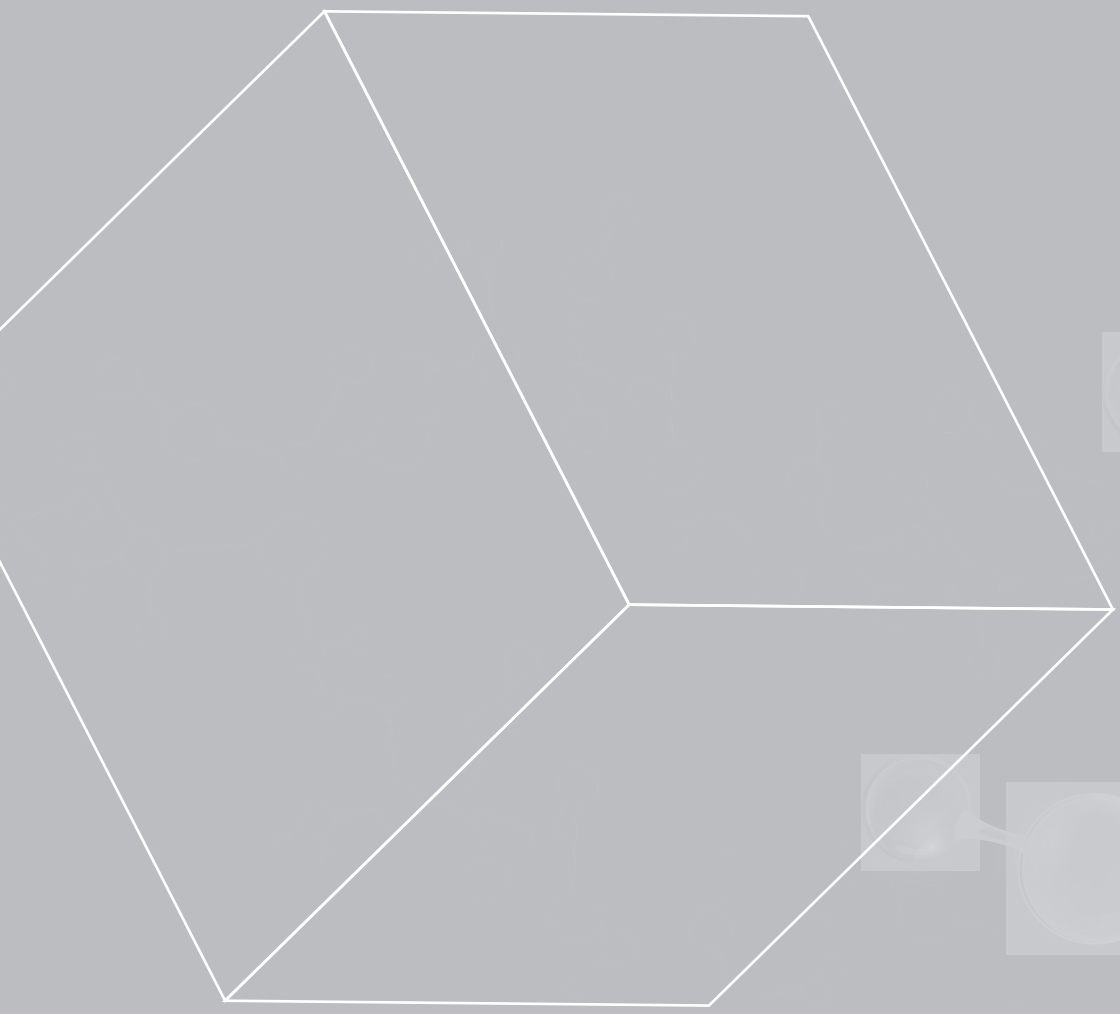

CHAPTER 6

Scale-up the productivity of synthesis of 3D graphene-based composite monolithic structures and study of high-pressure CO_2 adsorption performance

Chapter 6. Scale-up the productivity of synthesis of 3D graphene-based composite monolithic structures and study of high-pressure CO_2 adsorption performance

6.1. Introduction

In this chapter, to exploit the outstanding properties studied and discussed during this PhD project, 3D graphene-polymer monolithic structures were synthesized at larger, although still on laboratory scale, towards a more real application perspective.

The goal of this scale-up process was to develop larger 3D monoliths applying the same synthesis route and to understand how the productivity change impacts the self-assembly process, and consequently, the final products´ properties and adsorption performance. In fact, the straightforward and environmentally friendly method used for the production of monolithic structures attracts great attention because of easy transferability from laboratory to large-scale production compared to other synthesis procedures investigated so far and reviewed in Chapter 1.[1] Neat 3D rGO and composite structures were synthesized, analyzed, and their CO_2 adsorption capacity were studied. It is worth mentioning that, to the best of our knowledge, there is no any production scale-up reported for 3D graphene-based materials employed for CO_2 capture in the open literature.

Moreover, in this chapter the scope of the adsorption study was extended. Namely, to now the CO_2 adsorption capacity of the monoliths was studied at conditions of 25 °C and up to 1

atm. In this chapter, the adsorption capacity of the 3D monoliths is evaluated at two different temperatures, 25 °C and 60 °C, to obtain information on the heat of adsorption and energy consumption potential of the regeneration process. As well the CO_2 adsorption was studied at pressures as high as 20 atm (≈ 20 bars), which opens the possibility of analyzing graphene-based adsorbents for alternative practical application such as in pre-combustion or oxy-combustion systems. In fact, both CO_2 capture technologies imply a working pressure in the range of 20-30 bars.[2,3]

In this way, the stability of the porous structures could be evaluated at high pressures, too. For example, in case of carbon-based porous nanostructures, Casco et al.[4] claimed that narrow micropores (pores below 0.6 nm) govern the sorption behavior at 1 bar, whereas large micropores/small mesopores (pores below 2-3 nm) governs the sorption behavior at high pressure (45 bars). Moreover, Singh et al.[5] reported that there is a significant CO_2 adsorption at low pressure and linear adsorption at high pressures. This happen as the initial capture takes place due to the quick filling of the micropores present inside the porous structure. Afterwards, the adsorption occurs on the mesopores and the surface-active sites. Mainly, it has been reported that the high-pressure CO_2 capture largely correlates to the pore volume of micro- and narrow mesopores.[6–8] On the other hand, the role of heteroatoms in CO_2 capture capacity is particularly important at low pressures.[9]

The hierarchical porous structure of the adsorbent plays an important role in high-pressure CO_2 capture, but also does the BET surface area. The linear relationship between high pressure adsorption performance and BET surface area is also reported for various types of carbons, but not for all of them.[6] Besides, in most of the high pressures measurements, the CO_2 adsorption does not reach saturation along the apparent surface area at conditions used.[8]

These final work opens the opportunity to tailor the fabrication strategy for 3D porous graphene-based structures to maximize the overall CO_2 capture at any target pressure.

6.2. Experimental part

6.2.1. Materials

As in the previous chapters, aqueous dispersion of graphene oxide (GO) sheets of 4 mg/mL (Graphenea) was used as supplied. For chemical GO reduction L-ascorbic acid (AsA, ≥99 %, Sigma- Aldrich) was used. Technical grade monomers methyl methacrylate (MMA, Quimidroga) and glycidyl methacrylate (GMA, Sigma-Aldrich) were used without purification. Sodium dodecyl sulfate (SDS, Sigma-Aldrich), potassium persulfate (KPS, ≥99 %, Sigma-Aldrich) and sodium bicarbonate ($NaHCO_3$, Sigma-Aldrich) were used as received. Deionized water was used as polymerization media.

6.2.2. Synthesis of polymer dispersion

The synthesis and formulation of the functionalized polymethyl methacrylate latex is explained in Section 2.2.2.1. in Chapter 2. Shortly, glycidyl methacrylate/methyl methacrylate (GMA/MMA) in a ratio of 10/90 wt% were synthesized by means of batch emulsion polymerization process. As a results, a latex with a final solids content of 20 % were prepared with an overall conversion of 99 % and an average polymer particle diameter of 70 nm.

6.2.3. Synthesis of 3D rGO-based structures

The synthesis of 3D rGO-based structures either small or bigger structures were performed following the same procedure described during this project. For the synthesis of the

small monoliths 40 mL of GO (4 mg/mL) aqueous dispersion was used, while for bigger monoliths 240 mL with the same GO content. Shortly, 280 mL of GO aqueous dispersion was sonicated at 25 °C for 1 h. Then, the GO dispersion was mixed with an appropriate amount of polymer dispersion for 2 h at room temperature (this step was performed just in the case of 3D graphene-polymer composites). After that, the reducing agent AsA was added to the mixture (GO:AsA mass ratio 1:1 and 1:0.5) and stirred for 0.5 h. At this point, the rGO aqueous dispersion was divided in two different vessels, on the one hand, 40 mL for the synthesis of the small and 240 mL for the synthesis of the bigger structure. Both samples were placed in the oven overnight at same temperature (either at 45 °C or 90 °C). The formed hydrogels monoliths were purified by dialysis process, which was followed by measuring the water conductivity. Finally, the wet monoliths were dried by freeze-drying technique for three days.

6.2.4. Characterization

The characterization techniques regarding the polymer dispersion are explained in Section 2.2.3 in Chapter 2 and in Section I.1. of Appendix I.

On the other hand, regarding the characterization of the 3D structures, thermogravimetric analyses (TGA) were performed to estimate the amount of residual oxygen-containing functional groups within the monolithic structures and to study the thermal stability. The surface morphology of the structures was examined using a scanning electron microscopy (SEM). The porous texture of the monoliths was characterized by means of N_2 adsorption–desorption at –196 °C in a Micromeritics ASAP2020 apparatus. Detailed information of these characterization techniques is given in Section I.2 of Appendix I.

Finally, in terms of gas adsorption measurements, the materials´ CO_2 adsorption capacities were determined from their isotherms, measured using both a Micromeritics ASAP 20220 Analyzer (volumetrically) and an Intelligent Gravimetric Analyser (IGA, gravimetrically). Detailed information of these gas adsorption measurements is given in Section I.3 of Appendix I.

6.3. Results and discussion

6.3.1. Characteristics of 3D small and large structures

The effect of reduction conditions (temperature and amount of reducing agent) and the addition of different amounts of polymer particles on the synthesis, self-assembly process, and final properties of bigger 3D structures is discussed in this part in a view of different productivity. For that aim, a portfolio of small and large monoliths were synthesized at the same reduction conditions in absence or presence of polymer colloids. In Table 6.1, the nomenclature and synthesis conditions used in each system are presented. In the nomenclature, the first lyric correspond to small or big structure (S and B, respectively), the first number to reduction temperature (45 °C or 90 °C), the second number to the mass ratio of GO:ASA (1:1 or 1:0.5), and the last number, 10 or 40, to the amount of polymer.

Table 6.1. Nomenclature and synthesis conditions of each monolithic structure.

Material	Reduction temperature (°C)	GO:AsA mass ratio	Polymer amount
S_45_0.5	45	1:0.5	-
B_45_0.5	45	1:0.5	-
S_45_1	45	1:1	-
B_45_1	45	1:1	-
S_90_0.5	90	1:0.5	-
B_90_0.5	90	1:0.5	-
S_90_1	90	1:1	-
B_90_1	90	1:1	-
S_45_1_Pol (10)	45	1:1	10
B_45_1_Pol (10)	45	1:1	10
S_90_1_Pol (10)	90	1:1	10
B_90_1_Pol (10)	90	1:1	10
S_90_1_Pol (40)	90	1:1	40
B_90_1_Pol (40)	90	1:1	40

In the synthesis route, in terms of neat rGO structures (in absence of polymer particles), after the addition of reducing agent (AsA) the sample was divided in two amounts (40 mL and 240 mL) at two different vessels. Regarding the composites, the division was performed after the addition of polymer particles and reducing agent. The samples were then placed at the oven overnight obtaining 3D monolithic structures, where the yield of GO transformed to a monolith was measured gravimetrically to be in a range of 92 to 95 %. It is worth mentioning that the time left for formation of monoliths is more than necessary to form the monoliths. In Figure 6.1 and 6.2, the photos of both small and big hydrogels (before drying) are presented. Besides, in Figure 6.1, the dimensions of some monolithic structures are also shown.

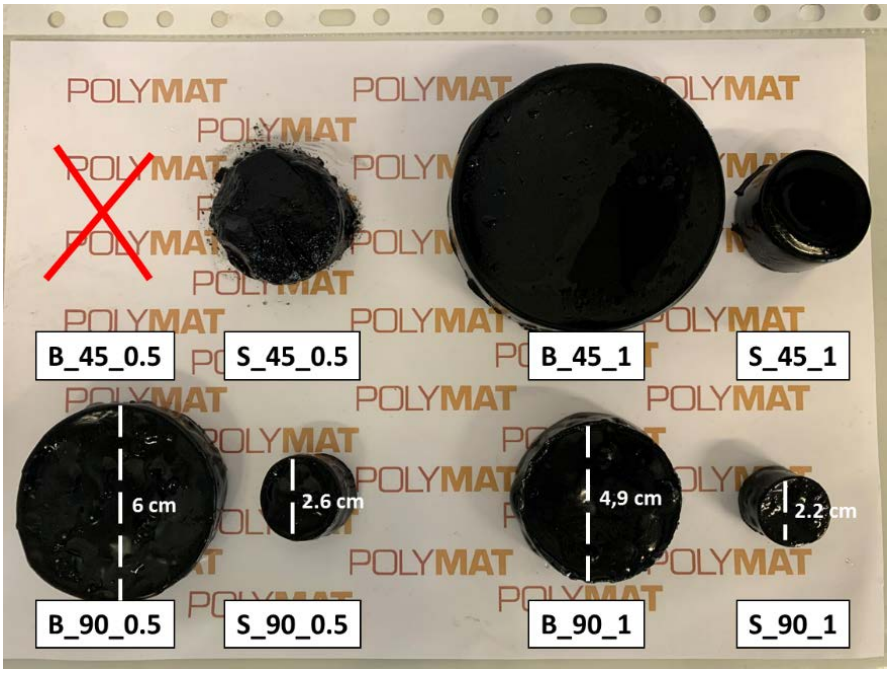

Figure 6.1. Photos of the small and big blank monoliths synthesized at 45 °C and 90 °C at GO:AsA ratio of 1:1 and 1:0.5.

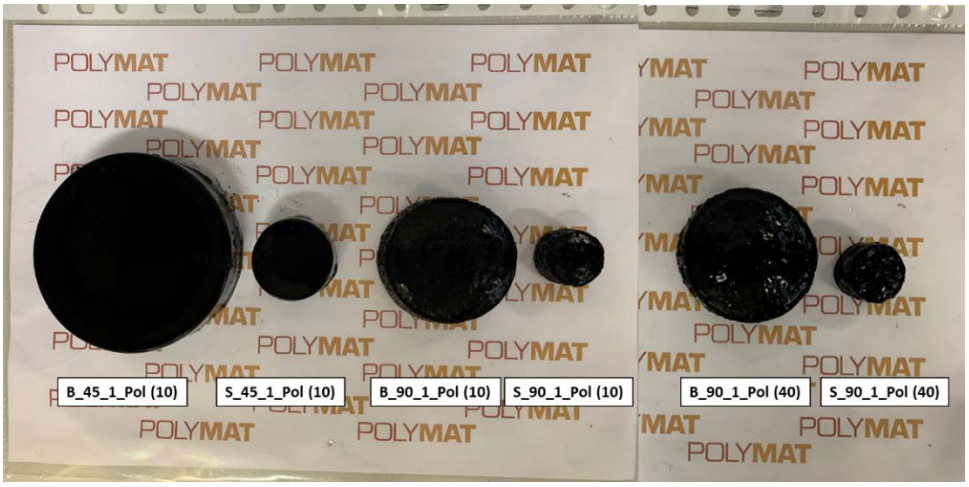

Figure 6.2. Photos of the small and big composite monoliths synthesized at 45 °C and 90 °C at GO:AsA mass ratio of 1:1 with polymer particles content of 10 wt% and 40 wt%.

In Figure 6.1 and 6.2, it can be observed that most of the monoliths were successfully produced either in small or big sizes. The only exception was B_45_0.5 structure, synthesized at lowest temperature (45 °C) and lowest amount of reducing agent (1:0.5). As it was explained in previous chapters, the reduction parameters play an important role on the formation of the 3D structure, as they determine the degree and rate of the GO reduction process, which provide the driving force for the structure formation. The conditions at which B_45_0.5 was synthesized (T^a=45 ºC and GO:AsA=1:0.5) were not powerful enough to reach the necessary driving force for the self-assembly of rGO platelets into a monolithic structure. This structure and the small one, S_45_0.5, were not analysed further. It may be also observed that the big structures have more than doubled diameter than that of small structures at least, even though the volume of the structures is much higher as the mass of the materials included in the monoliths is 6 fold increased.

In Figure 6.3–6.8, the SEM images of each small and their respective big structures are shown, where it can be seen that the all monolithic structures present a porous morphology.

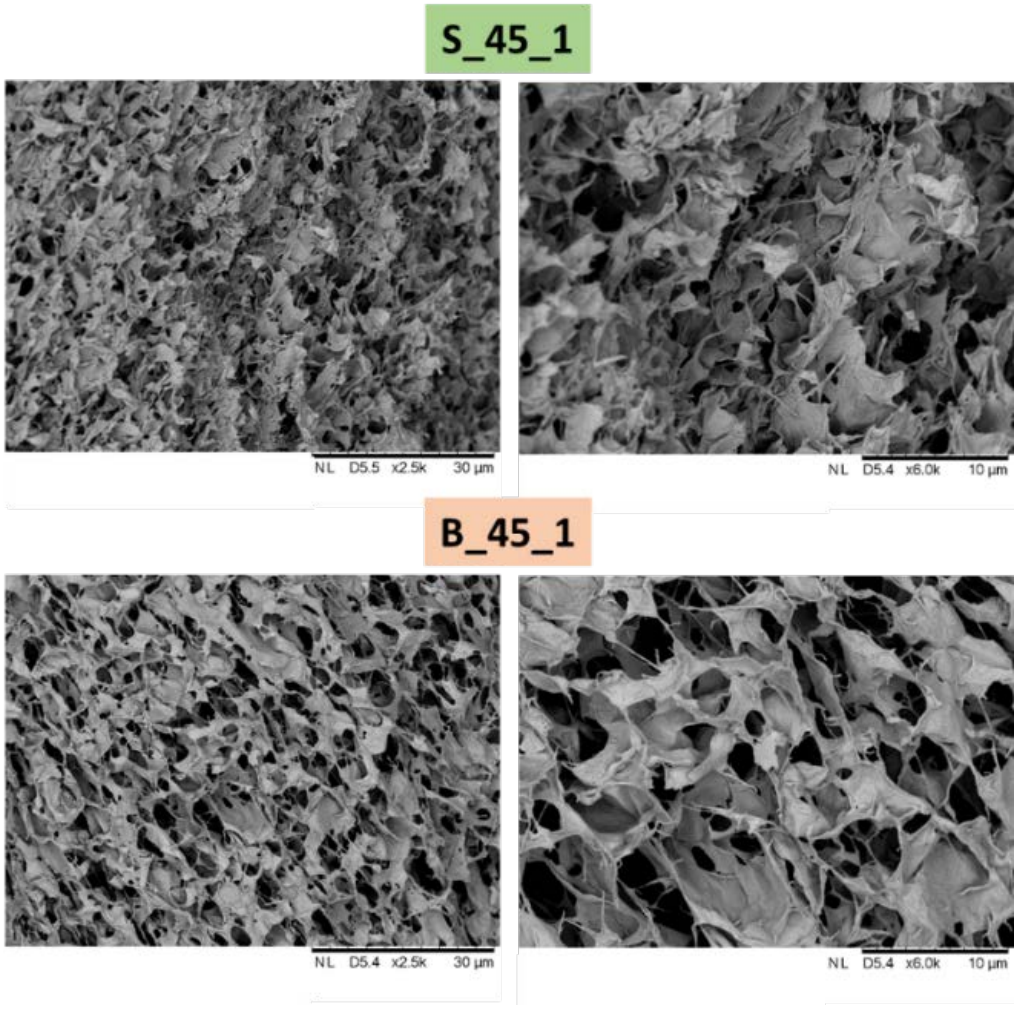

Figure 6.3. SEM images of small and big monolithic structures synthesized at 45 °C at GO:ASA mass ratio of 1:1, at 30 and 10 µm scale bars.

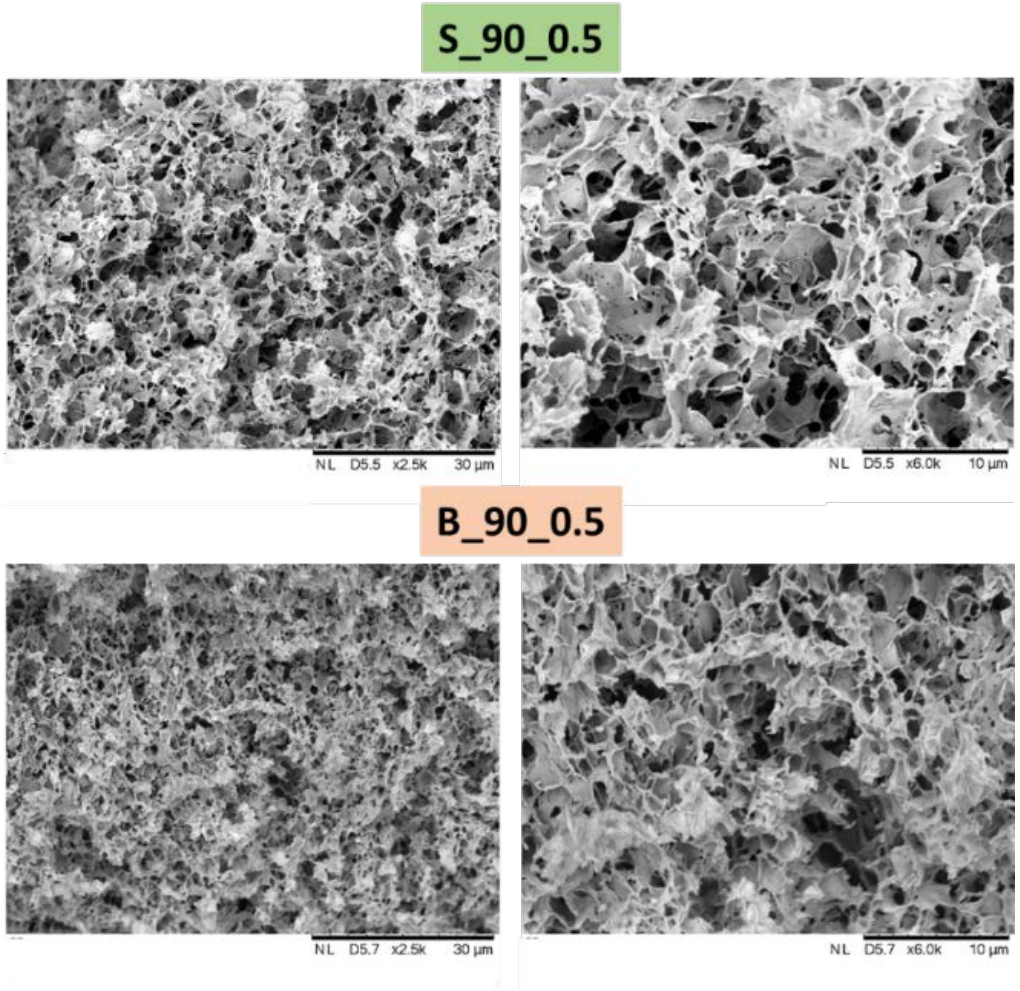

Figure 6.4. SEM images of small and big monolithic structures synthesized at 90 °C at GO:ASA mass ratio of 1:0.5, at 30 and 10 µm scale bars.

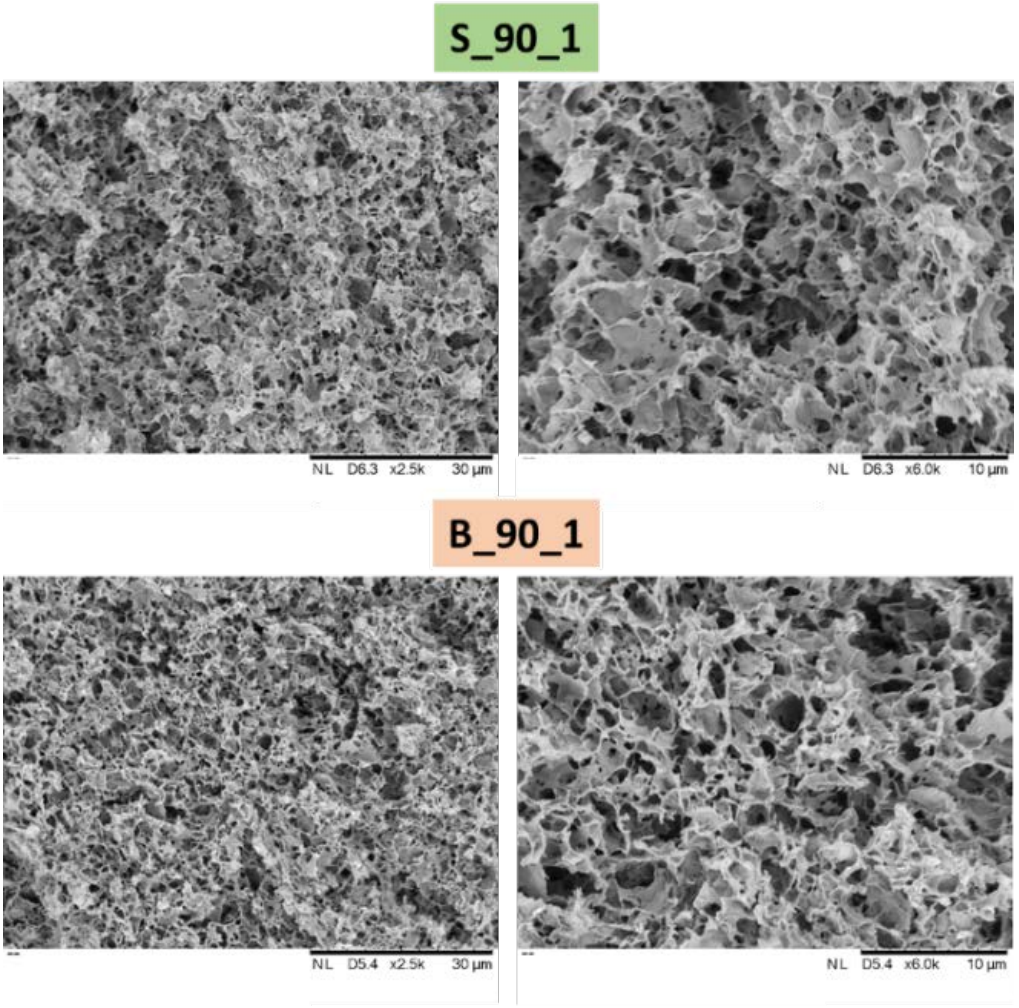

Figure 6.5. SEM images of small and big monolithic structures synthesized at 90 °C at GO:ASA mass ratio of 1:1, at 30 and 10 µm scale bars.

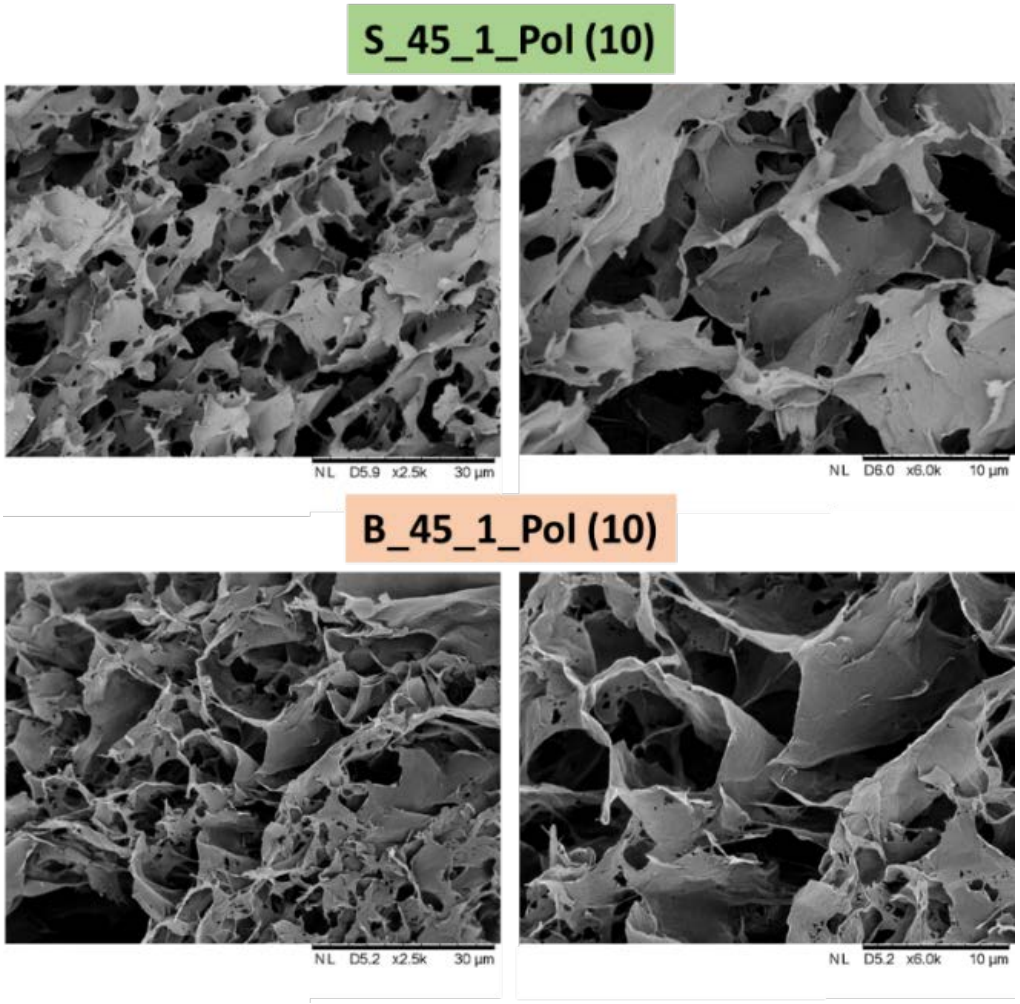

Figure 6.6. SEM images of small and big composite structures synthesized at 45 °C at GO:ASA mass ratio of 1:1 with 10 wt% addition of polymer particles. The scale bars are 30 and 10 µm.

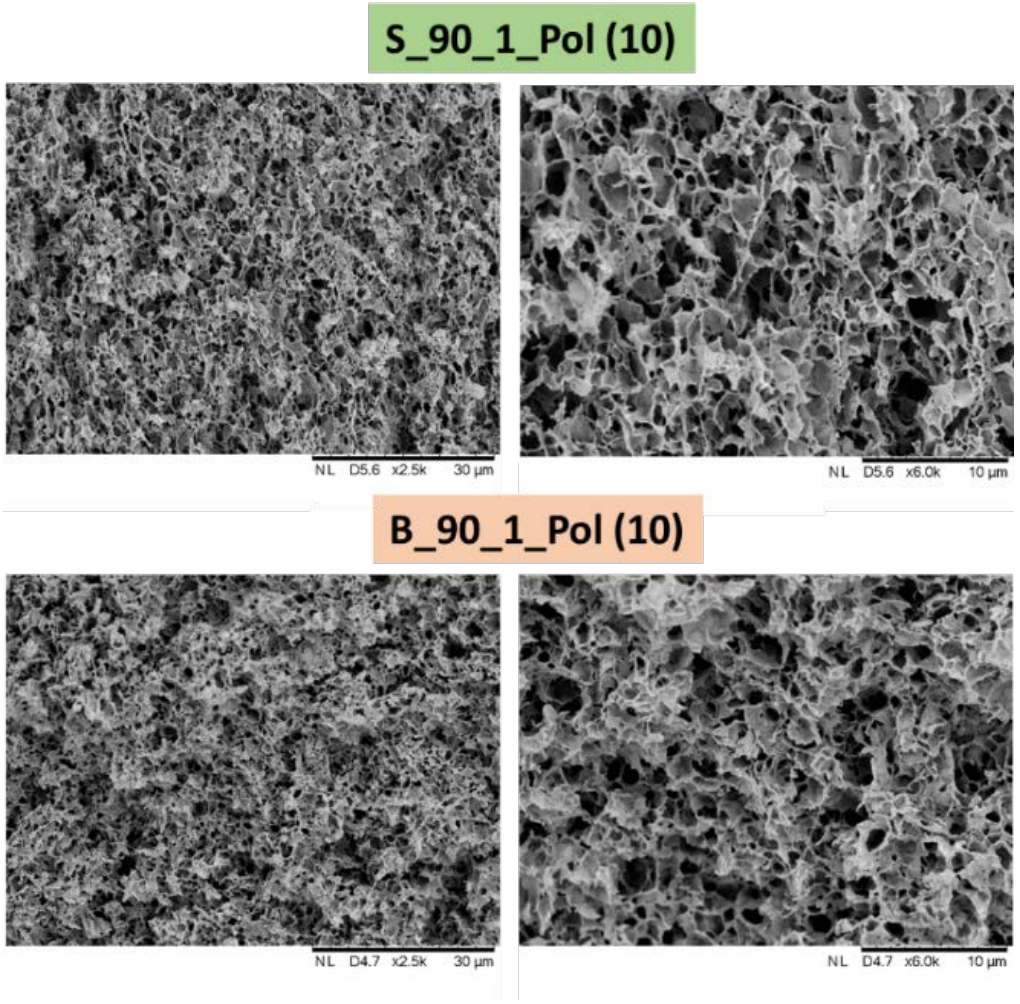

Figure 6.7. SEM images of small and big composite structures synthesized at 90 °C at GO:ASA mass ratio of 1:1 with 10 wt% addition of polymer particles. The scale bars are 30 and 10 µm.

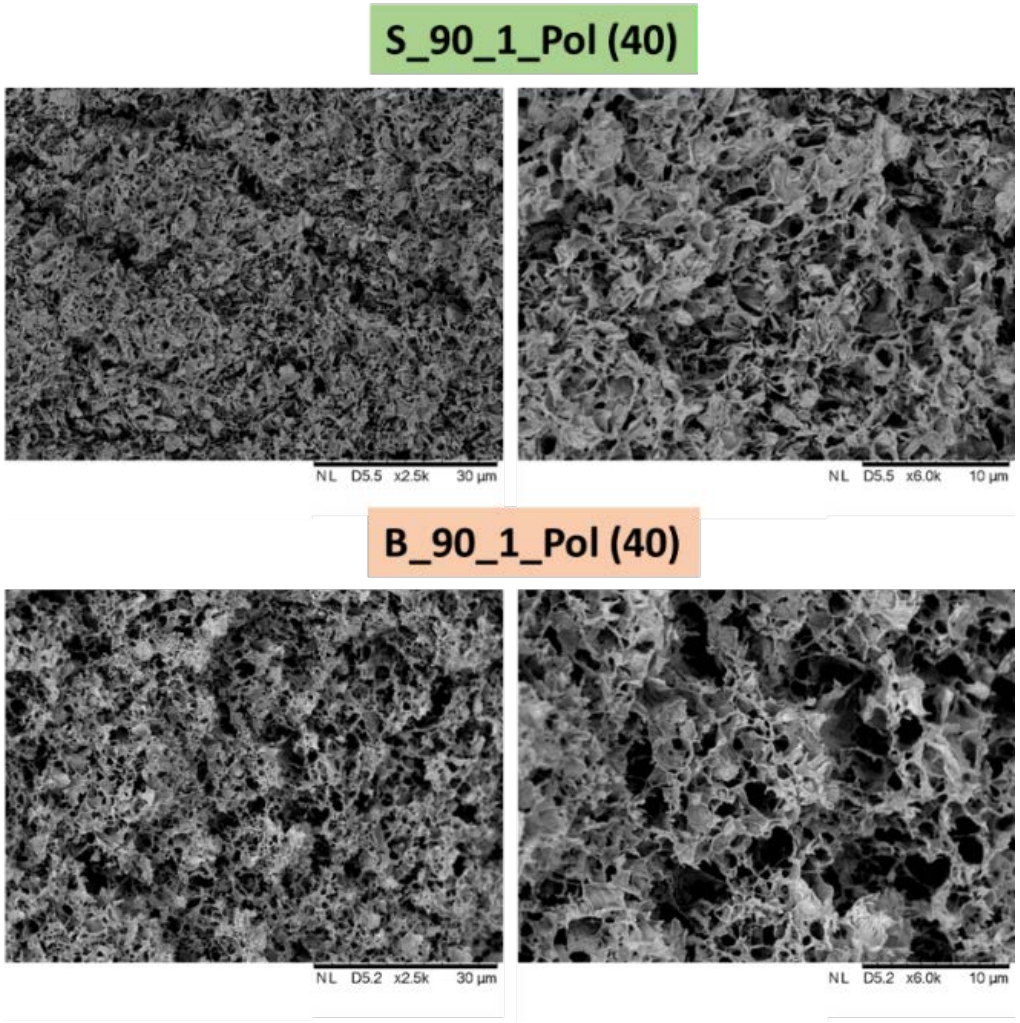

Figure 6.8. SEM images of small and big composite structures synthesized at 90 °C at GO:ASA mass ratio of 1:1 with 40 wt% addition of polymer particles. The scale bars are 30 and 10 µm.

In SEM images it can be observed that monoliths produced at either lower or higher amount of initial GO present quite similar porous morphology, i.e. there are hardly no differences between the macro porous structures. In terms of reduction conditions, the increase of reduction temperature, from 45 °C to 90 °C, results in an increase in the porosity and in the formation of

more compact structures, as observed in all chapters. In fact, in Figure 6.1, it can be seen that the monoliths synthesized at 90 °C, either with GO:AsA 1:1 or 1:0.5, possess a considerably lower volume than that obtained at 45 °C. Besides, the effect of AsA amount is clear from the comparison of the structure formed at GO:AsA 1:1 at 90 °C, which also produced more compact structure that to the structure obtained at lower GO:AsA 1:0.5 (Figure 6.1). The increased productivity did not affect this behaviour. On the other hand, the addition of polymer particles in composite monoliths did not produced significant difference in the porous structures at the several tens of micrometre dimensions observed in the SEM images.

The amount of residual oxygen-containing functional groups and thermal stability were evaluated by TGA, shown in Figure 6.9.

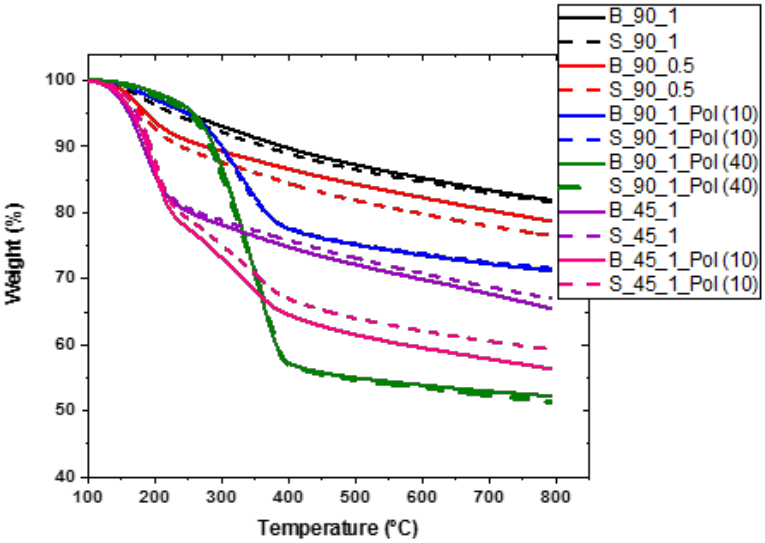

Figure 6.9. TGA thermographs for each monolithic structure. Big monoliths´ degradation is presented as continuous line and small monoliths´ degradation as dashed line.

Figure 6.9 shows that big monoliths were almost identically degraded compared to their respective small structures in each condition studied, indicating that the microstructure of small structures compared to their respective bigger materials are similar as observed in SEM images. In this case too, when monoliths are prepared under harder conditions (90 °C and GO:ASA 1:1), they need more energy to degrade until more or less 300 °C, where polymer degradation starts. In contrast, the monoliths prepared under milder conditions (45 °C, at GO:AsA mass ratio 1:1) were highly functionalized and were loosely packed. In Table 6.2, the amount of residual oxygen groups, calculated from the first degradation step (100- 225 °C), is presented.

To obtain a deeper insight into the morphology and textural properties of the small and big structures, N_2 adsorption-desorption experiments were carried out. The adsorption-desorption isotherms are presented in Figure 6.10, whereas the pore size distribution for each system is presented in Figure 6.11. In Figure 6.11, the left graphs correspond to dV/dD curve, in which the contribution of smaller pores are pronounced, while the right graphs correspond to dV/dlogD, representing the contribution of larger pores.[10] Besides, Table 6.2 provides information of the specific surface area (BET area), total volume of the pores, and volume of the micropores.

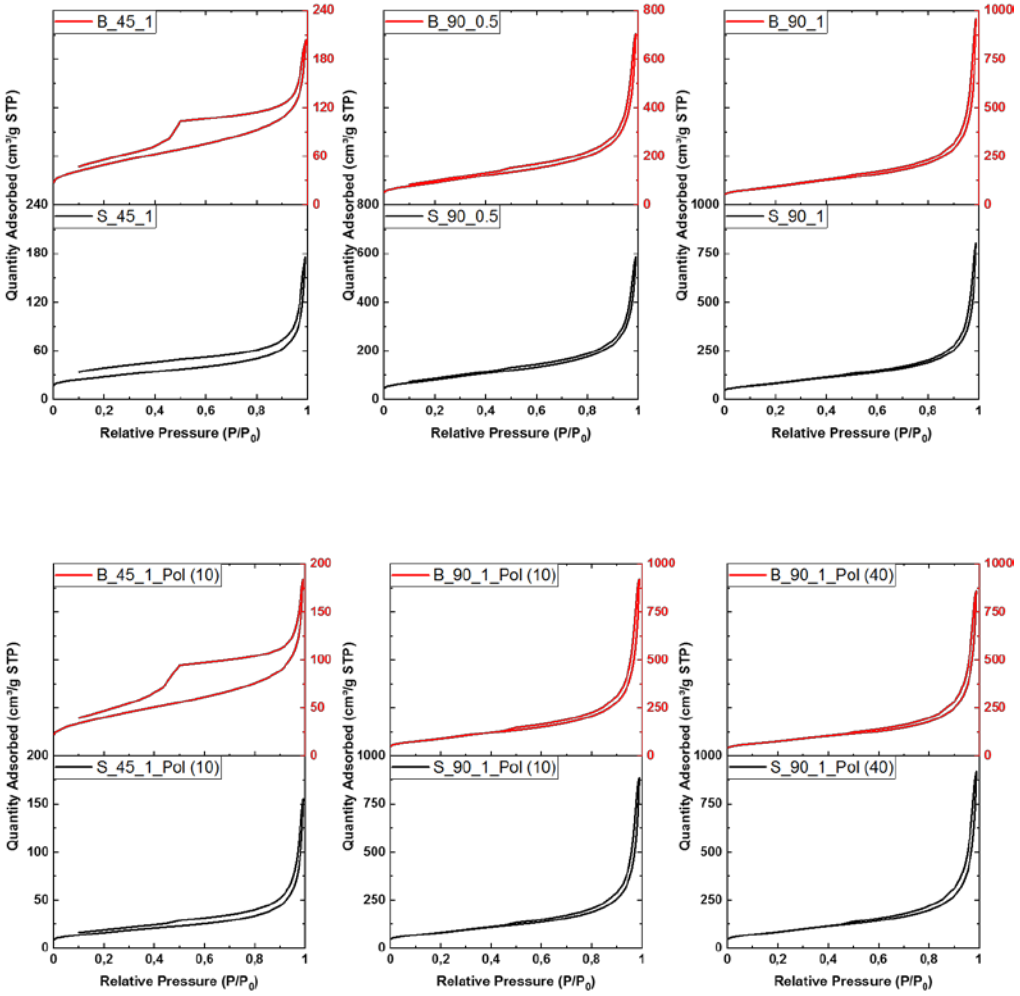

Figure 6.10. N_2 adsorption-desorption isotherms for small and large monolithic structures obtained at different reduction conditions.

From N_2 adsorption-desorption isotherms it can be observed that either small or big monoliths display a Type IV isotherm and Type H3 loop characteristic of mesoporous materials.[11] A similar N_2 adsorption-desorption behaviour is observed for small and big monoliths synthesized

at high temperatures (90 °C) at either 1:1 or 1:0.5 GO:AsA mass ratios, and with or without the presence of polymer particles. Nevertheless, some differences were observed for the materials synthesized at 45 °C. Although small and big structures present similar microstructure and thermal degradation performance, adsorption isotherms show that reduction temperature affects importantly in the textural properties. Samples synthesized at higher amount of initial GO and 45 °C exhibit a wider hysteresis loop. This is an indication that the large structures at 45 ºC have more developed mesoporosity and more pronounced capillary condensation effect. Probably, the platelets of rGO are pushed to aggregate by smaller driving force, resulting in creation in numerous small mesopores between the individual platelets joined together.

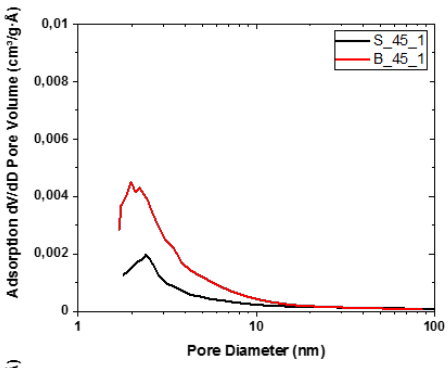
Adsorption dV/dD Pore Volume (cm³/g·Å)
Pore Diameter (nm)
S_45_1
B_45_1

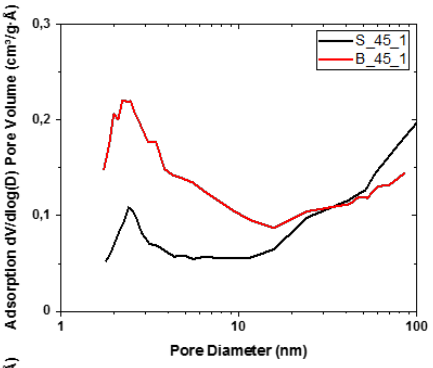
Adsorption dV/dlog(D) Pore Volume (cm³/g·Å)
Pore Diameter (nm)
S_45_1
B_45_1

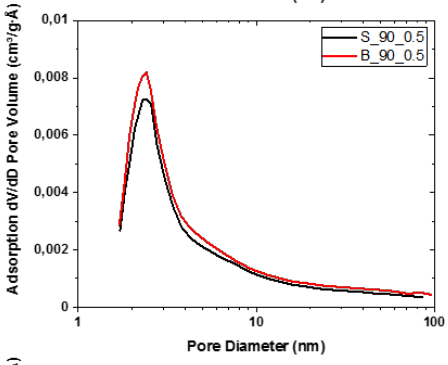
Adsorption dV/dD Pore Volume (cm³/g·Å)
Pore Diameter (nm)
S_90_0.5
B_90_0.5

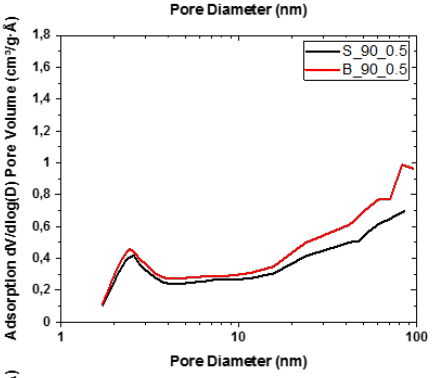
Adsorption dV/dlog(D) Pore Volume (cm³/g·Å)
Pore Diameter (nm)
S_90_0.5
B_90_0.5

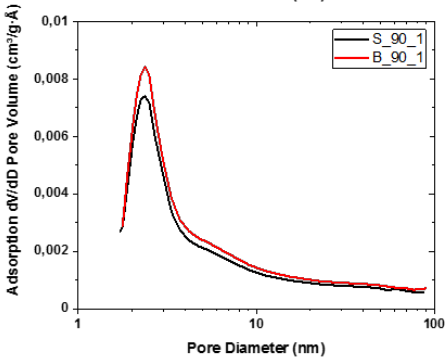
Adsorption dV/dD Pore Volume (cm³/g·Å)
Pore Diameter (nm)
S_90_1
B_90_1

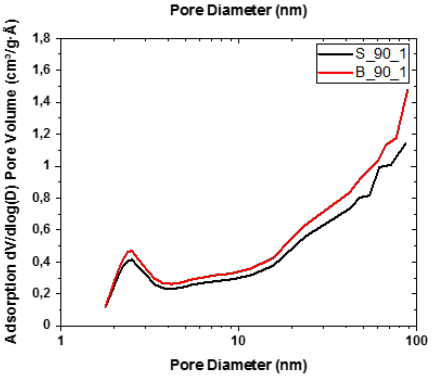
Adsorption dV/dlog(D) Pore Volume (cm³/g·Å)
Pore Diameter (nm)
S_90_1
B_90_1

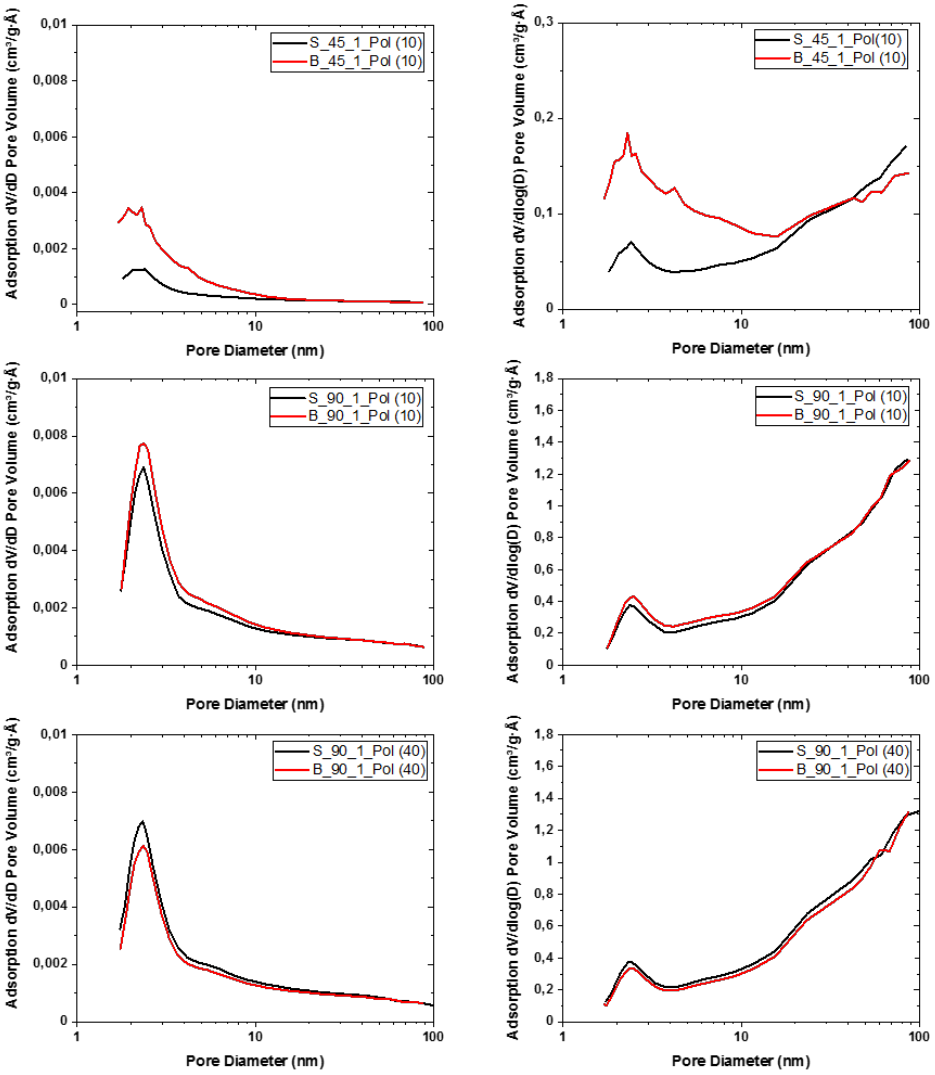

Figure 6.11. Pore size distributions for small and large monolith structures obtained at different conditions.

Comparing the pore size distributions of small and big structures shown in Figure 6.11, the difference between them may be observed in the micropores and small mesopores fractions, which is larger for the big structures. This difference decrease with increasing the reduction

temperature, resulting in almost identical features of the materials synthesized at 90 °C. The presence of polymer particles did not affect the observed trends.

In Table 6.2, the residual oxygen groups and textural properties are presented for different monoliths. The CO_2 adsorption capacities measured at 25 °C and 1 atm are also shown, while the CO_2 adsorption-desorption isotherms are presented in Figure 6.12.

Table 6.2. Amount of residual oxygen functionalities, textural properties, and CO_2 adsorption capacities of different monoliths.

Material	% O-functionalitiy	S_{BET} (m^2/g)	V_{total} (cm^3/g)	V_{micro} (cm^3/g)	% Micro	CO_2 adsorption (mmol/g)
S_45_1	18	98	0.272	0.013	4.7	1.04
B_45_1	18	178	0.315	0.009	2.8	0.69
S_90_0.5	9	293	0.905	0.020	2.2	0.80
B_90_0.5	8	332	1.089	0.021	1.9	0.64
S_90_1	5	301	1.242	0.021	1.7	0.75
B_90_1	4	340	1.481	0.026	1.8	0.64
S_45_1_Pol (10)	19	58	0.240	0.002	1.0	0.91
B_45_1_Pol (10)	20	145	0.284	0.006	2.1	0.68
S_90_1_Pol (10)	4	292	1.371	0.018	1.3	0.78
B_90_1_Pol (10)	4	324	1.421	0.024	1.7	0.64
S_90_1_Pol (40)	3	271	1.253	0.010	0.8	0.61
B_90_1_Pol (40)	3	279	1.328	0.013	1.0	0.54

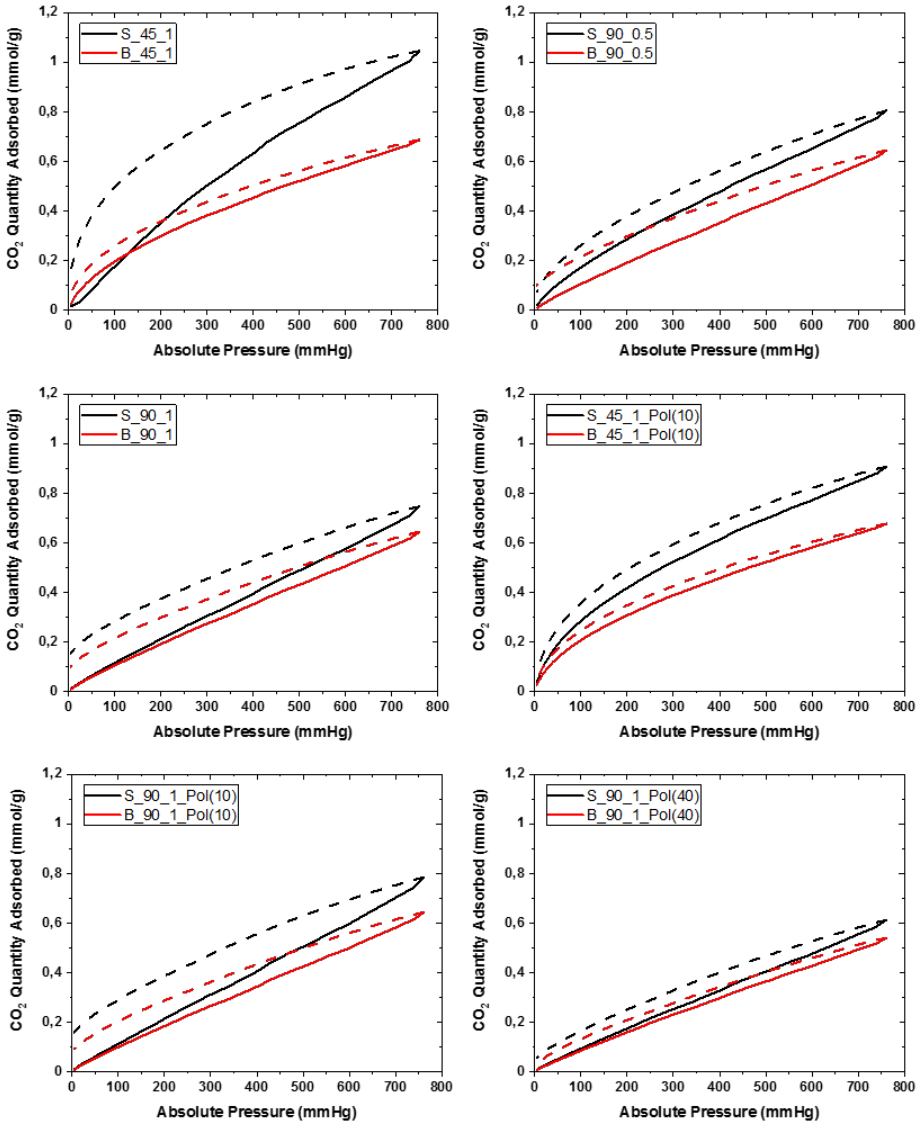

Figure 6.12. CO_2 adsorption (full line) – desorption (dashed line) isotherms for all the monoliths.

The same or similar concentration of residual oxygen-containing functional groups were obtained for each couple of systems. On the other hand, the specific BET area is in general larger for the big monoliths and this effect is much more pronounced for the monoliths synthesized at 45 ºC. For instance, S_45_1 has a BET area of 98 m^2/g, and B_45_1, has almost double surface area of 178 m^2/g. The large monoliths are more porous in all cases, probably due to higher quantity of small mesopores, as it can be observed in Figure 6.11. Nevertheless, the micropore fraction is lower for the large monoliths, in case of neat rGO structures, whereas in presence of polymers the trend is different. The effect of polymer is more important for the large structures and stimulates development of more micropores when the reduction is performed with higher quantities of material, although the differences are not very large.

Finally, the comparison of CO_2 adsorption capacities indicates that small monoliths have higher CO_2 capture than their respective big structures in all the systems studied, even so in monoliths synthesized at 90 °C there is only a slightly difference. During the results obtained through this PhD Thesis, it has been determined that a denser functionalization in terms of quantity of residual oxygen groups per available surface area, enhances the CO_2 adsorption of the resulting 3D structures. The results obtained in Table 6.2 also indicates the same behaviour, where smaller samples possess a much denser functionalization obtaining better adsorption capacities at the conditions studied. In fact, the highest CO_2 capture capacities were obtained for monoliths with the lowest BET area, but highest fraction of oxygen functionalities, S_45_1 and S_45_1_Pol (10), with 18 % and 98 m^2/g and 19 % and 58 m^2/g, respectively, obtaining 1.04 and 0.91 mmol/g CO_2 captured, respectively. Of course the functionalities from the polymer are additional, and the same quantity is distributed over smaller area in case of S_45_1_Pol(10) with respect to the big monolith obtained under same condition.

Interestingly, the large monoliths adsorbed very similar quantity of CO_2 of around 0.6 mmol/g independently on the conditions of synthesis and presence of polymer. Obviously, when higher productivity of monoliths is targeted, the parameters are less influencing, therefore the control of the properties and performance is more difficult. As we have noticed in all previous work, the CO_2 capture capacity is a result of interplay of BET surface area and fraction of oxygen functionalities with some effect of the pore size distribution, too. If we compare only the large structures between them, one may conclude that when produced at similar temperature they present similar functionalization and area, resulting in almost identical CO_2 adsorption. With other words the differences aroused from different conditions are either flattened or compensate between them, and as so the CO_2 adsorption.

Nevertheless, the results presented in Table 6.2 indicate that the process is scalable fairly well at 90 ºC, as the functionalization and porous properties are similar, as well as the CO_2 adsorption quantities, which open the way towards very well controlled synthesis of these monolithic materials at larger scale.

6.3.2. High-pressure CO_2 adsorption performance

The high-pressure CO_2 adsorption isotherms obtained at two temperatures (25 °C and 60 °C) and a pressure range from 0 to 20 atm are discussed in this part. The IGA equipment used for the high-pressure CO_2 adsorption measurements works under gravimetric conditions, whereas all the adsorption performances measured during this PhD project were evaluated by low-pressure volumetric apparatus (at 25 °C and in a pressure range from 0 to 1 atm).

Four different small samples were chosen for this characterization, one neat rGO monolith S_90_1, and three composite monoliths produced at different temperatures S_45_1_Pol (10),

and S_90_1_Pol (10), and with different polymer quantity S_90_1_Pol (40). The characteristics of these samples are already presented in Table 6.2, whereas the adsorption isotherms in the 0–20 atm pressure range performed at temperatures 25 ºC and 60 ºC are presented in Figure 6.13. Furthermore, enlarged view of the isotherms in 0 to 1 atm pressure range is also presented in Figure 6.13, in order to directly compare with the CO_2 capture results presented in Table 6.2. The temperature applied for each measurement is presented in brackets next to the nomenclature.

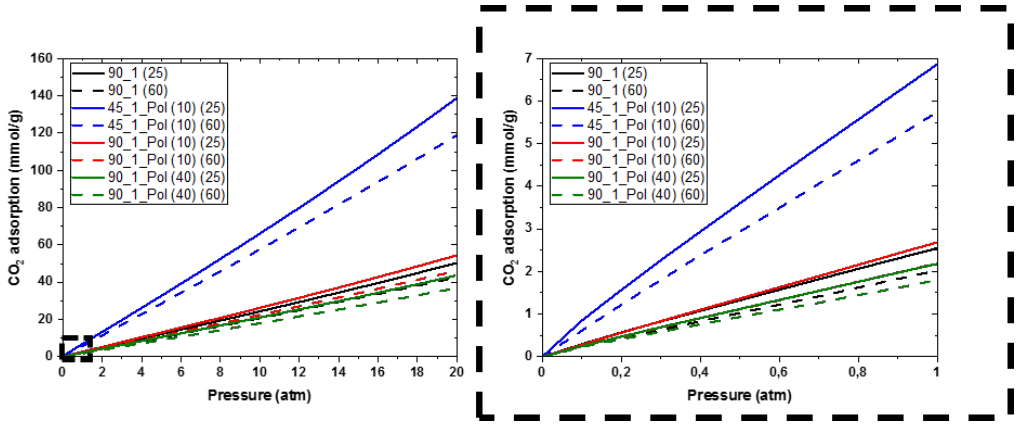

Figure 6.13. High-pressure CO_2 adsorption isotherms for different structures up to 20 atm. Furthermore, enlarged view of the pressure range of 0 to 1 atm is also presented.

One of the main factor determining the CO_2 adsorption by porous materials is the specific surface area. However, BET area may be predominant at high-pressures adsorption performances. Taking into account the BET data obtained in Table 6.2, the BET area increases from S_45_1_Pol (10) < S_90_1_Pol (40) < S_90_1_Pol (10) < S_90_1 (58 < 272 < 292 < 301, respectively). Thus, there is no any relationship between the BET surface area and CO_2 capture capacity (Figure 6.13). Probable reason could be that, at conditions measured until 20 atm of pressure, the CO_2 gas does not cover all the available or apparent surface area. Again, the

maximum adsorption was achieved by the material which is more densely functionalized S_45_1_Pol(10) having a fraction of 19 % oxygen functionalities distributed on relatively low surface area of 58 m^2/g.

On the other hand, adsorption phenomenon is an exothermic process in nature, therefore, as expected increasing adsorption temperatures from 25 °C to 60 °C decreases the uptake capacity as shown in Figure 6.13 for all the samples analyzed, characteristic for porous carbons.[12] For example, in case S_45_Pol (10) the amount of CO_2 adsorbed at 25 °C is 139 mmol/g, and when temperature is increased to 60 °C the adsorption drops to 119 mmol/g at same pressure (20 atm). Furthermore, adsorption capacities between 40-55 mmol/g were obtained with monoliths synthesized at 90 °C, with either presence or absence of polymer particles. This value is slightly higher than that reported in literature measured at 25 °C and at similar high pressures for carbon-based adsorbents, that reached up to 28 mmol/g.[6,8,13–16] Surprisingly, much higher adsorption capacity is obtained, 139 mmol/g, by S_45_1_Pol(10) (25 °C) sample. This monolith also showed one of the highest adsorption in Table 6.2 (volumetrically), although the difference with the other monoliths is not so pronounced as in gravimetrical experiments. This monolith possesses the highest residual oxygen groups and lowest surface area, therefore, the denser functionalization impacts the surface polarity of the monolith, which may be the reason of such a huge adsorption performance, as seen also during this thesis.[9] Besides, the pore size distribution is similar for all the systems studied, being S_45_1_Pol(10) sample with the lowest total volume of the pores. Thus, neither BET specific surface area nor pore size distribution could explain the huge adsorption capacity obtained by S_45_1_Pol(10) monolith.

In terms of polymer presence, in monoliths synthesized at 90 °C, it can be observed that samples with the highest amount of polymer particles (40 wt%) obtained the worst CO_2 captures. This is not surprising, these monolithic structures have shown worst residual oxygen functionalities and textural properties during the thesis that led to a drop in the adsorption performance. On the other hand, monoliths with the addition of 10 wt% present similar or slightly higher CO_2 captures than that of 3D neat rGO materials (S_90_1), tendency that can be also observed in this results (Table 6.2 and Figure 6.13).

In Table 6.3, the comparison of CO_2 adsorption capacities measured volumetrically (Table 6.2) and gravimetrically (Figure 6.13) at 25 °C and 1 atm, for S_45_1_Pol (10), S_90_1, S_90_1_Pol (10), and S_90_1_Pol (40) are presented. The density of oxygen functionalization, calculated as a ratio between the mass of oxygen functionalities present in 1 g of monolith divided by the specific surface area (m^2/g), is also shown in Table 6.3, demonstrating that this parameter perfectly explain the CO_2 adsorption behavior. Namely, S_45_1_Pol(10) presents more than one order of magnitude higher surface functionalization than the other monoliths and the highest adsorption. On the other hand, the other monoliths present similar density of oxygen functional groups and similar adsorption capacities.

Table 6.3. Comparison of CO_2 adsorption performance measured volumetrically and gravimetrically at 25 °C and up to 1 atm for different structures. Functionalization density is also presented.

Material	Volumetric CO_2 adsorption (mmol/g)	Gravimetrically CO_2 adsorption (mmol/g)	Functionalization density g oxygen groups/m^2
S_45_1_Pol (10)	0.91	6.9	0.33
S_90_1	0.75	2.55	0.016
S_90_1_Pol (10)	0.78	2.71	0.014
S_90_1_Pol(40)	0.61	2.2	0.011

Nevertheless, in Table 6.3, the results obtained from volumetrical and gravimetrical measurements of CO_2 adsorption do not match each other and the difference is relatively high. Higher adsorption capacities are obtained when gravimetrical instruments are used, although the tendency between individual monoliths is the same, i.e. the highest CO_2 adsorption capacity was obtained in S_45_1_Pol (10) and similar for the other three monoliths. Volumetric gas sorption analysis has better precision in measurements in the range of vacuum to atmospheric pressure compare with gravimetric sorption analysis. Instead, at high pressures (> 1 atm), gravimetric sorption analysis is the most reliable and well established technique.[17] Previous comparison of these two techniques has shown similar trend that the volumetrically determined gas sorption are usually lower than gravimetrical ones, attributed to an error during determination of the adsorbent volume of the volumetric technique.[18] Nevertheless, as in majority in this PhD project the comparison between the materials was performed, we consider that the error was similar in all measurements and the tendencies discussed are the same and unaffected by measurement technique.

Finally, based on the CO_2 adsorption isotherms at 25 °C and 60 °C from Figure 6.13, the isosteric heat of adsorption (Q_{st}) were calculated using the van´t Hoff equation. The results showed that the heat of adsorption from one sample to the other slightly varied and the values obtained were in the range of 4-13 KJ/mol, suggesting that CO_2 was adsorbed by physical adsorption process, as the reported rang of physical interaction between CO_2 and adsorbents is 5-40 KJ/mol.[19] In contrast, the heat of adsorption produced in chemical adsorption is typically between 40 and 800 KJ/mol.[20] This value is an indicator for the strength bond between the adsorbate (CO_2 gas) and the pore surface of the adsorbent. The high heat of adsorption is also related with high selectivity, nevertheless the regeneration step may be difficult. Therefore, the optimization of the binding energy of CO_2 in order to have high selectivity and low regeneration is necessary.

If the binding strength is too low, the volume of the adsorbent bed will be large; but, if it is too high, the cost of regeneration will be high. The combination of these values will decide the heating, and so, the regeneration efficiency.[21] Nevertheless, in the same work, when pack bed was contrasted to monoliths, the monoliths have shown less mass transfer resistance and improved efficiency of the mass transfer. As in this work the adsorption material is already in monolithic form, the low energy of adsorption will allow much easier regeneration, and it can be added to the list of the practical advances these monoliths are offering. On the other hand, the synthesis procedure in this chapter was the one in which the pre-treatment of the monoliths was already avoided, for which materials, as shown in Chapter 4, the selectivity was in range of several hundreds, excluding the possible limitation of low selectivity due to low adsorption heat.

6.4. Conclusions

In this Chapter 6, 3D graphene-polymer monolithic structures were synthesized at larger scale applying the same synthesis route and 6 fold higher quantities with respect to previous chapters, in order to study how the productivity increase will influence the self-assembly process and products´ properties. For that, small and large monoliths were synthesized at different conditions; reduction temperature (45 °C and 90 °C), amount of reducing agent (GO:AsA mass ratio 1:1 and 1:0.5), and amount of MMA-GMA polymer particles (10 or 40 wt% based on initial GO amount).

Large monoliths were formed under all applied synthesis conditions, except at the mildest conditions of 45 ºC and lowest amount of reducing agent, likely due to a lack of sufficient driving force for the self-assembly process.

The big monoliths in general presented similar fraction of oxygen functional groups and higher BET surface area than their small counterparts, which resulted in a drop of oxygen functionalities surface density, and subsequently, lower capacities for CO_2 adsorption. These differences are more pronounced at lower reduction temperatures and descent at increasing temperature, which implies that the scale-up process is more efficient under such conditions and provide very similar properties and performance between small and large monoliths. The highest CO_2 capture capacities were obtained by monoliths synthesized at 45 °C, with and without the addition of polymer particles, because of a denser functionalization over smaller surface area. Nevertheless, all the results indicate that the synthesis process is quite scalable at 90 °C which open the opportunity to control the synthesis of these 3D structures at larger scale.

Finally, the CO_2 adsorption performance of selected four of the small structures was studied under extended conditions, up to 20 atm pressure and at different temperatures (25 °C

and 60 °C). The adsorption performance at higher pressures was followed using gravimetric measurement technique, differently than all studies performed so far, using volumetric measurements. At pressures higher than 1 atm, the trends between the individual monoliths were kept the same as observed at lower pressure, governed by the same parameter of density of the oxygen functional groups on the monoliths surfaces. Nevertheless, an important difference of the absolute values of capturing capacity between the both methods gravimetric and volumetric was observed, probably due to an error occurring during volume determination in the volumetric method. Despite that, the same trends observed by both methods ensures accurate discussions of the tendencies obtained within this PhD project.

Based on the gravimetrically determined adsorption isotherms at two different temperatures 25 ºC and 60 ºC, the heat of adsorption was calculated for the mentioned selected monoliths, giving a values in a range of 4-13 KJ/mol. It indicates that CO_2 gas is adsorbed by physically onto the monoliths. Even though the high heat of adsorption is related with selectivity, the selectivity of these monoliths was improved by avoiding the pre-treatment step, as demonstrated previously, therefore, the low heat of adsorption suggest a low regeneration energy of these monoliths which is of great practical application importance. Thus, these 3D monoliths may be also applied in pre- and oxy-combustion technologies.

6.5. References

(1) Chandrasekaran, S.; Cerón, M. R.; Worsley, M. A. *CHAPTER 1. Engineering the Architecture of 3D Graphene-Based Macrostructures*; The Royal Society of Chemistry, 2021.

(2) Pardemann, R.; Meyer, B. Pre-Combustion Carbon Capture. *Handb. Clean Energy Syst.* **2015**, 1–28.

(3) Scheffknecht, G.; Al-Makhadmeh, L.; Schnell, U.; Maier, J. Oxy-Fuel Coal Combustion-A Review of the Current State-of-the-Art. *Int. J. Greenh. Gas Control* **2011**, *5* (SUPPL. 1), 16–35.

(4) Casco, M. E.; Martínez-Escandell, M.; Silvestre-Albero, J.; Rodríguez-Reinoso, F. Effect of the Porous Structure in Carbon Materials for CO2 Capture at Atmospheric and High-Pressure. *Carbon N. Y.* **2014**, *67*, 230–235.

(5) Singh, G.; Kim, I. Y.; Lakhi, K. S.; Joseph, S.; Srivastava, P.; Naidu, R.; Vinu, A. Heteroatom Functionalized Activated Porous Biocarbons and Their Excellent Performance for CO2 Capture at High Pressure. *J. Mater. Chem. A* **2017**, *5* (40), 21196–21204.

(6) Srinivas, G.; Krungleviciute, V.; Guo, Z. X.; Yildirim, T. Exceptional CO2 Capture in a Hierarchically Porous Carbon with Simultaneous High Surface Area and Pore Volume. *Energy Environ. Sci.* **2014**, *7* (1), 335–342.

(7) Ashourirad, B.; Sekizkardes, A. K.; Altarawneh, S.; El-Kaderi, H. M. Exceptional Gas Adsorption Properties by Nitrogen-Doped Porous Carbons Derived from Benzimidazole-Linked Polymers. *Chem. Mater.* **2015**, *27* (4), 1349–1358.

(8) He, J.; To, J. W. F.; Psarras, P. C.; Yan, H.; Atkinson, T.; Holmes, R. T.; Nordlund, D.; Bao, Z.; Wilcox, J. Tunable Polyaniline-Based Porous Carbon with Ultrahigh Surface Area for CO2 Capture at Elevated Pressure. *Adv. Energy Mater.* **2016**, *6* (14).

(9) Singh, G.; Ramadass, K.; Lee, J. M.; Ismail, I. S.; Singh, M.; Bansal, V.; Yang, J. H.; Vinu, A. Convenient Design of Porous and Heteroatom Self-Doped Carbons for CO2 Capture. *Microporous Mesoporous Mater.* **2019**, *287* (April), 1–8.

(10) Liu, K.; Ostadhassan, M. The Impact of Pore Size Distribution Data Presentation Format on Pore Structure Interpretation of Shales. *Adv. Geo-Energy Res.* **2019**, *3* (2), 187–197.

(11) Thommes, M.; Kaneko, K.; Neimark, A. V.; Olivier, J. P.; Rodriguez-Reinoso, F.; Rouquerol, J.; Sing, K. S. W. Physisorption of Gases, with Special Reference to the Evaluation of Surface Area and Pore Size Distribution (IUPAC Technical Report). *Pure Appl. Chem.* **2015**, *87* (9–10), 1051–1069.

(12) Ullah, R.; Ali H Salah Saad, M.; Aparicio, S.; Atilhan, M. Adsorption Equilibrium Studies of CO2, CH4 and N2 on Various Modified Zeolites at High Pressures up to 200 Bars. *Microporous Mesoporous Mater.* **2018**, *262* (November 2017), 49–58.

(13) Jalilov, A. S.; Ruan, G.; Hwang, C. C.; Schipper, D. E.; Tour, J. J.; Li, Y.; Fei, H.; Samuel, E. L. G.; Tour, J. M. Asphalt-Derived High Surface Area Activated Porous Carbons for Carbon Dioxide Capture. *ACS Appl. Mater. Interfaces* **2015**, *7* (2), 1376–1382.

(14) Hwang, C. C.; Tour, J. J.; Kittrell, C.; Espinal, L.; Alemany, L. B.; Tour, J. M. Capturing Carbon Dioxide as a Polymer from Natural Gas. *Nat. Commun.* **2014**, *5*, 1–7.

(15) Zhang, Z.; Xu, M.; Wang, H.; Li, Z. Enhancement of CO2 Adsorption on High Surface Area Activated Carbon Modified by N2, H2 and Ammonia. *Chem. Eng. J.* **2010**, *160* (2), 571–577.

(16) Youn, H. K.; Kim, J.; Chandrasekar, G.; Jin, H.; Ahn, W. S. High Pressure Carbon Dioxide Adsorption on Nanoporous Carbons Prepared by Zeolite y Templating. *Mater. Lett.* **2011**, *65* (12), 1772–1774.

(17) Patel, H. A.; Byun, J.; Yavuz, C. T. Carbon Dioxide Capture Adsorbents: Chemistry and Methods. *ChemSusChem* **2017**, *10* (7), 1303–1317.

(18) Belmabkhout, Y.; Frère, M.; De Weireld, G. High-Pressure Adsorption Measurements. A Comparative Study of the Volumetric and Gravimetric Methods. *Meas. Sci. Technol.* **2004**, *15* (5), 848–858.

(19) Creamer, A. E.; Gao, B.; Creamer, A. E.; Gao, B. *SpringerBriefs in Molecular ScienceCarbon Dioxide Capture: An Effective Way to Combat Global WarmingAdsorbents for CO2 Capture*; 2015.

(20) Gao, A. E. C. B. *Carbon Dioxide Capture: An Effective Way to Combat Global Warming*, 2015th ed.; Springer, Ed.; 2015.

(21) Sumida, K.; Rogow, D. L.; Mason, J. A.; McDonald, T. M.; Bloch, E. D.; Herm, Z. R.; Bae, T. H.; Long, J. R. Carbon Dioxide Capture in Metal-Organic Frameworks. *Chem. Rev.* **2012**, *112* (2), 724–781.

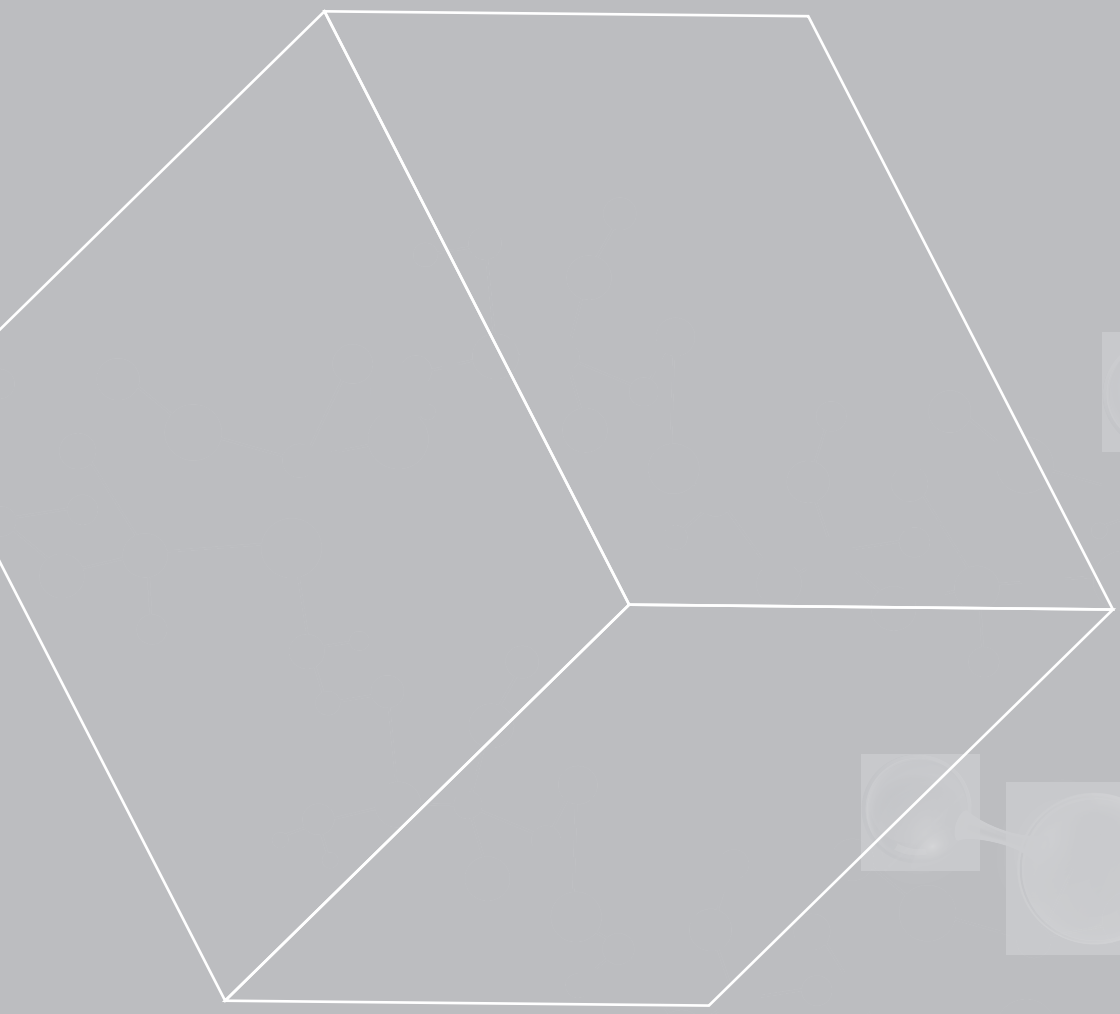

CHAPTER 7

Conclusions

Chapter 7. Conclusions

The substantial rise of CO_2 emission in the atmosphere is the primary reason of the global warming, and therefore, climate change. Several approaches, such as carbon capture and sequestration (CCS), have been considered to be potential ways in order to reduce anthropogenic CO_2 emissions. CCS solution transports the captured CO_2 from anthropogenic sources to a storage place avoiding the release to the atmosphere. The fossil-fuels power plants are the main contribution of the total CO_2 emission, and so, the principal point to capture CO_2, being post-combustion capture the most straightforward schema. CO_2 capture by physical adsorption separates the CO_2 gas from one phase and accumulates at a surface of a solid substance. Due to the attractive properties of both 3D graphene-based structures and polymer particles as adsorbents, the design of 3D porous graphene-polymer monolith composite structures for CO_2 capture post-combustion application has been carried out in this PhD Thesis.

The complex self-assembly hierarchical process of GO platelets occurred during their reduction to rGO, giving rise to 3D structures, characterized by consistency, low density, high porosity, and monolithic appearance. The chemical reduction of GO by reducing agent, AsA, at increased temperature eliminates the oxygen-containing functional groups from GO, producing much more hydrophobic rGO platelets. The surface energy of rGO platelets in the dispersion increases significantly, resulting in rGO self-organization towards the minimization of the interface between rGO and aqueous phases, obtaining 3D monolithic structures. The reduction parameters (amount of reducing agent and reduction temperature) play an important role

because they determine the degree and rate of the GO reduction process, which subsequently determine the resulting porous morphology.

A mechanism for the formation of the hierarchical porous structure was proposed. The hierarchical structure of the monoliths indicates that different self-assembly processes at different size scales of the respective building blocks are contributing toward the final structure formation. The micropores and the smaller mesopores may be formed during the initial restacking of the layers due to the reduction process and elimination of the oxygen-containing functionalities because the individual rGO are the smallest structural elements. Then, the joining of these small aggregates during further reduction forms the higher pore sizes (meso- and macropores).

The influence of the reduction conditions on the resulting 3D neat rGO structures´ properties was first analysed and relate to CO_2 adsorption performance measured at 1 atm and 25 °C. Mild synthesis conditions (low temperature and AsA concentration), results in monoliths with high functionalization degree and low BET area values, as probably the combination of low temperature and low AsA concentration did not provide sufficient driving force for the rGO self-assembly process. On the other hand, higher temperatures or AsA amounts produces more compact materials with very well-developed hierarchical porous structure and high porosities; however, lower contents of residual oxygen-containing functional groups. Reduction conditions that allow a relatively dense functionalization in combination with favourable textural properties determine a higher CO_2 adsorption capacity. Nevertheless, 3D neat rGO structures exhibited a slightly reduced capacity to capture CO_2 in 5 adsorption-desorption cycles. A solution was proposed to improve the mechanical stability of the monoliths by addition of a small amount of polymer particles, which indeed yielded a stable cycle operation.

In order to take advantage of the addition of the second constituent, polymer particles, in the graphene skeleton, functionalization of the polymer particles was carried out with the aim to not only improve the mechanical properties but also to enhance the CO_2 adsorption performance creating "CO_2-philic" groups that could interact with the adsorbate. Polymer particles were synthesized by emulsion polymerization in aqueous dispersed media process to avoid high-energy consuming processes and the use of volatile organic compounds that largely contribute to greenhouse gas effect. In this case, also, the graphene-polymer composites were synthesized by a chemical reduction of GO platelets, nevertheless prior to the reduction the GO aqueous dispersion is mixed with appropriate amount of polymer particles during which process the polymer particles are adsorbed onto the GO layers.

Two functional monomers, NaSS and AMPS, were copolymerized with the main monomer MMA. MMA particles were selected due to their high T_g, which ensures that during drying process the particles would not lost the particle morphology and will not entirely covered the rGO surface. Two different amount of polymer particles, 10 wt% and 40 wt%, were incorporated to the 3D monoliths at different reduction conditions. As in neat rGO results, mild conditions produces monoliths with high residual oxygen groups and low BET surface areas, and on the contrary, harder conditions results in lower functionality but higher surface areas. The addition of 10 % of polymer particles enlarged the amount of micropores, because the particles acted as spacers between the rGO layers. In terms of CO_2 adsorption, lower adsorption capacities were obtained for composites than for blank materials in most of the cases due to the higher affinity of graphene than of polymers towards CO_2. It was concluded that the interplay between the fraction of residual oxygen functional groups, textural properties and type and amount of polymers onto the monolithic materials determine the selective CO_2 capture.

As a way to improve the selectivity of CO_2 adsorption over N_2, the synthesis procedure of the 3D structures was modified towards augmentation of the fraction of oxygen functionalities and of the small mesopores. The pre-treatment step for GO dispersion carried out at 80 °C for 2.5 h eliminates certain quantity of oxygen functionalities from GO, resulting in decreasing the driving force for the monoliths formations and affects negatively the residual fraction of oxygen functionalities. Avoiding the pre-treatment step, 3D neat or composites monoliths present higher CO_2 and lower N_2 adsorption capacities. This effect was huge for the monoliths produced at the highest temperature (90 °C), resulting to selectivity values up to 621, which for the best authors´ knowledge, this value is maximum selectivity achieved by carbon-based structures at the conditions studied. The rise of CO_2 adsorption was also attributed to the increase of the functionalization while decreasing the BET area, resulting in densely functionalization surface. However, the morphology and textural properties of the monoliths produced with the modified synthesis could not explained the rise of N_2-phobicity. The attempts to obtain deeper understanding on the issue revealed that by modified synthesis procedure, the surface morphology of the graphene layers was impacted, producing rougher and more wrinkled surface, which likely induce less N_2 gas adsorption.

Size exclusion or molecular sieving effect is another mechanism to enhance the CO_2 adsorption of porous graphene structures. Crosslinked polymer particles were synthesized by emulsion polymerization process, in order to create chemical crosslinked polymer chains that prevent their complete collapsing, achieving a porous state. The crosslinked MMA polymer particles with a higher DVB amount results in an increase of the BET surface area. Nevertheless, the addition of 10 % crosslinked polymer particles, independently of the microstructure of the polymer particles (crosslinked or not), onto the graphene skeleton did not show any important improvement towards CO_2 adsorption. Instead, for the first time during this thesis, the addition of

40 % polymer particles enhance significantly the BET surface area and resulting functionalization of the structures, causing an improvement of CO_2 uptake.

Finally, 3D graphene-polymer monolithic structures were synthesized at larger scale applying the same synthesis route and 6 fold higher quantities with respect to previous chapters, in order to study how the productivity increase will influence the self-assembly process and products´ properties. For that, small and large 3D monoliths were synthesized at different reduction conditions and with and without the presence of polymer particles. Large monoliths were successfully synthesized under applied conditions, expect at lowest temperature and lowest amount of reducing agent, likely due to a lack of sufficient driving force for the self-assembly process. The big monoliths presented similar oxygen functional groups and higher BET area than their small counterparts, which resulted in a drop of functionalization density, and subsequently, lower CO_2 adsorption uptakes. Nevertheless, these differences are less pronounced at higher temperatures, which implies that the scale-up process is more efficient under such conditions. Thus, the synthesis process is quite scalable at 90 °C which opens the opportunity to control the synthesis of these 3D structures at larger scale.

The CO_2 adsorption performance of selected four small monoliths was studied up to 20 atm and at different temperatures by gravimetric measurement technique as a way to open the possibility of using graphene-based adsorbent for alternative application. The data obtained was compared to volumetric measurements up to 1 atm, and although different values were obtained, the trends between individual monoliths were kept the same, governed by the same parameter of density of the functional groups on the monoliths surfaces. The low heat of adsorption measured for the selected monoliths, in the range of physical adsorption, suggests a low regeneration energy and low selectivity. Nevertheless, the selectivity of these monoliths was

improved by avoiding the pre-treatment step. Thus, these 3D monoliths may be also applied in pre- and oxy-combustion technologies.

To sum up, the characteristics of the 3D porous graphene-polymer monoliths can be tailored by simple procedures resulting in competitive CO_2 adsorption capacities for practical applications.

Resumen y conclusiones

Resumen y conclusiones

El aumento de las emisiones de CO_2 en la atmósfera es la principal causa del calentamiento global y, por lo tanto, del cambio climático. Siendo el cambio climático uno de los problemas medioambientales más graves a los que se enfrenta el planeta. Por ello, se han considerado varias estrategias, como la captura y secuestro de carbono (CCS), como posibles soluciones para reducir las emisiones antropogénicas de CO_2. La estrategia CCS transporta el CO_2 capturado desde fuentes antropogénicas hasta un lugar de almacenamiento evitando así su liberación a la atmósfera, y de esta manera, prevenir o disminuir las consecuencias catastróficas del calentamiento global. La mayor fuente de las emisiones de CO_2 procede de la combustión de fósiles en las centrales eléctricas y, por lo tanto, son consideradas como el principal punto de captura de CO_2. La adsorción física con sólidos se plantea como una solución prometedora frente a otros procesos de captura de gas. La captura de CO_2 por el proceso de adsorción física separa el gas CO_2 de una fase acumulándose en la superficie de una sustancia sólida, en el presente contexto, debido a la unión de fuerzas débiles como fuerzas de van der Waals o fuerzas electrostáticas (fisisorción). En esta Tesis Doctoral se propone el uso de estructuras monolíticas tridimensionales (3D) compuestas de grafeno y partículas de polímero como adsorbentes sólidos para la captura de CO_2, ya que ofrecen claros beneficios en lo que respecta a la adsorción de CO_2.

El complejo proceso jerárquico de autoensamblaje de las plaquetas o láminas de óxido de grafeno (GO) dispersas en fase acuosa ocurre durante su reducción química a óxido de grafeno reducido (rGO), dando lugar a estructuras 3D, características por su consistencia, baja

densidad, alta porosidad y apariencia monolítica. La reducción química de GO mediante el agente reductor, ácido ascórbico (AsA), y la influencia de temperatura, elimina los grupos funcionales oxigenados presentes en el GO, obteniendo plaquetas de rGO con carácter hidrofóbico. De este modo, la energía superficial de las plaquetas de rGO dispersas en agua aumenta significativamente, dando como resultado el autoensamblaje de las plaquetas con el objetivo de minimizar la energía interfacial entre rGO y la fase acuosa, creando así estructuras monolíticas 3D. Los parámetros de reducción (cantidad de agente reductor y temperatura de reducción) juegan un papel muy importante, ya que determinan el grado y la velocidad del proceso de reducción del GO y, por ende, la morfología porosa resultante.

En el capítulo 2, se propuso un mecanismo jerárquico para la formación de la estructura 3D porosa. La estructura jerárquica de los monolitos indica que diferentes procesos de autoensamblaje en diferentes escalas de tamaño de los respectivos bloques de construcción (plaquetas de grafeno y plaquetas de grafeno-polímero) están contribuyendo a la formación de la estructura final. Los microporos y los mesoporos más pequeños se formarían durante el apilamiento inicial de las láminas de óxido de grafeno, debido al proceso de reducción y eliminación de los grupos funcionales oxigenados. Después, la unión de estos pequeños agregados durante la reducción adicional formaría los tamaños de poro más grandes (meso y macroporos).

Por otra parte, se analizó el efecto de las condiciones de reducción (temperatura y cantidad de AsA) en las propiedades resultantes de las estructuras monolíticas puras de rGO, y se relacionaron con el rendimiento de adsorción de CO_2, llevado a cabo en las siguientes condiciones: 1 atm y 25 °C. Las condiciones de síntesis moderadas (baja temperatura y concentración de AsA) dieron como resultado monolitos con alto grado de funcionalización y bajos valores de área superficial (BET). Probablemente, la combinación de baja temperatura y

baja concentración de AsA no proporcionó suficiente fuerza motriz para el proceso de autoensamblaje de las láminas de rGO y la conformación de un monolito con alta porosidad. Por el contrario, temperaturas más altas y mayores cantidades de AsA, produjeron materiales más compactos y más porosos, pero con contenidos más bajos de grupos funcionales residuales. Los resultados de adsorción de CO_2 concluyeron que las condiciones de reducción que dan lugar a una funcionalización relativamente densa en combinación con propiedades texturales favorables, determinan una mayor capacidad de adsorción. Sin embargo, el estudio de 5 ciclos de adsorción-desorción de CO_2 llevado a cabo en el mismo monolito de rGO puro, determinó una ligera disminución en la capacidad de adsorción en cada ciclo completado. Por consiguiente, se propuso la adición de una pequeña cantidad de partículas de polímero para la posible mejora de la estabilidad mecánica. El compuesto resultante mantuvo una capacidad de adsorción de ciclo estable.

En el capítulo 3, para sacar mayor provecho a la adición del segundo constituyente, partículas de polímero, se llevó a cabo la funcionalización de las partículas poliméricas con el objetivo no solo de mejorar las propiedades mecánicas, sino también de mejorar la capacidad de adsorción de CO_2 respecto a los monolitos puros de rGO. La incorporación de diferentes grupos funcionales a las cadenas poliméricas establece zonas "CO_2-fílicas" capaces de interactuar con el adsorbato. Las partículas de polímero se sintetizaron mediante la polimerización en emulsión, técnica que permite sintetizar partículas poliméricas dispersas en fase acuosa, y de este modo, evitar el uso de compuestos orgánicos volátiles, ya que contribuyen en gran medida a la emisión de los gases de efecto invernadero. Los compuestos de grafeno-polímero, al igual que las estructuras puras de rGO, se sintetizaron mediante la reducción química de las plaquetas de GO; sin embargo, en este caso, antes de proceder con la reducción, la dispersión acuosa de GO fue combinada con la cantidad adecuada de partículas

de polímero dispersas en fase acuosa. Durante este proceso, las partículas de polímero son adsorbidas en las láminas de GO.

La funcionalización de las partículas de polímero se llevó a cabo mediante la copolimerización de dos monómeros funcionales, NaSS y AMPS, con el monómero principal MMA. Las partículas de MMA se seleccionaron debido a su alta T_g, lo que garantiza que durante el proceso de secado las partículas no pierdan la morfología particular, y así, evitar cubrir por completo la superficie de rGO. Se incorporaron dos cantidades diferentes de partículas de polímero al esqueleto de grafeno, 10 % y 40 % en peso, a diferentes condiciones de reducción. Al igual que en los resultados obtenidos en los monolitos puros, en este caso también, las condiciones de síntesis moderadas produjeron monolitos con altos grupos de oxígeno residual y baja área superficial, en cambio, las condiciones más agresivas dieron como resultado una funcionalidad más baja y áreas de superficie más altas. Por otro lado, la adición de 10 % de partículas poliméricas aumentó la cantidad de microporos, debido a que las partículas actuaron como espaciadores entre las laminas de rGO. En relación a la captura de CO_2, se obtuvieron menores capacidades de adsorción para los materiales compuestos respecto a los materiales puros en la mayoría de los casos estudiados, debido a la mayor afinidad del grafeno con el CO_2 comparado con la menor afinidad de los polímeros. En el capítulo 3, se concluyó que la fracción de grupos funcionales de oxígeno residual, las propiedades texturales y el tipo y cantidad de polímeros determinan la captura selectiva de CO_2.

Con el objetivo de acrecentar la selectividad de CO_2 sobre N_2 en los procesos de adsorción, en el capítulo 4, se modificó el procedimiento de síntesis de las estructuras 3D, y así aumentar la fracción residual de funcionalidades de grupos de oxígeno y la cantidad de mesoporos, propiedades que dan lugar a una mayor interacción con el CO_2. El paso de pretratamiento de la dispersión de GO llevado a cabo en capítulos anteriores a 80 °C durante

2,5 h elimina cierta cantidad de grupos de oxígeno del GO, lo que reduce la fuerza motriz en la formación de monolitos y afecta negativamente a la fracción residual de funcionalidades. El descarte del paso de pretratamiento, dio lugar a monolitos puros o compuestos con mayores capacidades de adsorción de CO_2 y menores adsorciones de N_2. Este efecto fue muy significativo para los monolitos producidos a temperaturas más altas, dando como resultado valores de selectividad de hasta 621, que para el conocimiento de los autores, este valor es el máximo alcanzado por las estructuras a base de carbono en las condiciones estudiadas. El aumento de la adsorción de CO_2 también se atribuyó al aumento de la funcionalización localizada en una area superficial más pequeña, es decir, una funcionalización más densa. Sin embargo, la morfología y las propiedades texturales de los monolitos producidos con la síntesis modificada no justificaron las bajas adsorciones de N_2. Los intentos de obtener una comprensión más profunda sobre el tema revelaron que, mediante el procedimiento de síntesis modificado, la morfología de la superficie de las láminas de grafeno se vio afectada, produciendo una superficie más rugosa y arrugada, lo que probablemente induciría a una menor adsorción de N_2.

El efecto de exclusión molecular es otro mecanismo para mejorar la adsorción de CO_2 de las estructuras porosas. Por ese motivo, en el capítulo 5, partículas de polímero reticulado fueron sintetizadas mediante el proceso de polimerización en emulsión, con el fin de crear cadenas químicas de polímero reticulado con un mayor estado poroso. Las partículas de polímero de MMA reticuladas con una mayor cantidad de DVB dieron como resultado un aumento del área superficial BET. Sin embargo, la adición de un 10 % de partículas de polímero, independientemente de la microestructura de las partículas de polímero (reticuladas o no), sobre el esqueleto de grafeno, no mostró ninguna mejora importante en la adsorción de CO_2. Por el contrario, por primera vez durante esta tesis, la adición de un 40 % de partículas de polímero

mejoró significativamente el área de superficie BET y la funcionalización resultante de las estructuras, generando una mejora en la adsorción de CO_2.

Finalmente, en el capítulo 6, se sintetizaron estructuras monolíticas de grafeno-polímero 3D a mayor escala aplicando la misma ruta de síntesis y cantidades 6 veces mayores con respecto a los capítulos anteriores, con el fin de estudiar cómo el aumento de la productividad influye en el proceso de autoensamblaje y, por ende, en las propiedades texturales y de adsorción de los productos. Con este fin, se sintetizaron monolitos 3D pequeños y grandes en diferentes condiciones de reducción, y con y sin presencia de partículas poliméricas. Todos los monolitos se sintetizaron con éxito en las condiciones aplicadas, excepto el monolito a escala mayor sintetizado a la temperatura más baja y con la cantidad más pequeña de agente reductor, probablemente debido a la falta de fuerza motriz suficiente para el proceso de autoensamblaje. Los monolitos grandes presentaron grupos funcionales de oxígeno similares y un área BET más alta en comparación con las estructuras pequeñas, lo que resultó en una caída de la densidad de funcionalización y, en consecuencia, en una menor adsorción de CO_2. No obstante, estas diferencias en las propiedades entre los monolitos pequeños y grandes fueron menos pronunciadas cuando la síntesis se llevó a cabo a temperaturas más altas, lo que implica que el proceso de escalado es más eficiente en dichas condiciones.

Además, se investigó el rendimiento de adsorción de CO_2 de cuatro monolitos pequeños, pero en este caso, hasta 20 atm y a diferentes temperaturas, mediante la técnica de medición gravimétrica, como una forma de estudiar la posibilidad de utilizar el monolito en aplicaciones alternativas. Los datos obtenidos se compararon con medidas volumétricas hasta 1 atm, y a pesar de que se obtuvieron valores diferentes de un equipo a otro, las tendencias de adsorción entre monolitos se mantuvieron iguales, gobernadas por el mismo parámetro de densidad de los grupos funcionales en la superficie de los monolitos. Los valores de calor de adsorción

obtenidos afirmaron que la interacción existente entre el gas de CO_2 y las estructuras monolíticas es puramente física, lo que implica una baja energía de regeneración y, por el contrario, una baja selectividad. Aun así, el estudio llevado a cabo en el capitulo 4, mejoró la selectividad de estos monolitos al evitar el paso de pretratamiento en la síntesis.

En conclusión, se ha demostrado que las propiedades de los monolitos 3D compuestos de grafeno y partículas poliméricas pueden ser modificadas mediante procesos simples y respetuosos con el medio ambiente, dando lugar a capacidades de adsorción competitivas para uso práctico.

APPENDIX I

General characterization methods

Appendix I. General characterization methods

I.1. Latex characterization

I.1.1. Solids content and monomer conversion

The monomer conversion (X_M) is defined as a fraction of monomer that has been converted into polymer at any reaction time. In case MMA and GMA volatile monomers, the conversion was determined gravimetrically. Approximately 2 mL latex samples were withdrawn from the reactor and the free radical polymerization was immediately quenched by the addition of ≈ 0.1 mL of a 1 wt % hydroquinone (HQ) solution in water. The samples were dried in aluminum caps at 60 °C until constant weight was achieved. The solids content (SC), i.e. the non-volatile fraction of the dispersions, was calculated from the weight ratio between the dry solids and the latex (Equation I.1)

$$SC = \frac{Dry\ solid\ (g)}{Latex\ (g)} \qquad \text{Equation I.1}$$

The monomer conversion (X_M) was then calculated from the solids content of the dispersions according to Equation I.2,

$$X_M = \frac{m_{pol}}{m_{mon}} = \frac{SC * m_{latex-NPF}}{m_{mon}} \qquad \text{Equation I.2}$$

where NPF is the mass of the non-polymeric solids fraction of the sample (includes the surfactant, initiator and HQ), m_{latex} is the mass of the latex and m_{mon} is the amount of monomer.

I.1.2. Particle size

The particle size of the polymer dispersions were measured by dynamic light scattering (DLS) using a Zetasizer Nano Z (Malvern Panalytical, UK). The equipment determines the particle size by measuring the rate of fluctuations in laser light intensity scattered by particles as they diffuse through a fluid. The samples were prepared by dilution of the latex in double deionized water. The analyses were carried out at 25 ºC and a run consisted in 1 minutes of temperature equilibration followed by 3 size measurements of 120 seconds each. The values given from the DLS are z-average values obtained through cumulate analysis.

I.1.3. Gel content

The gel content (GC %) of the polymer was measured by means of latex centrifugation in THF for 24 h at 4 °C and 15000 rpm conditions (Sorvall Legend XTR, Thermo Scientific). The insoluble part was measured gravimetrically and the gel content was calculated according to (Equation I.3).

$$Gel\ Content\ (GC\%) = \frac{w_2}{w_1}\ x\ 100 \qquad \text{Equation I.3}$$

Where W_1 is the weight of the total polymer added in THF; and W_2 is the weight of the non-soluble polymer after centrifugation.

I.1.4. Molar mass and distribution

The molar mass distributions of the soluble fraction of the polymer particles (obtained by centrifugation extraction) were measured by THF-based Size Exclusion Chromatography (SEC). The samples were dried and then dissolved in THF to get a concentration of about 2

$mg_{polymer}/1mL_{THF}$. Then, the samples were filtered (polyamide Φ= 45μm) before injection into the SEC instrument. The setup consisted of an autosampler (Waters 717), a pump (LC-20A, Shimadzu), three columns in series (Styragel HR2, HR4, and HR6), and a differential refractometer detector (Waters 2410). The chromatograms were obtained at 35 °C using a THF flow rate of 1 mL/min. The equipment was calibrated using polystyrene standards, and therefore, the molar masses reported relate to polystyrene.

The molar mass of the solution polymers (Chapter 3) was measured via aqueous SEC (SEC/RI) with a 0.1 M NaNO3 solution as eluent at a flow rate of 0.6 mL/min and at 35° C. The equipment was calibrated using PEG standards, and therefore, the molar masses reported relate to the PEG. The equipment includes a LC20 pump (Shimadzu) coupled to aminiDAWN Treos multiangle (3 angles) light scattering laser photometer equipped with an He-Ne laser (l¼658 nm) and an Optilab T-Rex differential refractometer (l¼658 nm) (Wyatt Technology Corp., USA). Separation was achieved using three columns in series (Ultrahydrogel 120, 250, and 2000 with pore sizes of 120, 250, and 2000 A°, respectively, Waters, Barcelona, Spain).

I.1.5. Crosslinking degree

Crosslinking degree or crosslinking density of the polymer particles were related to the capacity of particles to swell in toluene ($g_{toluene}/g_{polymer}$). The strategy to analyse the swell capacity of the particles was the same described by Morton et al.[1] For that, the latex was mixed with toluene (2 mL toluene/g of polymer) for 1 h, and then centrifuged for 30 min at R.T. at 2000 rpm. Then, 2-propanol as internal standard was added and by gas chromatograph (GC) the amount of toluene swollen by polymer particles was calculated (GC-14A, Shimadzu). In GC, the column employed for separation was a BP624 (from SGE analytical science) of 50 m, an inner diameter

of 0.53 mm, and a film thickness of 3.0 µm. The calibration curve for toluene is presented in Figure I.1.

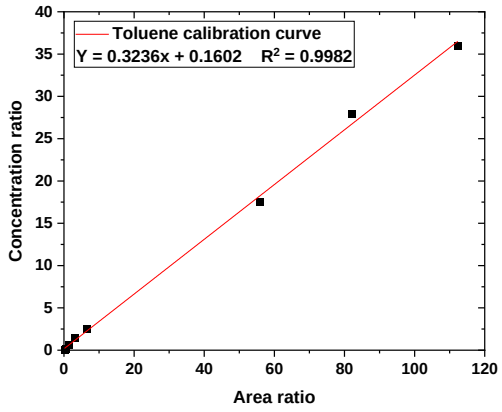

Figure I.1: Calibration curve of toluene by GC.

I.2. Characterization of the 3D monolithic structures

I.2.1. Solid-state ^{13}C-NMR

Chemical reduction process was studied by solid-state ^{13}C-NMR spectra by a Bruker 400 AVANCE III WB spectrometer (9.40 T) for 64 h at a resonance frequency of 100.6 MHz using the standard Bruker double-resonance magic-angle spinning (MAS) sample probe. The samples were packed into a cylindrical zirconia rotor (4 mm external diameter), and then, they were spun at an MAS frequency of 10 kHz. The spectra of the solid samples were recorded using the high-powder decoupled 13C pulse sequence, a time domain of 2 s, a spectral width of 55 kHz, and an interpulse delay of 5 s.

I.2.2. Thermogravimetric analysis (TGA)

Thermogravimetric analyses were performed in a TGA/DSC 3+ apparatus (Mettler Toledo) to study the thermal stability of 3D monolithic structures and to estimate the amount of residual oxygen-containing functional groups within the monolithic structure. Samples of approximately 5 mg were heated under N_2 atmosphere (90 mL/min) from 25 °C to 800 °C at a rate of 10 °C/min.

I.2.3. Pressure drop

The pressure drop through the 3D monoliths and silica carbide particles were measured by Digitron 2080 (Sifam Instrument Limited). The monolith or the particles were placed in a spot-welded cylindrical cartridge of AISI 304 stainless steel (50 µm thickness, Goodfellow) of 16 mm in diameter and different airflows were introduced. Two mesh covers were also spot welded to lock the assembly. A prepared sample and the equipment scheme are presented in Figure I.2.

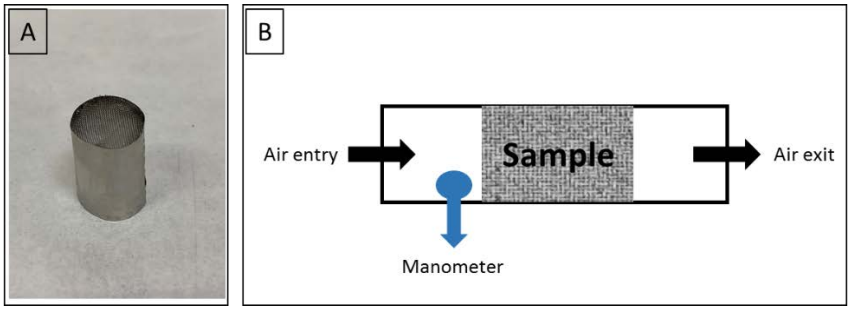

Figure I.2. A prepared sample (A) and the equipment scheme (B).

Before the measurement, a calibration of the valvule´s aperture (where the air come from) and the mass flow controller was carried out. In Figure I.3, the calibration curve is presented.

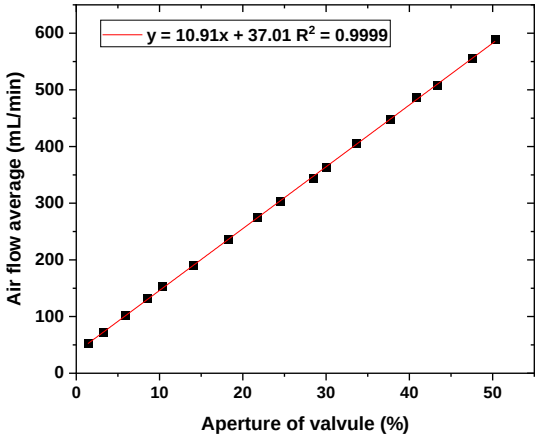

Figure I.3. Calibration curve of the air flow.

I.2.4. Microscopic techniques

I.2.4.1. Scanning Electron Microscopy (SEM)

Scanning electron microscopy (SEM, Hitachi TM3030 tabletop model) was used to study the surface morphology of the monoliths. Images were obtained at an accelerating voltage of 15 kV after the samples were coated with a thin layer of gold.

I.2.4.2. Transmission Electron Microscopy (TEM)

Transmission electron microscopy (TEM); a Tecnai TM G2 20 Twin device at 200 kV (FEI Electron Microscopes). Before analysis, the samples were embedded in epoxy resin, from which ultra-thin sections (80 nm) were cut with a diamond knife on Leica EMFC6 ultramicrotome device and places on a 200 mesh copper grid.

I.2.4.3. Atomic Force Microscopy (AFM)

The surface roughness of both rGO sheets and monoliths were analysed by means of atomic force microscope (AFM, Dimesion ICON from Bruker), using AFM based tapping technique with a resonant frequency of 320 kHz and spring constant 37 N/m. In terms of rGO sheets, prior to the analysis, GO aqueous dispersion with concentration of 0.01 mg/mL was placed into an ultrasonic bath for 15 min at 25 °C, a function of 45 KHz and at 70 % power conditions (Fisher, Bioblock Scientific). After that, in order to study and compared the pre-treated and non-treated rGO sheets, the GO aqueous dispersion was divided in two, and one of the samples was submitted to the pre-treatment step, and the other without it. Both of them were then reduced by AsA (GO:AsA 1:1) for 30 min at R.T., and finally were drop casted in a silicon wafer (4'' silicon wafer, TED PELLA, INC.) substrate.

I.2.5. X-ray Photoelectron Spectroscopy (XPS)

These measurements were carried out by the SGIKER service of the UPV/EHU, at Facultad de Ciencia y Tecnología X Ray Zerbitzua / Servicio de Rayos X Bº Sarriena, s/n 48940 Leioa – Bizkaia, Spain.

X-ray photoelectron spectroscopy (XPS) was used to study the surface chemical states of composing elements of monoliths. XPS measurements were performed in a SPECS system (Berlin, Germany) equipped with a Phoibos 150 1D-DLD analyzer and monochromatic radiation source Al Kαα (1486.7 eV).

An initial analysis was carried out to determine the elements present (wide scan: step energy 1 eV, dwell time 0.1 s, pass energy 80 eV) and detailed analysis of the elements detected

(detail scan: step energy 0.08 eV, dwell time 0.1 s, pass energy 30 eV) with an electron exit angle of 90º. The spectrometer was previously calibrated with Ag (Ag 3d5 / 2, 368.26 eV).

The spectra were adjusted using the CasaXPS 2.3.16 software, which models the Gauss-Lorentzian contributions, after a background subtraction (Shirley). The concentrations were calculated by correcting the values with relative atomic sensitivity factors (Scofield).

I.2.6. Textural properties

The porous texture of the monoliths was characterized by means of N_2 adsorption–desorption at –196 °C in a Micromeritics ASAP2020 apparatus. This technique gives information related to the textural properties of the 3D structures, based on the adsorption-desorption phenomena between the gas (N_2) and solid (adsorbent) at -196ºC. By interpreting the N_2 adsorption-desorption isotherms and applying different mathematical models, diverse textural parameters can be calculated, such as BET surface area, pore volume, and pore size distribution.

The measurements of the 3D structures were carried out in the borosilicate sample holder presented in Figure I.4.

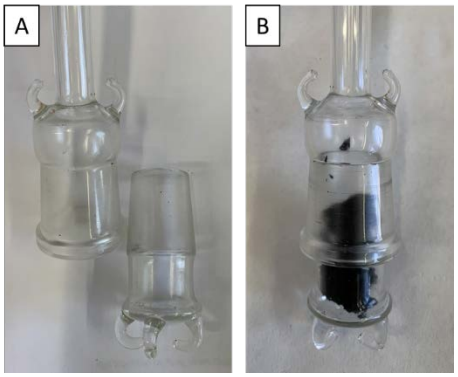

Figure I.4. Sample holder; (A) empty and (B) with the 3D structure.

Prior to the analysis, the materials were degassed at 60-100 ℃ during 8 h under vacuum, in order to remove moisture and other unwanted adsorbates. After degassing, the sample is analyzed by introducing N_2 as adsorbate and maintaining the temperature at -196 °C. The relative pressure is varied from values of 0.01 to values close to 1, and the N_2 volume adsorbed in the samples is measured at equilibrium. Once the saturation is reached, i.e. the pores of the sample are considered filled with N_2, desorption is carried out by decreasing the relative pressure and recording the volume of the gas adsorbed at each relative pressure. The equipment represents the N_2 adsorbed volume versus the relative pressure, obtaining a N_2 adsorption-desorption isotherm. The shape of the isotherm provides information about the porosity of the sample.

The surface area (BET, m^2/g) of the 3D monoliths was calculated by the BET method, named after their developers Stephen Brunauer, Paul Hugh Emmett and Edward Teller. It is a well-known theory for the physical adsorption of gas molecules on a solid surface, and it is an extension of the Langmuir theory.[2] The concept of the BET theory is based on the following hypotheses: uniform adsorption sites, gas molecules adsorb on a solid in layers infinitely (multilayer adsorption), the occupation probability of sites in layers higher than one is zero unless

all underlying sites are occupied, and the Langmuir theory can be applied to each layer. The BET equation describes the volume adsorbed at monolayer coverage, and it is expressed by Equation I.4:

$$\frac{p/p_0}{v\,(1-p/p_0)} = \frac{1}{v_m\,C} + \frac{C-1}{v_m\,C}\frac{p}{p_0} \qquad \text{(Equation I.4)}$$

where p and p_0 are the equilibrium and saturation pressure of adsorbates at the temperature of adsorption, v_m is the volume adsorbed at monolayer coverage, v is the gas volume adsorbed at a certain relative pressure, and C is BET constant.

To calculate the BET surface area, the adsorption isotherm has to be transformed into the "BET plot" in order to calculate the gas volume adsorbed in one layer (v_m). For that, $\frac{p/p_0}{v\,(1-p/p_0)}$ is plotted against p/p_0, where v_m and C can be calculated. Finally, the knowledge about the monolayer capacity v_m allows the calculation of the BET specific surface area (S_{BET}) (Equation I.5):

$$S_{BET} = V_{mol} * N_A * a \qquad \text{Equation I.5}$$

where V_{mol} is the molar volume, N_A is the Avogadro constant, and a is the cross section of an adsorbed molecule (in case of N_2 is 0.162 nm^2).

Nevertheless the BET method can be only adjusted in a limited part of the adsorption isotherm (the plot is linear in the range of relative pressures between 0.05 and 0.30) and in II and IV isotherm types (Figure I.5), where the hypothesis of the method are satisfied.

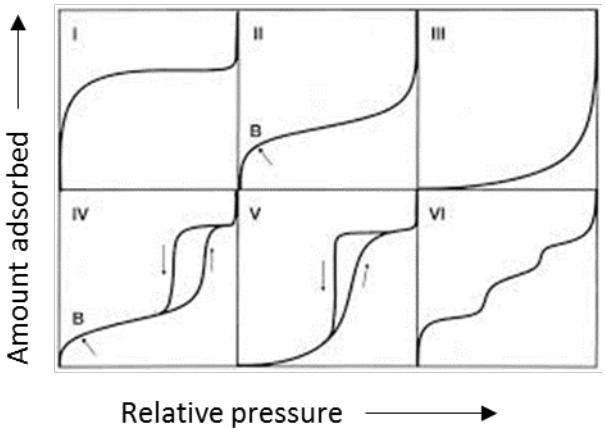

Figure I.5. Classification of physisorption isotherms according to IUPAC.[3]

On the other hand, the total pore volume was determined from single point adsorption at P/P_0 near to 0.995, under the assumption of the Gurvich rule, which assumes that at pressures close to saturation, the gas adsorbed corresponds to the total volume of the pores.

The pore size distribution was obtained by Barret-Joyner-Halenda (BJH) model using the adsorption isotherm.[4] Based on the Kelvin equation at each relative pressure, the pore size distribution can be obtained (Equation I.6). Nevertheless, the following assumptions should be satisfied: no micropores exist, the pore passage is rigid and suitable for cylindrical pores, and at highest relative pressure, all the pores have been filled.[5]

$$r_k = \frac{-2\,V_{mol}\,\sigma\,cos\Phi}{R\,T\ln(p/p_0)} \qquad \text{Equation I.6}$$

where r_K is capillary Kelvin radius, p/p_0 is the equilibrium pressure over the saturated vapor pressure of the adsorbed gas, V_{mol} is the mol volume of the liquid adsorbate, T is the

absolute temperature, R is the ideal gas constant, σ is the interfacial tension, and Φ is the wetting angle.

Finally, t-plot method was used for estimating the micropore volume without the need to measure the low pressure micropore-filling section of the isotherm, by comparison with a reference isotherm of nonporous material.

I.3. Gas adsorption measurements

I.3.1. CO_2 and N_2 adsorption capacity (volumetrically)

The materials' CO_2 and N_2 adsorption capacities were measured using a Micromeritics ASAP 2020 apparatus (i.e., volumetrically) at 25 °C. Prior to the measurements, samples were outgassed at 60-100 °C during 8 h under vacuum. The CO_2 and N_2 uptake isotherms were separately measured up to 1 atm under static conditions.

I.3.2. CO_2 adsorption capacity (gravimetrically)

The CO_2 adsorption capacity was also determined by an Intelligent Gravimetric Analyser (IGA, HIDEN Analytical, HAL IGA286) (i.e., gravimetrically) at 25 °C and 60 °C. Prior to the measurements, samples were outgassed at 25 °C during 3 h under vacuum. Then, the CO_2 adsorption uptake was measured in the pressure range of 0-20 atm under static conditions.

I.3.3. Selectivity

The CO_2/N_2 selectivity was calculated by the ideal adsorbed solution theory (IAST) using only data for the pure-component adsorption equilibria at the same temperature (25 °C) and on

the same adsorbent.[6] The individual isotherms were modelled by Langmuir, Freundlich, and their combined model isotherms. The validity of these models is evaluated by the correlation coefficient (R^2). R^2 closer to unity implies the best fitting towards the particular isotherm model, that in this case, Freundlich gave the highest R^2. The linear form of the Freundlich model used is shown by Equation I.7:

$$log\ q_e = logK_f\ + \left(1/n\right) log P_e \qquad \text{(Equation I.7)}$$

where q_e is the amount of gas adsorbed (cm^3/g); P_e is the equilibrium pressure (bar); and Kf ($cm^3/g\ bar^{1/n}$) and n are Freundlich constants.

The selectivity was calculated according Equation I.8:

$$S_{CO_2/N_2} = \left(q_{CO_2}/P_{CO_2}\right) / \left(q_{N_2}/P_{N_2}\right) \qquad \text{(Equation I.8)}$$

where q is the amount of CO_2 adsorbed (cm^3/g) and P is the partial pressure of respective gas.

The respective partial pressures of the components for these calculations were taken from the composition of flue gas from a coal-fired power plant, which contains approximately 15 % CO_2 and 85 % N_2.

I.4. References

(1) Morton, M.; Kaizerman, S.; Altier, M. W. Swelling of Latex Particles. *Rubber Chem. Technol.* **1959**, *32* (3), 814–824.

(2) Brunauer, S.; Emmett, P. H.; Teller, E. Adsorption of Gases in Multimolecular Layers. *J.*

Am. Chem. Soc. **1938**, *60* (2), 309–319.

(3) Thommes, M.; Kaneko, K.; Neimark, A. V.; Olivier, J. P.; Rodriguez-Reinoso, F.; Rouquerol, J.; Sing, K. S. W. Physisorption of Gases, with Special Reference to the Evaluation of Surface Area and Pore Size Distribution (IUPAC Technical Report). *Pure Appl. Chem.* **2015**, *87* (9–10), 1051–1069.

(4) Barrett, E. P.; Joyner, L. G.; Halenda, P. P. The Determination of Pore Volume and Area Distributions in Porous Substances. I. Computations from Nitrogen Isotherms. *J. Am. Chem. Soc.* **1951**, *73* (1), 373–380.

(5) Fu, S.; Fang, Q.; Li, A.; Li, Z.; Han, J.; Dang, X.; Han, W. Accurate Characterization of Full Pore Size Distribution of Tight Sandstones by Low-Temperature Nitrogen Gas Adsorption and High-Pressure Mercury Intrusion Combination Method. *Energy Sci. Eng.* **2021**, *9* (1), 80–100.

(6) PRAUSNITZ, A. L. M. and J. M. Thermodynamics of Mixed-Gas Adsorption. *A.1.Ch.E. J.* **1965**, *11* (1), 121–126.

APPENDIX II

Fitting curves by Freundlich model

Appendix II. Fitting curves by Freundlich model

II.1. Chapter 2

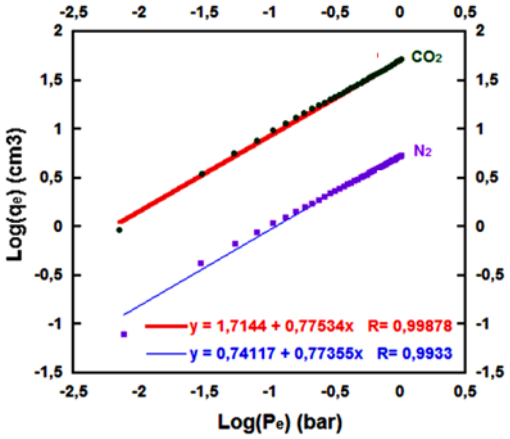

Figure II.1. Freundlich equation fitting curves for CO_2 isotherm (red curve and red fitting equation) and for N_2 isotherm (blue curve and blue fitting equation).

II.2. Chapter 3

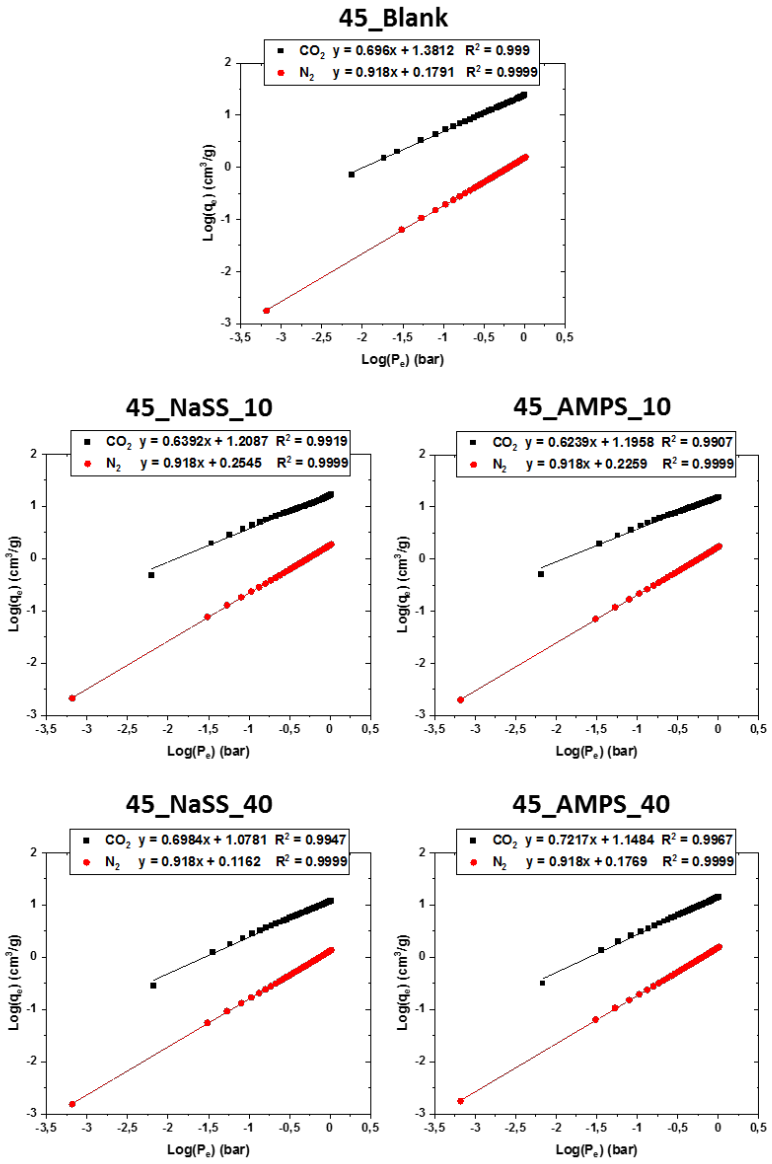

Figure II.2. Freundlich equation fitting curves for CO_2 isotherm (black curve) and for N_2 isotherm (red curve) for monoliths synthesized at 45 °C and GO:AsA mass ratio 1:1.

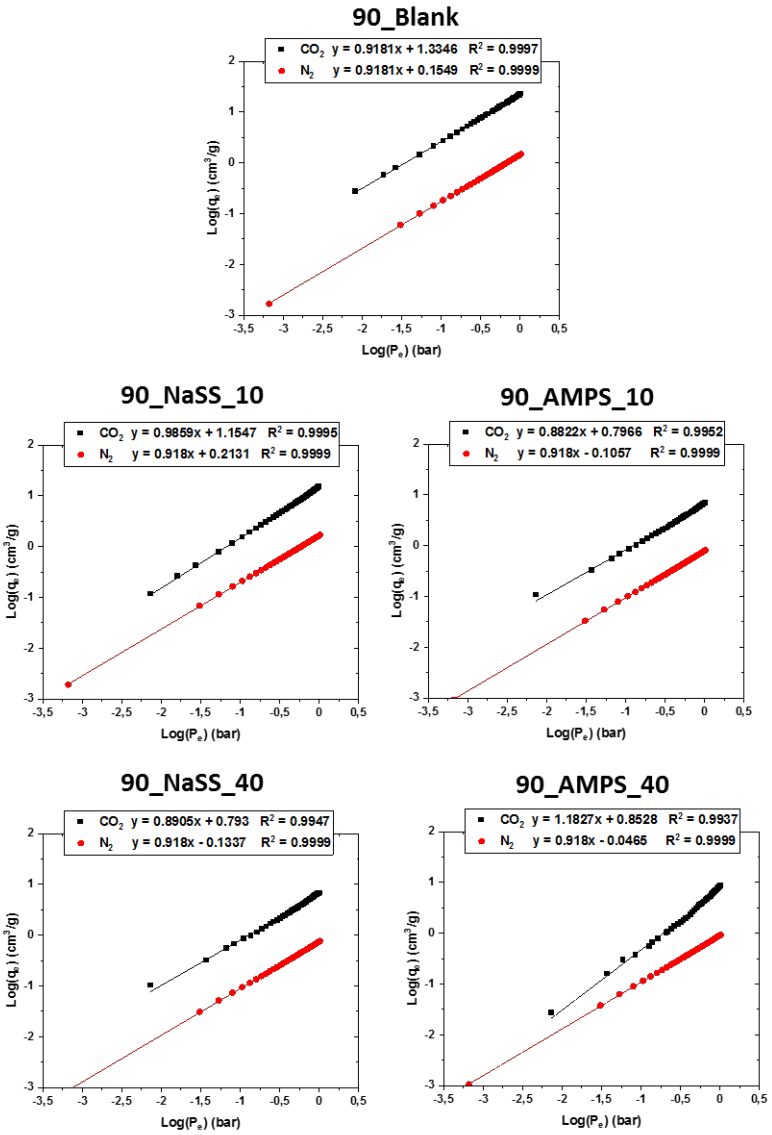

Figure II.3. Freundlich equation fitting curves for CO_2 isotherm (black curve) and for N_2 isotherm (red curve) for monoliths synthesized at 90 °C and GO:AsA mass ratio 1:1.

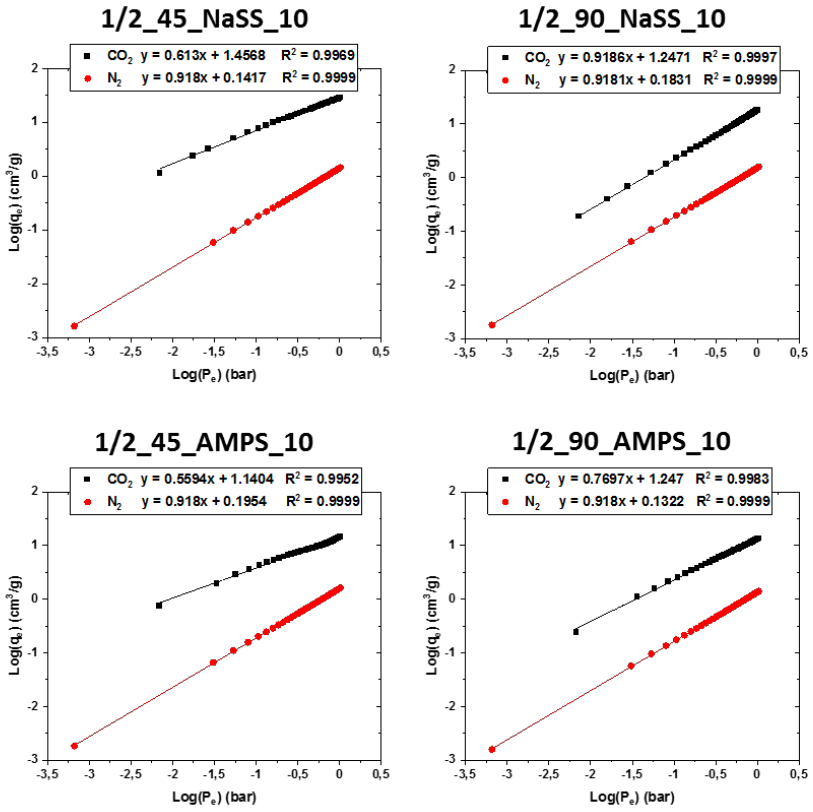

Figure II.4. Freundlich equation fitting curves for CO_2 isotherm (black curve) and for N_2 isotherm (red curve) for monoliths synthesized at 45 °C and 90 °C and GO:AsA mass ratio 1:0.5.

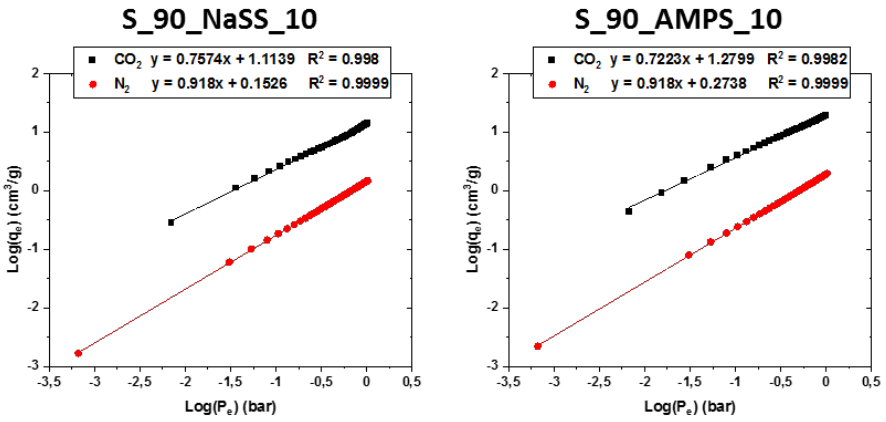

Figure II.5. Freundlich equation fitting curves for CO_2 isotherm (black curve) and for N_2 isotherm (red curve) for monoliths synthesized at 90 °C and GO:AsA mass ratio 1:0.5 using solution polymers.

II.3. Chapter 4

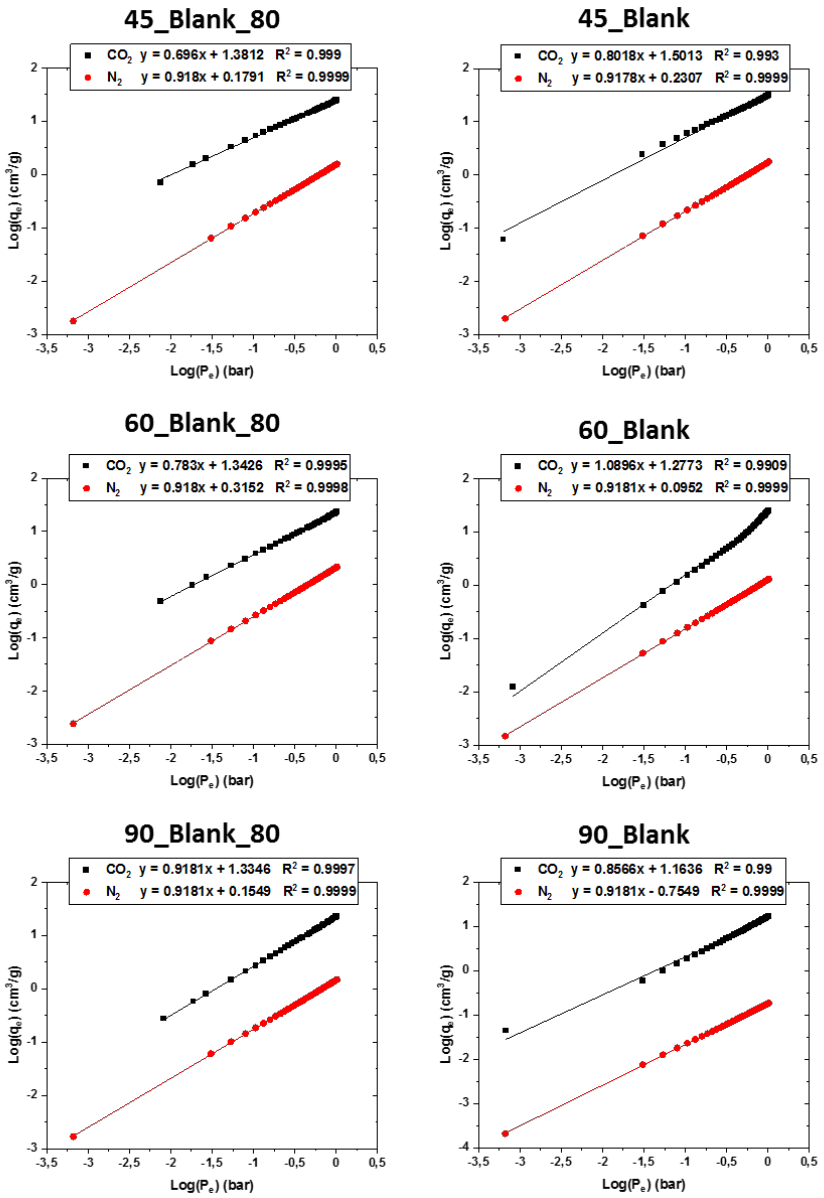

Figure II.6. Freundlich equation fitting curves for CO_2 isotherm (black curve) and for N_2 isotherm (red curve) for 3D rGO monoliths.

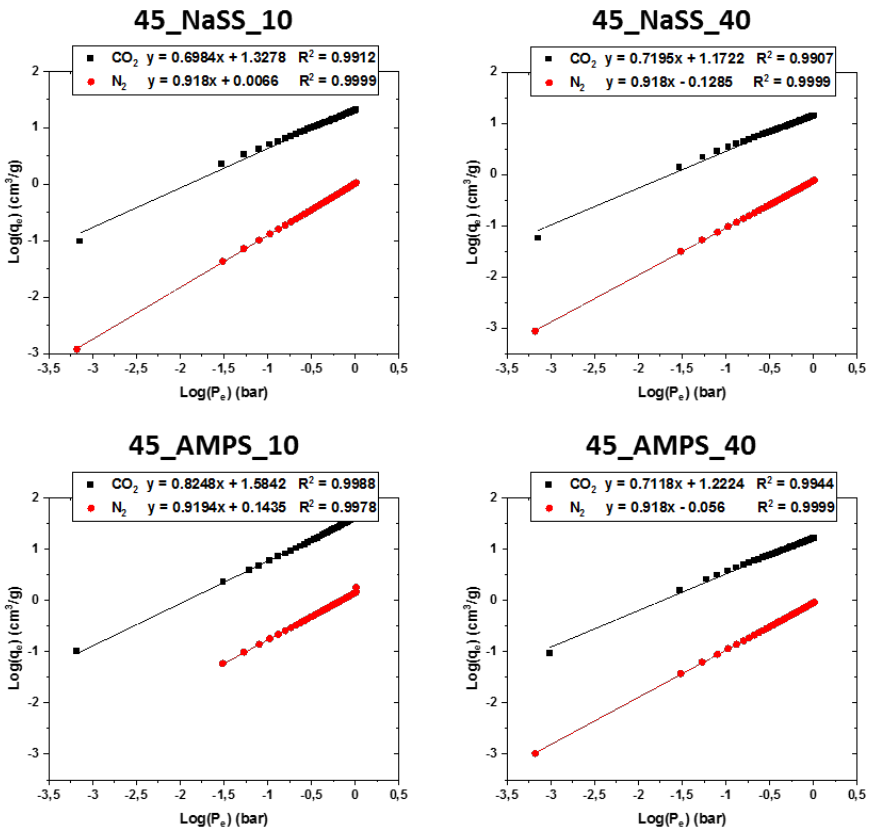

Figure II.7. Freundlich equation fitting curves for CO_2 isotherm (black curve) and for N_2 isotherm (red curve) for composites synthesized at 45 °C.

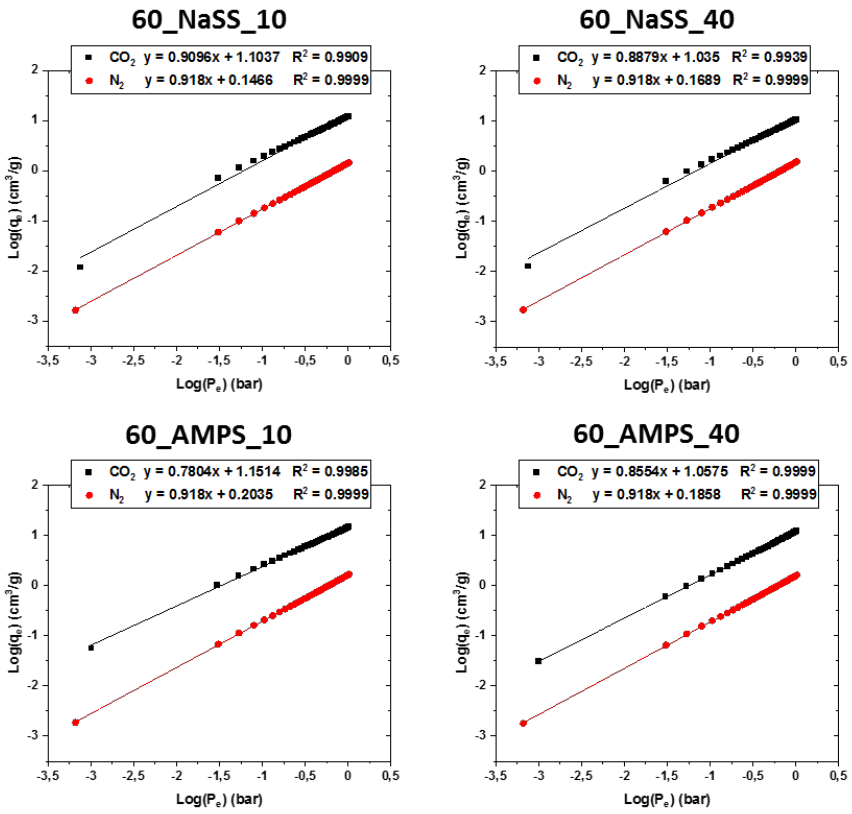

Figure II.8. Freundlich equation fitting curves for CO_2 isotherm (black curve) and for N_2 isotherm (red curve) for composites synthesized at 60 °C.

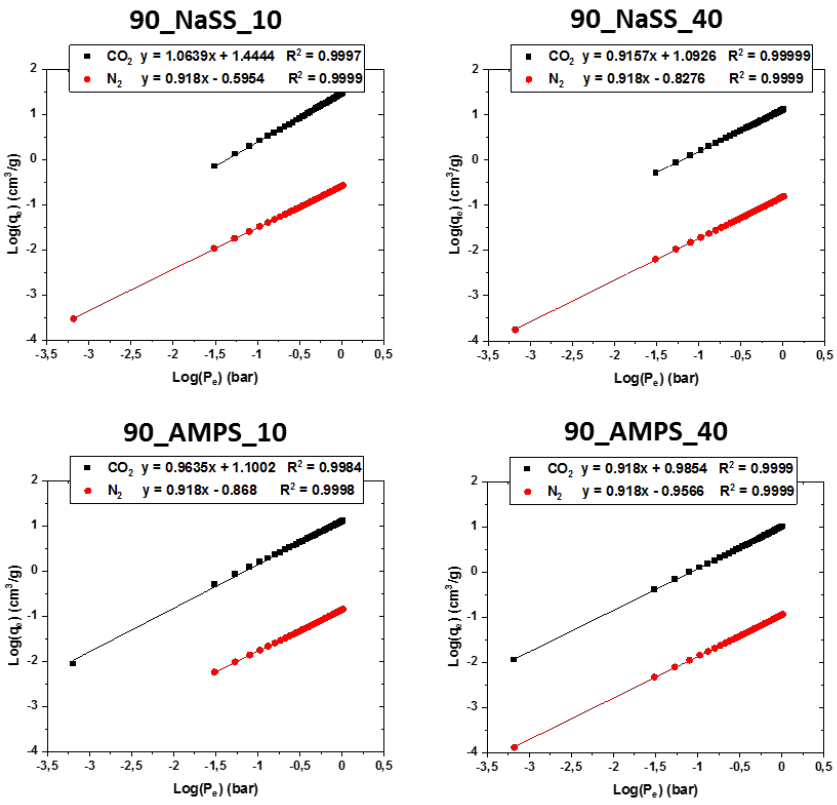

Figure II.9. Freundlich equation fitting curves for CO_2 isotherm (black curve) and for N_2 isotherm (red curve) for composites synthesized at 90 °C.

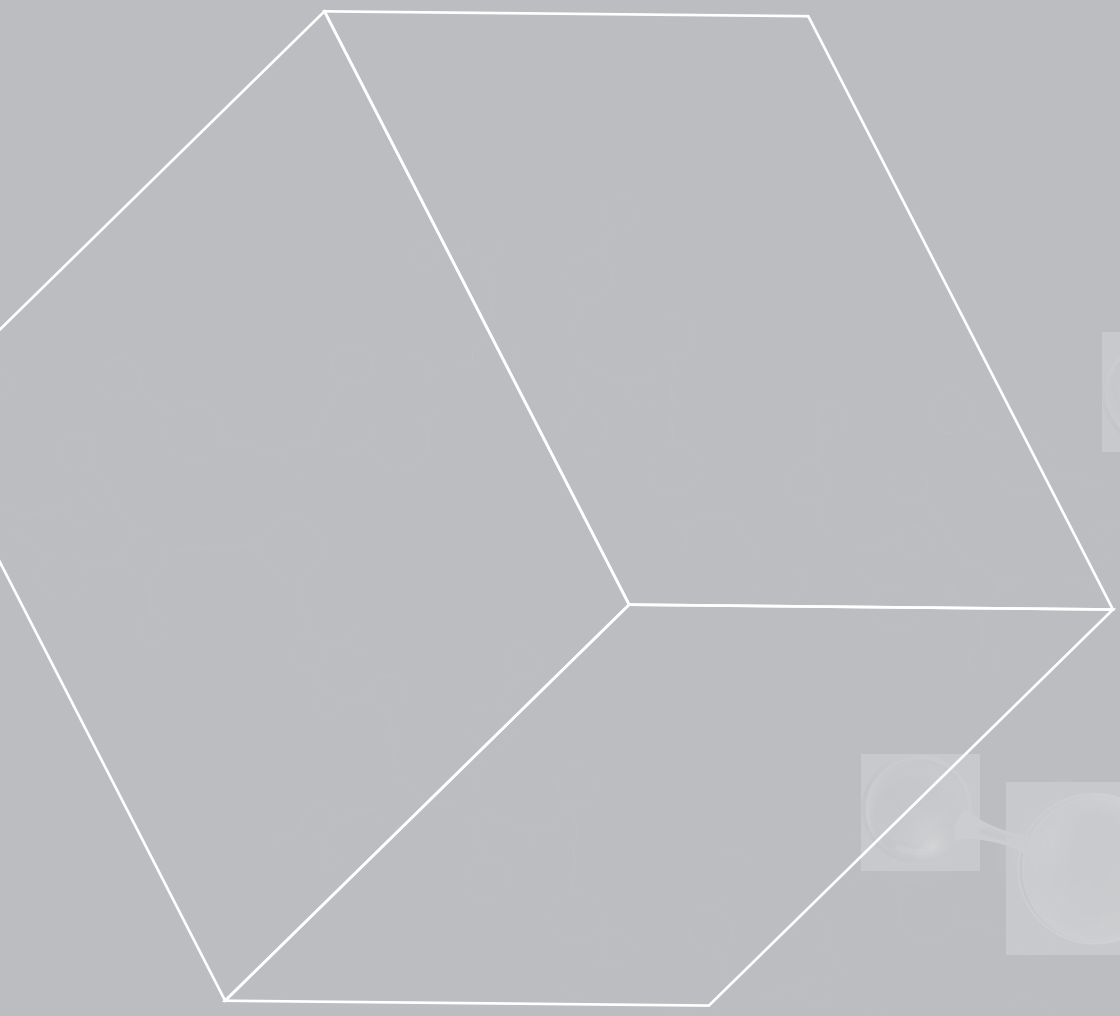

List of publications and conference presentations

List of publications and conference presentations

Publications

1. Politakos, N.; **Barbarin, I**.; Cantador, L. S.; Cecilia, J. A.; Mehravar, E.; Tomovska, R. Graphene-Based Monolithic Nanostructures for CO2 Capture. *Ind. Eng. Chem. Res*. **2020**, 59 (18), 8612–8621.

2. Politakos, N.; **Barbarin, I**.; Cordero-Lanzac, T.; Gonzalez, A.; Zangi, R.; Tomovska, R. Reduced Graphene Oxide/Polymer Monolithic Materials for Selective CO_2 Capture. *Polymers (Basel)*. **2020**, 12 (4).

3. Martínez-Álvarez, I.; Le Menach, K.; Devier, M. H.; **Barbarin, I**.; Tomovska, R.; Cajaraville, M. P.; Budzinski, H.; Orbea, A. Uptake and Effects of Graphene Oxide Nanomaterials Alone and in Combination with Polycyclic Aromatic Hydrocarbons in Zebrafish. *Sci. Total Environ*. **2021**, 775.

4. Politakos, N.; Cantador, L. S.; Cecilia, J. A.; **Barbarin, I**.; Tomovska, R. CO_2 Capture by Reduced Graphene Oxide Monoliths with Incorporated Ceo2 Grafted with Functionalized Polymer Brushes. *Appl. Sci*. **2021**, 11 (23).

5. **Barbarin, I**.; Politakos, N.; Serrano-Cantador, L.; Cecilia, J. A.; Sanz, O.; Tomovska, R. Towards Functionalized Graphene/Polymer Monolithic Structures for Selective CO_2 Capture. *Microporous Mesoporous Mater*. **2022**, 337 (April), 111907.

6. Stankovic B.; **Barbarin I**.; Sanz O.; Tomovska R.; Ruipérez F. Experimental and theoretical study of the effect of different functionalities of graphene oxide/polymer composites on selective CO_2 capture. *Submitted.*

7. **Barbarin, I**.; Politakos, N.; Serrano-Cantador, L.; Cecilia, J. A.; Sanz, O.; Tomovska, R. Creation of N_2-phobic morphology of 3D graphene/polymer monolithic structures for outstanding CO_2/N_2 selectivity. *Submitted.*

8. **Barbarin, I**.; Politakos, N.; Serrano-Cantador, L.; Cecilia, J. A.; Sanz, O.; Tomovska, R. Tailoring of textural properties of 3D composite monoliths made of graphene and highly crosslinked polymer particles towards improved CO_2 sorption. *Submitted.*

Patent

- Tomovska, R.; Politakos, N.; Barbarin, I. Fotocatalizadores de óxido de grafeno y semiconductor. *Submitted* to "Oficina Española de Patentes y Marcas" No/Ref: P185573ES.

Oral presentations

- "3D rGO/polymer porous composite monoliths for CO_2 capture" by Iranzu Barbarin and Radmila Tomovska. 2nd Coordination Meeting NATO SfP Project G5244. Prague 6-7 June, 2019.

- "Graphene-polymer porous composites for CO_2 capture". Tomovska, R; Politakos N., Barbarin, I. Invited lecture. GEP-SLAP. 8-12 May, 2022. Donostia-San Sebastián.

Poster presentations

- "3D Self-assembly graphene-polymer composites for CO_2 capture" by Iranzu Barbarin, Tomás Cordero-Lanzac, Nikolaos Politakos, and Radmila Tomovska. Sixth International Conference on Multifunctional, Hybrid and Nanomaterials. 11-15 March 2019, Sitges, Spain.